Silicalite-1 Membranes Synthesis, Characterization, CO_2/N_2 Separation and Modeling

Muhammad Tawalbeh

Thesis submitted to the
Faculty of Graduate and Postdoctoral Studies
In partial fulfillment of the requirements
for the Doctorate in Philosophy degree in Chemical and Biological Engineering

Department of Chemical and Biological Engineering
Faculty of Engineering
University of Ottawa

Statement of Contributions of Collaborators and/or Co-Authors

I hereby declare that the work presented here is my own effort and I am the sole author of this thesis. I am the one who performed all the experiments and the analyses under the scientific supervision of Dr. Handan Tezel and Dr. Boguslaw Kruczek. I have acknowledged other sources of information and assistance in analyses where applicable. The editorial and scientific reviews, as well as the comments were provided by my research project supervisors Dr. Handan Tezel and Dr. Boguslaw Kruczek.

Chapter 3 and Chapter 4 have two additional authors other than the thesis supervisors, Dr. C. Detellier and Dr. S. Letaief. Both Dr. C. Detellier and Dr. S. Letaief helped with the interpretation and the understanding of the morphology results. Dr. S. Letaief also assisted with the conduction of the morphology analysis.

In Chapters 5 and 6, M. Al-Ismaily was a co-author in addition to the supervisors. In Chapter 5 M. Al-Ismaily helped in coding the protocol that was used to recover the gas permeances from mixed gas permeation. In Chapter 6 M. Al-Ismaily helped in coding the solution of the equations that was used to extract the exchange diffusivity from the mixture permeation experiments and with building the optimization program that allowed the exchange diffusivities extraction. In chapter 6, D. Carter was also a co-author; he assisted in conducting gas separation experiments at high feed flow rates.

ABSTRACT

Zeolite membranes are considered to be a promising alternative to polymeric membranes and they have the potential to separate gases under harsh conditions. Silicalite-1 membranes in particular are easy to prepare and suitable for several industrial applications. In this research project, silicalite-1/ceramic composite membranes were prepared using the pore plugging hydrothermal synthesis method and supports with zirconium oxide and/or titanium oxide as active layers. The effect of the support's pore size on the morphology and permeation performance of the prepared membranes was investigated using five supports with different active layer pore sizes in the range of 0.14 – 1.4 μm.

The prepared membranes were characterized by X-ray diffraction (XRD), scanning electron microscope (SEM), electron diffraction spectrometer (EDS), single gas and binary gas mixtures permeation tests. The results confirmed the presence of a typical silicalite-1 zeolite structure with a high internal crystalline order grown inside the pores of the active layer of the supports, with a dense film covering most of the supports active layers. Silicalite-1 crystals in the prepared membranes were preferably oriented with either a- or b-axes perpendicular to the support surface.

Single gas permeation results illustrated that the observed permeances were not directly related to the kinetic diameter of permeants. Instead, the transport of the studied gases through the prepared membranes occurred by adsorption followed by surface diffusion mechanism. Binary gas tests performed with CO_2 and N_2 mixtures showed that the prepared

membranes were selective and very permeable with CO_2/N_2 permselectivities up to 30 and a CO_2 permeances in the order of 10^{-6} mol m^{-2} Pa^{-1} s^{-1}.

A model was developed, based on Maxwell−Stefan equations and Extended Langmuir adsorption isotherm, to describe the transport of binary CO_2 and N_2 mixtures through the prepared silicalite-1 membranes. The model results showed that the exchange diffusivities ($Đ_{12}$ and $Đ_{21}$) were less dependent on the feed pressure and feed composition compared to the permeances and the permselectivities. Hence, they are more appropriate to characterize the intrinsic transport properties of the prepared silicalite-1 membranes.

RÉSUMÉ

Les membranes à base de zéolites sont considérées comme une alternative prometteuse aux membranes de polymères et elles ont le potentiel de séparer les gaz dans des conditions extrêmes. En particulier, les membranes à base de silicalite-1 sont faciles à préparer et versatiles dans leurs applications industrielles. Dans cette thèse, des membranes composites à base de silicalite-1 et de céramiques furent préparées avec succès en utilisant la méthode de synthèse par obstruction hydrothermal de pores et supportées par des couche active faites d'oxyde de zircon ou de titane. L'effet de la taille des pores sur la morphologie et sur la performance de perméation des membranes préparées fut examiné en utilisant cinq supports avec une taille de pores dans les zones actives entre 0.14 et 1.4 µm.

Les membranes préparées furent caractérisées principalement par les méthodes de diffraction de rayons-X (XDR), de microscopie électronique à balayage (SEM), de spectrométrie d'électrons diffractés (EDS) et de perméation de gaz purs et de mixtures binaires. Les résultats confirment la présence d'une structure zéolite typique du silicalite-1 avec une grande cristallinité interne à l'intérieur des pores de la couche active sur les supports ainsi que d'un film dense recouvrant ceux-ci. Les cristaux de silicalite-1 présents dans les membranes préparées étaient orientés préférablement avec l’axe a ou b perpendiculaire à la surface du support.

Les résultats de perméation des gaz purs démontrent que la perméabilité observée n'est pas reliée directement au diamètre cinétique des perméats. Plutôt, le transport des gaz étudiés au

travers de ces membranes s'est fait par un mécanisme d'adsorption suivis d'une diffusion en surface. Les tests utilisant des gaz binaires furent faits avec un mélange de CO_2 et de N_2 et ont démontré que les membranes étaient sélectives et très perméables avec une sélectivité de perméation CO_2/N_2 jusqu'à 30 et une perméabilité de CO_2 de l'ordre de 10^{-6} mol m^{-2} Pa^{-1} s^{-1}.

Un modèle de la description du transport de mixtures binaires de CO_2 et de N_2 au travers des membranes de silicalite-1 préparées basé sur les équations de Maxwell-Stefan et de l'adsorption isotherme étendue de Langmuir a été développé. Ce modèle a démontré que les diffusivités d'échange ($Đ_{12}$ et $Đ_{21}$) sont beaucoup moins dépendantes aux conditions d'opération que la sélectivité de perméation et la perméabilité. Ainsi, il est plus approprié de caractériser les propriétés intrinsèques de transport des membranes préparées de silicalite-1.

"Glory to You (O Lord), knowledge we have none, except what You have taught us. Verily, it is You are, the all-knower and the all-wise"

Quraan, 2:32.

ACKNOWLEDGMENTS

To begin with, I would like to express my sincere gratitude and appreciation to my thesis supervisors Dr. Handan Tezel and Dr. Boguslaw Kruczek for their continuous encouragement, enthusiastic support and guidance through the past six years of my life.

I would like to extend my gratitude to the technical staff in the department of chemical and biological engineering: Louis Tremblay, Gerard Nina, and Franco Ziroldo for their cooperation and prompt help when needed especially during the time when I was building my experimental setup.

I wish to thank my friends in the department of chemical engineering for the good company and fruitful discussions that made the study and research journey more enjoyable. Many thanks to Dr. Sadok Letaief and Patrick Plouffe for the time and effort they put in translating the abstract of this thesis into French. I also would like to thank my colleagues and group members Dr. Peiyuan Li, Dr. Rudy Jones, Niloofar Abdehagh, David Carter, Siamak Lashkari, Qiang Wang and Golnaz Bissadi for their positive feedback and interesting discussions.

I express my gratitude and appreciation to Dr. Christion Detellier and Dr. Sadok Letaief from the Centre for Catalysis Research and Innovation, and Department of Chemistry at University of Ottawa for their generous contributions in terms of assistance and discussions.

I also express my gratitude to each of the professors in my thesis committee for taking the time to review this dissertation and for their suggestions.

I want to say thank you to my wife, Amani Al-Othman for her love, support and patience during this journey, and to my children Omar Alfarooq and Farah for filling my life with energy and joy.

Last and foremost, I wish to thank my parents, my brothers and sisters for their nonstop love and support to become the person I am today.

TABLE OF CONTENTS

LIST OF FIGURES

LIST OF TABLES

CHAPTER ONE

GERNERAL INTRODUCTION

Chapter 1 – General Introduction

1.1 Introduction

In general, membrane processes offer significant energy savings as opposed to the available traditional separation processes such as distillation and absorption. Compared to traditional thermal processes, membranes can achieve the separation tasks with an order of magnitude lower energy requirements [1]. Consequently, membranes have acquired an important position in chemical industry, and their use in separation processes has grown dramatically over the past 20 years [2,3].

Membranes have been used in gas separation processes. It is a rapidly-growing field of research resulting in commercial applications since 1980's and becoming viable alternative for the traditional methods. Membranes are proving to be one of the most significant unit operations used in industry in the last 25 years [4].

Membrane can be defined as a selective barrier that separates two phases and restricts the transport of various chemical species [3]. The feed to the membrane is separated into two streams: the retentate and the permeate. Either the retentate or permeate could be the product stream. In principle, all materials that form sufficiently thin and stable films can be used as membranes. This includes metal, glass, ceramic and polymers as well as liquids. Thus, a membrane can be homogenous or heterogeneous, symmetric or asymmetric, charged or uncharged, dense or porous, and solid or liquid. Membranes are normally classified according to their pore size, material they are made of, and morphology.

Zeolite membranes, which are a sub-division of the ceramic membranes, are basically crystalline silicates or aluminosilicates with a regular three dimensional pore structure grown on porous support. These crystalline materials have pore sizes between 0.3 and 1.3 nm [5], which gives them the potential to perform many industrially important separations. Zeolite membranes have many advantages over polymeric membranes. They provide better thermal stability; better solvent resistance, perfect shape selectivity and can withstand high pressures and temperatures [6]. MFI (Mordenite Framework Inverted) zeolites, in particular ZSM-5 (Zeolity Socony Mobil - five) and its Al-free analog, silicalite-1 that possess channels defined by 10-membered oxygen rings with a diameter of 5.5Å, have the potential to separate gases by molecular sieving [7,8]. However, this molecular sieving principle requires a zeolite membrane with no cracks or pinholes [9,10]. Nevertheless, a very high selectivity is also possible when the zeolite pore sizes are larger than the mixture of gas molecules. This is due to the difference in adsorption selectivities or the difference in diffusivities of the various components in the mixture [11,12].

Historically, the efforts to prepare zeolite membranes started in the late 1980s, but the first MFI type zeolite membranes with good permeation and separation properties were successfully prepared in early 1990s [13]. Among the different types of zeolites available, MFI zeolites are of particular interest because of their pore size (~ 5.5Å) which is suitable for several industrially important separations [14] and the relatively easy synthesis from a variety of silica sources and structure directing agents [15]. Besides, experiments proved that only the high silica to alumina zeolites show shape selective separation behaviour [16].

Thus, the most progress in preparation of zeolite membranes has been achieved for silicalite-1 zeolite. As a result, silicalite-1 has been chosen to prepare the membranes in this work.

Separation processes require a membrane with high permeability and selectivity. For zeolite membranes, for example, to have high permeability, the membrane active layer thickness needs to be quite small (on the order of microns) and preferably less than 100 nm [17]. However, zeolites do not have the inherent mechanical strength to form self-supported membranes in this thickness range; therefore, macroporous supports made of alumina, glass, or stainless steel are usually used to provide the essential mechanical strength [18].

Most researchers use alumina and stainless steel as support for zeolites membranes. However, using these materials as support is associated with several disadvantages. Using stainless steel as a support leads to a mechanical stress due to the difference in thermal expansion between the zeolite layer and the support [19]. As a result, a matching material in between the membrane and the support layers is needed, and the implantation of this matching material requires more heating which adds up more cost to the process. Using alumina as a membrane support also imposes another disadvantage, which is the dissolution of aluminium ions from the support under the harsh hydrothermal environment and their integration into the zeolite network. The dissolved aluminum from the support will replace the silicon in the network which will increase the number of cations needed in the network to balance the resultant negative charge [20]. Thus, it is clear that aluminum incorporation inside the zeolite structure leads to a less homogenous and more hydrophilic zeolite layer [16]. It was also shown that the presence of aluminum in zeolite network decreases the

molecular sieving ability of the zeolite membrane [21]. To eliminate these effects, chemically stable supports made of zirconia and/or titania are proposed in this thesis.

Zirconia and titania are more thermally and chemically stable than alumina [22,23], and they can withstand harsher environment [24]. Hence, the ions from these materials will not dissolve under the zeolite hydrothermal synthesis conditions into the zeolite network [25]. However, even if the dissolution occurs, they will not add any negative charge to the zeolite network; on the contrary, they will increase the network stability [26,27].

Zeolite membranes are usually synthesized using one of the following four methods: the in-situ crystallization method [28], vapor phase transport [29], secondary growth [6,30] and pore plugging methods [31,32]. The secondary growth method is the most commonly used synthesis method, while the pore plugging is a relatively new method. In comparison to the secondary growth, the pore plugging method is easier in terms of preparing large membrane areas that will not generate defects larger than the pore size of the support material. Another advantage of the pore plugging method is that the zeolite crystals in the membranes prepared are protected against shocks and abrasion since they are inside the pores of the support [31]. Pore plugging method also allows a better control of the membrane thickness by limiting the zeolite layer growth on top of the active layer of the support to few microns. Any crystallization below the active layer of the support will not have a significant effect on the membrane performance due to the difficulty of plugging the large pores of the layers below the active layer. Due to the previous advantages, pore plugging synthesis method was chosen to prepare the silicalite-1 membranes in this thesis.

Modeling the multicomponent diffusion within the zeolite layer pores is crucial for successful design, prediction of the permeation and dynamic behaviour, optimization of the operating conditions, and scaling up of any zeolite membrane based process. Membranes are usually characterized using permeances or permeabilities. However, it has been shown that the permeances in zeolite membranes are highly dependent on the feed pressure and the feed composition [33-35]. Furthermore, altering feed pressure and/or feed composition can decrease or increase the gas permeances by an order of magnitude. The permeation through zeolite membranes is governed by both the adsorption/surface diffusion and the activated micropore diffusion mechanisms. Thus, Maxwell-Stefan (M-S) approach appears to be the most successful and physically sound approach to describe multicomponent mixtures diffusion through zeolite membranes [36-38]. Many recent studies have used M-S equations to interpret the results of the permeation experiments [32, 39-41].

The M-S approach allows the prediction of the mixtures permeation characteristics based on the single component adsorption and diffusion properties [36]. Usually, to simplify the M-S equations of a mixture, the binary exchange diffusivities are assumed to be equal. This assumption is justified by the reciprocity nature of Vignes correlation [42] that is usually used to estimate the exchange diffusivities for binary mixtures. For this assumption to be valid, the adsorption saturation capacities for the two components in the mixture should be equal. In this research project, a model has been developed, based on Maxwell-Stefan equations. The single component adsorption, diffusivity, and the extended Langmuir adsorption isotherm, were used to describe the transport of CO_2/N_2 binary mixture through silicaite-1 membrane. This model was used to estimate the exchange diffusivities from the

binary permeation experiments. Two scenarios were considered during the model development. In the first scenario the exchange diffusivities were assumed equal while in the other scenario, they were assumed non-equal. A comparison between the results from both scenarios was made to validate the assumption in the first scenario.

1.2 Research objectives

The principal objective of this work was to develop easy to scale up tubular Silicalite-1 zeolite gas separation membranes by the pore plugging synthesis method using supports with active layers made of zirconia and/or titania. In support of the principal objective, a sub objective of this research project was to study and investigate the properties of the synthesized membranes, including their applicability for the separation of CO_2/N_2 mixtures at different feed pressures and feed compositions. A second sub objective of this work was to study the effect of the pore size of the active layer of the supports on the morphology and the permeation properties of prepared membranes. A third sub objective of this research project was to develop a detailed model based on Maxwell-Stefan equations to describe the transport of CO_2/N_2 binary mixtures through the prepared membranes. The model was developed to rely on the single component adsorption and diffusivity data for the prepared membranes, as well as the Extended Langmuir model to represent the behaviour of the gas mixture and to provide a better characterization of the prepared membranes with varying the operating conditions. A fourth sub objective of this research project was to develop a model to extract the permeances as well as the permselectivities from the non-zero stage cut experiments due to the high permeation rate of the prepared membranes. This sub objective took place of another sub objective that was originally proposed to measure the diffusion

coefficients of some single gases through the prepared membranes using the constant pressure membrane permeation technique [43]. The original sub objective was cancelled due to the highly permeable membranes.

1.3 Thesis structure and organization

This thesis consists of seven chapters. The current one is the thesis introduction. Chapter two provides the background for this project. Chapters three and four are independent scientific articles that were published in a refereed scientific journal. Chapter five was submitted as a refereed scientific journal. Chapter six is to be submitted as a scientific article in a refereed scientific journal. Therefore, each one of them can be read independently. However, due to this structure, the common ideas, experimental procedures and the project core problem has been reiterated throughout these chapters where applicable. The contributions, conclusions, and recommendations that resulted from the entire thesis are presented in chapter seven. Three appendices are also provided at the end of this thesis. Further details on Chapters 3 to 6 are presented below:

CHAPTER 3 - Separation of CO_2 and N_2 on zeolite silicalite-1 membrane synthesized on novel support; published in Separation Science and Technology 47 (2012) 1606 – 1616.

This paper reports the successful synthesis and properties of a silicalite-1 membrane prepared using pore plugging synthesis on a novel tubular support with a 0.45 µm-pore size active layer consisting of zirconium and titanium oxides. This membrane was characterized by XRD, SEM, EDs and by CO_2 and N_2 single gas and binary gas mixtures permeation tests. This membrane showed an exceptional performance for binary CO_2/N_2 gas mixtures. The

permselectivity for this membrane was as high as 26 with the corresponding CO_2 permeance of 6 x $10^{-8\ 6}$ mol m^{-2} Pa^{-1} s^{-1}, while the highest stage cut for this membrane was around 30%. However, this membrane was the only successful membrane out of five membranes with different pore sizes that were prepared in the same synthesis batch.

CHAPTER 4 - Synthesis and characterization of silicalite-1 membrane prepared on a novel support by the pore plugging method; published in Journal of Porous Materials 20 (2013) 1047 – 1421.

This paper was written in parallel with the previous paper and it investigated the effect of pore size of the support on the morphology properties of the prepared membranes. In this paper, parameters including surface coverage, zeolite layer thickness, crystal size and shape, zeolite penetration depth were used to quantify the membrane morphology. Five flat supports with different pore sizes for their active layer in the range of 0.14 - 1.4 μm were studied. The morphology results showed that the membrane prepared using the 0.45 μm support had a unique morphology compared to other supports with the most preferably oriented zeolite layer. The membrane prepared using the 0.45 μm support had the highest uniform zeolite film as well as the highest zeolite crystal penetration.

CHAPTER 5 – Effect of support pore size on morphology and performance of tubular silicalite-1 membranes; submitted to Journal of Membrane Science.

This paper presents the results for the effect of pore size of the supports on the morphology and permeation properties of the membranes prepared using five tubular supports with different pore sizes for their active layer in the range of 0.14 - 1.4 μm. A new zeolite

synthesis autoclave was used to insure that the tubular supports had a vertical orientation during the whole synthesis. Keeping the tubes in a vertical position prevents the formed crystals in the solution from being attached to the support surface. This showed an improvement in the prepared zeolite membranes quality. The EDS (Electron diffraction spectrometer) results illustrated that all membranes had high concentrations of Si within the active layer of their support, suggesting successful pore-plugging of the support active layer. Except the membrane synthesized using the support with 0.14 μm pore size, all membranes were very selective with CO_2/N_2 permselectivities up to 30 at low pressure differentials. The membranes also were very permeable with a CO_2 permeance in the order of 10^{-6} mol m^{-2} Pa^{-1} s^{-1}. The stage cut at high pressures was as high as 95% for most of the membranes. At these high stage cut values the composition of the high permeable gas at the high pressure side decreased dramatically due to the high permeation rate, which in turn imposed the development of a mathematical model to extract the permeances from the non-zero stage cut experiments.

CHAPTER 6 - Modeling the transport of CO_2, N_2 and their binary mixtures through thin silicalite-1 membrane using Maxwell−Stefan equations; to be submitted to Microporous and Mesoporous Materials.

In this paper, a model based on Maxwell−Stefan equations and Extended Langmuir isotherm was developed for the transport of binary mixtures of CO_2 and N_2 through the prepared silicalite-1 membranes. To apply this model a modification was made to the permeation setup to allow performing the binary permeation experiments at very high feed flow rates and to insure the stage cut values to be less than 5%. The effect of the total feed pressure and

feed composition on the exchange coefficients, $Đ_{12}$ and $Đ_{21}$, were investigated. The exchange coefficients calculated were practically independent of the total feed pressure but they decreased by 55 – 60 % when the CO_2 concentration in the feed stream increased from 15% to 85%. Since the exchange diffusivities showed smaller dependency on the feed pressure and feed composition than the respective permeances, hence, they are more appropriate to characterize the intrinsic transport properties of silicalite-1 membranes.

1.4 References:

1- W.J. Koros, Evolving beyond the thermal age of separation processes: Membranes can lead the way, AIChE J. 50 (2004) 2326 – 2334.

2- S.-L. Wee, C-T. Tye, S. Bhatia, Membrane separation process - pervaporation through zeolite membrane, Separation and Purification Technology 63 (2008) 500 – 516.

3- M.T. Ravanchia, T. Kaghazchia, A. Kargarib, Application of membrane separation processes in petrochemical industry: a review, Desalination 235 (2009) 199 – 244.

4- P. Bernardo, E. Drioli, G. Golemme, Membrane gas separation: A review/state of the art, Ind. Eng. Chem. Res. 48 (2009) 4638 – 4663.

5- Y. Hasegawa, T. Ikeda, T. Nagase, Y. Kiyozumi, T. Hanaoka, F. Mizukami, Preparation and characterization of silicalite-1 membranes prepared by secondary growth of seeds with different crystal sizes, J. Membrane Science 280 (2006) 397 – 405.

6- F. Jareman, C. Andersson, J. Hedlund, The influence of the calcination rate on silicalite-1 membranes, Microporous Mesoporous Materials 79 (2005) 1 – 5.

7- K. Kusakabe, S. Yoneshige, A. Murata, S. Morooka, Morphology and gas permeance of ZSM-5-type zeolite membrane formed on a porous α-alumina support tube, J. Membrane Science 116 (1996) 39 – 46.

8- T.Q. Gardner, J.L. Falconer, R.D. Noble, Adsorption and diffusion properties of zeolite membranes by transient permeation, Desalination 149 (2002) 435 – 440.

9- J. Hedlund, M. Noack, P. Kölsch, D. Creaser, J. Caro, J. Sterte, ZSM-5 membranes synthesized without organic templates using a seeding technique, J. Membrane Science 159 (1999) 263 – 273.

10- E.E. McLeary, J.C. Jansen, F. Kapteijn, Zeolite based films, membranes and membrane reactors: Progress and prospects, Microporous Mesoporous Materials 90 (2006) 198 – 220.

11- R.J.R. Uhlhorn, K. Keizer, J. Burggraaf, Gas transport and separation with ceramic membranes. Part I. Multilayer diffusion and capillary condensation, J. Membrane Science 66 (1992) 259 – 269.

12- Y.S. Lin, Microporous and dense inorganic membranes: current status and prospective, Separation Purification Technology 25 (2001) 39–55.

13- A. Julbe, I. Europen, M. De Montpellier, Zeolite membranes - A short overview, in Studies in Surface Science and Catalysis edited by J. Cejka, H. van Bekkum 157 (2005) 135 – 160.

14- H.H. Funke, M.G. Kovalchick, J.L. Falconer, R.D. Noble, Separation of hydrocarbon isomer vapors with silicalite zeolite embranes, Ind. Eng. Chem. Res. 35 (1996) 1575 – 1582.

15- B.M. Lok, T.R. Cannan, C.A. Messina, The role of organic molecules in molecular sieve synthesis, Zeolites 3 (1983) 282 – 291.

16- J. Caro, M. Noack, and P. Kolsch, Zeolite membranes: from the laboratory scale to technical applications, Adsorption 11 (2005) 215 – 227.

17- J.N. Armor, Materials needs for catalysts to improve our environment, Chemistry Materials 6 (1994) 730 – 738.

18- A. Javaid, Membranes for solubility-based gas separation applications, Chemical Engineering J. 112 (2005) 219 – 226.

19- W.C. Wong, L.T.Y. Au, P.P. Lau, C.T. Ariso, K.L. Yeung, Effects of synthesis parameters on the zeolite membrane morphology, J. Membrane Science 193 (2001) 141 – 161.

20- E. Bourgeat-lami, P. Massiani, F. Di Renzo, P. Espiau, and F. Fajula, Study of the state of aluminium in zeolite-β, Applied Catalysis 72 (1991) 139 – 152.

21- J. Caro, M. Noack, Zeolite membranes – recent development and progress, Microporous Mesoporous Materials 115 (2008) 215 – 233.

22- A. Larbot, J.-P. Fabre, C. Guizard, L. Cot, J. Gillot, New inorganic ultrafiltration membranes: titania and zirconia membranes, J. Am. Ceram. Soc. 72 (1989) 257 – 261.

23- C.-H. Chang, R. Gopalan, Y.S. Lin, A comparative study on thermal and hydrothermal stability of alumina, titania and zirconia membranes, J. Membrane Science 91 (1994) 27 – 45.

24- R. Gopalan, C.-H. Chang, Y.S. Lin, Thermal stability improvement on pore and phase structure of sol-gel derived zirconia, J. Mater. Sci. 30 (1995) 3075 – 3081.

25- P. Ferreira, A. Ferreira, M. R. Soares, Synthesis and Structural Characterization of Zirconium Silicates, Chem. Mater. 13 (2001) 355 – 363.

26- Q. Xu, M.A. Marc, Sol-Gel route to synthesis of microporouse ceramic membranes: thermal stability of TiO_2-ZrO_2 mixed oxides, J. Am. Ceram. Soc. 76 (1993) 2093 – 2097.

27- R. Gopalan, C.-H. Chang, Y.S. Lin, Thermal stability improvement on pore and phase structure of sol-gel derived zirconia, J. Mater. Sci. 30 (1995) 3075 – 3081.

28- S.P. Davis, E.V.R. Borgstedt, S.L. Suib, Growth of zeolite crystallites and coatings on metal surfaces, Chem. Mater. 2 (1990) 712 – 719.

29- T. Matsufuji, N. Nishiyama, M. Matsukata, K. Ueyama, Separation of butane and xylene isomers with MFI-type zeolite membranes synthesized by a vapour-phase transport method, J. Membrane Science 178 (2000) 25 – 34.

30- A. Gouzinis, M. Tsapatsis, On the preferred orientation and microstructural manipulation of molecular sieve films prepared by secondary growth, Chem. Mater. 10 (1998) 2497 – 2504.

31- S. Miachon, E. Landrivon, M. Aouine, Y. Sun, I. Kumakiri, Y. Li, O. Pachtova Prokopova, N. Guilhaume, A. Giroir-Fendler, H. Mozzanega, J.-A. Dalmon, Nanocomposite MFI-alumina membranes via pore-plugging synthesis: preparation and morphological characterization, J. Membrane Science 281 (2006) 228 – 238.

32- S. Miachon, P. Ciavarella, L. van Dyka, I. Kumakiri, K. Fiaty, Y. Schuurman, J. A. Dalmona, Nanocomposite MFI-alumina membranes via pore-plugging synthesis: specific transport and separation properties, J. Membrane Science 298 (2007) 71 – 79.

33- D.W. Shin, S.H. Hyun, C.H. Cho, M.H. Han, Synthesis and CO_2/N_2 gas permeation characteristics of ZSM-5 zeolite membranes, Microporous Mesoporous Mater. 85 (2005) 313 – 323.

34- M. P. Bernal, J. Coronas, M. Menendez, and J. Santamarıa, Separation of CO_2/N_2 mixtures using MFI-type zeolite membranes, AIChE J. 50 (2004) 127 – 135.

35- J.C. Poshusta, R.D. Noble, J.L. Falconer, Temperature and pressure effects on CO_2 and CH_4 permeation through MFI zeolite membranes, J. Membrane Science 160 (1999) 115 – 125.

36- J.M. van de Graaf, F. Kapteijn, J.A. Moulijn, Modeling permeation of binary mixtures through zeolite membranes, AIChE J. 45 (1999) 497 – 511.

37- R. Krishna, R. Baur, Analytical solution of the Maxwell-Stefan equations for multicomponent permeation across a zeolite membrane, Chemical Engineering J. 97 (2004) 37 – 45.

38- J.G. Martinek, T.Q. Gardner, R.D. Noble, J.L. Falconer, Modeling transient permeation of binary mixture through zeolite membranes, Ind. Eng. Chem. Res. 45 (2006) 6032 – 6043.

39- M. Kanezashi, Y.S. Lin, Gas Permeation and Diffusion Characteristics of MFI-Type Zeolite Membranes at High Temperatures, J. Physical Chemestry C 113 (2009) 3767 – 3774.

40- R. Krishna, J.M. van Baten, Hydrogen Bonding Effects in Adsorption of Water−Alcohol Mixtures in Zeolites and the Consequences for the Characteristics of the Maxwell−Stefan Diffusivities, Langmuir 26 (2010) 10854 – 10867.

41- M. Pera-Titus,C. Fite, V. Sebastian, E. Lorente, J. Llorens, F. Cunill, Modeling

pervaporation of ethanol/water mixtures within ‘real' zeolite NaA membranes, Ind. Eng. Chem. Res. 47 (2008) 3213 – 3224.

42- A. Vignes (1966) Diffusion in binary solutions, Ind. Eng. Chem. Fundam 5 (1966) 189 – 199.

43- B. Kruczek, T. Matsuura, Limitations of a constant pressure-type testing system in determination of gas transport properties of hydrophilic films, J. Membrane Science 177 (2000) 129 – 142.

CHAPTER TWO

BACKGROUND

Chapter 2 - Background

This chapter provides a theoretical background for membranes, zeolites and zeolite membranes. It is also devoted to review different membranes classifications, the main membrane technology terminologies, and to outline the common occurring transport mechanisms in gas separation membranes. A review on zeolite membranes preparation methods as well as the most important factors affecting the zeolite membrane synthesis is also provided. A section on modeling the diffusion in zeolite membranes is also presented at the end of this chapter.

2.1 Gas Separation Membranes

Membranes technology has been proven to be technically and economically superior to other emerging technologies such as cryogenic distillation, absorption and pressure swing adsorption [1,2]. This superiority is due to several advantages for membrane technology, including low capital investment, low weight, low energy and space requirements, environmentally friendly and easy expansion and high process flexibility [2,3]. Membrane gas separation is used these days in a variety of applications, as shown in Table 2-1 [2]. Nowadays, all commercial gas separation membranes are formed from organic polymeric materials. At the same time, the major research effort in the field of gas separation membranes is focused on the development of inorganic membranes.

2.2 Membrane Technology Terminologies

This section aims to present the common terminologies used in membrane technology. The feed refers to the stream that is fed to the membrane for separation. The retentate is the

stream rejected by the membrane. The permeate is the part of the feed that passes through the membrane. Sweep gas represents another stream consisting of an inert gas that is used sometimes to remove the amount permeated through the membrane from the permeation cell in order to maintain the concentration gradient across the membrane. The flux is defined as the flow through the membrane per unit area. The permeance is the flux of a component normalized with partial pressure difference across the membrane as shown in Eq. 2.1. Permeances and fluxes may be based on volumetric, molar, or mass flow rates.

Table 2-1 Gas separation membrane main applications [2].

Common gas separation	**Applications**
O_2/N_2	Oxygen enrichment, inert gas generation
H_2/Hydrocarbons	Refinery Hydrogen recovery
H_2/N_2	Ammonia purge gas
H_2/CO	Syngas ratio adjustment
CO_2/Hydrocarbons	Acid gas treatment, landfill gas upgrading
H_2O/Hydrocarbons	Natural gas dehydration
H_2S/Hydrocarbons	Sour gas treating
He/Hydrocarbons	Helium separation
He/N_2	Helium recovery
Hydrocarbons/Air	Hydrocarbons recovery, pollution control
H_2O/Air	Air dehumedification

$$P_i = \frac{V_i}{A_m \Delta p_i} \tag{2.1}$$

where (P_i) is the component i permeance, (V_i) is the steady state permeation rate, (Δp_i) is the partial pressure gradient across the membrane of component i, and (A_m) is the membrane area.

Ideal selectivity or permeance ratio is often used to describe membrane separability. Ideal selectivity is calculated using single gas permeances as follows:

$$\alpha^*_{i,j} = \frac{P_i}{P_j} \tag{2.2}$$

Permselectivity may refer to the permeance ratio when calculated using permeances measured from gas mixture experiments. Separation factor or actual selectivity, on the other hand, is calculated using the mole fractions of the permeate and feed streams as follows:

$$\alpha_{i,j} = \frac{y_i / y_j}{x_i / x_j} \tag{2.3}$$

where ($\alpha^*_{i,j}$) is the permeance ratio, ($\alpha_{i,j}$) is the separation factor, (y_i), (y_j), (x_i), and (x_j) are the mole fractions of components i and j on the permeate stream and feed stream, respectively.

Stage cut is defined as the ratio of the permeate flow rate to the feed flow rate as follows:

$$SC = \frac{q_P}{q_F} \tag{2.4}$$

where (q_P) and (q_F) are the permeate flow rate and the feed flow rate, respectively.

2.3 Membrane Transport Mechanisms

Membranes usually possess different types of pore structures depending on the formation process. The pores can be highly connected and tortuous or non-connected and straight and could be classified according to their size as macropores, mesopores or micropores [3]. Assuming that pores in membranes are composed of a bundle of capillary tubes, transport of gases through these capillary tubes can be described based on the kinetic theory of gases [4]. Therefore, the following diffusion mechanisms can dominate: Poiseuille's flow, Knudsen diffusion, surface diffusion, capillary condensation or micropore diffusion. However, the gas permeation process is also strongly dependent on the pore size and pore size distribution of the membrane, operating pressure and temperature, and the nature of the membrane and the permeating molecules [5]. Fig. 2-1 shows the different transport mechanisms through porous membranes [6].

Below is a brief description of the common occurring diffusion mechanisms in porous membranes.

2.3.1 Poiseuille's Flow

This flow mechanism occurs primarily through molecule–molecule collisions and the mean free path of the gas molecules is smaller than the pore size [7]. The driving force in this case is the composition gradient. However, if a pressure gradient is applied in such systems, this will lead to a bulk (laminar) flow that is described by Poiseuille’s equation. This flow is often described as Poiseuille flow or viscous flow. This type of flow is characterized by its high flux but with no separation.

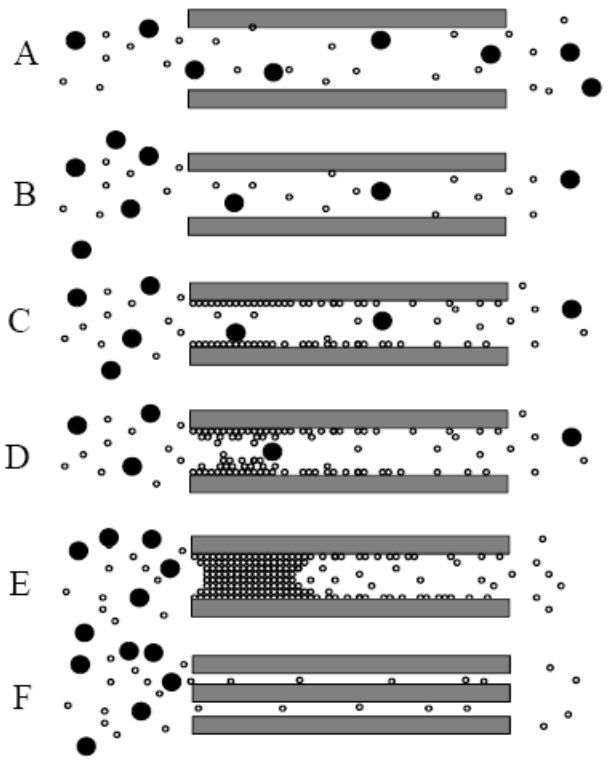

Figure 2-1 Transport mechanisms through porous membranes [6] A: Poiseuille's flow, B: Knudsen flow, C: surface flow, D: multilayer adsorption, E: capillary condensation, F: molecular sieving.

2.3.2 Knudsen Diffusion

This flow mechanism occurs when the mean free path of the gas molecules is greater than the pore size. In this case, the probability of collisions of the molecules with the pore wall is higher than the one occurring among molecules. The separation selectivity in this type of diffusion is proportional to the ratio of the inverse square root of the molecular weights. This diffusion mechanism often occurs in macroporous and mesoporous membranes [3,8-10]. Knudson diffusion is limited by the differences in molecular weights of the gases and is therefore only of practical importance for the separation of light gases from heavy gases.

Fluxes through the membrane by Knudson diffusion are relatively high. However, separation of gases by Knudson diffusion has a limited selectivity, and the theoretical selectivity is decreased by effects like concentration polarization and back diffusion.

2.3.3 Capillary Condensation

If one of the gases in the surface flow is a condensable gas under the conditions inside the pores of the membranes, then the surface flow is said to follow Capillary condensation. This occurs in mesopores and small macropores, at certain critical relative pressures that can be calculated via the Kelvin equation. The molecules will condense at a lower pressure than their vapor pressure because of the effect of the surface tension in the capillary pores. In this case, the pore gets completely filled by the condensed gas then the formation of menisci at both ends of the pore occurs and transport can take place through hydrodynamic flow driven by capillary pressure difference between the two ends. As pressure increases, the gas transport via this mechanism represents the ultimate limit of adsorption. Theoretically, this type of gas transport is beneficial to achieve very high selectivities, due to the formation of the liquid layer of the condensable gas at low temperature and or high partial pressures. This liquid layer will act as a block layer to prevent further flow of the non-condensable gases [8,10,11], resulting in an enrichment of the strongly adsorbing components in the permeate product. However, at high temperatures and/ or low partial pressures of strongly adsorbing components, the weakly adsorbing gases permeate faster through the membrane pores while the strongly adsorbing gases are retained.

2.3.4 Surface Diffusion

If the permeating species exhibits a strong affinity for the membrane surface and eventually adsorb along the pore walls at low temperature and/or high pressure, then surface diffusion occurs. In this type of diffusion, separation occurs as a result of differences in the amount adsorbed of the permeating species. Surface diffusion is usually observed to happen in parallel with other transport mechanisms such as Knudsen diffusion [9,12]. Several models were developed in literature to describe surface diffusion. These can be divided into three categories:

1- The hydrodynamic model: in this model the adsorbed gas is considered as a liquid film, which can glide along the surface under the influence of a pressure gradient [13].

2- The hopping model: this model assumes that molecules can hop over the surface. The surface flux is calculated by the mean hopping distance and the velocity, with which the molecules leave their site [14].

3- The random walk model: this model is the most frequently used model in literature. It is based on the two-dimensional form of Fick's law. In most cases it is assumed that molecules jump from one site to another. This process is an activated process and the energy of activation is a fraction of the heat of adsorption. This means that strongly adsorbed species are less mobile than weakly adsorbed species [15].

2.3.5 Micropore Diffusion

If the pore size becomes comparable to the molecular size, then this type of diffusion may be considered as surface diffusion. In this regard, in which diffusion is perceived as an "activated" process then the separation becomes a strong function of many factors, such as molecular shape and size, pore size, and interactions between the pore wall and gas molecules. This type of diffusion mechanism is reported to be found and dominant in microporous zeolite membranes and carbon molecular sieves [3,10].

Solution-diffusion mechanism on the other hand is widely accepted to be the main mechanism of transport in dense polymeric materials [3,16,17]. This mechanism is, generally speaking, can be described in three steps: the first one being when gas molecules are absorbed by the membrane surface on the upstream end, followed by the diffusion of the gas molecules through the polymer matrix. The third step involves the evaporation of gas molecules on the downstream end. In this mechanism, the separation is achieved between the different permeants due to the difference in solubility coefficient and diffusivity coefficient. The solubility coefficient is the ratio between the dissolved concentration and the partial pressure of the penetrant at the high pressure side of the membrane. The diffusivity coefficient is a measure of the mobility of the penetrant passing through the voids of the polymeric membrane. Solubility or sorption of gases becomes a complex process in glassy polymers, and has been described in literature by a combination of Henry's law and Langmuir expressions which is usually referred to as "dual mode sorption theory" [18]. Diffusion in glassy polymers is an activated process and the permeability, diffusivity, and solubility are often expressed by Arrhenius relations. Solution-diffusion can be adopted to

describe the transport through inorganic adsorbent membranes, because the same three steps can be distinguished in the transport across these membranes. However, unlike dense polymers, diffusion of penetrant across the inorganic adsorbent membranes is limited to the surface of the membrane pores. Also, the driving force for diffusion is a gradient of surface occupancy than a simple concentration gradient. Consequently, the transport in inorganic adsorbent membranes is often referred to as a surface diffusion

In inorganic adsorbent membranes, the molecules adsorbed on the high pressure side of the membrane, diffuse along the pore walls in the direction of decreasing the chemical potential, then desorb from the low pressure side of the membrane. The separation is achieved in this mechanism due to the difference in the amount adsorbed of the permeating species and the difference in their micropore diffusivity coefficient.

2.4 Membranes Classification

Membranes are usually classified according to their pore size, the material they are made of, or their morphology. Membranes with pore sizes larger than 10 μm are considered filters. Microfiltration membranes have pore sizes in the range of 0.1 – 10 μm and are capable of removing suspended and colloidal particles like blood cell, bacteria, and latex emulsions. Ultrafiltration membranes have pore size in the range of 2 – 100 nm and can remove dissolved molecules such as proteins like albumin or pepsin. Nanofiltration membranes have pore size less than 10 nm and can separate small molecules like divalent salts, sugar and dissociated acids. Reverse osmosis membranes have pore size in the range of 3 – 5 nm and

separate material like sodium and chloride on the molecular level. Gas separation requires membranes with smaller pore size [19].

Membranes can be also classified according to their morphology. They could be porous or nonporous (dense). Porous membranes could be further classified as symmetric and asymmetric [20]. In Symmetric types, where the properties of the membrane do not change throughout the cross section of the membrane while in asymmetric (composite) types, the membrane is composed of a thin selective layer on the top of a strong support layer, providing the mechanical strength. It is also possible to manufacture the support and the active thin layer in one step as in phase inversion technique [21]. Asymmetric membranes are superior compared to symmetric membranes because the flux is determined by the thickness of the thin top thin layer and not by the whole membrane thickness. Most ceramic membranes have an asymmetric membrane structure with either a dense or a porous active layer.

Nonporous membranes consist of a dense film through which the permeants are transported by diffusion. Nonporous membranes provide high selectivity in gas separation but the permeabilities are usually low. The separation of mixture components in nonporous membranes is related directly to their relative solubility and diffusivity in the membrane material. Therefore, nonporous membranes can separate components of similar size if their solubility in the membrane material is significantly different [22].

Membranes are also classified according to the materials they are made of as organic, inorganic, or hybrid. Organic membranes include polymers, whereas ceramics, carbon and

metal membranes are examples of inorganic membranes. Hybrid membranes on the other hand, are a combination of organic and inorganic materials. Liquid membranes can be either organic or inorganic. Liquids with an appropriate carrier are used for facilitated transport and they are held within the pores of organic and inorganic membranes [19].

Polymeric membranes can be categorized into two distinct groups: glassy membranes and rubbery membranes. The glass transition temperature is lower than the ambient for the rubbery membranes and higher than the ambient for those of the glassy membranes. When it comes to the permeation of gases, the two categories behave differently. Glassy membranes are more permeable to smaller molecular size gas molecules whereas rubbery ones have the ability to allow the permeation of condensable gases more easily. Polymeric membrane could be either symmetric, where the properties of the membrane do not change throughout the cross section of the membrane or asymmetric (composite), in which the membrane is composed of a thin selective layer on the top of a strong support layer providing the mechanical strength [23].

Polymeric membranes are in general preferred under mild temperatures (20 – 100 ^{o}C) and can be easily fabricated; it is also possible to fabricate the support layer and the active thin layer in one step as in phase inversion technique [23]. Polymeric membranes are favoured in large scale operations and can be also classified into porous and non-porous materials. The porous materials contain fixed pores in which their dimensions determine the selectivity of the membrane. Non-porous membranes on the other hand are used in gas separation and

pervaporation [24]. The permeability and the selectivity of these membranes are determined by the intrinsic properties of the material.

Inorganic membranes on the other hand, include ceramic, carbon and metal membranes. Ceramic membranes are characterized by being more fragile and more expensive compared to polymer membranes. However, these materials are also characterized by their ability to withstand harsher chemical environments and higher temperatures and can be cleaned on site. Inorganic membranes also include carbon membranes which are intermediates between polymeric membrane and ceramics membranes. The process done before the carbonization is similar to that of polymeric membranes, while, the final membrane properties are close to that of ceramic membranes. Carbon membranes are characterized by their potential use under relatively high temperatures and stability in most chemical environments. An exception for that is being under oxidative conditions at temperatures of (350 – 400 ^{o}C) [25]. Inorganic membranes have several advantages and disadvantages when compared to organic membranes and they are summarized in Table 2-2 [5].

Metal membranes are used in specialized applications. One example is in semiconductors applications, such as macroporous and nanopourous silicon. Another important example of metal membrane materials is the nonporous hydrogen separating palladium membrane [26].

Hybrid membranes on the other hand are synthesized from organic and inorganic materials. Principally, there are two methods to synthesis the hybrid membranes, either by dispersing inorganic nanoparticles in a continuous polymer phase (solution blending), or by in situ polymerization within the pores of a porous inorganic structure [27].

Currently, polymer membranes are the most widely used for gas separation applications because of their relatively low cost of manufacturing as hollow fibers with high surface areas [28]. However, polymers cannot operate at high temperatures or in harsh chemical environments. Inorganic membranes can separate mixtures at high temperature, but there are some limitations for the existing inorganic membranes [29]. Silica membranes are not stable in humid atmosphere at high temperatures, carbon membranes have low fluxes, and metal membranes are vulnerable to surface poisoning and suffer from hydrogen embrittlement. Zeolite membranes have the ability to sieve molecules at high temperature, high pressure, and in chemically harsh environments, and thus have significant potential to become a practical alternative for the traditional separation methods.

Table 2-2 Advantages and disadvantages of inorganic membranes when compared to organic membranes [5].

Advantages of inorganic membranes	Disadvantages of inorganic membranes
Long term stability at high temperatures	High capital cost
Resistance to harsh chemical environments	Brittleness of non-metallic membranes
Resistance to high pressure drops	Low membrane surface per module volume
Inertness to micobiological degradation	Difficulty in achieving high selectivities in large scale microporous membranes
Easy cleaning after fouling	Generally low permeability of highly selective dense membranes at medium temperatures
Easy catalytic activation	Difficult membrane to module sealing at high temperatures

Since the membranes prepared in this work were inorganic, hence, they will be discussed in more detail in the following section.

2.5 Inorganic Membranes

The inorganic membranes, with a few exceptions, are porous and are characterized by a well-defined static pore structure that can be either highly connected and torturous or non-connected and straight. This depends on the formation process. The pores in inorganic membranes can be classified according to their size as follow: macropores (>500 Å), mesopores (500–20 Å) or micropores (<20 Å) [30], across which, gas transport may occur via different mechanisms.

There are two main types of microporous membranes, namely crystalline zeolite membranes and amorphous membranes such as silica and carbon membranes [19]. The practically useful crystalline microporous membranes have polycrystalline structure, consisting of many crystallites packed together without any crystallite boundary gaps in the ideal case [31]. Carbon membranes and zeolite membranes are among the most important inorganic membranes tested for gas separation applications. Carbon molecular sieve membranes have been investigated by many researchers and the results of selectivities and permeabilities obtained were far above those obtained by the best polymers [32]. Despite these results, carbon membranes were not employed in industry due to their cost, brittleness and aging of carbon surface due to chemical reactions [33]. Despite that, nanoporous carbon membranes were developed by Air Products in 1990's. Their results showed that nanoporous carbon membranes could be used for the separation of different gas mixtures such as hydrogen,

methane, ethane, propane and butane [34]. However, Air Products discontinued the work in 2003 due to problems related to aging and deactivation of the membranes [35].

Zeolites and zeolite membranes will be discussed in more details in the following sections. But first a background on the zeolites will be presented.

2.6 Zeolites

Zeolites are crystalline aluminosilicates, discovered by a Swedish scientist in the 18th century. They were denoted as "zeolites" from the Greek word "zeo" and "litos" which means a boiling stone [36,37]. Zeolites have a three dimensional framework of oxygen ions with either Si^{4+} or an Al^{3+} ions positioned within the tetrahedral sites [38,39]. The AlO_2^- in the zeolite's structure determines the framework charge, and this charge is balanced by cations that occupy the non-framework positions. The zeolites framework may be described by the following empirical formula written in oxide form [37]:

$$M_{2/n}O \cdot Al_2O_3 \cdot XSiO_2 \cdot YH_2O$$

Where M is the exchangeable cation and n represents the cation's valence. These cations are generally from the group I or II ions such as Li^+, Na^+, K^+, Mg^{2+} or Ca^{2+}. However, other metal, non-metal and organic cations may also be used to balance the framework charge. These cations are present either during synthesis or added through post synthesis ion exchange. X represents the SiO_2/Al_2O_3 ratio in the zeolite framework and since Al^{3+} does not occupy adjacent tetrahedral sites, then the value of X should be equal to or greater than one. Y on the other hand represents the degree of hydration. Zeolites are illustrated by a network of channels or pores. The opening or the size of these pores varies from zeolite type to another, ranging from 0.3 to 1.3 nm [37,40]. The charge balancing cations and water

molecules are located in the pores of the zeolite. Zeolite structures are classified in terms of their framework type and each framework type is assigned a three-letter code according to the rules of the IUPAC (International Union of Pure and Applied Chemistry) Commission on Zeolite Nomenclature in 1978 [41]. By far, more than 213 zeolite framework types have been recognized by the Structure Commission of the International Zeolite Association [42].

Zeolites are used mainly in adsorption, catalysis, ion exchange and membranes. They are generally prepared by hydrothermal treatment. Synthesis mixture of zeolite commonly contains silica source, alumina source, a mineralizing agent, templating agent (shape directing agent) and water. The mixture is heated in an autoclave and the mixture composition, synthesis temperature and synthesis time usually determines the type of zeolite that will crystallize. After the zeolite synthesis, a calcination step where the zeolite is heated in air is required to decompose and burn the templating agent that is blocking the pores.

Zeolites are stable at relatively high temperatures (>900 ^{o}C) [27]. They typically possess moderate surface area (300–600 m^2/g) and a very narrow pore size distribution [43]. The narrow pore size distribution, along with the small pore diameter, make zeolites a perfect candidate for molecular sieving separations where the steric effects can be exploited to exclude larger molecules from being adsorbed. Moreover, zeolites' pore size depends on the number of membered rings around the pore. The pore size could be small (0.34–0.4 nm) like in NaA and SAPO-34 with 6 and 8 membered rings, medium (0.5–0.6 nm) like in MFI zeolite with 10 membered rings and large (0.7–0.8 nm) like in NaY and NaX with 12 membered rings [44]. This thesis work is focused on the synthesis of MFI type zeolite and

more specifically silicalite-1 type membrane; hence, MFI type zeolite will be explained in more detail in the following section.

2.7 MFI Type Zeolite

MFI (Mordenite Framework Inverted) zeolite is one of the most prepared and industrially used zeolites. It is commonly used as a catalyst and frequently used to prepare membranes due to the suitable pore size and a relatively high chemical and thermal stability [45]. MFI zeolites are usually synthesized with Si/Al ratios in the range from 10 to ∞. Moreover, the aluminum containing MFI form is commonly referred to as ZSM-5 and the aluminum- free from is commonly referred to as Silicalite-1 [46]. MFI has a three-dimensional network of 10-membered ring pores, with straight pores running in the b direction (100 crystallographic axis) with an elliptical cross section of 0.53 × 0.56 nm (Fig. 2-2). These straight pores are interconnected with sinusoidal pores running along the a direction (010 crystallographic axis) with a circular cross section of 0.51 × 0.55 nm, as shown in Fig. 2-2 [29]. MFI is usually used as a catalyst for acid catalyzed reactions such as isomerization, aromatization and catalytic cracking of olefins and paraffins [47].

2.8 Zeolite Membranes

Zeolite membranes have the ability to discriminate the components of gaseous or liquid mixtures dependent on their molecular size (molecular sieving), due to the regular three dimensional pore structures. They are able to separate molecules not only by molecular sieving [35,48] but also by preferential adsorption [48,49]. In principal, all zeolite types can be formed as membranes, however, only 15 structures, out of the 213 different zeolite structures identified by International Zeolite Association (IZA), have been explored in

preparation of zeolite membranes. Moreover, experiments revealed that only the high-silica types showed shape selective separation behaviour (molecular sieving function).

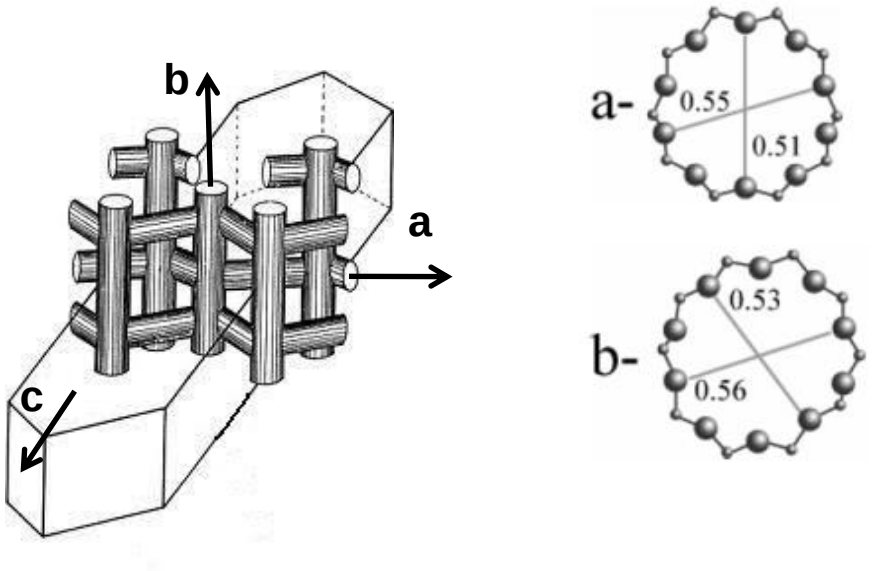

Figure 2-2 Schematic representation of MFI crystal with typical coffin shape. The channel system with the pore openings (nm) running in two directions as shown (adapted from reference [29]).

Silicalite-1, the Al-free MFI structure, received enormous attention and that is because silicalite-1 is relatively easy to prepare, provides chemical and thermal stability, and allows oxidative regeneration [50]. Hence, most progress in the development of zeolite molecular sieves and zeolite membranes was accomplished using silicalite-1. It is important to highlight that, in order to perform the molecular sieving function; the membranes must have neither defects nor pinholes larger than 2 nm. However, templates (structure directing agents) that are often used in zeolite membranes synthesis incorporated in the zeolite

structure. These templates must be removed by calcination (at temperatures >400 ^{o}C) in order to open up the pore structure and render the material useful as a membrane. Removal of the template is associated usually with shrinkage of the zeolite crystallites, which often creates or enlarges the intercrystalline pores [51]. Furthermore, a compressive stress develops in the zeolite films during the cooling process of the calcination [52]. Consequently, all zeolite membranes reported so far contain intercrystalline nonzeolitic pores (defects) in addition to the well-defined zeolitic pores. In the following section, the main synthesis methods used to prepare zeolite membranes will be discussed.

2.9 Zeolite Membranes synthesis Methods

Zeolite membranes are generally formed by a hydrothermal deposition method using aluminosilicate or silicate precursors in aqueous solution on suitable porous support. Although the mechanisms of the hydrothermal reactions were investigated extensively, they are still not fully understood [53]. The most promising and commonly used technique to prepare the zeolite membranes is what is called the composite technique, i.e. formation of the zeolite thin layer at the top of a porous support [52]. In addition to that support, one or more mesoporous intermediate layers are often necessary to bridge the pore size gab that is present between the large pores of the macroporous support layer and the small pores of the microporous top layer. A variety of porous substrates has been used to support the zeolite membranes, the most employed ones were porous alumina and stainless steel. Furthermore, the zeolite layer can be crystallized hydrothermally in one step on the top of the support [54] or inside the pores of the support (pore plugging) [55,56] which is known as in situ synthesis, or in several steps using seed crystals that grow together to form a continuous

supported zeolite layer in a subsequent hydrothermal synthesis, which is known as secondary growth synthesis [57,58]. Hence, zeolite membranes can be prepared by three main methods:

1- In-Situ Crystallization Method [5,59]: This is a one-step process during which both nucleation and growth of the zeolite material take place in presence of the support. The bare porous support is brought into contact with the zeolite precursors and submitted to hydrothermal synthesis conditions. The zeolite layers are to be formed from nuclei appearing during the hydrothermal treatment and their distribution on the support depend on many factors such as the local support surface properties, which are difficult to control. The crystal growth process competes with the formation of nuclei which may limit the nuclei density due to mass-transfer limitations towards the support. For this reason, the formation of a thick zeolite supported film layer may be necessary to obtain a continuous layer made of inter-grown zeolite crystals. However, at higher synthesis temperatures (~190 ^{o}C) relatively thick (30–100 μm), well crystallised zeolite layers are developed from the surface of the support, while at lower synthesis temperatures (<150 ^{o}C) it is favoured for the zeolite crystals to growth inside the macropore of the ceramic support leading to what is called “Pore Plugging” [55].

2- Vapor Phase Transport method [60]: this method involves two steps; an amorphous gel containing silica, aluminum is first coated on the support then followed by crystallization. The water for the hydrothermal synthesis comes as

saturated vapor from the bottom of the autoclave with a template that can be either in the water or in the gel. In this manner, a strict control of the zeolite amount is allowed. By controlling the amount of gel applied the membrane thickness may be well controlled. However, the produced crystals are most likely randomly oriented. Furthermore, since the zeolite crystals density is higher than that of the gel, the crystallization process produces a large number of intercrystalline voids, which must be filled through a dissolution-recrystallization process. As a result, it is very difficult to make a thin and crack free film on a porous support using this method.

3- Secondary Growth Synthesis method [61-64]: this synthesis method is the most commonly used method for zeolite membrane preparation. In this method, initial seeding step takes place and in the meantime, small zeolite seed crystals are deposited on top of the support. These seeds can be then grown under hydrothermal zeolite synthesis conditions forming continuous zeolite layer. These seeds can be attached to the support surface by two methods [65,66]: Firstly, by adjusting the zeta potential between the support and the silica seeds by changing the pH of the solution, and secondly by creating a positive surface charge by adsorbing cationic polymers on the support to which the negative charged zeolite seeds become attached. The seed characteristics including the size, shape and concentration have the ability to affect the zeolite orientation in the crystal layer, which in turn has the influence on transport properties.

Secondary Growth Synthesis offers considerable advantages compared to the in situ crystallization synthesis such as improved control over the membrane microstructure like channel orientation and thickness, higher reproducibility, and a wider range of synthesis conditions. Elimination of the nucleation step due to the pre-existence of nuclei on the support surface leaves crystal growth as the main film formation mechanism and thus adds improved flexibility in zeolite film and membrane preparation [65]. Nevertheless, the role of the seed layer is dual. It does not only lead to growth without the need for nucleation but also may prohibit or limit the incorporation of newly formed crystals [67]. Based on the above, the final zeolite film quality will depend on the quality of the seed layer. The absence of close-packed seeds throughout the area of the support might contribute to the development of defects. As an example, by seeding of the support, MFI zeolite layers of different crystal orientation can be obtained. MFI zeolite membranes often show crystal orientation perpendicular to the plane of the support surface (*c*-axis) [68]. However, under certain secondary growth conditions other crystal orientations were observed like a-orientation [69], *b*-orientation [70] or intermediate orientations [71].

In an effort to decrease the defects and the fragility of the produced zeolite membranes, synthetic routes have been investigated, in which the zeolite is formed within the pores of the support (pore plugging), rather than as a thin film on top of the support [55,56,72]. MFI zeolite membranes produced by pore plugging technique on α-alumina support have been reported in several studies to give high performance in many gas separation systems [73,74]. As the reaction is carried out at low temperatures (>150 ^{o}C) over a long period of time (4–6 days), growth of zeolite was persuaded within the pores of the support. However, at higher

temperatures (~190 ^{o}C), nucleation and crystal growth was much more rapid, resulting in the formation of an outer layer of large crystals on the support [75]. Despite the fact that the mechanisms for these two different membrane synthesis methods are still not fully understood, it is clear that at lower temperatures, a longer contact with of the support with the highly alkaline oligomeric silicalite solution will lead to heterogeneous nucleation at the support surface, followed by a slow growth of the crystals within the support pores [76]. As a result, a more stable membrane is obtained where the zeolite phase is formed primarily inside the pores of the support. Yet, plugging the pores will add another resistance to the gas transport which will reduce the membrane permeability.

The main factors affecting the zeolite membranes synthesis will be discussed in the following section.

2.10 Main Factors Affecting Zeolite Membrane Synthesis

A large number of parameters affect the zeolite formation, mainly, alkalinity, water content, organic templates, crystallization temperature, crystallization time, aging time and seeding. Below is a brief discussion of these parameters and their effect on the zeolite film formation.

Alkalinity in the zeolite crystallization system is defined as OH^{-}/Si ratio or H_2O/Na_2O ratio. At high alkalinity the solubility of Si increases, the polymerization degree of silicate anions decreases, and the polymerization of the polysilicate anions increases. Thus, as the alkalinity increases the nucleation period decreases and the zeolite crystallization period increases [77]. Furthermore, the alkalinity affects also the particle size of the zeolite crystal. Alkalinity

increase will result in a decrease of zeolite crystals, as well as in a narrower crystal size distribution [78].

Water acts as a solvent in the hydrothermal synthesis process; therefore, the concentrations of the reactants will be changed with the variation of the water content, which will affect the crystallization process. Principally, increasing the water content will cause a lower super saturation, which will favour the crystal growth over the nucleation, and consequently, large crystals can be obtained [79].

Templating agents such as tetrapropylammonium hydroxide (TPAOH) are used in zeolite synthesis. This templating agent acts as pore filler and also as a structure directing agent to form specific building units [80]. Templating agent type and the templating agent/Si ratio affect significantly the formation of zeolites by influencing the nucleation process and crystal growth, by lowering the chemical potential of the lattice formed [81]. Furthermore, the hydrophobic/hydrophilic characteristics of the templating agent greatly influence the synthesis of pure silica zeolite such as silicalite-1 [82]. Based on that, the choice of organic templating agent is of crucial importance in the formation of a particular zeolite structure.

Temperature is another important factor in the zeolite synthesis. Crystallization temperature usually determines the zeolite phase synthesised. Both nucleation and crystal growth rates increase by increasing the crystallization temperature [83]. In particular, the crystal growth rate over the nucleation rate. Therefore, larger crystals are obtained at higher temperatures. In addition, temperature also affects the morphology of the zeolite crystals. It is reported that

the length/width ratio of silicalite-1 crystals increased by increasing the crystallization temperature [84].

Crystallization time is very important in the zeolite synthesis. The crystallinity usually increases with time. However, since the zeolites are thermodynamically metastable phases, hence, some phases appear and then are sequentially replaced by more stable phases. As an example LTA (Linde Type A) and FAU (Faujasite type) zeolites dissolve to form SOD (Sodalite type) and GIS (Gismondine type) zeolites, respectively with prolonged crystallization time [85].

Aging time, which is the time between the mixing step and the heating step, has a strong effect on the kinetics of nucleation and crystal growth of zeolites [86-88]. It is also believed that the origin nuclei are formed during the aging period. Aging also increases the nucleation rate, reducing the crystallization duration, reducing the crystal size and increasing the crystal population.

Seeding, which is usually used to improve the zeolite film quality, offers many advantages such as: better control of the zeolite film orientation [56,65,89,90], higher synthesis reproducibility [56,65,90,91], shorter crystallization time and that is due to the reduction of the induction time for nucleation [92]. However, seeding adds to the complexity of the membranes synthesis by introducing extra parameters such as the seed size and the thickness of the seed film.

2.11 Modelling the Diffusion in Zeolite Membranes

The diffusion in zeolite membranes could be described by micro scale models or macro scale models. Examples of micro scale models used for the diffusion in zeolites are molecular dynamics, Monte-Carlo and force field simulations. In micro scale models the molecules are modelled on an atomic scale taking the effect of the quantum mechanics into consideration. They all experience a heavy computational burden that requires supper computers to be able to obtain reliable diffusivities [93]. On the other hand, macro scale models require significantly less computational tasks. The main disadvantage of using macro scale models for the diffusion in zeolites is assuming that the diffusing components as a continuous phase (continuum). This assumption is not suitable when dealing with diffusion in zeolites or zeolite membranes. This is because the zeolite pores are comparable to the molecules sizes and the zeolite layer thickness is comparable to the mean free path of the molecules. However, the macro models still the most frequently used models to model the diffusion in zeolites and zeolite membranes. The most used macro scale models to model the diffusion in zeolites are the generalized Fick's law, the activated diffusion model and Maxwell-Stefan approach. Maxwell-Stefan approach is the most successful, physically sound and widely accepted approach to describe multicomponent mixtures diffusion through zeolite membranes [94-96].

The generalized Maxwell-Stefan equations were developed based on the irreversible thermodynamics theories to describe the multicomponent diffusion of non-ideal fluids, for instance gases, liquids, or electrolytes. The generalized Maxwell-Stefan equation for mixture diffusion in zeolites may be written as [97,98]:

$$-\nabla\mu_i = RT\frac{u_i}{Đ_i} + RT\sum_{\substack{j=1\\ j\neq i}}^{n}\theta_j\frac{u_i - u_j}{Đ_{ij}} \tag{2.5}$$

where $\nabla\mu_i$ (J/mol) is the chemical potential for component i, which represents the fundamental driving force (under isothermal conditions) for the mass transport, R is the gas constant (8.314 J/mol.K) , T is the absolute temperature (K), u_i *and* u_j (m/s) are the velocities of component i and j with respect to the surface, respectively, θ_j is the occupancy or fractional loading of component j (dimensionless), $Đ_{ij}$ is the Maxwell-Stefan (M-S) surface diffusion coefficient (m^2/s) or the exchange diffusivity between molecules i and j, and $Đ_i$ is the MS surface diffusion coefficient between molecule i and the wall (m^2/s). Eq. 2.5 can be rearranged, after multiplying each term with θ_i, as follows:

$$-\frac{\theta_i}{RT}\nabla\mu_i = \frac{\theta_i u_i}{Đ_i} + \sum_{\substack{j=1\\ j\neq i}}^{n}\theta_i\theta_j\frac{u_i - u_j}{Đ_{ij}} \tag{2.6}$$

where θ_i is the occupancy or fractional loading of components i (dimensionless). The occupancy for components i and j is given by:

$$\theta_i = \frac{q_i}{q_i^{sat}} \tag{2.7}$$

$$\theta_j = \frac{q_j}{q_j^{sat}} \tag{2.8}$$

where q_i, q_j, q_i^{sat} and q_i^{sat} are the adsorption capacities (mol/kg) for components i and j and the saturation adsorption capacities (mol/kg) for components i and j, respectively.

Substituting Eq. (2.7) and Eq. (2.8) into the right hand side of Eq. (2.6), gives:

$$-\frac{\theta_i}{RT}\nabla\mu_i = \frac{q_i u_i}{q_i^{sat}Đ_i} + \sum_{\substack{j=1 \\ j\neq i}}^{n} q_i q_j \frac{u_i - u_j}{q_i^{sat} q_j^{sat} Đ_{ij}} \tag{2.9}$$

The flux for each component can be written as product of the zeolite density (ρ_s), adsorbed concentration and velocity, hence, the occupancies are converted into fluxes using Eq. (2.10) [99]:

$$J_i = \rho_s q_i^{sat} \theta_i u_i = \rho_s q_i u \tag{2.10}$$

Eq. 2.10 can be rearranged as follows:

$$u_i = \frac{J_i}{\rho_s q_i^{sat} \theta_i} = \frac{J_i}{\rho_s q_i} \tag{2.11}$$

Substituting Eq. (2.11) into Eq. (2.9) gives:

$$-\frac{\theta_i}{RT}\nabla\mu_i = \frac{1}{\rho_s}\left(\frac{J_i}{q_i^{sat}Đ_i} + \sum_{\substack{j=1 \\ j\neq i}}^{n} \frac{q_j J_i - q_i J_j}{q_i^{sat} q_j^{sat} Đ_{ij}}\right) \tag{2.12}$$

The chemical potential gradient and the surface coverage gradient can be related via a matrix of thermodynamic factors given by [98]:

$$\frac{\theta_i}{RT}\nabla\mu_i = \sum_{j=1}^{n} \Gamma_{ij} \nabla\theta_j \tag{2.13}$$

where Γ_{ij} is a thermodynamic correction factor defined by:

$$\Gamma_{ij} = \theta_i \frac{\partial \ln p_i}{\partial \theta_j} = \frac{\theta_i}{p_i}\frac{\partial p_i}{\partial \theta_j} \tag{2.14}$$

where p_i is the partial pressure of component *i*.

Equating Eq. 2.12 and Eq. 2.13 gives:

$$\sum_{j=1}^{n} \Gamma_{ij} \nabla \theta_j = -\frac{1}{\rho} \left(\frac{N_i}{q_i^{sat} Đ_i} + \sum_{\substack{j=1 \\ j \neq i}}^{n} \frac{q_j N_i - q_i N_j}{q_i^{sat} q_j^{sat} Đ_{ij}} \right) \quad (2.15)$$

Eq. 2.15 allows the estimation of the binary mixture diffusivities using only pure component diffusivities, pure component adsorption isotherms and a binary adsorption isotherm model that satisfactorily predicts the binary mixture adsorption data from the pure component adsorption isotherms.

2.12 References:

1- M.T. Ravanchia, T. Kaghazchia, A. Kargarib, Application of membrane separation processes in petrochemical industry: a review, Desalination 235 (2009) 199 – 244.

2- A.F. Ismail, N. Ridzuan, S.A. Rahman, Latest development on the membrane formation for gas separation, Membrane Sci. Tech. 24 (2002) 1025 – 1043.

3- J. Karger, D.M. Ruthven, Diffusion in zeolites and other microporous solids, Wiley, New York (1992).

4- T.T. Moore, W.J. Koros, Non-ideal effects in organic–inorganic materials for gas separation membranes, J. Molecular Structure 739 (2005) 87 – 98.

5- J. Caro, M. Noack, P. Kolsch and R. Schafer, Zeolite membranes – state of their development and perspective, Microporous Mesoporous Materials, 38 (2000) 3.

6- N.W. Ockwig, T.M. Nenoff, Membranes for hydrogen separation, Chemical Reviews 107 (2007) 4078 – 4110.

7- H.W. Liepmann, Gas kinetics and gas dynamics of orifice flow, J. Fluid Mechanics 10 (1961) 65 – 79.

8- J. Kong, K. Li, An improved gas permeation method for characterising and predicting the performance of microporous asymmetric hollow fibre membranes used in gas absorption, J. Membrane Science, 182, 1 – 2 (2001) 271 – 281.

9- W.J. Koros, G.K. Fleming, Membrane-based gas separation J. Membrane Science 83 (1993) 1 – 80.

10- D.E. Fain, Membrane gas separation principles, Material Research Society Bulletin 19 (1994) 40 – 43.

11- R. Ash, R.M. Barrer, C.G. Pope, Flow of Adsorbable Gases and Vapours in a Microporous Medium. I. Single Sorbates, Proceedings of the royal society 271 (1963) 1 – 18.

12- M.C. Porter, Handbook of Industrial Membrane Technology, Noyes Publications (1990).

13- S.V. Sotirchos, V.N. Burganos, Transport of gases in porous membranes, Material Research Society Bulletin 24 (1999) 41 – 45.

14- E.R. Gilliland, R.F. Baddour, J.L. Russell, Rates of flow through microporous solids AIChE J. 4 (1958) 90 – 96.

15- M. Ponzi, J. Papa, J.B.P. Rivarola, G. Zgrablich, On the surface diffusion of adsorbable gases through porous media AIChE J. 23 (1977) 347 – 352.

16- L.M. Robeson, The upper bound revisited, J. Membrane Science 320 (2008) 390 – 400.

17- R.J.R. Uhlhorn, K. Keizer, J. Burggraaf, Gas transport and separation with ceramic membranes. Part I. Multilayer diffusion and capillary condensation, J. Membrane Science 66 (1992) 259 – 269.

18- B. Freeman, I. Pinnau, Separation of gases using solubility-selective polymers, Trends Polymeric Science 5 (1997) 167 – 173.

19- M. Mulder, Basic principles of membranes technology, Klumer Academic Publishers (1996).

20- F. Kapteijn, J. van de Graaf, J. Moulijn, Proc. 4th workshop on the optimisation of catalytic membrane reactor systems, Oslo (1997).

21- D. Shah, K. Kissick, A. Ghorpade, R. Hannah, D. Bhattacharyya, Pervaporation of alcohol–water and dimethylformamide–water mixtures using hydrophilic zeolite NaA membranes: mechanisms and experimental results, J. membrane sciense 197 (2000) 185 – 205.

22- B.D. Freeman, N. Carolina, "Basis of permeability/selectivity tradeoff relations in polymeric gas Separation membranes, Macromolecules 32 (1999) 375 – 380.

23- R.E. Kesting, Synthetic polymeric membranes, a structural prospective, John Wiley & Sons, New York (1985).

24- W.J. Koros, I. Pinnau, Polymeric gas separation membrane, D.R. Paul, Y. P. Yampolskii (eds), CRC Press, Boca Raton (1993) 209 – 272.

25- K.G. Beltsios et al. In F. Schueth, K.S.W. Sing, J. Weitkamp (Eds.), Handbook of Porous Solids, vol. 4, Wiley-VCH Verlag GmbH & Co., Weinheim, Germany, 2002, 2281.

26- B. Hamilton, Porous silicon, Semiconductor Science and Technology 10 (1995) 1187 – 1207.

27- A. Julbe, Zeolite membranes – syntheses, charaterization and application, Chap. 6, Intoduction to zeolite science and practice, 3rd ed., Elsevier (2007).

28- M. Freemantle, “Membranes for gas separation, Chem. Eng. News 83 (2005) 49 – 57.

29- J. Caro, M. Noack, and P. Kolsch, Zeolite membranes: from the laboratory scale to technical applications, Adsorption 11 (2005) 215 – 227.

30- P. Pandey, R.S. Chauhan, Membranes for gas separation, Progress in Polymer Science 26 (2001) 853 – 893.

31- E.E. McLeary, J.C. Jansen, F. Kapteijn, Zeolite based films, membranes and membrane reactors: progress and prospects, Microporous Mesoporous Materials 90 (2006) 198 – 220.

32- R.W. Barker, Membrane Technology and Applications, 2nd ed, 2004, John Wiley & Sons.

33- L. Kang, Ceramic Membranes for Separation and Reaction, Wiley, 2007.

34- M.B. Rao, S. Sircar, Nanoporous Carbon membranes for separation of gas mixtures by selective surface flow, J. Membrane Science 85 (1993) 253 – 264.

35- K.M. Steel, W.J. Koros, An Investigation of The effects of pyrolysis parameters on gas separation properties of carbon materials, Carbon 43 (2005) 1843 – 1856.

36- C. Colella, A.F. Gualtieri, Cronstedt’s zeolite, Microporous Mesoporous Materials 105 (2007) 213 – 221.

37- R. Szostak, Molecular Sieves. 2nd ed, Blackie Academic& Professional, London, 1998.

38- W.M. Meier, D.H. Olson, Atlas of Zeolite Structure Types, Butterworth-Heinemann, London, 1992.

39- J.V. Smith, Definition of a zeolite, Zeolites 4 (1984) 309 – 310.

40- R. Szostak, Molecular Sieves; Principles of Synthesis and Identification, Van Nostrand Reinhold, New York (1989).

41- L.B. McCusker, F. Liebau, G. Englhardt, Nomenclature of structural and compositional characteristics of ordered microporous and mesoporous materials with inorganic hosts, Pure Appl. Chem. 73 (2001) 381–394.

42- http://www.iza-online.org

43- N.J. Newsam. In A.K. Cheetham, P. Day (eds), Solid state chemistry compounds, New York, Oxford University press (1992).

44- C.H. Baerlocher, L.B. McCusker, D.H. Oslon, Atlas of zeolite framework types, 5th ed. Elsevier, Amsterdam (2001).

45- F. Jareman, C. Andersson, J. Hedlund, The influence of the calcination rate on silicalite-1 membranes, Microporous Mesoporous Materials 79 (2005) 1 – 5.

46- M. Lassinantti, F. Jareman, J. Hedlund, D. Creaser, J. Sterte, Preparation and evaluation of thin ZSM-5 membranes synthesized in the absence of organic template molecules, Catalysis Today 67 (2001) 109–119.

47- N.Y. Chen, W.E. Garwood, F.G. Dwyer, Shape selective catalysis in industrial applications, Marcel Dekker Inc., New York and Basel (1989).

48- J. Dong, Y.S. Lin, W. Liu, Multicomponent hydrogen/hydrocarbon separation by MFI-type zeolite membranes, AIChE J. 46 (2000) 1957 – 1966.

49- L.J.P. van den Broeke, F. Kapteijn, J. A. Moulijn, Transport and separation properties of a silicalite-1 membrane—II. Variable separation factor, Chemical Engineering Science 54 (1999) 259 – 269.

50- M. Noack, J. Caro, Zeolite membranes, In: F. Schueth, K.S.W. Sing, J. Weitkamp (Eds.), Handbook of Porous Solids, vol. 4, Wiley-VCH Verlag GmbH & Co., Weinheim, Germany, 2002, 2433 – 2507.

51- L.B. Mccusker, F. Liebau, G. Engelhardt, International union of pure and applied chemistry nomenclature of structural and compositional characteristics of ordered microporous and mesoporous materials with inorganic hosts q (IUPAC recommendations 2001) Physical Chemistry Division 58 (2003) 3 – 13.

52- J. Dong, Y.S. Lin, M.Z.-C. Hu, R.A. Peascoe, E.A. Payzant, Template-removal-associated microstructural development of porous-ceramic-supported MFI zeolite membranes, Microporous Mesoporous Materials 34 (2000) 241 – 253.

53- C.S. Cundy, P.A. Cox, The hydrothermal synthesis of zeolites: Precursors, intermediates and reaction mechanism, Microporous Mesoporous Materials 82 (2005) 1 – 78.

54- R. Xu, W. Pang, J. Yu, Q. Huo, J. Chen, Chemistry of zeolites and related porous materials: synthesis and structure, John wiley & Sons (Asia) Pte Ltd. Singapore (2007).

55- S. Miachon, E. Landrivon, M. Aouine, Y. Sun, I. Kumakiri, Y. Li, O. Pachtova Prokopova, N. Guilhaume, A. Giroir-Fendler, H. Mozzanega, J.-A. Dalmon, Nanocomposite MFI-alumina membranes via pore-plugging synthesis: preparation and morphological characterization, J. Membrane Science 281 (2006) 228 – 238.

56- S. Miachon, P. Ciavarella, L. van Dyk, I. Kumakiri, K. Fiaty, Y. Schuurman, J.-A. Dalmon, Nanocomposite MFI-alumina membranes via pore-plugging synthesis:

specific transport and separation properties, J. Membrane Science 298 (2007) 71 – 79.

57- G. Li, E. Kikuchi, M. Matsukata, The control of phase and orientation in zeolite membranes by the secondary growth method, Microporous Mesoporous Materials 62 (2003) 211 – 220.

58- M. Pan, Y.S. Lin, Template-free secondary growth synthesis of MFI type zeolite membranes, Microporous Mesoporous Materials 43 (2001) 319 – 327.

59- L.C. Boudreau, J.A. Kuck, M. Tsapatsis, Deposition of oriented zeolite A films: in situ and secondary growth, J. Membrane Science 152 (1999) 41 – 59.

60- K. Okamoto, H. Kita, K. Horii, K. Tanaka, Zeolite NaA membrane: preparation , single gas permeation, and pervaporation and vapor permeation of water/organic liquid mixtures, Ind. Eng. Chem. Res. 40 (2001) 163 – 175.

61- Y. Hasegawa, T. Ikeda, T. Nagase, Y. Kiyozumi, T. Hanaoka, F. Mizukami, Preparation and characterization of silicalite-1 membranes prepared by secondary growth of seeds with different crystal sizes, J. Membrane Science 280 (2006) 397 – 405.

62- Q. Zhao, J. Wang, N. Chu, X. Yin, J. Yang, C. Kong, A. Wang, J. Lu, Preparation of high-permeance MFI membrane with the modified secondary growth method on the macroporous α-alumina tubular support, J. Membrane Science 320 (2008) 303–309.

63- M.P. Bernal, G. Xomeritakis, M. Tsapatsis, Tubular MFI zeolite membranes made by secondary (seeded) growth, Catalysis Today 67 [2001] 101 – 107.

64- C. Algieri, G. Golemme, S. Kallus, J.D. . Ramsay, Preparation of thin supported MFI membranes by in situ nucleation and secondary growth, Microporous Mesoporous Materials 47 (2001) 127 – 134.

65- M.C. Lovallo, A. Gouzinis, M. Tsapatsis, Synthesis and characterization of oriented MFI membranes prepared by secondary growth, AIChE J. 44 (1998) 1903 – 1913.

66- D. Uzio, J. Peureux, A. Giroir-Fendler, J. A. Dalmon and J. D. F. Romasy, In Studies in Surface Science & Catalysis, Vol. 87, Rouquerol et al. (eds) 1994, 411.

67- J. Caro, M. Noack, Zeolite membranes – recent development and progress, Microporous Mesoporous Materials 115 (2008) 215 – 233.

68- Z. Wang, Y. Yan, Controlling crystal orientation in zeolite MFI thin films by direct in situ crystallization, Chem. Mater. 13 (2001) 1101 – 1207.

69- J.H. Koegler, H. Van Bekkum, J.C. Jansen, Growth model of oriented crystals of zeolite Si-ZSM-5, Zeolites 19 (1997) 262 – 269.

70- Y. Tanaka, T. Tsuru, T. Yoshioka, M. Asaeda, Gas permeation properties of MFI zeolite membranes prepared by the secondary growth of colloidal silicalite and application to the methylation of toluene, Microporous Mesoporous Materials 54 (2002) 257 – 268.

71- Z. Lia, G. Bonilla, I. Diaz, J.G. Nery, K. Sujaoti, M.A. Amat, E. Kokkoli, O. Terasaki, R.W. Thompson, M. Tsapatsis, D.G. Vlachos, Microstructural optimization of a zeolite membrane for organic vapor separation, Science 300 (2003) 456 – 460.

72- J. Coronas and J. Santamaria, Separations Using Zeolite Membranes, Separation Purification Methods 28 (1999) 127 – 177.

73- G.E. Romanos, Th.A. Steriotis, E.S. Kikkinides, N.K. Kanellopoulos V. Kasselouri, J.D.F. Ramsay , P. Langlois , S. Kallus, Innovative methods for preparation and testing of Al_2O_3 supported silicalite-1 membranes, J. European Ceramic Society 21 (2001) 119 – 226.

74- J. Ramsay, S. Kallus, Zeolite membranes, in: Recent advances in gas separation by microporous ceramic membranes, N.K. Kanellopoulos (ed.), Elsevier, Amsterdam (2000).

75- J. Ramsay, S. Kallus, Membrane science & technology series (6), in: Recent advances in gas separation by microporous ceramic membranes, N.K. Kanelloppoulos (eds), Elsevier, Amsterdam, (2000).

76- W. Meise, F.E. Schwocho, Adv. Chem. Ser., (1973) 169.

77- S.G. Fegan, B.M. Lowe, Effect of alkalinity on the crystallization of silicalite-1 precursors, J. Chem. Soc. Faraday Trans. 82 (1986) 785 – 799.

78- D.W. Breck, Zeolite molecular sieves, structure, chemistry and use, Wiley, New York, 1974.

79- F. Delprate, L. Delmotte, J.L. Guth, L. Huve, Synthesis of new silica-rich cubic and hexagonal faujasites using crown-ether-based supramolecules as templates, Zeolites 10 (1990) 546 – 552.

80- S.T. Wilson, B.M. Lok, C.A. Messina, T.R. Cannan, E.M. Flanigen, Aluminophosphate molecular sieves: A new class of microporous crystalline inorganic solids, J. Am. Chem. Soc. 104 (1982) 1146 – 1147.

81- G.R. Gavalas, Zeolite membranes for Gas and liquid separations, In: Materials Science of Membranes for Gas and Vapor Separation, Edited by Y. Yampolskii, I. Pinnau, B. Freeman, John Wiley & Sons, Ltd. (2006).

82- H. Kacirek, H. Lechert, Rates of crystallization and a model for the growth of sodium-Y zeolites, J. Phys. Chem. 80 (1976) 1291 – 1296.

83- N.N. Feoktistova, S.P. Zhdanov, W. Lutz, M. Büllow, On the kinetics of crystallization of silicalite I, Zeolites 9 (1989) 136 – 139.

84- M.E. Davis, R.F. Lobo, Zeolite and molecular sieve synthesis, Chem. Mater. 4 (1992) 756 – 768.

85- T.A.M. Twomey, M. Mackay, H.P.C.E. Kuipers, R.W. Thompson, In situ observation of silicalite nucleation and growth: A light-scattering study, Zeolites 14 (1994) 162 – 168.

86- Q. Li, B. Mihailova, D.Creaser, J. Sterte, Aging effects on the nucleation and crystallization kinetics of colloidal TPA-silicalite-1, Microporous Mesoporous Mater. 43 (2001) 51 – 59.

87- M. Ogura, Y. Kawazu, H. Takahashi, and T. Okubo, Aluminosilicate species in the hydrogel phase formed during the aging process for the crystallization of FAU zeolite, Chem. Mater. 15 (2003) 2661 – 2667.

88- A. Gouzinis, M.Tsapatsis, On the preferred orientation and microstructural manipulation of molecular sieve films prepared by secondary growth, Chemistry Materials 10 (1998) 2497 – 2504.

89- J. Hedlund, S. Mintova, J. Sterte, Controlling the preferred orientation in silicalite-1 films synthesized by seeding, Microporous Mesoporous Materials 28 (1999) 185 – 194.

90- M.C. Lovallo, M. Tsapatsis, Preferentially oriented submicron silicalite membranes", AIChE J. 42 (1996) 3020 – 3029.

91- X. Lin H. Kita, K. Okamoto, Silicalite membrane preparation, characterization and separation performance, Industrial Engineering Chemistry Research 40 (2001) 4069 – 4078.

92- G. Xomeritakis, A. Gouzinis, S. Nair, T. Okubo, M. He, M.R. Overney, M. Tsapatsis, Growth, microstructure and permeation properties of supported zeolite (MFI) films and membranes prepared by secondary growth, Chemical Engineering Science 54 (1999) 3521 – 3531.

93- E.J. Keil, R. Krishna, M.O. Coppens, Modeling of diffusion in zeolites, Rev. Chem. Eng. 16 (200) 71 – 197.

94- J.M. van de Graaf, F. Kapteijn, J.A. Moulijn, Modeling permeation of binary mixtures through zeolite membranes, *AIChE J.* 45 (1999) 497 – 511.

95- R. Krishna, R. Baur, Analytical solution of the Maxwell-Stefan equations for multicomponent permeation across a zeolite membrane, Chemical Engineering J. 97 (2004) 37 – 45.

96- J.G. Martinek, T.Q. Gardner, R.D. Noble, J.L. Falconer, Modeling transient permeation of binary mixture through zeolite membranes, Ind. Eng. Chem. Res. 45 (2006) 6032 – 6043.

97- R Taylor & R. Krishna, Multicomponent Mass Transfer, Wiley, New York, 1993.

98- R. Krishna, A unified approach to the modelling of intraparticle diffusion in

adsorption processes, Gas Separation and Purification 7 (1993b) 91 – 104.

99- R. Krishna, Diffusion of binary mixtures across zeolite membranes: entropy effects on permeation selectivity, Int. Comm. Heat Mass Transfer 28 (2001) 337 – 346.

CHAPTER THREE

This Chapter is based on

Separation of CO_2 and N_2 on Zeolite Silicalite-1 Membrane Synthesized on Novel Support

M. Tawalbeh[1], F. H. Tezel[1,2], S. Letaief[2], C. Detellier[2], B. Kruczek[1]

[1] Department of Chemical and Biological Engineering, University of Ottawa, 161 Louis Pasteur Street, Ottawa, ON, Canada K1N 6N5

[2] Centre for Catalysis Research and Innovation and Department of Chemistry, University of Ottawa, 10 Marie Curie, Ottawa, Ontario, Canada K1N 6N5

In: Separation Science and Technology 47:11 (2012) 1606 – 1616.

This paper presents an investigation for the morphology and CO_2/N_2 permeation results of a silicalite-1 membrane that was prepared on a tubular zirconium and titanium oxides active layer support with 0.45 μm pore size. It was aimed at verifying the possibility of preparing selective membranes by combining the zirconium and titanium oxides supports and the pore plugging synthesis method. Eleven membranes were prepared and the results showed that only three had a high CO_2/ N_2 selectivity. The best permeation results were for the membrane presented in this paper. This membrane was then cut to perform morphology

studies which are also presented in this paper. Simultaneously, a thorough analysis for the effect of the support pore size on the morphology of the silicalite-1 membranes prepared on flat zirconium and/or titanium oxides active layer supports using pore plugging synthesis method was also performed. Five supports with different pore sizes for their active layer in the range of 0.14 - 1.4 μm were investigated. The results of these morphology analyses are presented in Chapter 4. In this paper there are additional two authors other than the supervisors, C. Detellier and S. Letaief. Both Dr. C. Detellier and Dr. S. Letaief helped with understanding and interpretation of the morphology results. Dr. S. Letaief also helped with the conduction of the morphology analysis.

Chapter 3 - Separation of CO_2 and N_2 on Zeolite Silicalite-1 Membrane Synthesized on Novel Support

Abstract

This paper reports on the properties of an MFI-type zeolite (silicalite-1) membrane synthesized on a novel tubular support with a 0.45 μm-pore size active layer consisting of zirconium and titanium oxides. Even though the membrane was synthesized by a pore plugging method, apart from penetrating into the support, the silicalite-1 crystals formed a 1.5 μm layer on top of the support. After the zeolite synthesis, the Si constituted more than 35% of the active layer of the support, which implies small size and close packing of the silicalite-1 crystals in the pores of the active layer.

Single gas permeation tests with N_2 and CO_2 revealed comparable N_2 and CO_2 permeances. Gas separation tests performed using CO_2/N_2 mixtures at different total feed pressures and feed compositions lead to CO_2/N_2 permselectivities as high as 26.0, with the corresponding CO_2 permeance of 6×10^{-8} mol/m^2 Pa s. The effects of changing the partial pressure gradient of CO_2 across the membrane by means of varying the total feed pressure and the feed composition on the CO_2 permeance and CO_2/N_2 permselectivity are discussed.

Keywords: Zeolite Silicalite-1 Membranes, Gas Permeation, CO_2/N_2 Separation.

3.1 Introduction

The use of membranes in gas separation processes is a rapidly growing field of research resulting in commercial applications since 1980's. While most of the commercial gas separation applications utilize polymeric membranes, inorganic membranes, in particular zeolite membranes have attracted a lot of research interests in the last decade because of their inherent advantages over the polymeric membranes. Zeolite membranes show better thermal, chemical and structural stability compared to polymeric membranes [1]. On the other hand, they lack of full reproducibility [2,3]. Zeolite membranes can be used at high temperatures and pressures and can operate in harsh chemical environments. Zeolite membranes are widely explored for applications of gas separation [4], membrane reactors [5], pervaporation [6], shape selective sensors [7], electrodes [8], and corrosion protection coatings [9]. Various types of zeolite membranes have been successfully prepared at the laboratory scale, with the most prominent examples of: LTA [6], MFI [10], FAU [11], and SAPO-34 [12].

Zeolite membranes are basically crystalline silicates and aluminosilicates with a regular three dimensional pore structure grown on a porous supports. These crystalline materials have pore sizes between 0.3 and 1.3 nm [4], which give them the potential to perform many industrially important separations. Zeolite membranes can separate gases by molecular sieving when the size of one component exceeds the zeolitic pore opening [7,10], provided that there are no cracks or pinholes in their structure [5,13]. Nevertheless, a very high selectivity is also possible when the zeolite pore sizes are larger than the mixture gas molecules and this is due to the differences in affinity and diffusivity of the various components from the mixture in the pores of the membrane [5,14].

Among the different types of zeolites available, MFI zeolites (ZSM-5 and silicalite-1) are of particular interest because of their pore size of 0.55 nm, which is suitable for several industrially important separations [15]. MFI zeolites are relatively easy to synthesize from a variety of silica sources and structure directing agents [15]. Zeolite membranes are generally synthesized by a hydrothermal deposition method using silicate or aluminosilicate precursors in aqueous solution. Zeolite membranes are synthesized on various porous supports via in-situ crystallization [6], vapor phase transport [16], secondary growth [4,17-19] and pore plugging methods [20,21]. The most commonly used method is the secondary growth method.

Most zeolite membranes are synthesized on alumina and stainless steel supports. However, using as alumina and stainless steel as a membrane support may lead to dissolution of the respective ions from the support and their integration into the zeolite network under a harsh hydrothermal environment. These Al^{3+} or Fe^{3+} ions could replace some of the silicon ions, which results in a negatively charged lattice structure and thus an increase in membrane hydrophilicity [22]. While an increase in membrane hydrophilicity might be desirable in some applications, in particular those involving polar gases such as CO_2 [23], it has also been shown that presence of aluminum in zeolite network may promote defect formation in the membrane structure [24]. These two opposing effects are likely responsible for a significant variation in the CO_2/N_2 permselectivity of zeolite silicalite-1 membranes reported in the literature. Furthermore, considering possible incorporation of Al^{3+} or Fe^{3+} into the lattice structure, the final product would be a ZSM-5 rather than silicalite-1 zeolite. The problems associated with alumina and stainless steel supports could be eliminated by using

supports made of titanium and zirconium oxides. These supports are more chemically stable than alumina [25] and they can withstand harsher environments. Furthermore, zirconium and titanium ions generally do not dissolve and integrate into the zeolite network under the zeolite hydrothermal synthesis conditions [26], but even if the dissolution and integration occurred, the zirconium and titanium ions would not add any negative charge to the zeolite network; on the contrary, they would increase the network stability [27].

In this paper we report synthesis of silicalite-1 membranes by the pore plugging technique on a novel tubular support in which the active layer of the support is made of zirconium and titanium oxides. The properties of the synthesized membranes, including those for the separation CO_2/N_2 mixtures at different feed pressures and feed compositions are discussed. By plugging the pores of the active layer of the support, it is anticipated that its thickness will control the membrane permeance. Moreover, the by preventing incorporation of Al^{3+} or Fe^{3+} ions into the zeolite network, it is anticipated that the resulting membrane will exhibit representative selective properties of the silicalite-1 zeolite.

3.2 Experimental

3.2.1 Porous Supports

Commercial ceramic asymmetric porous tubes with an active layer containing titanium oxide and zirconium oxide were purchased from TAMI Industries (Nyons, France) and used as membrane supports. The tubes had the outside diameter of 1 cm and the wall thickness equal to 2 mm, with the active layer inside the tube. The average pore size of the active layer of the tube selected for the membrane synthesis was 0.45 μm. This pore size was chosen

based on the preliminary investigation with disks of different pore sizes ranging from 0.14 μm to 1.4 μm, which is reported elsewhere [28].

3.2.2 Membrane preparation

The membrane synthesis protocol used in this work was adapted from the protocol developed for the membrane synthesis on flat discs having the same pore size and the same composition of the active layer as the tubes used in this work [28].

3.2.2.1 Zeolite precursor solution preparation

Fumed silica (Sigma-Aldrich, Oakville, ON, Canada) was used as a silicone source and a 5.5 g was dissolved in approximately 46 mL of 1 M tetrapropylammonium hydroxide (TPAOH) (Fluka's Purum, Sigma-Aldrich, Oakville, ON, Canada) solution. The TPAOH/Si mole ratio was chosen to be 0.5. The final concentration of the solution was adjusted by adding deionized water to obtain a 50 mL solution with the following overall molar composition: 1 SiO_2 – 0.5 TPAOH – 27.8 H_2O [20]. The solution was then left under stirring for 3 days at room temperature for maturation. The maturation was followed by subjecting the solution to a centrifugal device for 30 min at 5000 rpm to remove any large particles that could exist in the solution, which would limit the precursor penetration inside the pores of the support.

3.2.2.2 Hydrothermal synthesis and drying

Hydrothermal synthesis process was carried out inside a Teflon lined stainless steel autoclave. The external surface of the support was covered by a Teflon tape to ensure the growth of the zeolite layer only at the inside surface of the supports. The zeolite precursor

solution was poured in the autoclave containing the supports until the supports were completely immersed in the solution. After 30 min, the level of the solution inside the autoclave was checked and if necessary more solution was added to compensate for the fraction that had penetrated inside the pores of the support.

The autoclave was then closed and placed in an oven, preheated to 160^{o}C, for 4 days. After the synthesis, the membranes were removed from the autoclave, and washed with deionized water. The washed membranes were then dried at 100^{o}C for 24 h.

3.2.2.3 Calcination

Calcination of the dried membranes was carried out inside a programmable oven (Vulcan 3-550) at 500^{o}C for 4 hr with heating and cooling rate of 1.0^{o}C/min. This low heating and cooling rate was used to prevent defect formation [17]. The calcination was done to remove the templates from the zeolite pores as well as to enhance the bonding between the zeolite layer and the support. After calcination, the samples were kept in a desiccator under dry atmosphere.

The zeolite powder remaining on the autoclave Teflon lining was also collected, washed, calcined, and then kept for CO_2 and N_2 adsorption isotherms measurements.

3.2.3 Membrane characterization

3.2.3.1 Morphology and microstructure

Scanning electron microscope (SEM) was performed using a JEOL JSM-7500F Field Emission Scanning Microscope (from JEOL, Japan) operating with primary electron beams of 2 keV. The samples of the ceramic support and the synthesized membrane were analyzed also in situ with an electron diffraction spectrometer (EDS) Tracor-Northen Series Z-II spectrometer (Zeiss, Oberkochem, Germany) operating with primary electron beams of 20 keV to get the compositions. The samples were mounted on a specimen holder and covered with a conductive carbon tape.

3.2.3.2 Gas adsorption

Volumetric method was used to generate the adsorption isotherms for CO_2 and N_2 gases on the powder collected from the inner wall of the autoclave Teflon lining. An AccuSorb 2100E Physical Adsorption Analyzer supplied by Micromeritics Instrument Corporation, equipped with high precision pressure transducers and thermocouples was used to perform the adsorption experiments. Pressure changes were recorded via data acquisition using a National Instruments data acquisition card and Labview 6.1 installed on a computer. A powder sample of approximately 0.6 g was first regenerated at 350^{o}C under vacuum (~ 10^{-3} Pa) for 24 hours before performing the adsorption experiments. Helium was used to measure the dead volume in the gas phase since silicalite-1 has a negligible adsorption capacity for helium. Adsorption experiments were performed at ambient temperature (~23^{o}C) to be consistent with the conditions of permeation experiments. Adsorption isotherm data were obtained at pressures up to 4.8 atm. The gases used in adsorption experiments as well as in

the gas permeation experiments were carbon dioxide, nitrogen and helium, all purchased from Linde, Canada Limited, Ottawa, Canada, with purity 99.99, 99.998 and 99.999, respectively.

3.2.3.3 Gas permeation/separation experiments

The synthesized tubular membranes were connected to stainless steel tubes and sealed inside a custom made stainless steel membrane module. The ends of the membrane were connected to tygon tubes by the epoxy resin. Then, the tygon tubes were connected to the stainless steel tubes using the epoxy resin as well. The details of the custom made membrane module used in gas permeation/separation tests are shown in Fig. 3-1.

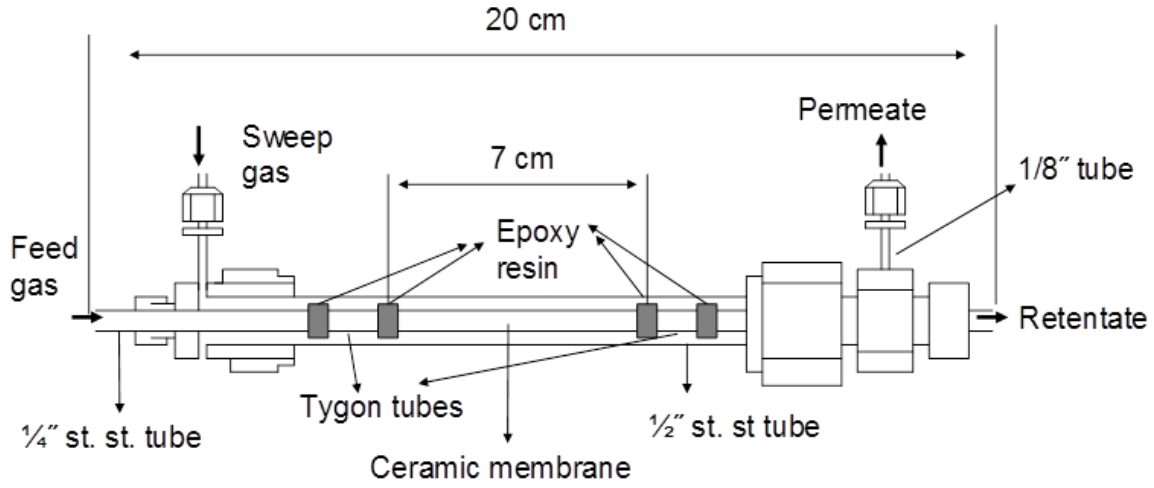

Figure 3-1 Schematic diagram for the custom made tubular membrane module used as permeation cell.

Fig. 3-2 presents the schematic diagram of the setup used in gas permeation/separation experiments. Single gas permeation experiments were performed first with N_2 followed by CO_2. The feed gas flow rate in all single gas experiments was set at 100 cm^3(STP)/min by

means of the mass flow controllers, MFC1 and MFC2, for CO_2 and N_2, respectively. The feed pressure was controlled manually and measured with a pressure gauge (PG) and the permeate flow was measured using a bubble flow meter (BFM). The experiments were considered to attain a steady state when the permeate flow rate reached a constant value. The separation experiments were performed using different compositions of the CO_2/N_2 feed mixture and different feed pressures. The feed composition was controlled by setting the appropriate flow rates of CO_2 and N_2 with the MFC1 and MFC2, respectively. The total feed flow rate in all separation experiments was maintained constant at 100 cm^3(STP)/min. An on-line gas chromatograph (GC) equipped with an 80x100 mesh Porapak Q column and a thermal conductivity detector (TCD) with helium as a carrier gas was used to analyze the permeate composition. The composition of the feed for a given setting of the mass flow controllers was verified using the GC prior to the actual gas separation experiment. The time for the experiment to reach steady state was determined by measuring the permeate flow rate and composition. When the two reached a plateau, it was considered that a steady state was reached. The steady state was typically reached within the first 6 hours, but each experiment was carried out for at least two days. All gas permeation and separation experiments were performed at ambient temperature (~23^{o}C).

The membrane performance at different conditions was evaluated on the basis of the gas permeance, P_i, the apparent selectivity, α_{CO_2/N_2}, and the permeance ratio, $\alpha^*_{CO_2/N_2}$, which are defined as follows:

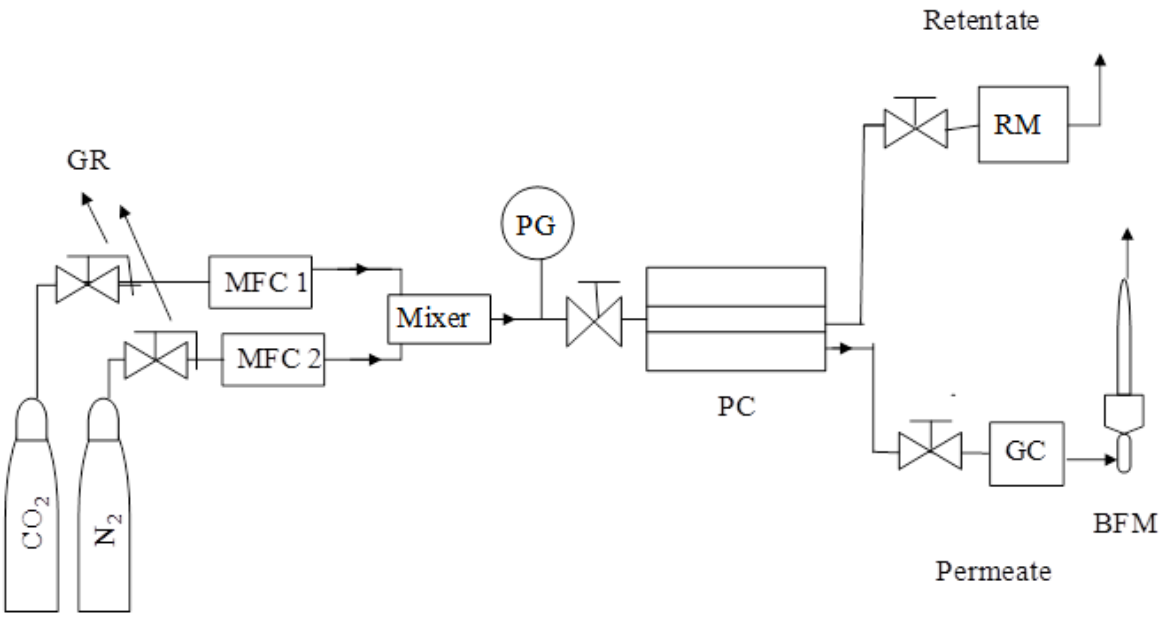

Figure 3-2 Gas permeation/separation setup (BFM: bubble flow meter, GR: gas regulator, GC: gas chromatograph, MFC: mass flow controller, PC: permeation cell, PG: pressure gauge, RM: rotameter).

$$P_i = \frac{q_i}{A_m\left(p_{i,F} - p_{i,P}\right)} \tag{3.1}$$

$$\alpha_{CO_2/N_2} = \frac{y_{CO_2}/y_{N_2}}{x_{CO_2}/x_{N_2}} \tag{3.2}$$

$$\alpha^*_{CO_2/N_2} = \frac{P_{CO_2}}{P_{N_2}} \tag{3.3}$$

where subscripts P and F denote the permeate side and the feed side of the membrane, respectively; q_i is the steady state permeation rate of i across the membrane (mol/s); p_i is the partial pressure of component I (Pa); A_m is the membrane area (m^2); y and x are the mole fractions in the permeate and the feed, respectively. The permeance ratios were determined

from single gas and mixed gas permeation tests. In case of the former, the permeance ratio is referred to as the ideal selectivity, while in the latter case it is referred to as the permselectivity.

Since the stage cut, i.e., the ratio of the permeate flow rate (q_P) to the feed flow rate (q_F) was significantly greater than zero in all tests, Eq. (3.1) could not be used directly for the calculation of the gas permeances in gas separation tests. Instead, the following procedure was used.

The membrane is divided into N differential elements of equal area along the direction of the gas flow. The feed is entering to the 1st element and the retentate is leaving at the N^{th} element of the membrane. Both feed and permeate are assumed to be in a plug flow flowing in the same direction, with the feed in the tube and the permeate in the shell side of the membrane module. Their respective compositions are changing along the membrane module because of the selective permeation of the components. The permeances of CO_2 and N_2 are assumed to be independent of the feed pressure and composition. Using guessed permeances and assuming perfect mixing in each differential element, the respective permeation rates in the last element, i.e., the N^{th} element of the membrane are calculated by differentiating Eq. (3.1) and rearranging it:

$$\left(dq_i\right) = P_i[(p_{i,R})_N - (p_{i,P})_N]dA_m \tag{3.4}$$

where: $\left(p_{i,R}\right)_N = x_i p_F$ and $\left(p_{i,P}\right)_N = y_i p_P$ in which (x_i) and (y_i) are the measured compositions of the retentate (R) and permeate (P), respectively, and p_F and p_P are the measured total pressures of the feed and permeate, respectively. Knowing $(dq_i)_N$ (determined from the flow rate and the composition of the permeate) and assuming that p_F and p_P are constant, the partial pressures on both sides of the membrane in the N-1 element are calculated from:

$$\left(p_{i,R}\right)_{N-1} = \left[\frac{q_{i,R} + \left(dq_i\right)_N}{\sum_i q_{i,P} - \sum_i \left(dq_i\right)_N}\right] p_F \tag{3.5}$$

$$\left(p_{i,P}\right)_{N-1} = \left[\frac{q_{i,P} + \left(dq_i\right)_N}{\sum_i q_{i,P} - \sum_i \left(dq_i\right)_N}\right] p_P \tag{3.6}$$

In turn, the partial pressures on both sides of the membrane allow the calculation of the permeation rates of both gases in the N-1 element using Eq. (3.4). By continuing the above procedure, the composition and the flow rate of the gas entering the 1st element of the membrane (i.e., the composition and the flow rate of the feed stream) are determined, and compared with the respective values measured experimentally. The procedure continues until the guessed permeances of CO_2 and N_2 yield the actual composition and the flow rate of the feed. The equations were solved using Excel Solver. The number of differential elements in all calculations was set to be N = 100. With N > 100, the calculated permeances were the same as those for N = 100 to the 3rd significant digit.

The above procedure also allows for the determination of the concentration profile at both sides of the membrane. In turn, knowing the concentration profiles allows the calculation of the average mole fraction at both sides of the membrane and the log mean partial pressure difference across the membrane. The log mean partial pressure difference across the membrane is the actual driving force for the permeation through the membrane. Consequently, replacing the partial pressure difference with the log mean partial pressure difference in Eq. (3.1) leads to the respective gas permeance determined using the procedure described above.

3.3 Results and Discussion

3.3.1 SEM and EDS analyses

Fig. 3-3 presents SEM micrographs of the membrane surface of the support without silicalite-1 (Fig. 3-3A) and the composite membrane with the silicalite-1 on the surface (Fig. 3-3C), as well as the SEM micrograph of the cross section before (Fig. 3-3B) and after (Fig. 3-3D) silicalite-1 synthesis. The corresponding compositions determined by the EDS analysis at different distances from the membrane surface are summarized in Table 3-1.

Comparison of Fig. 3-3A with Fig 3-3C indicates that the synthesized zeolite crystals are covering the entire surface of the composite membrane. The crystals are isometric and their size ranges from 0.5 – 1.5 μm. The synthesized crystals have the so called coffin shape, which is the characteristic shape of the silicalite-1 zeolite crystals [29].

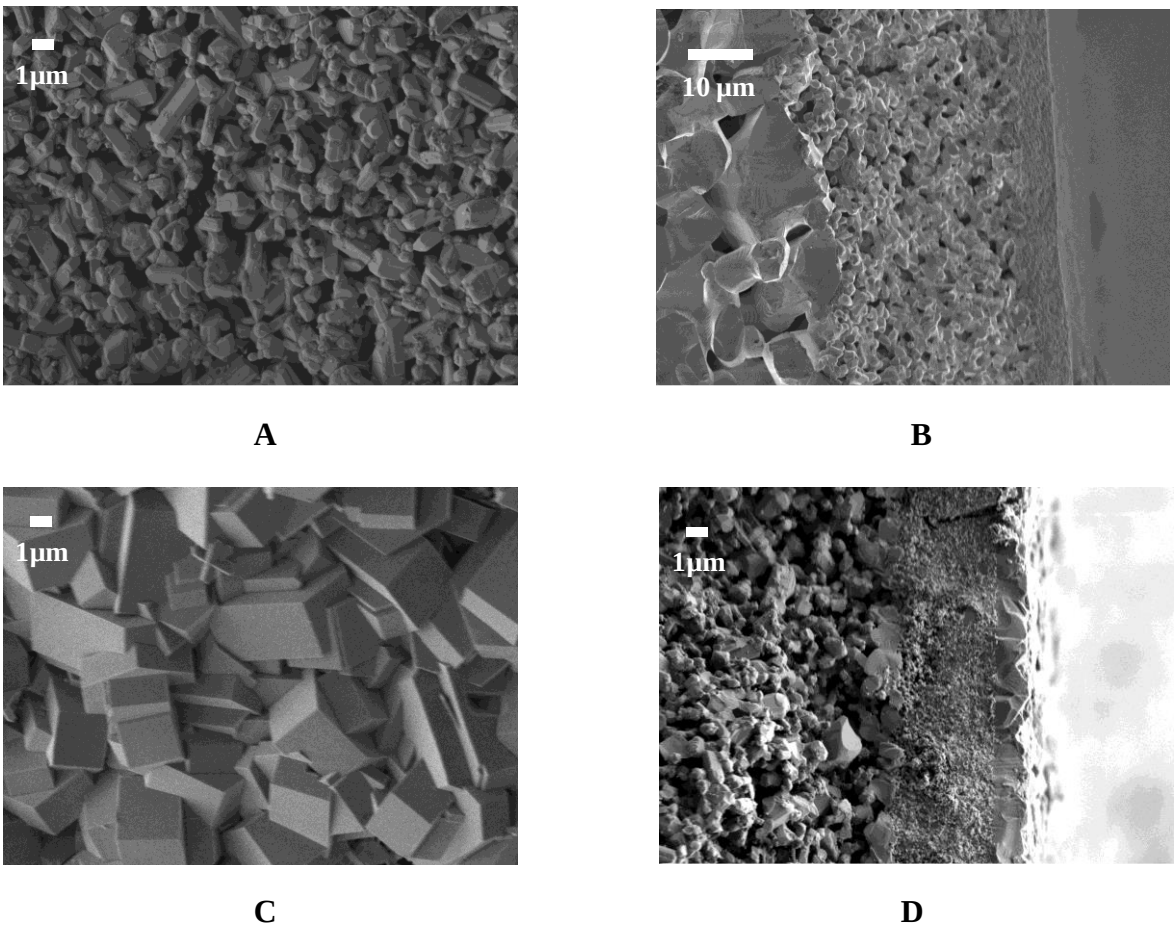

Figure 3-3 SEM micrographs of surface of the support before (A) and after (C) silicalite-1 synthesis, as well as the cross section of the support before (B) and after (D) the silicalite-1 cross synthesis.

Focusing on the porous support cross section before the membrane synthesis (Fig. 3-3C), there are three distinct layers. The 5 μm top layer represents the active layer of the support and has, according to the membrane supplier, the pore size of 0.45 μm, which is consistent with the micrograph presented in Fig. 3-3A showing the top surface of support before the zeolite synthesis. The support's active layer was followed by an intermediate layer of thickness of 30 μm. The intermediate layer is more porous and has larger pores than the

active layer; it contains mainly titanium oxide. The highly porous layer, which follows the intermediate layer, contains mostly alumina and represents the rest of the support.

Considering Fig. 3-3D, it is evident that after the synthesis of silicalite-1 by the pore plugging technique, there is an additional top layer of thickness of approximately 1.5 μm on top of the active layer of the support. Fig 3-3D is shown in a greater magnification than Fig. 3.3B and consequently only a part of the intermediate layer of the support is seen there, while the porous sub-layer consisting mostly of alumina does not appear in Fig. 3-3D. It is important to emphasize that the thickness of the active layer in Fig. 3-3D appears to be approximately 5 μm, which is in good agreement with the observation based on Fig. 3-3B. It can also be noticed in Fig. 3-3D that at the interface between the active and intermediate layers of the support there are individual crystals, which are similar to the silicalite-1 crystals at the top surface of the synthesized membrane seen in Fig. 3-3C.

According to the EDS analysis, which are summarized in Table 3-1, the top layer of the support of thickness approximately 5 μm (Fig. 3-3A), contains only ZrO_2 and TiO_2, with the former being the major component. The concentration of Zr gradually decreases from 78.5% at 1 μm from the surface to 71.9% at 5 μm from the surface as can be seen from Table 3-1. On the other hand, the intermediate layer contains mostly ZrO_2 and TiO_2 with TiO_2 being the major component. For example, 15 μm from the surface there is 95.4% of Ti and only 3.4% of Zr, with the balance of 1.2% being Al. The porous layer, which follows the intermediate layer, contains mostly alumina and some TiO_2 as indicated by the EDS analysis 30 μm from the support surface, which shows 84.8% of Al and 14.5% of Ti.

Table 3-1 EDS analysis of the support before and after the zeolite synthesis.

Distance from the top surface		1 μm	5 μm	10 μm	15 μm	30 μm
Support before zeolite synthsis	Element	Atomic%	Atomic%	Atomic%	Atomic%	Atomic%
	Al	0.0	0.0	0.2	1.2	84.8
	Si	0.0	0.0	0.0	0.0	0.0
	Ti	21.5	28.1	86.9	95.4	14.5
	Zr	78.5	71.9	12.9	3.4	0.7
	Totals	100.0	100.0	100.0	100.0	100.0
Support after zeolite synthesis	Element	Atomic%	Atomic%	Atomic%	Atomic%	Atomic%
	Al	0.0	0.0	0.0	3.9	37.9
	Si	99.1	35.3	22.4	10.2	4.4
	Ti	0.2	21.8	46.5	85.0	57.6
	Zr	0.7	42.9	31.1	0.9	0.1
	Totals	100.0	100.0	100.0	100.0	100.0

The EDS analyses of the cross section of the composite membrane quantitatively confirm the qualitative observation based on the SEM micrographs. First of all, the top layer of the composite membrane 1 μm from its surface consists virtually of pure silica (99.1% of Si), which is consistent with Fig. 3-3D. Furthermore, silicalite-1 penetrates and fills the pores of the active layer, which is indicated by 35.3% of Si at 5 μm from the surface of the composite membrane. It is important to emphasize that since the pore size of the active layer is 0.45 μm, silicalite-1 crystals inside the active layer cannot be as large as those seen on the top surface of the composite membrane (Fig. 3-3C) and those at the interface between the active and intermediate layer of the support (Fig. 3-3D). Silicalite-1 also penetrates into the intermediate layer of the support, which is indicated by 22.4% and 10.2% of Si at 10 μm and 15 μm, respectively, from the top surface of the composite membrane. However, due to the

relatively high porosity and large pores of the intermediate layer compared to the active layer of the support, and since the gas would take a path of the least resistance to flow, the intermediate layer in combination with the silicalite-1 crystals formed there is not expected to have any contribution to the selective properties of the synthesized composite membrane.

It is important to emphasize that the formation of pure zeolite layer on top of the active layer of the support was not expected, because of the pore plugging synthesis method. Formation of pure zeolite layer is characteristic for the secondary growth synthesis method. In comparison to the secondary growth method, the thickness of the silicalite-1 layer reported in this study of 1.5 μm (Fig. 3-3D) is at the lower end of the range of thicknesses. The latter varies from a fraction of micrometer as recently reported in references [30-32] to tens of micrometers [17-19, 33]. Unlike the secondary growth method, the pure silicalite-1 layer on top of the active layer of the support observed in this study is not expected to have selective properties on its own, because the size of the crystals in this layer is comparable to its thickness.

3.3.2 Single gas adsorption isotherms:

Equilibrium adsorption isotherms of single CO_2 and N_2 gases at 23^{o}C on the silicalite-1 powder collected from the inner wall of the autoclave Teflon lining were determined for pressures up to 4.8 atm by using the constant volume technique and are presented in Fig. 3-4. The points in this figure correspond to the experimental data, while the curves indicate the Langmuir adsorption isotherm curve fits obtained by a nonlinear regression of the experimental data points. These results are in an excellent agreement with the results from

previous work performed by Li et al. using commercial silicalite-1 samples [34]. However, the observed adsorption capacity in this work was to some extent higher than Li's results due the fact that the temperature was slightly higher in Li's study. The adsorption capacity of silicalite-1 zeolite for CO_2 is greater than that for N_2 within the pressure range studied, which is expected because of a greater polarizability and a greater quadrupole moment of CO_2 compared to N_2 [35].

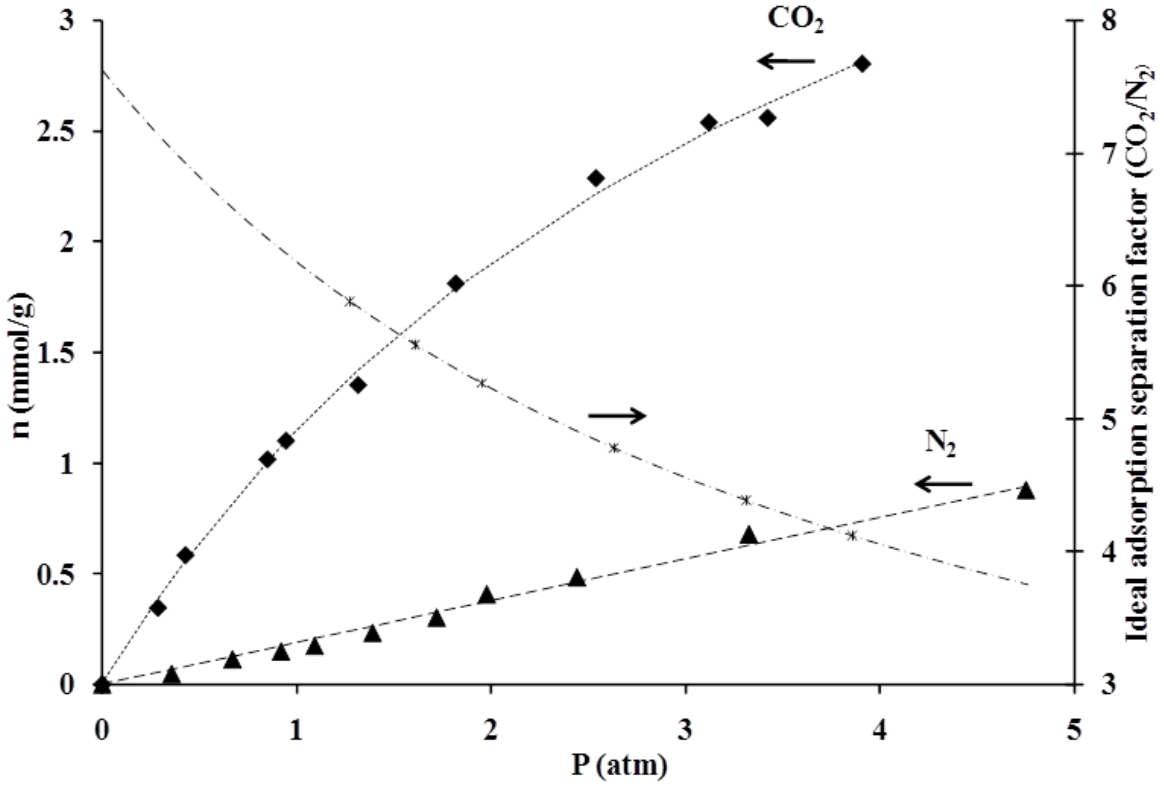

Figure 3-4 CO_2 and N_2 pure component adsorption isotherms and the ideal adsorption separation factor (CO_2/N_2) on silicalite-1 powder at 23°C. For the isotherms, the points represent the experimental data, and the lines are the fitted Langmuir isotherms based on the experimental data.

In addition to the equilibrium adsorption isotherms, Fig. 3-4 presents the corresponding ideal adsorption selectivity for CO_2/N_2, $\alpha^{Ads}_{CO_2/N_2}$, which represents the ratio of the equilibrium adsorption capacities for CO_2 and N_2. The ideal adsorption selectivity decreases with pressure from roughly 7.6, when the pressure approaches to zero, to approximately 3.8 at 4.8 atm. While the adsorption capacity for both CO_2 and N_2 increases with pressure, the slope of the CO_2 isotherm gradually decreases. This curvature of the CO_2 isotherm, combined with nearly linear adsorption for N_2 leads to the decrease in the ideal adsorption selectivity with pressure.

3.3.3 Single gas permeation experiments

Considering that the pore size of silicalite-1 zeolite is 5.5 Å while the kinetic diameters of CO_2 and N_2 are 3.3 Å and 3.6 Å, respectively, the transport of these gases through this zeolite membrane should occur by a surface diffusion mechanism [33,36]. In this mechanism the molecules are first adsorbed at the high pressure side of the membrane and then diffuse along pores from the high pressure to the low pressure side of the membrane. The difference between the equilibrium adsorption capacities at the high and low pressure sides of the membrane represents the driving force for surface diffusion.

Fig. 3-5 shows the permeances of both CO_2 and N_2 from the respective single gas experiments plotted as a function of the pressure gradient across the membrane. The CO_2 permeance of approximately 5 x 10^{-8} mol/m^2 Pa s appears to be practically independent of the pressure gradient, but the N_2 permeance decreases continuously as the pressure gradient increases. As a result, at pressures gradients greater than 2 atm the synthesized membrane

becomes CO_2 selective, but the largest ideal CO_2/N_2 selectivity, i.e., the single gas permeance ratio, is less than 1.5. The ideal CO_2/N_2 selectivities observed in this work are comparable to the values reported in reference [37] for the silicalite-1 membrane synthesized on the alumina support and those reported in reference [33] the for silicalite-1 membrane synthesized on stainless steel support. On the other hand, these ideal selectivities are significantly lower than the value of 13.4 reported by Guo et al. for the stainless-steel-net imbedded zeolite silicalite-1 membrane [38].

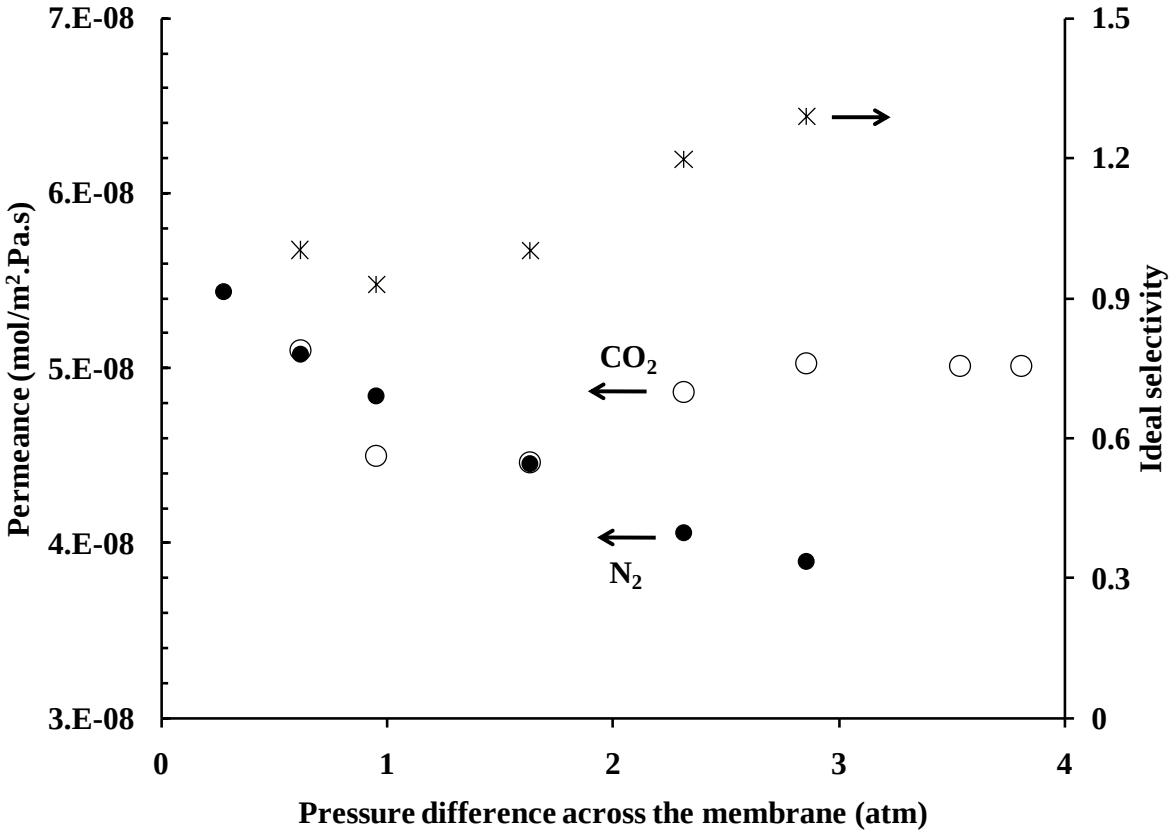

Figure 3-5 Single component CO_2 and N_2 permeances through silicalite-1 membrane as well as ideal selectivity as a function of pressure difference across the membrane. All experiments performed at ambient temperature (~23°C) with permeate side at atmospheric pressure.

The permeate side of the membrane is always around the atmospheric pressure. Therefore, considering the equilibrium adsorption isotherms shown in Fig. 3-4, for a given pressure gradient across the membrane, the driving force for the surface diffusion of CO_2 is 4 to 7 times greater than that for the surface diffusion of N_2. Consequently, if the diffusivities of CO_2 and N_2 in silicalite-1 pores were comparable, the synthesized membrane would be much more CO_2 selective than what appears to be its ideal selectivity based on the results presented in Fig. 3-5. However, the diffusivity of N_2 is greater than that of CO_2 in this zeolite. According to Makrodimitris et al. [39], the diffusivities in silicalite-1 range from 24 – 95 $x10^{-10}$ m^2/s for CO_2 and from 160 – 250 $x10^{-10}$ m^2/s for N_2. Although the above ranges of the diffusivity values are quite wide, the difference between the diffusivities of N_2 and CO_2 in silicalite-1 is sufficiently large to explain virtually no ideal CO_2/N_2 selectivity in the synthesized silicalite-1 membrane, since fast diffusion of N_2 is compensated for its low adsorption capacity for this adsorbent.

In addition, the comparison of the results presented in Figs. 3-4 and 3-5 provides indirectly information about the effect of pressure on the diffusivities of CO_2 and N_2 in silicalite-1. The permeance of CO_2 appears to be independent of the pressure gradient of CO_2 across the membrane. According to Fig 3-4, the driving force for the surface diffusion of CO_2 decreases with pressure as explained earlier, the diffusivity of CO_2 in silicalite-1 must then be increasing with pressure. This is consistent with the results reported by Papadopoulos et al. [40], and Barbaro and Jiang [41], but inconsistent with the results of Krishna et al. [42], Krishna and van Baten [43], and Selassie et al. [44]. On the other hand, the permeance of N_2 decreases with increasing pressure gradient of N_2 across the membrane. According to Fig. 3-

4, the driving force for the surface diffusion of N_2 appears to be independent of pressure due to the linear adsorption isotherm within the studied pressures. The diffusivity of N_2 in silicalite-1 must then be decreasing with pressure, which is consistent with the results reported by Krishna and van Baten [43], and Selassie et al. [44].

3.3.4 Gas mixture separation experiments

The actual separation potential of the synthesized composite membrane was evaluated in the gas separation experiments. These experiments involved equimolar mixture of CO_2 and N_2 at different feed pressures as well as the experiments with different feed compositions at a constant feed pressure. Since, the stage cut in all gas separation experiments was greater than zero, the permeances of the individual gases were determined using the procedure discussed in the experimental section, which relies on the assumptions that the permeances of the individual components from the mixture are independent of the feed composition and the total feed pressure.

Fig. 3-6 demonstrates the effect of the average composition of CO_2 at the high pressure side of the membrane on the CO_2 and N_2 permeances determined from a series of experiments performed at the constant total feed pressure of 5.2 atm and five different feed compositions. The insert in Fig. 3-6 presents the plot of the average mole fraction of CO_2 at the high pressure side of the membrane, determined by integration of the concentration profile at the high pressure side of the membrane, versus the mole fraction of CO_2 in the feed stream. Since the results depicted in Fig. 3-6 were CO_2 selective and all experiments were performed at a non-zero stage cut, the average mole fraction of CO_2 at the high pressure side

of the membrane is lower than the mole fraction of CO_2 in the feed stream, with the difference between the two increasing with the mole fraction of CO_2 in the feed stream.

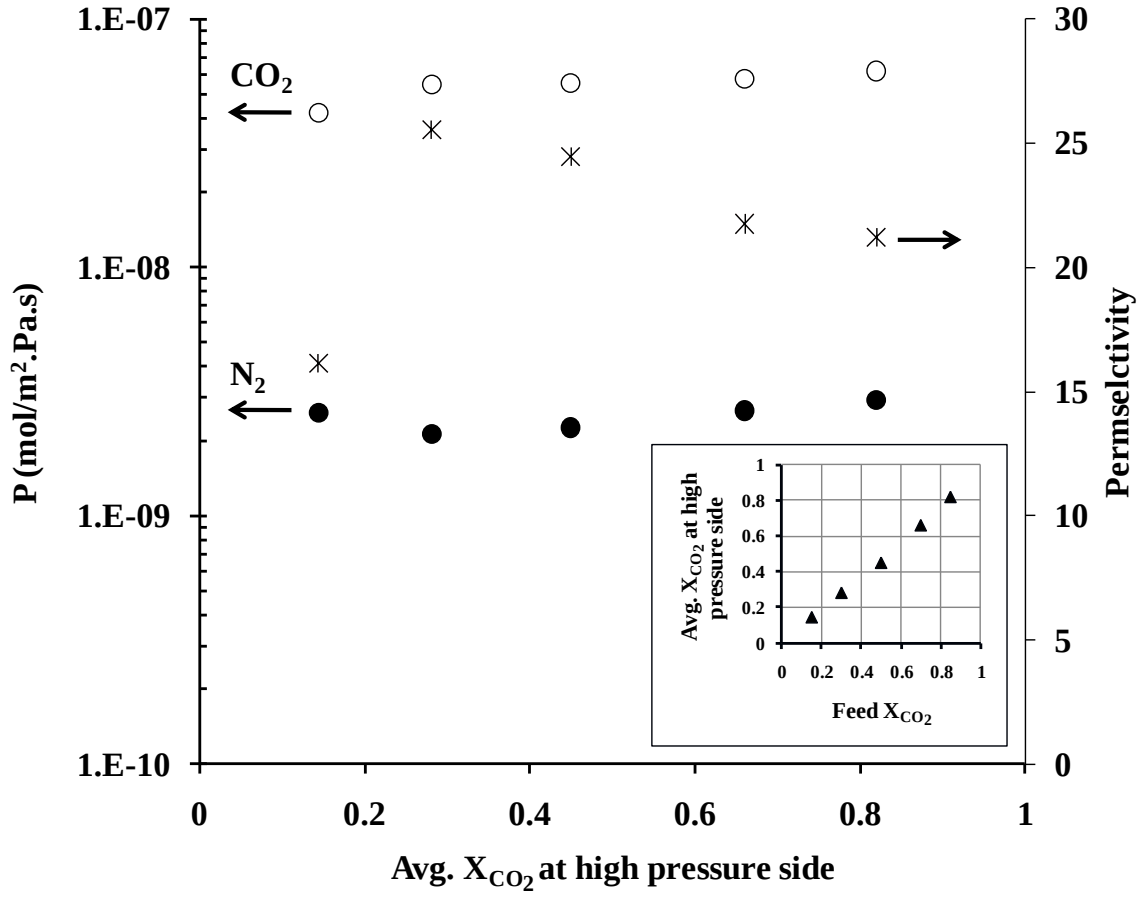

Figure 3-6 CO_2 and N_2 permeances in gas mixture through silicalite-1 membrane as well as permselectivity as a function of average CO_2 mole fraction in the high pressure side of the membrane at 5.2 atm total feed pressure. All experiments performed at ambient temperature.

The CO_2 permeance in Fig. 3-6, which ranges from 4.5 x 10^{-8} to 6.5 x 10^{-8} mol/m^2 Pa s, is comparable to the CO_2 permeance from the single gas permeation tests (5 x 10^{-8} mol/m^2 Pa s); however the permeance of N_2 drops to values ranging between 2 x 10^{-9} mol/m^2 Pa s and 3

x 10^{-9} mol/m^2 Pa s, which is more than one order of magnitude less compared to the permeances from the single gas permeation tests of N_2. As a result, the CO_2/N_2 permselectivity in the actual gas separation experiments reaches the value as high as 26.0.

The reduction of the N_2 permeance in the presence of CO_2 is a result of a preferential adsorption of the latter on silicalite-1, which is evident in Fig. 3-4. Since the pore size of silicalite-1 (5.5 Å) is not even twice the kinetic diameter of CO_2, the preferentially adsorbed CO_2 molecules block the N_2 molecules from entering the pores of the silicalite-1 membrane, which leads to very high CO_2/N_2 permselectivities evident in Fig. 3-6

Considering the effect of the average composition at the high pressure side of the membrane on the CO_2 and N_2 permeances, it can be noticed that while both permeances have a tendency to increase with the average mole fraction of CO_2, this trend is not very strong. It is important to emphasize that one of the assumptions for the determination of the permeances of the individual gases from the mixed gas experimental data was the independence of the gas permeance on the feed composition, which in principle is confirmed by the results shown in Fig. 3-6.

In general, except for the lowest average mole fraction of CO_2, the CO_2/N_2 permselectivity exceeds 20. The lowest permselectivity value of 16 for the feed's CO_2 mole fraction of 0.15 most likely arises from "insufficient" concentration of CO_2 at the high pressure side of the membrane, which results in a less effective blocking of the N_2 molecules from the pores of silicalite-1 crystals. Indeed, the N_2 permeance for the mole fraction of CO_2 of 0.15 is greater

than that for the mole fraction of 0.30, and this is despite the fact in general the N_2 permeance increases slightly with the concentration of CO_2 at the high pressure side of the membrane.

The change in the composition of the feed stream also affects the driving force for the transport of the individual components across the membrane. The permeance data shown in Fig. 3-6 is re-plotted in Fig. 3-7 as function of the log mean partial pressure gradient of the individual gases across the membrane. The insert in Fig. 3-7 shows the variation of the log mean partial pressure gradients of CO_2 and N_2 as a function of the mole fraction of CO_2 in the feed gas. It is evident that varying the partial pressure gradient of the individual gases across the membrane by means of varying the feed composition while maintaining the total feed pressure constant leads to relatively small variations in the permeances of the individual gases, as already indicated in the discussion pertaining to Fig. 3-6.

Alternatively to changing the partial pressure gradients of the individual gases across the membrane by changing the feed composition, the same can also be accomplished by changing the total feed pressure while maintaining the feed composition constant. In this case, the partial pressure gradients of both components increase simultaneously with the increase in the total feed pressure. The results of a series of experiments in which the total feed pressure was varied from 2.5 to 7.7 atm, while using the equimolar feed mixture of CO_2 and N_2, are presented in Fig. 3-8, where the CO_2 and N_2 permeances are plotted versus the respective log mean partial pressure gradients, while the CO_2/N_2 permselectivity is plotted versus the log mean partial pressure gradient of CO_2. The insert in Fig. 3-8 shows the

variation of the partial pressure gradients of CO_2 and N_2 as a function of the total feed pressure of the gas mixture.

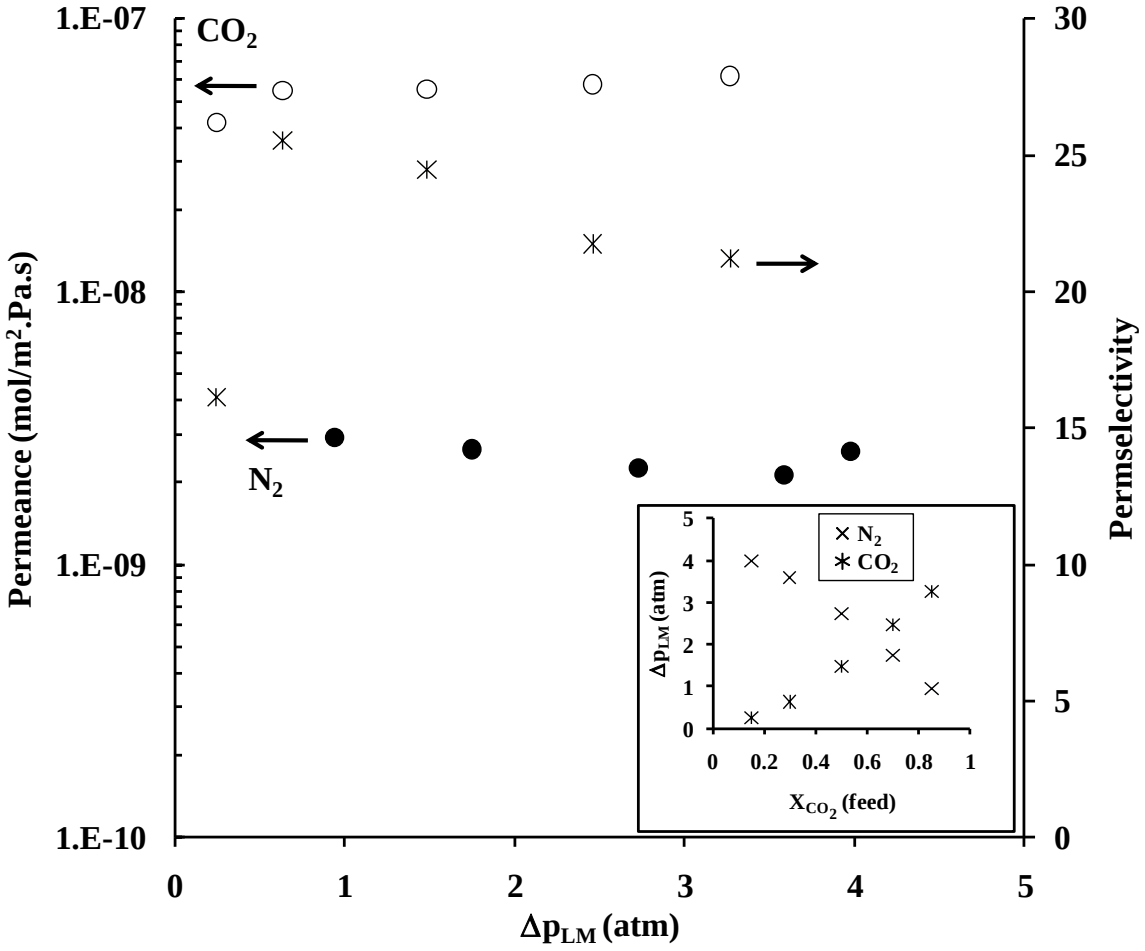

Figure 3-7 CO_2 and N_2 permeances through silicalite-1 membrane as well as their permselectivity as a function of log mean partial pressure difference across the membrane at the total feed pressure of 5.2 atm and different feed compositions. All experiments performed at ambient temperature (~23°C) with permeate side at atmospheric pressure.

Since the silicalite-1 membrane depicted in Fig. 3-8 was CO_2 selective, despite using the equimolar gas mixture as a feed, the log mean partial pressure gradient of N_2 across the membrane is greater than that of CO_2. For example, for the maximum total feed pressure of 7.7 atm, which corresponds to the total pressure gradient of 6.7 atm with 1 atm pressure in the permeate side of the membrane, the log mean partial pressure gradient of N_2 is approximately 4.2 atm while that of CO_2 is only 2.5 atm as shown in Fig. 3-8 insert. Except for the lowest total feed pressure, the CO_2 permeance is approximately constant at the value of 5×10^{-8} mol/m^2 Pa s, which is in the excellent agreement with results from the single gas permeation tests with CO_2 and gas separation experiments at the constant total feed pressure with different feed compositions. On the other hand, the N_2 permeance generally increases with pressure from 1.5×10^{-9} mol/m^2 Pa s to 4×10^{-9} mol/m^2 Pa s. The resulting CO_2/N_2 permselectivity shows an interesting trend with the maximum value of 25 at the partial pressure gradient of CO_2 of 1.5 atm corresponding to the feed pressure of 5.2 atm. As the total feed pressure increases, the average mole fraction of CO_2 at the high pressure side of the membrane (not shown in Fig. 3-8) decreases from 0.496 to 0.438. This decrease in mol fraction is due to increase of the stage cut with total feed pressure. On the other hand, this decrease is rather small, and the observed trend between the CO_2/N_2 permselectivity and the log mean partial pressure difference of CO_2 across the membrane should be attributed to the effect of the total feed pressure.

In general, as the total feed pressure increases it is expected that the CO_2/N_2 permselectivity of zeolite membranes should decrease as for example in reference [38]. There are two reasons for this expected decrease in permselectivity. First of all, as the pressure increases

the contribution of non-selective transport through defects (Knudsen diffusion and/or Poiseuille flow) increases. Also, as the pressure increases, the relative difference between the adsorption capacities for CO_2 and N_2 in MFI zeolites decreases [45]. The latter effect is illustrated in Fig. 3-4 by a decrease in the ideal adsorption separation factor for CO_2/N_2 with pressure. The fact that the CO_2/N_2 permselectivity in Fig. 3-8 increases with the total feed pressure at low pressures must be a result of an interplay of the effect of the pressure on the equilibrium concentrations of CO_2 and N_2 at the high pressure side of the membrane, and the effect of these concentrations on the diffusivity of the adsorbed gases in the pores of the membrane. In addition, there may be a coupling effect between the equilibrium concentrations of the individual gases at the high pressure side of the membrane species and their diffusivities in the pores of the silicalite-1 crystals. The actual physical interpretation of the observed optimum total feed pressure is beyond the scope of the current paper, but similar effect of the total feed pressure on CO_2/N_2 permselectivity was also observed by Sebastian et al. for Na-ZMS-5 and B-ZMS-5 membranes [45].

In comparison to the literature values for zeolite silicalite-1 membranes, the highest CO_2/N_2 permselectivity of 26.0 observed in this work is comparable to value of 25.5 reported by Ando et al. [46]. Typical CO_2/N_2 permselectivities of silicalite-1 membranes reported in literature range from 5.5 [47] to 10 [48]. On the other hand, our permselectivity is considerably less than 68.7 reported by Guo et al. for the stainless-steel-net imbedded zeolite silicalite-1 membrane [38]. It should be emphasized that the value of 68.7 was obtained in a test carried out at the feed pressure of 1 atm, while the permeate side was swept with argon. However, at the feed pressures of 2 and 3 atm. the CO_2/N_2 permselectivity dropped to 30

and 18, respectively [38]. Moreover, according to Lindmark and Hedlund (2010), silicalite-1 grown on stainless-steel net supports is likely to incorporate Fe^{3+} ions into its lattice. This would result in a more polar zeolite, and enhanced CO_2 adsorption and transport [23].

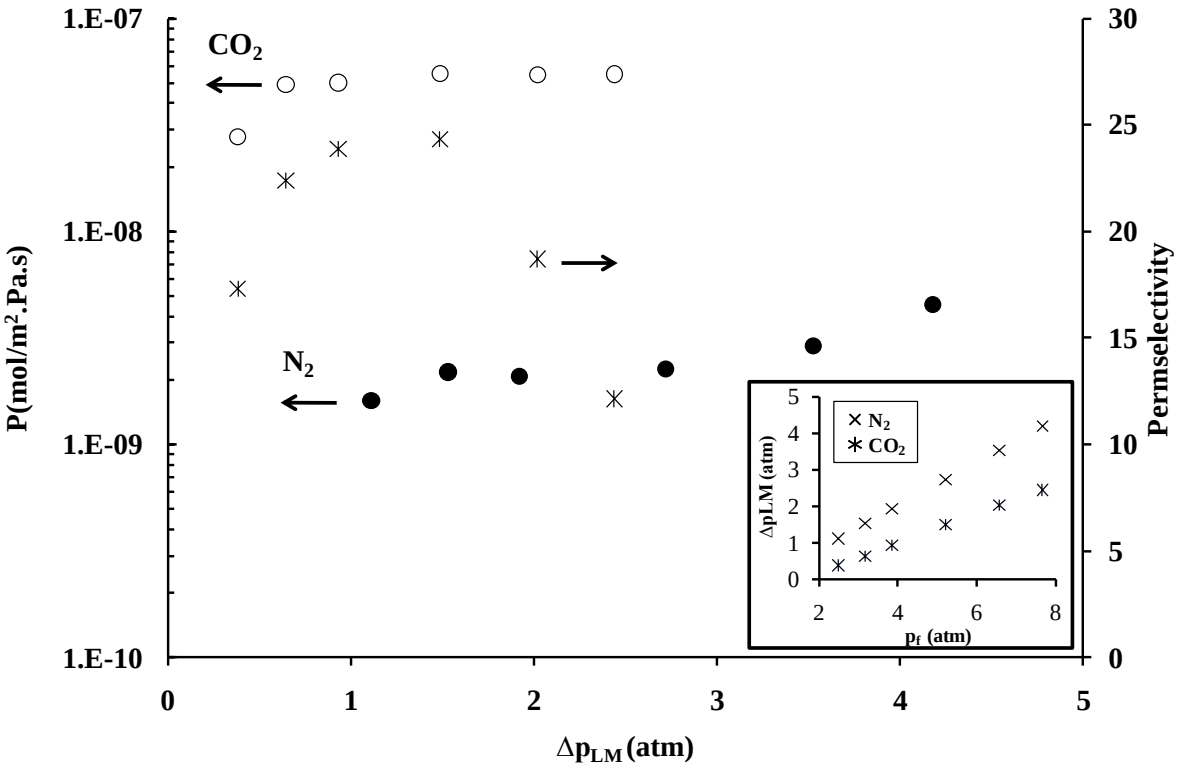

Figure 3-8 CO_2 and N_2 permeances through silicalite-1 membrane as well as permselectivity as a function of log mean partial pressure difference across the membrane for equimolar feed composition of CO_2 and N_2 at different total feed pressure. All experiments performed at ambient temperature (~23°C) with permeate side at atmospheric pressure.

Considering the CO_2 permeance of silicalite-1 zeolite membranes, the literature values are in the order of 10^{-8} to 10^{-7} mol/m^2 Pa s. Therefore, the CO_2 permeance of 6 x 10^{-8} mol/m^2 Pa s reported in this work is not very competitive. On the other hand, the fact that CO_2

permeance observed in this work is practically independent of the total feed pressure indicates minimization of the defects in the membrane structure, which is very desirable. One of the reasons for a relatively low CO_2 permeance might be attributed to formation of a pure silicalite-1 layer on top of the active layer of the support. This layer, because it consists of crystals of size comparable to its thickness, is not expected to contribute to the selective properties of the membrane. On the other hand, this layer most likely provides additional resistance to the transport of gases across the membrane.

Another reason for a relatively low CO_2 permeance of the membrane synthesized in this work might be inherently related to the pore plugging synthesis method. Since the gas transport in this type of membranes takes place only through the porous part of the active layer of the support, the effective surface area for the gas transport is less than the macroscopic surface area of the membrane. In turn, increasing the porosity of the active layer of the support would increase the effective surface area of the membrane. In addition, since the thickness of the selective layer is generally determined by the thickness of the active layer of the support, decreasing the thickness of the latter should also increase permeance of the membrane. Finally, the synthesis protocol should be optimized to eliminate or to minimize the thickness of the pure zeolite layer on top of the active layer of the support.

Taking the thickness of the selective layer as 6.5 μm (1.5 μm pure silicalite-1 layer + 5 μm active layer of the support), the corresponding CO_2 permeability of the silicalite-1 zeolite membrane is approximately 1.160×10^3 Barrer. The combination of this CO_2 permeability

with the CO_2/N_2 permselectivity of 26.0 places this membrane right at the upper bound for CO_2/N_2 separation [49], which makes it attractive for, for example, capture of CO_2 from flue gases.

3.4 Conclusions

The composite silicalite-1 zeolite membrane has been successfully synthesized on a novel zirconium oxide /titanium oxide support by the pore plugging method. The synthesized silicalite-1 formed a thin 1.5 μm layer on the top of the support and penetrated into its active layer. The size of crystals in the silicalite-1 layer was comparable to its thickness, which suggests that any selective properties of the composite membrane should arise from the crystals formed inside the 5 μm-thick active layer of the support. Since the pore size of the active layer was 0.45 μm, the silicalite-1 crystals inside this layer must be much smaller than those on top of it. Moreover, the crystals inside the active layer were tightly packed, as indicated by more than 35% of Si (the balance being Zr and Ti) 5 μm from the top surface of the composite membrane, or approximately 3.5 μm from the interface of the silicalite-1 layer and the active layer of the support.

Single and mixed gas permeation experiments with CO_2 and N_2 confirmed the adsorption characteristics of the synthesized composite membranes. The single gas CO_2 and N_2 permeances were comparable, but the N_2 permeance in mixed gas permeation tests decreased by more than one order of magnitude leading to the CO_2/N_2 permselectivities as high as 26.0. While this value is not the highest one reported in the literature for the CO_2/N_2 permselectivity of silicalite-1 membrane, it might be representative for this zeolite. This is

because the CO_2 permeance of the membrane was practically independent of the total feed pressure, which indicates minimization or even elimination of the defects in the membrane structure. In addition, since the synthesis of the zeolite was carried out on the support consisting of only from zirconium and titanium oxides, the synthesized zeolite did not incorporate any trivalent ions, which induce its polarity and thus enhance the transport of polar CO_2.

Acknowledgments

The authors acknowledge the financial support received from Natural Science and Engineering Research Council of Canada (NSERC) and from the University of Ottawa. The Canada Foundation for Innovation and the Ontario Research Fund are gratefully acknowledged for infrastructure grants to the Center for Catalysis Research and Innovation.

Nomenclature:

A_m: membrane permeation area (m^2).

Å: Angstrom.

p_F: measured pressure in the feed side of the membrane (atm).

$p_{i,F}$: partial pressure of component i at the membrane feed side (atm).

$p_{i,R}$: partial pressure of component i at the membrane retentate side (atm).

$p_{i,P}$: partial pressure of component i at the membrane permeate side (atm).

p_P: measured pressure in the permeate side of the membrane (atm).

P_i: membrane permeance of component *i* (mol//m^2.Pa.s).

q_F: feed flow rate (mol/s).

q_i: permeation rate of component *i* across the membrane (mol/s).

$q_{i,R}$: permeation rate from high pressure side in shell *i* (mol/s).

$q_{i,P}$: permeation rate to low pressure side in shell *i* (mol/s).

q_P: permeate flow rate (mol/s).

x_i : measured composition of component i in the retentate stream.

y_i : measured composition of component i in the permeate stream.

Greek Letters

α : membrane apparent selectivity

α^* : membrane permselectivity

α_{CO_2/N_2}^{Ads} : pure gas adsorption selectivity of CO_2 and N_2 at any given pressure

3.5 References

1- Y.S Lin, I. Kumakiri, N.B. Nair, H. Alsyouri, Microporous inorganic membranes, Sep. Purif. Methods 31 (2002): 229 – 379.

2- A. Navajas, R. Mallada, C. Tellez, J. Coronas, M. Menendez, J. Santamaria, Study on the reproducibility of mordenite tubular membranes used in the dehydration of ethanol, J. Membrane Science 299 (2007) 166 – 173.

3- K. Sato, K. Sugimoto, T. Nakane, Mass-production of tubular NaY zeolite membranes for industrial purpose and their application to ethanol dehydration by vapor permeation, J. Membrane Science 319 (2008) 244 – 255.

4- Y. Hasegawa, T. Ikeda, T. Nagase, Y. Kiyozumi, T. Hanaoka, F. Mizukami, Preparation and characterization of silicalite-1 membranes prepared by secondary

growth of seeds with different crystal sizes, J. Membrane Science 280 (2006) 397 – 405.

5- E.E. McLeary, J.C. Jansen, F. Kapteijn, Zeolite based films, membranes and membrane reactors: Progress and prospects, Microporous Mesoporous Materials 90 (2006) 198 – 220.

6- K. Okamoto, H. Kita, K. Horii, K. Tanaka, Zeolite NaA membrane: preparation , single gas permeation, and pervaporation and vapor permeation of water/organic liquid mixtures, Ind. Eng. Chem. Res. 40 (2001) 163 – 175.

7- Y. Yan, T. Bein, Zeolite thin films with tunable molecular-sieve function, J. Am. Chem. Soc. 117 (1995) 9990 – 9994.

8- S. Kornic, M. Baker, Nanoporous zeolite film electrodes, Chem. Commun. 16 (2002) 1700 – 1701.

9- X.L. Cheng, Z.B. Wang, Y.S. Yan, Corrosion-resistant zeolite coating by in situ crystallization, Electrochem, Solid State Lett. 4 (2001) B23 – B26.

10- J. Dong, Y.S. Lin, M.Z.-C. Hu, R.A. Peascoe, E.A. Payzant, Template removal associated microstructural development of ceramic supported MFI zeolite membranes, Microporous Mesoporous Mater. 34 (2000) 241 – 253.

11- C. Covarrubias, R. Garcia, R. Arriagada, J. Yanez, H. Ramanan, Z. Lai, M. Tsapatsis, Removal of trivalent chromium contaminant from aqueous media using FAU-type zeolite membranes, J. Membrane Science 312 (2008) 163 – 173.

12- M. Hong, S. Li, J.L. Falconer, R.D. Noble, Hydrogen purification using a SAPO-34 membrane, J. Membrane Science 307 (2008) 277 – 283.

13- J. Hedlund, M. Noack, P. Kölsch, D. Creaser, J. Caro, J. Sterte, ZSM-5 membranes synthesized without organic templates using a seeding technique, J. Membrane Science 159 (1999) 263 – 273.

14- R.J.R. Uhlhorn, K. Keizer, J. Burggraaf, Gas transport and separation with ceramic membranes. Part I. Multilayer diffusion and capillary condensation, J. Membrane Science 66 (1992) 259 – 269.

15- M.P. Bernal, G. Xomeritakis, M. Tsapatsis, Tubular MFI zeolite membranes made by secondary (seeded) growth, Catalysis Today 67 [2001] 101 – 107.

16- T. Matsufuji, N. Nishiyama, M. Matsukata, K. Ueyama, Separation of butane and xylene isomers with MFI-type zeolite membranes synthesized by a vapour-phase transport method, J. Membrane Science 178 (2000) 25 – 34.

17- M. Pan, Y.S. Lin, Template-free secondary growth synthesis of MFI type zeolite membranes, Microporous and Mesoporous Materials 43 (2001) 319 – 327.

18- D. Shen, W. Xiao, J. Yang, N. Chu, J. Lu, D. Yin, J. Wang, Synthesis of silicalite-1 membrane with two silicon source by secondary growth method and its pervaporation performance, Sep. Purifi. Tech. 76 (2011) 308 – 315.

19- E. Dincer, A. Culfaz, H. Kalipcilar, Effect of seeding on the properties of MFI type zeolite membranes, Desalination 200 (2006) 66 – 67.

20- S. Miachon, E. Landrivon, M. Aouine, Y. Sun, I. Kumakiri, Y. Li, O. Pachtova Prokopova, N. Guilhaume, A. Giroir-Fendler, H. Mozzanega, J.A. Dalmon, Nanocomposite MFI-alumina membranes via pore-plugging synthesis: preparation and morphological characterization, J. Membrane Science 281 (2006) 228 – 238.

21- S. Miachon, P. Ciavarella, L. van Dyka, I. Kumakiri, K. Fiaty, Y. Schuurman, J. A. Dalmona, Nanocomposite MFI-alumina membranes via pore-plugging synthesis: specific transport and separation properties, J. Membrane Science 298 (2007) 71 – 79.

22- W.C. Wong, L.T.Y. Au, P.P. Lau, C.T. Ariso, K.L. Yeung, Effects of synthesis parameters on the zeolite membrane morphology, J. Membrane Science 193 (2001) 141 – 161.

23- J. Lindmark, J. Hedlund, Carbon dioxide removal from synthesis gas using MFI membranes, J. Membrane Science 360 (2010) 284 – 291.

24- A. M. McAleer, L. V. C. Rees, A. K. Nowak, Ion exchange and aluminum distributions in ZSM-5 zeolites, Zeolites 11 (1991) 329 – 336.

25- C.-H. Chang, R. Gopalan, Y.S. Lin, A comparative study on thermal and hydrothermal stability of alumina, titania and zirconia membranes, J. Membrane Science 91 (1994) 27 – 45.

26- P. Ferreira, A. Ferreira, M. R. Soares, Synthesis and Structural Characterization of Zirconium Silicates, Chem. Mater. 13 (2001) 355 – 363.

27- Q. Xu, M.A. Anderson, Sol-Gel route to synthesis of microporouse ceramic membranes: thermal stability of TiO_2-ZrO_2 mixed oxides, J. Am. Ceram. Soc. 76 (1993) 2093 – 2097.

28- M. Tawalbeh, F.H. Tezel, B. Kruczek, S. Letaief, C. Detellier, Synthesis and characterization of silicalite-1 membrane prepared on a novel support by the pore plugging method, J. Porous Materials 20 (2013) 1047 – 1421.

29- N. Navascues, C. Tellez, J. Coronas, Synthesis and adsorption properties of hollow silicalite-1 spheres, Microporous Mesoporous Mater. 112 (2008) 561 – 572.

30- J. Motuzas, R. Mikutaviciute, E. Gerardin, A. Julbe, Controlled growth of thin and uniform TS-1 membranes by MW-assisted heating, Microporous Mesoporous Mater. 128 (2010) 136 – 143.

31- P.-S. Lee, X. Zhang, J.A. Stoeger, A Malek, W. Fan, S. Kumar, W.C. Yoo, S. Al Hashimi, R.L. Penn, A. Stein, M. Tsapatsis, Sub-40 nm zeolite suspensions via disassembly of three-dimensionally ordered mesoporous-imprinted Silicalite-1, J. Am. Chem. Soc. 133 (2011) 493 – 502.

32- V. Kumar, X. Zhang, B. Elyassi, D.D. Brewer, M. Gettel, S. Kumar, J.A. Lee, S. Maheshwari, A. Mittal, C.-Y. Sung, M. Cococcioni, L.F. Francis, A.V. McCormick, K.A. Mkhoyan, M. Tsapatsis, Dispersible exfoliated zeolite nanosheets and their application as a selective membrane, Science 334 (2011) 72 – 75.

33- W.J.W. Bakker, L.J.P. van den Broeke, F. Kapteijn, J.A. Moulijn, Temperature dependence of one-component permeation through a silicalite-1 membrane, AIChE J. 43 (1997) 2203 – 2214.

34- P. Li, F.H. Tezel, Pure and binary adsorption equilibria of carbon dioxide and nitrogen on silicalite, J. Chem. Eng. Data 53 (2008) 2479 – 2487.

35- M.A. Morrison, P.J. Hay, Molecular properties of N_2 and CO_2 as functions of nuclear geometry - polarizabilities, quadrupole moments, and dipole moments, J. Chem. Phy. 70 (1979) 4034 – 4043.

36- W. Zhu, P. Hrabanek, L. Gora, F. Kapteijn, J.A. Moulijn, Role of adsorption in the permeation of CH_4 and CO_2 through a silicalite-1 membrane, Ind. Eng. Chem. Res. 45 (2006) 767 – 776.

37- C. Algieri, P. Bernardo, G. Golemme, G. Barbieri, E. Drioli, Permeation properties of a thin silicalite-1 (MFI) membrane, J. Membrane Science 222 (2003) 181 – 190.

38- H. Guo, G. Zhu, H. Li, X. Zou, X. Yin, W. Yang, S. Qiu, R. Xu, Hierarchical growth of large-scale ordered zeolite silicalate-1 membranes with high permeability and selectivity for recycling CO_2, Angew. Chem Int. Ed. 45 (2006) 7053 – 7056.

39- K. Makrodimitris, G.K. Papadopoulos, D.N. Theodorou, Prediction of permeation properties of CO_2 and N_2 through silicalite via molecular simulations, J. Phys. Chem. B 105 (2001) 777 – 788.

40- G.K. Papadopoulos, H. Jobic, D.N. Theodorou, Transport diffusivity of N_2 and CO_2 in silicalite: coherent quasielastic neutron scattering measurements and molecular dynamics simulations, J. Phys. Chem. B 108 (2004) 12748 – 12756.

41- R. Babarao, J. Jiang, Diffusion and separation of CO_2 and CH_4 in silicalite, C168 Schwarzite, and IRMOF-1: A comparative study from molecular dynamics simulation, Langmuir 24 (2008) 5474 – 5484.

42- R. Krishna, J.M. van Baten, E. Garcia-Perez, S. Calero, Incorporating the loading dependence of the Maxwell-Stefan diffusivity in the modeling of CH_4 and CO_2 permeation across zeolite membranes, Ind. Eng. Chem. Res. 46 (2007) 2974 – 2986.

43- R. Krishna, J.M. van Baten, Kinetic monte carolo simulation of the loading dependence of diffusion in zeolities, Chem. Eng. Technol. 28 (2005) 160 – 167.

44- D. Selassie, D. Davis, J. Dahlin, E. Feise, G. Haman, D.S. Sholl, D. Kohen, Atomistic Simulations of CO_2 and N_2 Diffusion in Silica Zeolites: The Impact of Pore Size and Shape, J. Phys. Chem. C. 42 (2008) 16521 – 16531.

45- V. Sebastian, I. Kumakiri, R. Bredesen, M. Menendez, Zeolite membrane for CO_2 removal: Operating at high pressure, J. Membrane Science 292 (2007) 92 – 97.

46- Y. Ando, Y. Hirano, S. Mase, H. Taguchi, Preparation and characterization of monolithic and planar element of zeolite membranes, Proc. ICIM (1998) Nagoya, Japan, 124 – 127.

47- L.J.P. van den Broeke, W.J.W. Bakker, F. Kapteijn, J.A. Moulijn, Transport and separation properties of a silicalite-1 membrane – I. Operating conditions, Chem. Eng. Sci. 54 (1999) 245 – 258.

48- S. Mase, Y. Ando, Y. Hirano, H. Taguchi, Planer type module with zeolite (MFI) membranes, Proc. ICIM (1998) Nagoya, Japan, 652 – 655.

49- L.M. Robeson, The upper bound revisited, J. Membrane Science 320 (2008) 390 – 400.

CHAPTER FOUR

This Chapter is based on

Synthesis and Characterization of Silicalite-1 Membrane Prepared on a Novel Support by the Pore Plugging Method

M. Tawalbeh[1], F. H. Tezel[1], B. Kruczek[1], S. Letaief[2], C. Detellier[2]

[1] Department of Chemical and Biological Engineering, University of Ottawa, 161 Louis Pasteur Street, Ottawa, ON, Canada K1N 6N5

[2] Centre for Catalysis Research and Innovation and Department of Chemistry, University of Ottawa, 10 Marie Curie, Ottawa, Ontario, Canada K1N 6N5

In: Journal of Porous Materials 20 (2013) 1407 – 1421.

This paper presents the effect of the support pore size on the silicalite-1 membrane morphology. Five supports with different pore sizes in the range of 0.14 - 1.4 μm were investigated. Flat supports were used at this stage due to the simplicity of preparing the membranes and conducting the morphology analysis. However, the effect of the support pore size on the silicalite-1 membrane morphology for the tubular supports were performed and presented in Chapter 5. Single gas permeation experiments for He and N_2 were

performed using the tubular supports and membranes. In this paper, there are additional two authors other than the supervisors, C. Detellier and S. Letaief. Both Dr. C. Detellier and Dr. S. Letaief helped with the understanding and the interpretation of the morphology results. Dr. S. Letaief also helped in conducting the morphology analysis.

Chapter 4 - Synthesis and Characterization of Silicalite-1 Membrane Prepared on a Novel Support by the Pore Plugging Method

Abstract

The effect of the support pore size on the membrane morphology was investigated for zeolite silicalite-1 membranes synthesized by pore plugging method on supports with zirconium oxide and/or titanium oxide active layer. Parameters including surface coverage, zeolite layer thickness, crystal size and shape, zeolite penetration depth were used to quantify the membrane morphology. Five supports with different pore sizes for their active layer in the range of 0.14 - 1.4 μm were investigated. The X-Ray diffraction (XRD) analysis showed a typical silicalite-1 zeolite structure with a high internal crystalline order grown inside the pores as well as on top of all supports. The XRD results also showed that the silicalite-1 crystals in the synthesized membranes are not randomly oriented. The crystallographic preferred orientation (CPO) analysis revealed that the degree of orientation toward either the a-axis or b-axis perpendicular to the support surface, increased by decreasing the pore size of the support. The 0.45 μm support had the most preferably oriented zeolite layer for access of molecules entering into the membrane structure with the highest number of crystals oriented with the b-axis (the one with straight channels) perpendicular to the support surface.

The scanning electron micrographs (SEM) analysis of the membranes revealed a dense and continuous surface morphology with the highest crystal size of silicalite-1 around 1.5 μm on

the surface of the support with the 0.45 μm pore size. SEM micrographs also showed a continuous layer grown over four supports out of five supports with different pore sizes that were investigated, with no layer observed on the 1.4 μm pore size support. The average thickness of the zeolite layer was in the range of 0.7 to 1.4 μm, depending on the pore size of the support. The supports with 0.2 and 0.45 μm pore sizes had the most uniform zeolite layer thickness while the support with 0.8 μm pore size active layer had the least uniform zeolite layer thickness. The electron diffraction spectrometer (EDS) analysis confirmed the formation of pure silicalite-1 layer at the surface as well as inside the pores of all supports. The highest silicalite-1 crystal penetration was for the supports with 0.45 and 1.4 μm pore sizes.

Single gas permeation experiments with He and N_2 gases at 296 K illustrated that regardless of the pore size of the support, the He and N_2 permeances were constant despite the change of the pressure across the membranes. The highest permeances were observed for the membrane prepared using the 0.45 μm pore size support, while the lowest permeances were for the membrane prepared using the 1.4 μm pore size support. These results confirmed the selective properties of the prepared membranes. No matter what is the pore size of the support or the feed pressure, N_2 permeances were around three times higher than those for He.

Keywords: Inorganic Membranes, Silicalite-1, Pore Size Effect, Pore Plugging, Adsorbent Membranes

4.1 Introduction

The use of zeolite membranes as an alternative to polymeric gas separation membranes is a research area that has received enormous attention in recent years [1–3]. Zeolite membranes have many advantages over polymeric membranes. They provide better thermal stability; better solvent resistance, perfect shape selectivity and can withstand high pressures and temperatures [4]. Most of the work reported on zeolite membranes for gas separation has been concerned with MFI type zeolites, i.e. silicalite-1 or its Al-containing analogue ZSM-5. MFI zeolites are of particular interest because of their pore size (~ 5.5Å) which is suitable for several industrially important separations [5] and the relatively easy synthesis from a variety of silica sources and structure directing agents [6].

Zeolites do not typically have the inherent mechanical strength to form self-supported membranes; therefore, the zeolite membranes are formed on macroporous supports [7]. Zeolite membranes are synthesized by the in-situ crystallization method [8], vapor phase transport [9], secondary growth [4,10] and pore plugging methods [11,12]. Of these the secondary growth method is the most commonly used synthesis method, while the pore plugging is a relatively new method. In comparison to the secondary growth, the pore plugging method is easier in terms of preparing large membrane areas that will not generate defects larger than the pore size of the support material. In addition, the zeolite crystals in the membranes prepared by the pore plugging method are protected against shocks and abrasion since they are inside the pores of the support [11]. One more advantage for the pore plugging method is to have a better control of the membrane thickness by limiting the zeolite layer growth on top of the active layer of the support to few microns. Any crystallization below the active layer of the support will not have a significant effect on the

membrane performance due to the difficulty of plugging the considerably large pores of the layers below the active layer.

The permeation characteristics of zeolites and membrane morphology are usually affected by chemical and physical properties of the support used and by the hydrothermal synthesis method. The most important properties of the support materials are: chemical composition, pore size, and roughness. Many materials are used as supports for zeolite membranes such as: glass, alumina, stainless steel, mullite, carbon, and silicon carbide (SiC) [1], but the most used materials are alumina and stainless steel. The stainless steel support is advantageous because of the good ductility, the easy sealing and the corrosion resistance. However, using stainless steel as a support leads to mechanical stresses due to the difference in thermal expansion between the zeolite layer and the support [13]. To overcome this problem a matching material is needed between the membrane and the support layers, and the implantation of this matching material requires more heating which adds up more cost to the membrane preparation process. Using alumina as a support imposes a disadvantage due to the dissolution of aluminum ions from the support and their integration into the zeolite network under the harsh hydrothermal environment. The dissolved aluminum from the support will replace the silicon in the network which will increase the number of cations needed in the network to balance the resultant negative charge [14]. As a result, incorporation of aluminum inside the zeolite structure leads to a heterogeneous and polar surface, and enhances the hydrophilicity of the membrane [15]. While an increase in membrane hydrophilicity might be desirable in some applications, it is also shown that presence of aluminum in zeolite network decreases the molecular sieving ability of the

zeolite membrane [16]. To eliminate these effects, chemically stable supports made from titanium oxide and zirconium oxides were used in this study.

It is believed that the support pore size plays a central role in determining the optimal crystal size and the thickness of the zeolite membrane. Yet, the studies of the effect of the support pore size on the morphology of zeolite membranes did not receive much attention. The limited information on the effect of pore size of the support available in the literature and can be summarized as follows: 1) using supports with large pore size favours the deep penetration of zeolite crystals inside the pores of the support, and formation of irregular zeolite layers [17] with a possibility of incomplete coverage of the support [17,18], and 2) supports with small pore size would form a more homogenous zeolite layer, but with a lower degree of penetration [17].

The objective of this study was to investigate the effect of support pore size on the morphology of the zeolite silicalite-1 membranes synthesized by the pore plugging method using supports with zirconium oxide and/or titanium oxide as the active layer. Focusing on the support pore sizes in the range of 0.14 to 1.4 μm, the synthesized membranes were characterized by the X-ray diffraction (XRD), silicon-29 solid state cross polarization/magic angle spinning nuclear magnetic resonance (^{29}Si CP/MAS NMR), thermal gravimetric analysis (TGA), differential thermal gravimetric analysis (DTGA), scanning electron microscope (SEM), and electron diffraction spectrometer (EDS).

4.2 Experimental Procedures

4.2.1 Porous Supports

Commercial (INSIDE DisRAM) ceramic asymmetric porous discs and (INSIDE Ceram) ceramic asymmetric porous tubes with zirconium oxide and/or titanium oxide active layer were purchased from TAMI Industries (Nyons, France) and used as membrane supports.

The discs had a diameter of 4.7 cm and a thickness of 2 mm while the tubes had an outside diameter of 10 mm and a wall thickness of 2 mm. The active layer for the tubular supports is located inside the tube.

Five discs and five tubes with the following pore sizes in their active layers were used: 0.14, 0.2, 0.45, 0.8 and 1.4 μm. The supports with larger pore sizes, i.e. 0.8 and 1.4 μm, consisted of two layers, the active layer made from pure titanium oxide and the porous mechanical support layer made from pure aluminum oxide. The supports with smaller pore sizes, i.e. 0.14, 0.2 and 0.45 μm, consisted of three layers, the active layer made from the mixture of titanium oxide and zirconium oxide, the intermediate layer made from pure titanium oxide, and the porous mechanical support layer made from pure aluminum oxide. The active layers for all supports have approximately the same porosity of 0.23. The discs were used for the morphology characterization of the prepared zeolite membranes while the tubes were used for the gas permeation characterization.

4.2.2 Membrane preparation

Silicalite-1 layer was synthesized on top of the support's active layer as well as inside the pores of the active layer by pore plugging synthesis method [11,12]. The procedure followed for the syntheses is adapted from the work of Miachon et al. [11] and is explained in the following sections.

4.2.2.1 Zeolite precursor solution preparation

5.5 g of fumed silica (Sigma-Aldrich, Oakville, ON, Canada) was used as a silicone source and it was dissolved in approximately 46 mL of 1 M tetrapropylammonium hydroxide (TPAOH) (Fluka's Purum, Sigma-Aldrich, Oakville, ON, Canada) solution. The most commonly used TPAOH/Si mole ratio in the literature is between 0.35 and 0.5 to provide a pH close to 14 [11]. The TPAOH/Si mole ratio used in this study was chosen to be 0.5. The final concentration of the solution was adjusted by adding deionized water to obtain a 55 mL solution with the following overall molar composition: 1 SiO_2 – 0.5 TPAOH – 27.8 H_2O. The solution was then left under stirring for 3 days at room temperature for maturation. The maturation was followed by subjecting the solution to a centrifugal device for 30 min at 5000 rpm to separate large particles from the solution, to avoid any seeding for the crystallization. Also, these large particles, if not removed, would limit the precursor penetration inside the pores of the support. The leftover solution at the top of the container was used as the zeolite precursor solution for the hydrothermal synthesis.

4.2.2.2 Hydrothermal synthesis and drying

Hydrothermal synthesis process was carried out inside a Teflon lined stainless steel autoclave. The bottom and side surfaces of the flat supports and the external surface of the tubular supports were covered by a Teflon tape to ensure the growth of the zeolite layer only at the top of the supports' active layers and not at the bottom or side surfaces. The supports with different pore sizes were placed inside the autoclave together. The zeolite precursor solution was poured into the autoclave containing the supports until all the supports were completely immersed in the solution. After 30 min, the level of the solution inside the autoclave was checked and when necessary, more solution was added to compensate for the fraction that had penetrated inside the pores of the support. The autoclave was then closed, placed in an oven that was preheated to 160^{o}C for 4 days. After the synthesis, the membranes and the powder collected from the autoclave Teflon lining wall were washed with deionized water. The washed membranes and powder were then dried at 100^{o}C for 24 h.

4.2.2.3 Calcination

The calcination of the dried powder was carried out inside a programmable oven (Vulcan 3-550, Degussa-Ney Dental Inc., Yucaipa, CA, USA) at different calcination temperatures ranging from 200 to 600^{o}C, for 4 h with both heating and cooling rates of 1.0^{o}C/min. The low heating and cooling rates were chosen to prevent defect formation in the silicalite-1 layer due to the difference in thermal expansion between the silicalite-1 and the support [19]. The calcination also helped enhance the bonding between the zeolite layer and the support. The dried membranes' calcination was carried out at 500^{o}C for 4 h with a heating

and cooling rate of 1.0°C/min. After calcination, all the samples were kept in a desiccator under dry atmosphere until further characterization.

4.2.3 Characterization of membranes and powder

Morphology and microstructure characterizations were performed using either the powder collected from the autoclave Teflon lining inner wall (TGA,DTGA, ^{29}Si CP/MAS NMR, pore size distribution, pore volume and BET surface area analyses) or the flat synthesized composite membranes discs (XRD, SEM and EDS analyses).

4.2.3.1 ^{29}Si CP/MAS NMR analysis

The silicon-29 solid state cross polarization/magic angle spinning nuclear magnetic resonance (^{29}Si CP/MAS NMR) spectra were collected at room temperature using a Bruker AVANCE 500 NMR spectrometer operating at 99.35 MHz for ^{29}Si. Approximately 50 mg of the powder was packed in 4 mm O.D. zirconia rotors which were spun at the magic angle with a typical spinning rate of 4 kHz. A ramped CP pulse sequence was used for all ^{29}Si NMR cross polarization experiments. The recycle delay time was 2 s, and the proton 90° pulse was 4 μs. The contact time to allow the transfer of magnetization between protons and ^{29}Si nuclei was 10 ms. The ^{29}Si NMR singles were externally referenced to the $-Si(CH_3)_3$ resonance of tetrakis trimethylsilyl silane at -9.9 ppm, corresponding to tetramethylsilane at 0 ppm.

4.2.3.2 TGA and DTGA analyses

The thermal gravimetric analysis (TGA) and differential thermal gravimetric analysis (DTGA) were recorded using a TA Instruments SDT 2960 differential scanning calorimeter - thermal gravimetric analysis (DSC-TGA) instrument under N_2 flow (100 mL/min). Approximately 10 – 20 mg of the powder sample was placed in a platinum crucible on the pan of a microbalance and heated from room temperature to 1000^{o}C with a heating rate of 10^{o}C/min while being purged with N_2.

4.2.3.3 Pore size distribution, pore volume and BET surface area

Pore size distribution, pore volume and Brunauer–Emmett–Teller (BET) surface area were determined by N_2 adsorption-desorption at -196^{o}C (77 K) for the calcined powder. The measurements were performed on a Micromeritics ASAP-2010 volumetric adsorption analyzer instrument (Micromeritics, Norcross, GA, USA). The samples were degassed at 120^{o}C for 8 h under high vacuum prior to the measurement on the same apparatus. The degassing process was terminated when the vacuum pressure reached 0.4 Pa. For the purpose of data analysis, the molecular cross-section area of 0.162 nm^2 was used for the N_2 molecule. The typical range of thicknesses of the adsorbate chosen for the statistical t-plot measurements was 3.5 to 5 Å, the technique was described in more details elsewhere [20]. The BET specific surface area was evaluated using the BET method based on nitrogen adsorption data at 77 K in the relative pressure range from 0.04 to 0.2. The pore volume, area distributions and the pore size distributions were evaluated using the BJH (Barrett-Joyner-Halenda) data interpretation method [21] with the modified Kelvin equation. The total pore volume was assessed from the adsorbed amount at a relative pressure of about

0.99. Moreover, BJH method was used in this analysis because it can be successfully applied to almost all types of porous materials.

4.2.3.4 XRD analysis

X-Ray diffraction (XRD) analyses were performed using a Philips PW 3710 diffractometer equipped with Ni-filtered CuKα radiation (λ = 1.54059 Å) operating with a generator voltage of 45 kV and current of 40 mA. The angular range (2θ) and the step width for the measurement were 0 – 90 and 0.03, respectively. The count time for the recording was 10 s per step. The flat membranes were mounted at room temperature on a specially designed holder.

4.2.3.5 SEM and EDS analyses

Scanning electron microscope (SEM) analysis was performed using a JEOL JSM-7500F Field Emission Scanning Microscope (JEOL, Tokyo, Japan) operating with primary electron beams of 2 keV. Electron dispersive spectrometer (EDS) Tracor-Northen Series Z-II spectrometer (Zeiss, Oberkochem, Germany) coupled to the SEM, with roughly 1 μm spatial resolution, was used to evaluate the composition at different depths for the supports and the synthesized membranes. The EDS was operated with primary electron beam of 20 keV accelerating voltages and 8 mm lens distance. Flat samples of the supports and the synthesized membranes were mounted on a specimen holder and covered with a conductive carbon tape before the analyses were conducted.

4.2.4 Gas permeation experiments

Gas permeation experiments were carried out in a constant pressure (CP) system using tubular supports as well as the membranes synthesized using these supports. The details of the experimental setup were given elsewhere [22]. The experiments were carried out in a parallel flow configuration with the feed flowing in the tube side of the module, and the permeate flowing in the same direction in the shell side of the module without any sweep gas. The feed flow rate was controlled by mass flow controllers. The retentate and permeate flow rates were measured by a rotameter (RM) and a bubble flow meter, respectively. The feed, the retentate and the permeate pressures were measured by a high accuracy pressure transducers.

All the supports and the tubular membranes synthesized in this work were tested with single He and N_2 gases. The single gas permeation experiments for the supports and the prepared membranes were carried out at total feed pressures up to 2.0 and 4.5 atm (absolute), respectively. The permeation tests were carried out for 6 hours. After the completion of the N_2 permeation tests, the membranes were regenerated with pure He at a feed pressure of 2.0 atm (absolute) for 12 h. All gas permeation tests as well as membrane regenerations were carried out at ambient temperature (~23^{o}C).

The gas permeation tests allowed characterizing the prepared membranes on the basis of the gas permeance. For gas *A*, the gas permeance (P_A) (mol/m^2.Pa.s), which is the measure of membrane productivity, is determined based on the steady state permeation rate (V_A) (mol/s), the partial pressure gradient across the membrane (Δp_A) (Pa), and the membrane area (A_m) (m^2):

$$P_A = \frac{V_A}{A_m \Delta p_A} \tag{4.1}$$

4.3 Results and Discussion

4.3.1 ^{29}Si CP/MAS NMR analysis

Fig. 4-1 shows the ^{29}Si CP/MAS NMR spectra of the synthesized silicalite-1 powder collected from the inner surface of the autoclave after calcination at different temperatures for 4 h with heating and cooling rates of 1.0^{o}C/min. Calcination at different temperatures was performed to show the effect of calcination temperature on the removal of the templates from the zeolite pores and to determine the lowest calcination temperature that can be used with the current calcination procedure to completely remove the templates from the zeolite pores. The peaks appearing in Fig. 4-1 are attributed to the so called Q^n, where Q stands for quaternary, which is related to the ability to form siloxane groups. Furthermore, the value of n, which could be 0, 1, 2, 3 and 4, for a given Si atom, indicates the number of other silicone atoms in direct connection with it through an oxygen atom (Si – O – Si) [23]. When the calcination was carried out at relatively low temperatures (200 – 400^{o}C), there were two broad resonances at around -102 ppm and -112 ppm, which are attributed to Q^3 (Si – $(SiO)_3OH$) and Q^4 (Si – $(SiO)_4$), respectively [24]. The presence of the -102 ppm peak indicates a lack of both continuity and connection between the silica tetrahedra, which is due to the presence of uncondensed (Si – O – H) bonds [25]. However, when the calcination is carried out at 500^{o}C or higher temperatures, the -102 peak disappears and only the peak at around -112 ppm is present, which is the characteristic peak for the pure silicalite-1 (Si – $(SiO)_4$) [26]. These results show the continuous condensation of Si – OH during the calcination step. This provides evidence for the continuous solid state transformation

throughout the calcination step, leading to the formation of a three-dimensional ($Si - (SiO)_4$) network. Furthermore, it is evident from Fig. 4-1 that the Q^4 peak becomes sharper with increasing calcination temperature, which indicates that a three dimensional ($Si - (SiO)_4$) network is becoming more and more ordered [23].

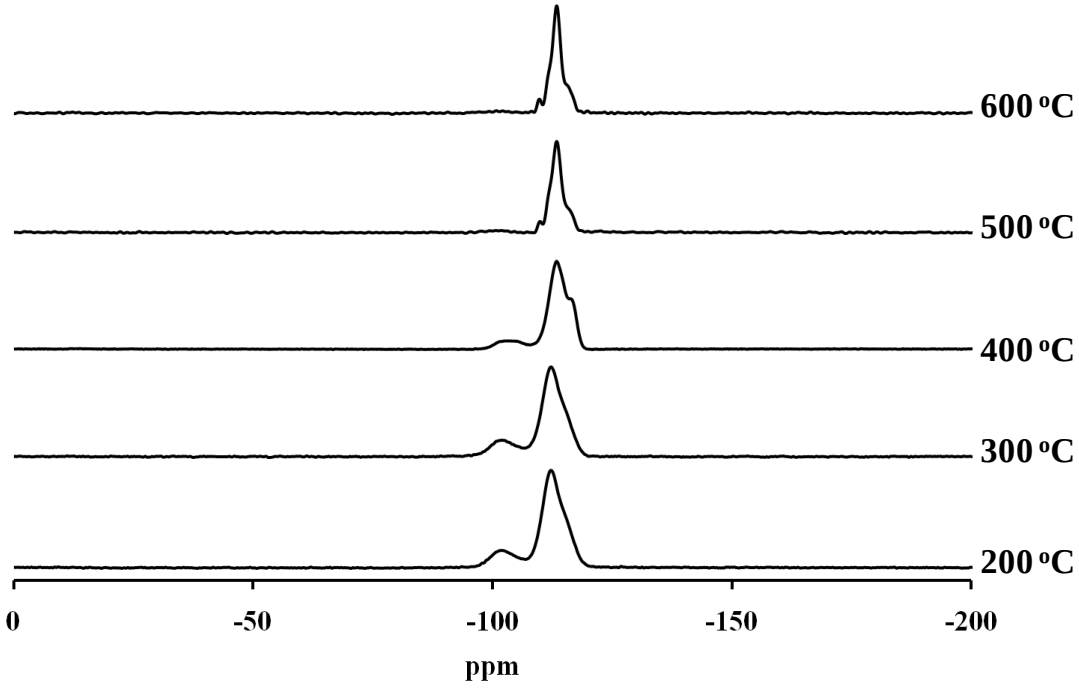

Figure 4-1 ^{29}Si CP/MAS NMR spectra of silicalite-1 powder collected from the lining of the autoclave after calcination at different temperatures.

The results shown in Fig. 4-1 indicate that 500°C is the lowest among the investigated temperatures that allows the complete removal of the templates from the zeolite pores in the current calcination procedure. It is well known that the templates can be removed at temperatures lower than 500°C, but lower temperatures require longer calcination times. For example, the complete removal of the templates at 400°C require calcination times greater than 20 h [27], as opposed to the 4 h calcination time used in this study.

4.3.2 TGA and DTGA analyses

Thermal analyses were carried out for the synthesized silicalite-1 powder collected from the autoclave lining before and after the calcination step at 500^{o}C. The analysis was carried out to confirm the complete removal of the templates from the zeolite pores through the calcination step and to check the stability of the synthesized zeolite at temperatures up to 1000^{o}C. The TGA and DTGA curves of the uncalcined sample are illustrated in Fig. 4-2a. As can be seen from the figure, the total weight loss of the uncalcined sample is approximately 35%. This weight loss occurs in four stages, which correspond to four distinct peaks on the DTGA curve. The first weight loss peak at about 163^{o}C is attributed to desorption of water [28]. The second peak at around 275^{o}C is due to desorption of TPAOH from the external surface of the zeolite crystallites [29]. The third peak (at around 370^{o}C) and the fourth peak (at around 450^{o}C) are attributed to the subsequent decomposition of the organic template trapped in the zeolite pore channels [30]. Consequently, the template should be completely removed at less than 500^{o}C, which again validates the chosen calcination temperature of 500^{o}C. This is further confirmed by the TGA and DTGA curves of the calcined sample shown in Fig. 4-2b. It is clearly seen from this figure that there is only a 3 – 4% weight loss in the temperature range from 200 – 1000^{o}C. This not only proves the complete removal of the templates from the zeolite pores after calcination, but also shows that there is no thermal decomposition of the zeolite structure up to 1000^{o}C.

4.3.4 XRD analysis

XRD patterns of the supports after the zeolite synthesis, for five different pore size supports are shown in Fig. 4-3. It can be noticed that, in addition to the support peaks, there are two

additional peaks at 2θ ≈ 9° and 2θ ≈ 24°. According to the XRD patterns provided by the International Zeolite Association (IZA) [31], these additional peaks correspond to silicalite-1 (MFI zeolite) as shown in the "top left" of the pattern in Fig. 4-3. Therefore, the XRD analyses provided additional confirmation of the successful formation of silicalite-1 zeolite by the pore plugging synthesis method used in this study.

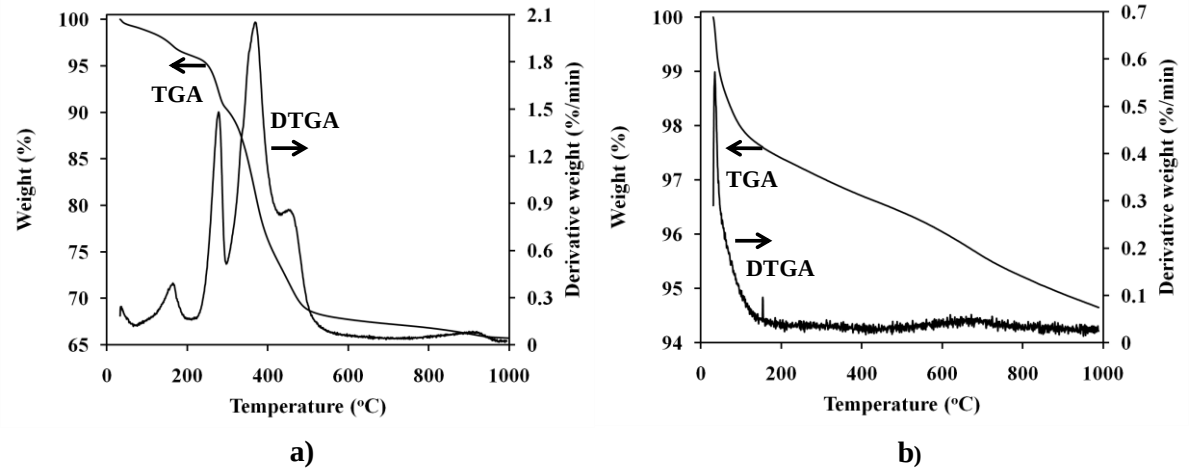

Figure 4-2 TGA and DTGA curves for silicalite-1 powder collected from the lining of the autoclave a) before calcination and b) after calcination at 500°C.

The XRD patterns in Fig. 4-3 confirm different composition of the large pore size supports (0.8 and 1.4 µm) and the small pore size supports (0.14, 0.2 µm and 0.45 µm). The latter ones have three extra peeks at 2θ ≈ 31°, 51° and 61°, which are the characteristics peaks of zirconia [32]. These are indicated in this figure by (O). The peaks at 2θ ≈ 27°, 36°, 55° and 57° are the characteristics peaks of titania [33] which are indicated by (Δ) in Fig. 4-3. The two small peaks at 2θ ≈ 42° and 69° indicated in this figure by (□) are believed to be for the alumina layer under the titania and zirconia layers.

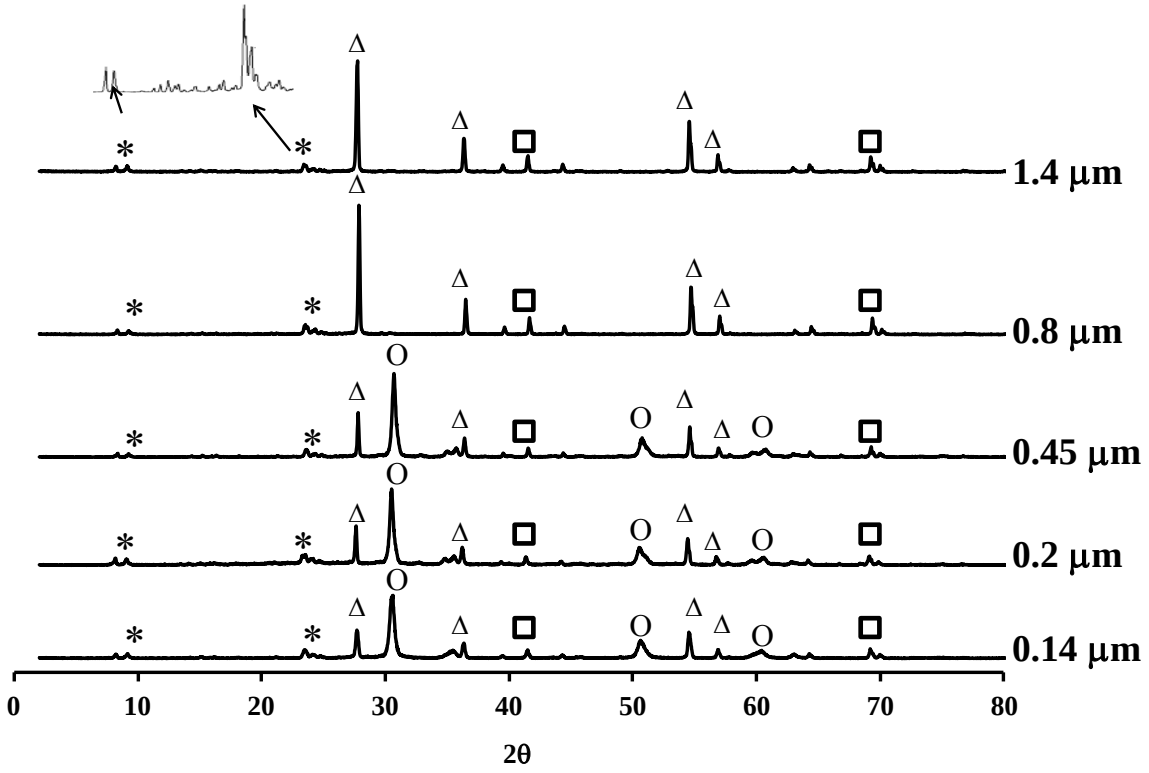

Figure 4-3 XRD patterns obtained for five supports with different pore sizes after growing the zeolite by pore plugging method, where *, Δ , O, and □ are corresponding to the peaks of silicalie-1, titania, zirconia and the alumina, respectively.

To investigate the orientation of the silicalite-1 crystals in the synthesized membranes, the XRD patterns shown in Fig. 4-3 are presented again in Fig. 4-4 focusing on small 2θ values. Since the silicalite-1 peaks are dominating in the small 2θ range (7.5–10^o, 22–25^o), the focus in Fig. 4-4 has been on the 2θ region between 5^o and 27^o. It is evident from this figure that the relative intensities of the silicalate-1 peaks differ depending on the pore size of the support. As a reference, Fig. 4-5 presents the XRD pattern of a powder collected from the autoclave lining wall that was suspended in a glycerol gel. Assuming that such prepared sample will have randomly oriented crystals, the comparison of the patterns in Fig. 4-4 with

the reference pattern in Fig. 4-5 allows investigation of the effect of the support on the orientation of the silicalite-1 crystals in the synthesized membranes. Since the patterns in Fig. 4-4 are different from the reference pattern in Fig. 4-5, it can be concluded that silicalite-1 crystals in the membranes are not randomly oriented.

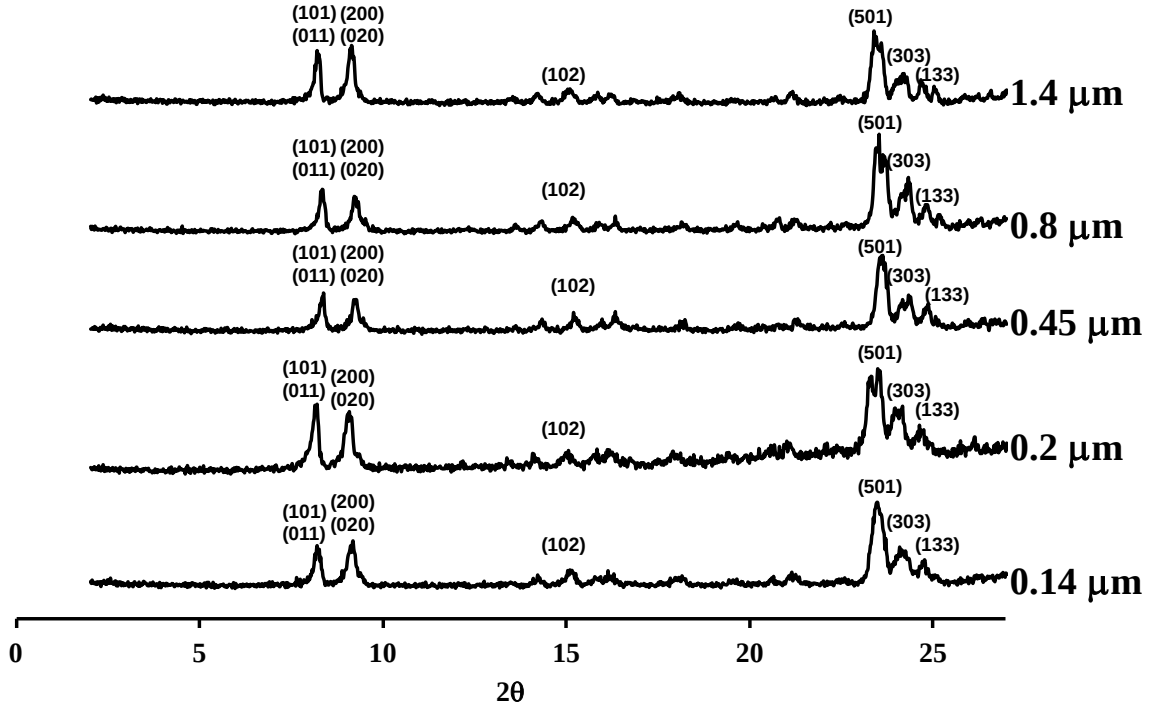

Figure 4-4 XRD patterns of the five supports in the 2θ region between 5º and 27º after growing the zeolite by pore plugging method.

The crystallographic faces and axes of a silicalite-1 crystal are shown in the top left corner of Fig. 4-5. This figure shows the silicalite-1 crystals that consist of sinusoidal channels along the {100} axis (crystallographic a-axis) with a circular cross section that is interconnected with the straight channels that are along the {010} axis (crystallographic b-axis) with an elliptical cross section [35]. Although, there are no direct channels in the {001}

axis (crystallographic c-axis), the transport in this direction is possible by hopping between the straight and sinusoidal channel networks [35]. Crystallographic b-axis is the easiest one for the molecules to go through since it is straight, followed by a-axis, followed by c-axis.

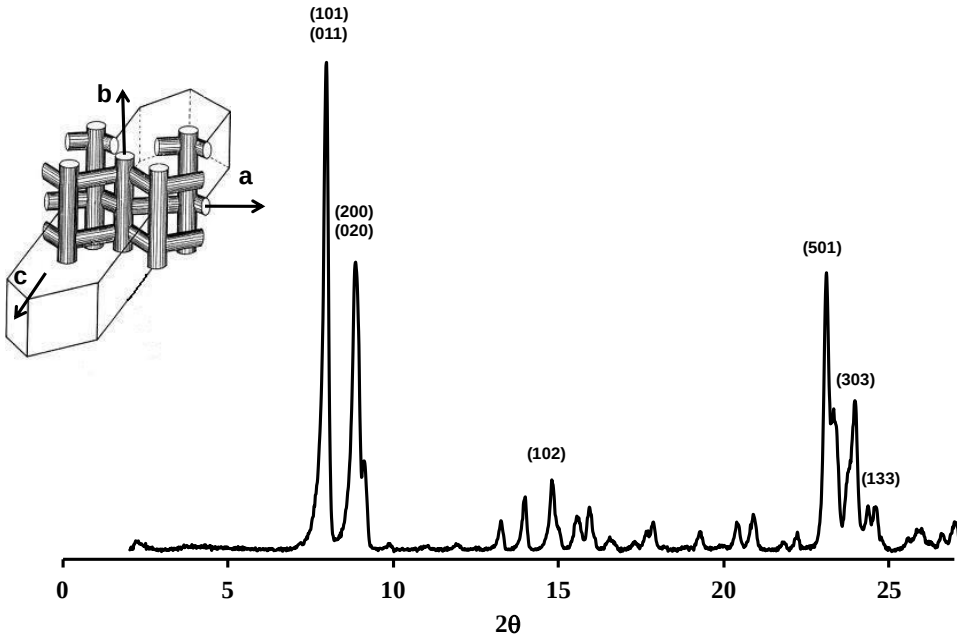

Figure 4-5 XRD pattern obtained for a random sample prepared from the zeolite powder collected from the autoclave lining wall. The top left insert shows a silicalite-1 crystal with the crystallographic faces and axes [34].

To facilitate the investigation of the changes in orientation of the zeolite layers for the supports with different pore sizes, the crystallographic preferred orientation (CPO) based on two different peaks in the XRD pattern is defined as follows [36]:

$$CPO\frac{(X)}{(Y)}=\frac{\left(\frac{I_S^{(X)}}{I_S^{(Y)}}-\frac{I_P^{(X)}}{I_P^{(Y)}}\right)}{\frac{I_S^{(X)}}{I_S^{(Y)}}} \tag{4.2}$$

where I is the peak intensity (in counts/step), *(X)* and *(Y)* are the two different peaks (considered in comparison), with subscripts: P and S representing the randomly oriented powder and the zeolite layer sample, respectively.

Theoretically, the CPO can be calculated using any peak, or combination of peaks. However, from a practical point of view it is not suitable to use some peaks since their intensities are very low due to a preferred orientation in the zeolite crystals [37]. Peaks with low intensity have large relative error which leads to inaccurate results. The (133) peak was used as a reference peak because it usually has a quite large intensity in most of the TPA-Silicalite-1 films [37] and it was relatively intense in all of the samples analyzed in this work. Two other peaks were chosen to examine the crystals' orientations in the zeolite layers: the (200)+(020) peak and the (501) peak [38]. The (200)+(020) peak were used instead of the (200) peak alone since it is not possible to separate the (200) peak from the (020) peak. To measure the crystals directed with the a-axis or b-axis perpendicular to the support surface, the (200)+(020) peak can be used. Furthermore, the (133) peak can be used to measure the crystals with the c-axis directed with an angle of 35^{o} from the normal to the support surface [39].

Based on that, CPO[(200)+(020)]/(133) will illustrate the fraction of crystals directed with either a-axis or b-axis perpendicular to the support surface. If the value of CPO[(200)+(020)]/(133) is equal to one, that means all the crystals in the zeolite layer are oriented with either a-axis or b-axis perpendicular to the support surface and that c-axis is parallel to the support surface. If the CPO[(200)+(020)]/(133) values are higher than 0.5 [37], then larger fraction of the zeolite layer crystals are directed with their a-axis or b-axis perpendicular to the support surface, compared to c-axis perpendicular to the support surface. This is preferable to help the gas molecules go through the silicalite-1 membrane, since a-axis and b-axis are the easiest ones to go through in the silicalite-1 structure.

The calculated CPO[(200)+(020)]/(133) values are summarized in Table 4-1. As can be seen from Table 4-1, the CPO[(200)+(020)]/(133) values were higher than 0.5 for all zeolite layers except for the layer synthesized on the 1.4 μm support. The highest CPO[(200)+(020)]/(133) value of 0.63 was for the zeolite layer grown on the 0.14 μm support and this value decreased with increasing pore size of the support. Since the CPO[(200)+(020)]/(133) values are not equal to zero, this confirms that the crystals in the synthesized layers are not randomly oriented. The crystals in the synthesized zeolite layers were preferably oriented with either the a-axis or b-axis perpendicular to the support surface for all supports except for the 1.4 μm pore size support. This also shows that as the pore size of the support decreases, more crystals were oriented toward either the a-axis or b-axis perpendicular to the support surface. The crystal growth inside the small pore sizes limits the random growth of the zeolite crystals which leads to the formation of particular oriented

zeolite layers. This is consistent with the fact that as the pore size of the support increases the crystals tend to grow and orient randomly.

Table 4-1 CPO and SEM main results.

Support pore size (μm)	CPO [(200)+(020)]/(133)	CPO (501)/(133)	Zeolite crystal size (μm)	Zeolite layer thickness (μm)
0.14	**0.63**	**0.81**	**0.7**	**0.7**
0.20	**0.61**	**0.44**	**0.7**	**1.2**
0.45	**0.55**	**0.25**	**1.5**	**1.4**
0.80	**0.51**	**0.66**	**0.7**	**1.0**
1.40	**0.38**	**0.64**	**0.7**	**-**

In order to further differentiate between the crystals oriented to the a-axis from the crystals oriented to the b-axis perpendicular to the support surface in the zeolite layers, the (501) peak and (133) peak were selected [37]. The CPO(501)/(133) values will illustrate the fraction of the zeolite layer crystals with their a-axis perpendicular to the support surface with respect to the crystals with their b-axis perpendicular to the support surface. As described before for CPO[(200)+(020)]/(133), if CPO(501)/(133) value is approaching unity, then almost all the crystals on the zeolite layer are having their a-axis perpendicular to the support surface [38,39]. If the CPO(501)/(133) values are higher than 0.5, then larger fraction of the zeolite layer crystals are directed with their a-axis perpendicular to the support surface, rather than with their b-axis perpendicular to the support surface.

The summary of the CPO(501)/(133) values are shown in Table 4-1. It is clearly seen from Table 4-1 that the CPO(501)/(133) values reach the minimum at 0.5 for the 0.45 μm support. This indicates that the zeolite layer synthesized on the 0.45 μm support has the lowest

fraction of crystals directed with the a-axis and the highest fraction of crystals directed with the b-axis perpendicular to the support surface. This should facilitate the diffusion of the molecules through straight channels, thus minimizing the resistance to transport of gases in the membranes synthesized on the 0.45 μm support.

Pore size distribution analysis provided that the mean pore size of the powder collected from the autoclave inner wall Teflon lining was 5.8 Å, which is very close to the literature value of 5.5 Å for silicalite-1. The corresponding BET surface area, the micropore area and the micropore volume of the sample were 397m^2g^{-1}, 25.3 m^2g^{-1} and 0.159 cm^3g^{-1}, respectively. These values are also in very good agreement with the literature values for silicalite-1 [40].

4.3.5 SEM and EDS analyses

These analyses were performed to observe the external morphology, crystalline structure (shape and size), distinct layers, thickness and chemical composition for the supports before and after the zeolite synthesis. Fig. 4-6 and Fig. 4-7 show the SEM micrographs for surfaces and cross-sections, respectively, after the zeolite synthesis for the supports with five different pore sizes.

It is evident from Fig. 4-6 that the silicalite-1 crystals are covering the entire surface of the membrane supports for all pore sizes. The crystals have the so called coffin shape, which is the common shape of the silicalite-1 zeolite crystals [41]. The silicalite-1 crystals average size for the supports with different pore sizes are summarized on Table 4-1. As can be seen from Fig. 4-6 and Table 4-1 the size of the silicalite-1 crystals grown on the top of the 0.45

μm pore size support is significantly larger than the silicalite-1 crystals sizes grown on top of the other supports. The crystals grown on top of the 0.45 μm pore size support are around 1.5 μm, and the crystal sizes grown on top of the other supports were around 0.7 μm.

The differences observed in crystal sizes grown on the various supports might be attributed to the difference in supports' active layer composition. As previously mentioned in section 2.1 there is a difference in chemical composition for the supports with various pore sizes. For example the support with 0.14 μm pore size had an active layer composition of 85% zirconium oxide and 15% titanium oxide. The support with 0.2 μm pore size had an active layer composition of 82% zirconium oxide and 18% titanium oxide, and the support with 0.45 μm pore size had an active layer composition of 78% zirconium oxide and 22% titanium oxide. The supports with 0.8 and 1.4 μm pore sizes have active layers consisting of pure titanium oxide. Therefore, it is anticipated that the difference in the composition of the support's active layer would have an influence on the crystals' growth and hence, their size. This will be further investigated in a future work using supports with the same pore size with different compositions.

It can also be seen from Fig. 4-6 that there is no noticeable difference in the orientation of the zeolite crystals covering the surface of the supports with different pore sizes. Therefore, it is anticipated that the variation of the crystals' orientation with the pore size of the support, as shown previously in the XRD analyses, is due to the differences of the crystals' orientation inside the pores of the support and not at the surface.

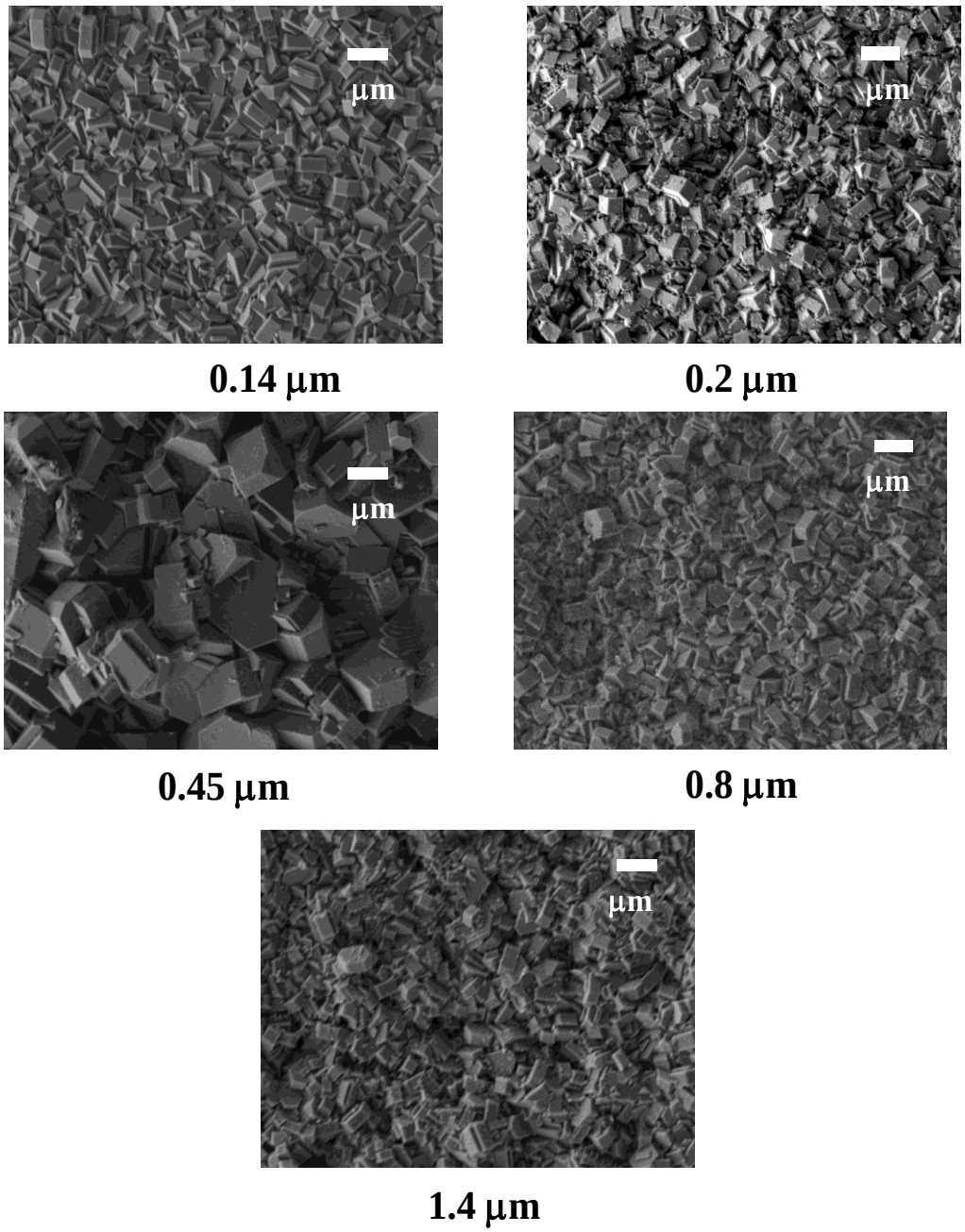

Figure 4-6 Surface SEM micrographs of synthesized membranes for supports with different pore sizes as indicated below each picture.

Fig. 4-7 shows the cross-section SEM micrographs of the supports with different pore sizes after the zeolite synthesis. It is evident from this figure that while a silicalite-1 layer was

formed on top of all supports, the characteristic of each formed layer is different depending on the pore size of the support. For the supports with the 0.2 and 0.45 μm pore sizes, the silicalite-1 layers formed are uniform, dense and continuous with an average thickness of around 1.2 and 1.4 μm, respectively, with 0.45 μm pore size membrane having the thickest zeolite layer on top of the support, among the membranes studied. The uniformity of the zeolite layer formed on top of these supports with small pore sizes is in agreement with what was reported in literature [17]. The silicalite-1 layer formed on top of the supports with 0.14 and 0.8 μm pore sizes are not uniform and their average thickness is around 0.7 and 1.0 μm, respectively (keep in mind the different scales for different SEM micrographs). The zeolite layer formed on top of the support with the 0.14 μm pore size was expected to be the most uniform layer [17,18] since it had the smallest pore size among the supports looked at in this study. This was not the case, which might have been due to some roughness of that support. It was difficult to observe a distinguished silicalite-1 layer on top of the support with the 1.4 μm pore size. The non-uniformity of the zeolite layer formed on top of the support with the 0.8 μm pore size as well as the incomplete coverage of the support with the 1.4 μm pore size were in agreement with the findings that were reported in the literature for supports with large pore sizes [17,18]. The zeolite layer thicknesses for all different supports are summarized in Table 4-1.

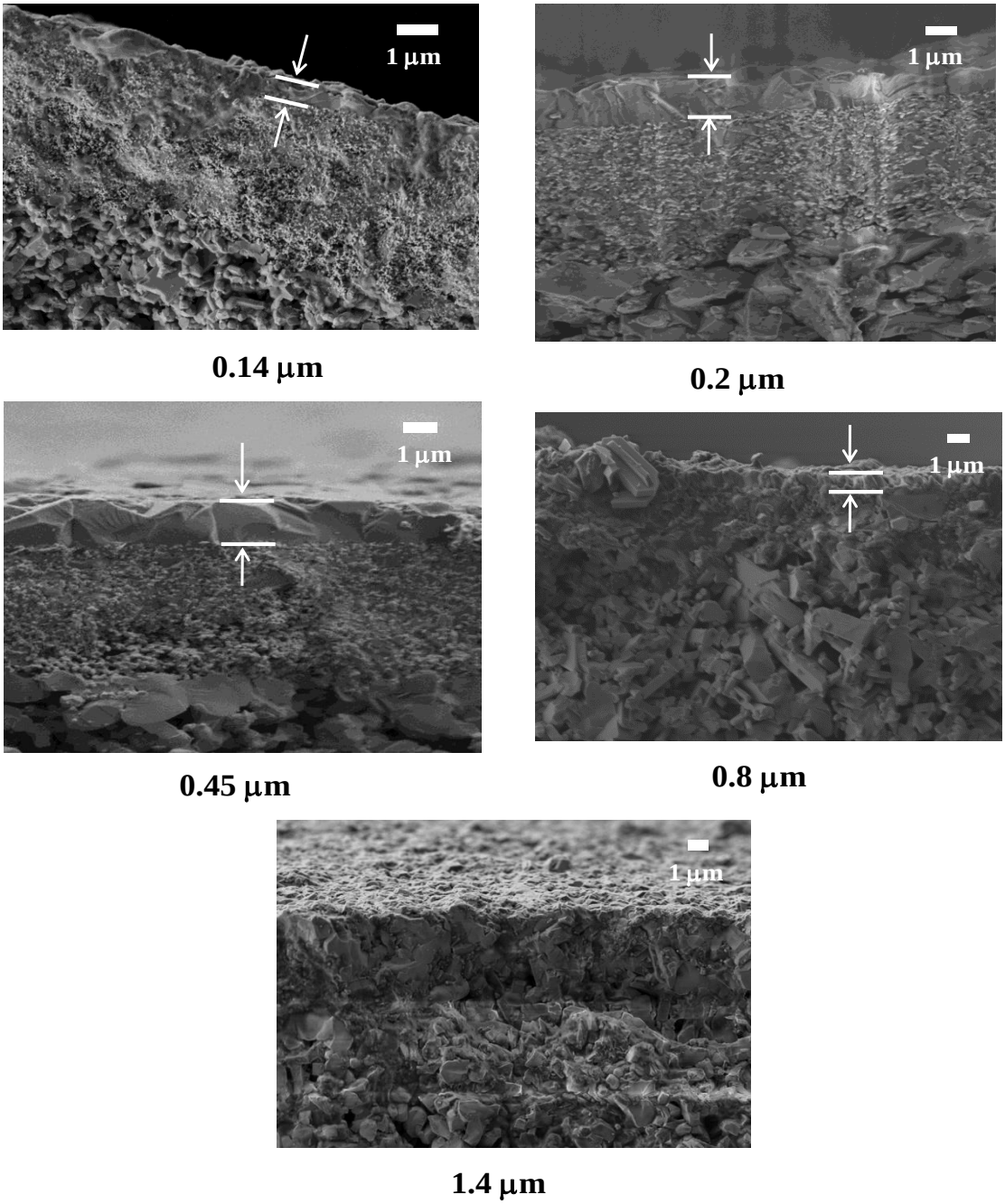

Figure 4-7 Cross-section SEM micrographs of synthesized membranes for supports with different pore sizes as indicated below each micrograph.

The silicon distribution results obtained by EDS as a function of the distance from the top surface for all the membranes studied after silicalite-1 synthesis is graphically presented in

Figs. 4-8a and 4.8b. It is evident for a given composition of the support (a mixture of zirconium oxide and titanium oxide as shown in Fig. 4-8a or pure titanium oxide as shown in Fig. 4-8b), that as the pore size increases, the penetration of Si increases. For the zeolite membrane synthesized on the support with the 0.45 μm pore size, the silicone is the major component even at 5 μm from the membrane surface. Since the thickness of the pure silicalite-1 zeolite layer was shown to be 1.4 μm, this indicates a complete pore plugging of the active layer of the support. This has been confirmed in another work of the current authors, in which the silicalite-1 membrane prepared using the support with the 0.45 μm pore size and tested in gas separation experiments involving CO_2/N_2 mixtures showed a very high selectivity towards CO_2 [22].

As shown in Fig. 4-8a the quantity of the silicone present 5 μm from the surface of the composite membranes synthesized with the 0.14 and 0.2 μm pore size supports was only 12.99% and 19.53%, respectively. These amounts are significantly smaller than the silicon amount that is present in the 0.45 μm pore size support. Taking into consideration that all the supports have the same porosity of 0.23, it is very likely that complete plugging of all active layer pores by the silicalite-1 zeolite in the supports with 0.14 and 0.2 μm pore sizes may not have been occurred.

Fig. 4-8b shows that the membrane prepared with the 1.4 μm pore size support has the highest zeolite penetration and silicone was the major component in the top 5 μm of the support (53.28%). This membrane should be further investigated by permeation/ separation experiments in order to confirm the possibility of plugging all the pores of the active layer.

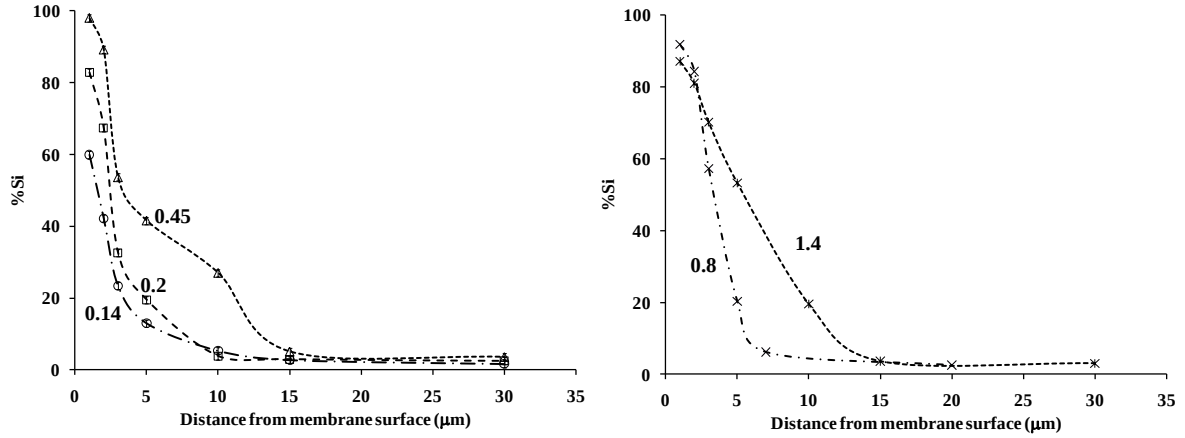

Figure 4-8 Silicon distribution as a function of distance from the top surface for all the membranes studied after silicalite-1 synthesis, a) for supports with pore sizes 0.14, 0.2 and 0.45 mm with active layers as a mixture of zirconium oxide and titanium oxide and b) for supports with pore sizes of 0.8 and 1.4 μm active layers of pure titanium oxide determined by EDS.

These results are in agreement with those reported in the literature which indicate that as the support pore size increases, for a given composition, the zeolite crystals penetration inside the pores of the support increases [17].

It should be emphasized that the previous studies in literature have investigated the pore plugging method to synthesize silicalite-1 membranes using alumina supports. Furthermore, in those studies the Si/Al ratio determined from the EDS analysis have been reported. However, no distinction has been made between the Al from the alumina support and the Al incorporated in the zeolite structure due to the aluminum ions dissolution during the hydrothermal synthesis. As mentioned earlier, under the harsh hydrothermal synthesis the aluminum ions dissolve from the support and integrate into the silicalite-1 network.

Integration of aluminum ions into the silicalite-1 network transforms the silicalite-1 into ZSM-5. On the other hand, supports used in this study have zirconium oxide and/or titanium oxide top active layers without any aluminum. Zirconium oxides and/or titanium oxide active layers are much more chemically stable than alumina under the highly basic conditions [42,43] and they can withstand harsher environments. Furthermore, zirconium and titanium ions generally do not dissolve and integrate into the zeolite network under the zeolite hydrothermal synthesis conditions. Based on that the zirconium oxides and titanium oxide layers acted as a buffer coating layers between the highly basic synthesis solution and the alumina in the supports' underneath layers [44], and hence, depressed the alumina dissolution and prevented the aluminum ions from penetrating into the silicalite-1 network, for both the crystals synthesized on top of the supports and inside the pores of the active layer.

It should be also stressed out that the formation of a zeolite layer on top of the supports in the synthesis procedure used in this work was not expected. However, once the top portion of the pores in the active layer is plugged, nothing prevents the formation of the pure zeolite layer above. Comparable to this condition occurs as well in the secondary growth method when pure zeolite layer is grown on top of the support, the formation of the zeolite crystals inside the support's pores is unavoidable, eventually leading to a partial or a complete support pore plugging [13].

Since the size of the crystals in the pure zeolite layer formed on top of the support is comparable to the pure zeolite layer thickness, it is anticipated that this layer cannot have

any selective properties on its own, and it is not expected to contribute to the membrane selectivity. This is due to the possibility of gaps between randomly packed crystals. However, this layer may provide an additional resistance to gas transport thus, decreasing the membrane permeance. The effect of the thin layer on top of the support and the silicalite formed inside the pores of the support active layer can only be assessed by gas permeation experiments.

The thickness of the membranes prepared in this study is compared with the thickness of the membranes prepared by the secondary growth method in the literature. In the latter, the thickness varies from a fraction of micrometer as recently reported in literature [45] to 70 μm [2,19] depending on the synthesis protocol, the type of the zeolite, the composition of the support, and the pore size of the support. In this study, the thickness of the membrane obtained is the thickness of the support active layer (3-10 μm) plus the thickness of the pure zeolite layer formed on top of the support. This is the maximum possible membrane thickness. As it was evident from the EDS analysis, the pores of the active layer might not be completely plugged throughout the entire thickness of the active layer. Moreover, it is also unlikely to plug the notably larger pores of the layers beyond the active layer.

The major disadvantage of the pore plugging synthesis method is that plugging the support pores adds more resistance to gas transport in the pore plugged membranes compared to the secondary growth membranes. However, pore plugging synthesis method has many advantages such as it will not generate defects larger than the pore size of the support

material, the prepared zeolite layer is protected against shocks and abrasion, and it provides a better control of the membrane thickness.

Therefore, the analyses done in this study after the preparation of the membrane confirm a unique morphology synthesized by the pore plugging synthesis method, which is distinctly different from the membranes synthesized by the secondary growth method reported in the literature.

Other two unique aspects of this study include the combination of the pore plugging method with Ti and Zr containing supports, as well as the combination of SEM, EDS, and XRD analyses for the characterization of the zeolite membranes.

4.3.6 Single gas permeation

To further characterize the prepared membranes, single gas permeation experiments were carried out using the tubular supports with five different pore sizes of the active layer as well as the membranes prepared using these tubular supports. Single gas permeation experiments were carried out at different total feed pressures. The comparison of single gas permeances provides information about the permeation mechanism through the membranes as well as the ideal selectivity of the membrane for a given pair of gases. The particular interest of this work was in the permeation behavior of gases with low or negligible adsorption capacities on silicalite-1. So, He and N_2 gases were chosen for the single gas permeation experiments.

The effect of the feed pressure on the single gas permeances of He and N_2 for all supports is summarized in Fig. 4-9. Regardless of the pore size of the support, the He and N_2 permeances were virtually constant for all supports and independent of the feed pressure as well. It is clear from Fig. 4-9 that no matter what is the pore size of the support or the feed pressure, N_2 and He permeances were extremely high and both were between 8.9×10^{-5} and 2.4×10^{-4} mol s^{-1} m^{-2} Pa^{-1}. It is evident also from Fig. 4-9 that none of the supports are selective and no selective separation is expected with just the supports.

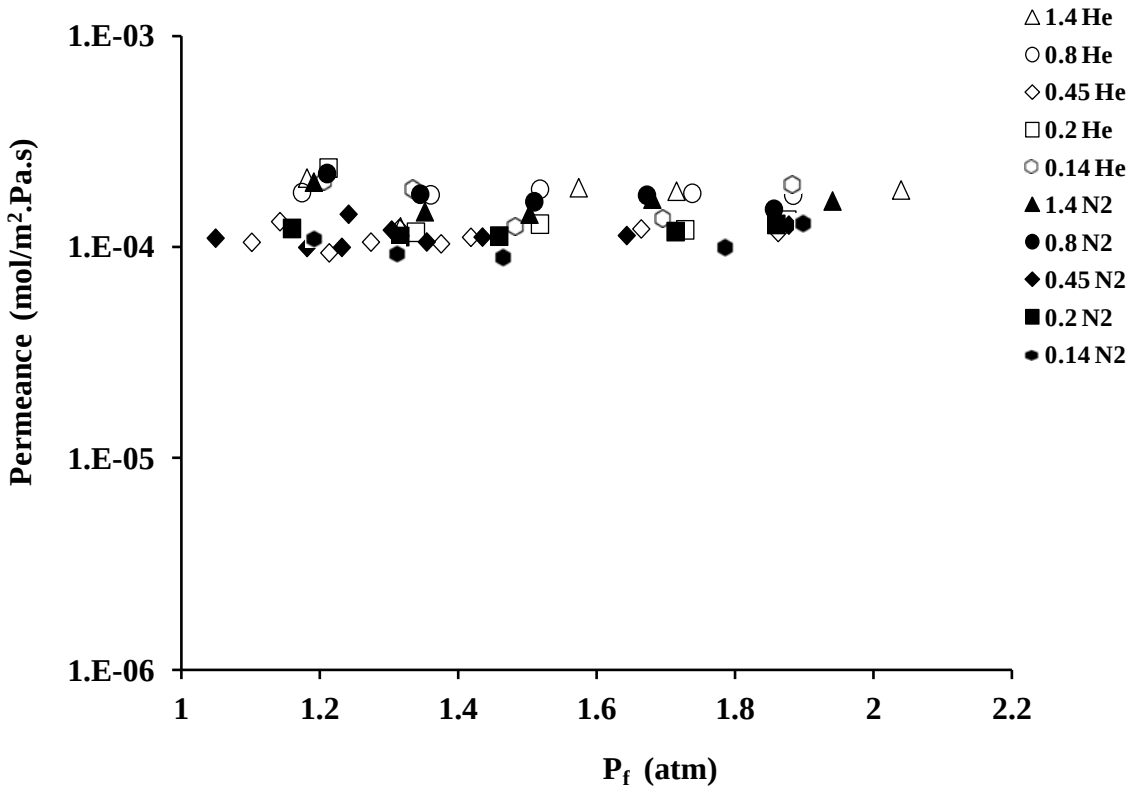

Figure 4-9 Single gas He and N_2 permeances through the supports with five different pore sizes as a function of feed pressure. All experiments performed at ambient temperature (293 K) with permeate side open to atmospheric pressure.

Fig. 4-10 shows the results for single gas permeation experiments with prepared Silicalite-1 membranes with five different pore sizes. It is evident from Fig. 4-10 that the membranes synthesized using the supports with the smallest pore size of 0.14 μm showed a very high permeability with insignificant selectivity. Hence, the performance of the membranes synthesized on the 0.14 μm support is not included in the subsequent discussion.

It is also clearly seen from Fig. 4-10 that the He and N_2 permeances were constant regardless of the pore size of the support and regardless of the feed pressure. These results were expected because the shape of the pure adsorption isotherm is linear for both gases on silicalite-1 in the pressure range used in gas permeation experiments. It can be seen also from Fig. 4-10 that the He and N_2 permeances were around 3.5×10^{-7} and 1.1×10^{-6} mol s^{-1} m^{-2} Pa^{-1}, respectively. Consequently, no matter what is the pore size of the support or the feed pressure, N_2 permeances were around three times higher than those for He.

The highest He and N_2 permeances were observed for the membrane prepared using the 0.45 μm pore size support, while the lowest permeances were for the membrane prepared using 1.4 μm pore size support (see Fig. 4-10). This is in agreement with the CPO analysis where the membrane prepared with the 0.45 μm pore size support had the most preferably oriented zeolite layer while the membrane prepared with the 1.4 μm pore size support had the least preferably oriented zeolite layer. Furthermore, it is important to emphasize that the effective thickness of the zeolite layers prepared in this work is almost the same as the thickness of the active layers of the supports which is approximately 5 μm regardless of the pore size of the support.

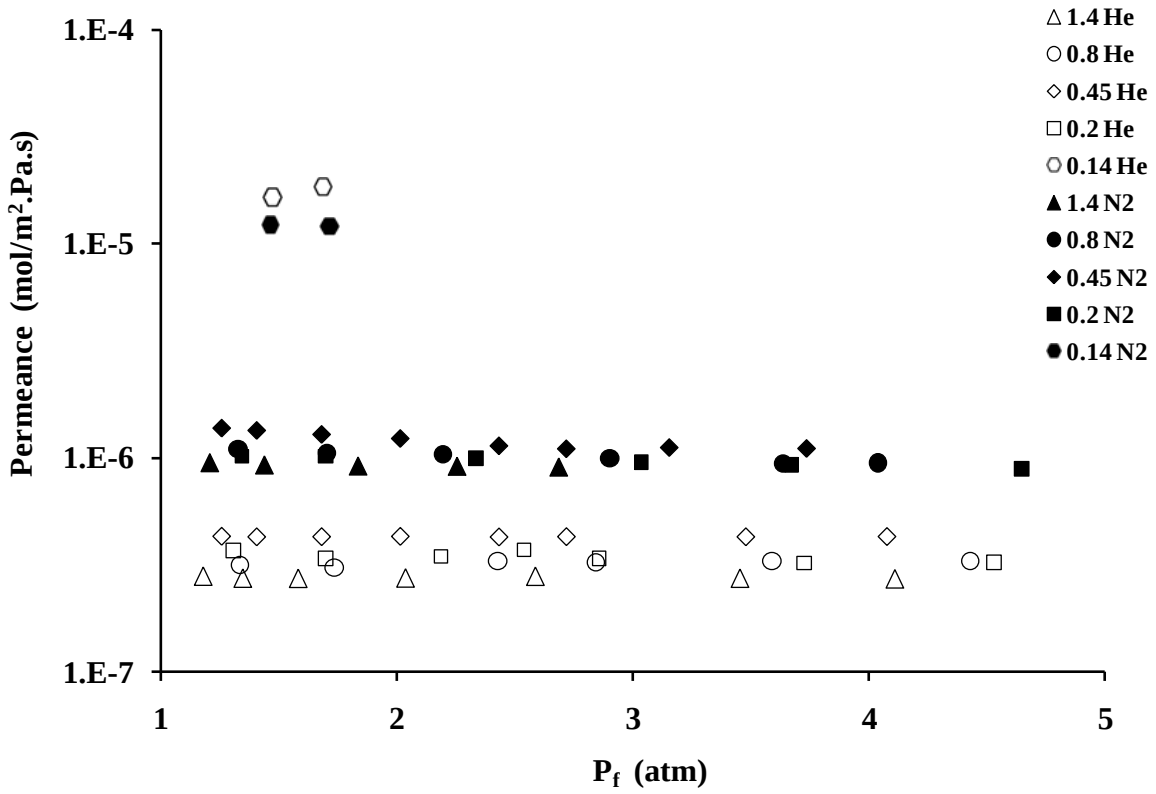

Figure 4-10 Single gas He and N_2 permeances through silicalite-1 membranes for supports with different pore sizes as a function of feed pressure. All experiments performed at ambient temperature (293 K) with permeate side open to atmospheric pressure.

The N_2/He permeance ratios observed in this work were comparable to the value of 2.5 reported by Takata et al. [46] for ZSM-5 membranes prepared using alumina supports, and to the value of 2.2 reported by Jareman and Hedlund [47] for Silicalite-1 membranes prepared using alumina supports. However, the N_2/He permeance ratios observed in this work were higher than the values of unity that was reported by Aoki et al. [48], Bakker et al [49] and Lai and Tsapatsis [50] for MFI membranes.

4.4 Conclusions

Composite silicalite-1 membranes have been prepared by pore plugging synthesis method on novel zirconium oxide and/or titanium oxide supports with different pore sizes in their active layers. The formation of the silicalite-1 crystals and the orientation of the silicalite-1 crystals grown inside the pores as well as on top of the supports were investigated by XRD analysis. The XRD results confirm the successful formation of the silicalite-1 zeolite by the pore plugging synthesis method. These XRD results also showed a typical silicalite-1 structure with a high internal crystalline order grown inside the pore of the support as well as on top of the supports for all different pore sizes studied. It is evident from the XRD results that the silicalite-1 crystals in the synthesized membranes were not randomly oriented. The CPO analysis revealed that the degree of orientation toward either the a-axis or b-axis perpendicular to the support surface, decreased by increasing the pore size of the support. The 0.45 μm support had the most preferably oriented zeolite layer with the highest number of crystals oriented with the b-axis perpendicular to the support surface which is expected to help for the transport of molecules through the membrane since this axis has straight channels.

The SEM and EDS analysis were used to investigate the synthesized membranes' morphology and the penetration of the zeolite crystals inside the pores of the supports. As expected, zeolite crystals penetrated inside the pores of the active layers of all five supports. However, the extent of the penetration, i.e. pore plugging, depended on the pore size and the chemistry of the active layer of the support. For a given chemistry of the active layer, the pore plugging increased with increasing pore size of the support. In addition to pore plugging, zeolite crystals also formed a thin continuous layer on top of the active layer of all

supports except for the largest, 1.4 μm pore size support. The most uniform and the thickest zeolite layer was 1.4 μm thick and it was observed on top of the 0.45 μm pore size support. The morphology of this membrane is also distinct from the other membranes studied because of the largest size of the crystals in the pure zeolite layer on top of the active layer (see Fig. 4-6). This distinct morphology of the pure zeolite layer on the membrane synthesized using the 0.45 μm pore size support cannot be attributed to the most complete plugging of the pores of the active layer, since the membrane synthesized using the 1.4 μm pore size support also showed a quite complete pore plugging without a continuous zeolite layer.

Absence of alumina in the active layer of the supports indicates that the intermediate layer of the supports successfully prevented migration of aluminum ions from the aluminum layer to the active layer of the support during the hydrothermal synthesis of silicalite-1 zeolite. Consequently, the supports used in this study should allow a better control of Si/Al ratio compared to the commonly used alumina supports. This might be of critical importance when preparing the actual gas separation membranes.

Gas permeation experiments using He and N_2 single gases at 293 K showed that regardless of the pore size of the support, He and N_2 permeances were constant despite the change of the pressure across the membranes. The highest permeances were observed for the membrane prepared using the 0.45 μm pore size support, while the lowest permeances were for the membrane prepared using the 1.4 μm pore size support. These results confirmed the selective properties of the prepared membranes and no matter what is the pore size of the

support or the feed pressure, N_2 permeances were around three times higher than those for He.

Acknowledgments

The authors acknowledge the financial support received from Natural Science and Engineering Research Council (NSERC) of Canada and from the University of Ottawa. The Canada Foundation for Innovation and the Ontario Research Fund are gratefully acknowledged for infrastructure grants obtained by the Center for Catalysis Research and Innovation.

Abbreviations

BET: Brunauer–Emmett–Teller

BJH: Barrett-Joyner-Halenda data interpretation method

CP: cross polarization

CPO: crystallographic preferred orientation

DSC: differential scanning calorimeter

DTGA: differential thermal gravimetric analysis

EDS: electron diffraction spectrometer

IZA: International Zeolite Association

MAS: magic angle spinning

NMR: nuclear magnetic resonance

SEM: scanning electron microscope

TAOH: tetrapropylammonium hydroxide

TGA: thermal gravimetric analysis

TPA: tetrapropylammonium

XRD: X-Ray diffraction

4.5. References

1- A. Tavolaro, E Drioli, Zeolite membranes, Adv. Mater. 11 (1999) 975 – 996.

2- M. Kazemimoghadam, T. Mohammadi, Synthesis of MFI zeolite membranes for water desalination, desalination 206 (2007) 547 – 553.

3- W. Yuan, Y.S. Lin, W. Yang,, Molecular sieving MFI-type zeolite membranes for pervaporation separation,, J. Am. Chem. Soc. 126 (2004) 4776 – 4777. H

4- F. Jareman, C. Andersson, J. Hedlund, The influence of the calcination rate on silicalite-1 membranes, Microporous Mesoporous Materials 79 (2005) 1 – 5.

5- H.H. Funke, M.G. Kovalchick, J.L. Falconer, R.D. Noble, Separation of hydrocarbon isomer vapors with silicalite zeolite membranes, Ind. Eng. Chem. Res. 35 (1996) 1575.

6- A. Javaid, Membranes for solubility-based gas separation applications, J. Chemical Engineering, 112 (2005) 219 – 226.

7- B.M. Lok, T.R. Cannan, C.A. Messina, The role of organic molecules in molecular sieve synthesis, Zeolites 3 (1983) 282 – 291.

8- S.P. Davis, E.V.R. Borgstedt, S.L. Suib, Growth of zeolite crystallites and coatings on metal surfaces, Chem. Mater. 2 (1990) 712 – 719.

9- T. Matsufuji, N. Nishiyama, M. Matsukata, K. Ueyama, Separation of butane and xylene isomers with MFI-type zeolite membranes synthesized by a vapour-phase transport method, J. Membrane Science 178 (2000) 25 – 34.

10- A. Gouzinis, M. Tsapatsis, On the preferred orientation and microstructural manipulation of molecular sieve films prepared by secondary growth, Chem. Mater. 10 (1998) 2497 – 2504.

11- S. Miachon, E. Landrivon, M. Aouine, Y. Sun, I. Kumakiri, Y. Li, O. Pachtova Prokopova, N. Guilhaume, A. Giroir-Fendler, H. Mozzanega, J.-A. Dalmon, Nanocomposite MFI-alumina membranes via pore-plugging synthesis: preparation and morphological characterization, J. Membrane Science 281 (2006) 228 – 238.

12- S. Miachon, P. Ciavarella, L. van Dyk, I. Kumakiri, K. Fiaty, Y. Schuurman, J.-A. Dalmon, Nanocomposite MFI-alumina membranes via pore-plugging synthesis: specific transport and separation properties, J. Membrane Science 298 (2007) 71 – 79.

13- C. Kong, J. Lu, J. Yang, J. Wang, Preparation of silicalite-1 membranes on stainless steel supports by a two-stage varying-temperature in situ synthesis, J. Membrane Science 285 (2006) 258 – 264.

14- E. Bourgeat-Lami, P. Massiani, F.D. Renzo, P. Espiau, F. Fajula, Th.D. Courieres, Study of the state of aluminium in zeolite-β, Applied Catalysis 72 (1991) 139 – 152.

15- N.Y. Chen, Hydrophobic properties of zeolites, J. Physical Chemistry 80 (1978) 60 – 64.

16- J. Caro, M. Noack, Zeolite membranes – recent development and progress, Microporous Mesoporous Materials 115 (2008) 215 – 233.

17- G.E. Romanos, Th.A. Steriotis, E.S. Kikkinides, N.K. Kanellopoulos, V. Kasselouri, J.D.F. Ramsay, P. Langlois, S. Kallus, Innovative methods for preparation and testing of Al_2O_3 supported silicalite-1 membranes, J. European Ceramic Society 21 (2001) 119 – 126 .

18- E. Landrivon, S. Miachon, I. Kumakiri, M. Matsukata, J.-A. Dalmon, MFI-alumina composite membrane. Influence of the support porous structure on the separative performance, Fuel Chemistry Division Preprints 48 (2003) 394 – 395.

19- M. Pan, Y.S. Lin, Template-free secondary growth synthesis of MFI type zeolite membranes, Microporous Mesoporous Materials 43 (2001) 319 – 327.

20- S. Storck, H. Bretinger, W.F. Maier, Characterization of micro- and mesoporous solids by physisorption methods and pore-size analysis, Applied Catalysis A: General 174 (1998) 137 – 146.

21- E.P. Barrett, L.G. Joyner, P.P. Halenda, The determination of pore volume and area distributions in porous substances. I. Computations from nitrogen isotherms, J. Am. Chem. Soc. 73 (1951) 373 – 380.

22- M. Tawalbeh, B. Kruczek, F. H. Tezel, S. Letaief, C. Detellier, Separation of CO_2 and N_2 Gases Using A Novel Zeolite Membrane, Sep. Sci. Tech. 47 (2012) 1606 – 1616.

23- G. Defontaine, A. Barichard, S. Letaief, C. Feng, T. Matsuura, C. Detellier, Nanoporous polymer – clay hybrid membranes for gas separation, J. Coll. Interf. Sci. 343 (2010) 622 – 627.

24- R. Ravishankar, C. Kirschhock, B.J. Schoeman, P.Vanoppen, P.J. Grobet, S. Storck,| W.F. Maier, J.A. Martens, F.C. De Schryver, P.A. Jacobs, Physicochemical

characterization of silicalite-1 nanophase material, J. Phys. Chem. B 102 (1998) 2633 – 2639.

25- A. Manna, B.D. Kulkarni, R.K. Ahedi, A. Bhaumik, A.N. Kotasthane, Synthesis of silicalite-1 in bicontinuous microemulsion containing AOT, J. Coll. and Interf. Sci. 213 (1999) 405 – 411.

26- J.M. Chezeau, L. Delmotte, J.L. Guth, Z. Gabelica, Influence of synthesis conditions and post synthesis treatments on the nature and quantity of structural defects in highly siliceous MFI zeolites: a high-resolution solid-state ^{29}Si n.m.r. study, Zeolites 11 (1991) 598 – 606.

27- X. Lin, H. Kita, K. Okamoto, Silicalite membrane preparation, characterization, and separation performance, Ind. Eng. Chem. Res. 40 (2001) 4069 – 4078.

28- J. Dong, J. Zou, Y. Long, Synthesis and characterization of colloidal TBA-silicalite-2, Microporous Mesoporous Materials 57 (2003) 9 – 19.

29- M. Soulard, S. Bilger, H. Kessler, J.L. Guth, Thermoanalytical characterization of MFI-type zeolites prepared either in the presence of OH^- or of F^- ions, Zeolites 7 (1987) 463 – 470.

30- L.M. Parker, D.M. Bibby, J.E. Patterson, Thermal decomposition of ZSM-5 and silicalite precursors, Zeolites 4 (1984) 168 – 174.

31- M.R. Othman, S.C. Tan, S. Bhatia, Separability of carbon dioxide from methane using MFI zeolite–silica film deposited on gamma-alumina support, Microporous Mesoporous Materials 121 (2009) 138 – 144.

32- S.P. Naik, A.S.T. Chiang, R.W. Thompson, F.C. Huang, Formation of silicalite-1 hollow spheres by the self-assembly of nanocrystals, Chem. Mater. 15 (2003) 787 – 792.

33- Y. Ma, J. Guan, S. Wu, J. Liu, Q. Kan, W. Zhang, Synthesis and characterization of belt-like silicalite-1 nanocrystals with mesoporous structure, Materials Letters 64 (2010) 2523 – 2525.

34- J. Caro, M. Noack, and P. Kolsch, Zeolite membranes: from the laboratory scale to technical applications, Adsorption 11 (2005) 215 – 227.

35- M.C. Lovallo, M. Tsapatsis, Preferentially oriented submicron silicalite membranes, AIChE J. 42 (1996) 3020 – 3029.

36- J.P Verduijn, A.J. Bons, M.H. Anthonis, L.H. Czarnetzki, Int. Patent Appl. PCT WO 96/01683.

37- J. Hedlund, Control of the preferred orientation in MFI films synthesized by seeding, J. Porous Materials 7 (2000) 455 – 464.

38- J. Heldund, S. Mintova, J. Sterte, Controlling the preferred orientation in silicalite-1 films synthesized by seeding, Microporous Mesoporous Materials 28 (1999) 185 – 194.

39- M.A. Ulla, R. Mallada, J. Coronas, L. Gutierrez, E. Miro, J. Santamaria, Synthesis and characterization of ZSM-5 coatings onto cordierite honeycomb supports, Applied Catalysis A: General 253 (2003) 257–269.

40- L. Tosheva, B. Mihailova, V. Valtchev, J. Sterte, Silicalite-1 macrostructures – preparation and structural features, Microporous Mesoporous Materials 39 (2000) 91 – 101.

41- I. Diaz, E. Kokkoli, O. Terasaki, M. Tsapatsis, Surface structure of zeolite (MFI) crystals, Chem. Mater. 16 (2004) 5226 – 5232.

42- A. Larbot, J.-P. Fabre, C. Guizard, L. Cot, J. Gillot, New inorganic ultrafiltration membranes: titania and zirconia membranes, J. Am. Ceram. Soc. 72 (1989) 257 – 261.

43- R. Gopalan, C.-H. Chang, Y.S. Lin, Thermal stability improvement on pore and phase structure of sol-gel derived zirconia, J. Mater. Sci. 30 (1995) 3075 – 3081.

44- M. Kanezashi, J. O'Brien, Y.S. Lin, Thermal stability improvement of MFI-type zeolite membranes with doped zirconia intermediate layer, Microporous Mesoporous Materials 103 (2007) 302–308.

45- J. Motuzas, R. Mikutaviciute, E. Gerardin, A. Julbe, Controlled growth of thin and uniform TS-1 membranes by MW-assisted heating. Microporous Mesoporous Materials 128 (2010) 136 – 143.

46- Y. Takata, T. Tsuru, T. Yoshioka, M.Asaeda, Gas permeation properties of MFI zeolite membranes prepared by the secondary growth of colloidal silicalite and application to the methylation of toluene, Microporous Mesoporous Materials 54 (2002) 257 – 268.

47- F. Jareman, J. Hedlund, Permeation of H_2, N_2, He, and SF_6 in real MFI membranes, Microporous Mesoporous Materials 83 (2005) 326 – 332.

48- K. Aoki, V.A. Tuan, J.L. Falconer, R.D. Noble, Gas permeation properties of ion-exchanged ZSM-5 zeolite membranes, Microporous Mesoporous Materials 39 (2000) 485 – 492.

49- W.J.W. Bakker, L.J.P. Broeke, F. Kapteijn, J. Moulijn, Temperature dependence of one-component permeation through a silicalite-I membrane, AIChE J. 43 (1997) 2203 – 2214.

50- Z. Lai, M. Tsapatsis, Gas and organic vapor permeation through b-oriented MFI membranes, Ind. Eng. Chem. Res. 43 (2004) 3000 – 3007.

CHAPTER FIVE

This Chapter is based on

Effect of Support Pore Size on Morphology and Performance of Tubular Silicalite-1 Membranes

M. Tawalbeh, F. H. Tezel, M. Al-Ismaily, B. Kruczek

Department of Chemical and Biological Engineering, University of Ottawa, 161 Louis Pasteur Street, Ottawa, ON, Canada K1N 6N5

Submitted to the Journal of Membrane Science

This paper illustrates the effect of the support pore size on the tubular silicalite-1 membrane morphology and CO_2/N_2 permeation performance. Five zirconium and/or titanium oxides active layer supports with different pore sizes for their active layer in the range of 0.14 - 1.4 μm were investigated. To improve the membrane synthesis reproducibility, the autoclave design was modified by inserting a Teflon holder that was specially designed to ensure vertical position of the supports during the hydrothermal synthesis. Keeping the tubes in a vertical position is believed to prevent the formed crystals in the solution from being attached to the support surface and consequently high stage cut values were observed in gas

separation tests. Hence, a protocol adapted from the procedure presented in Geankopolis (2003) was used to recover the gas permeances and the permselectivity from mixed gas permeation tests assuming that the permeances are independent of the feed composition and the total feed pressure. M. Al-Ismaily was a co-author of this paper in addition to the supervisors. M. Al-Ismaily helped in coding the protocol that was used to recover the gas permeances and the permselectivity from mixed gas permeation.

Chapter 5- Effect of Support Pore Size on Morphology and Performance of Tubular Silicalite-1 Membranes

Abstract

Silicalite-1/ceramic composite membranes were prepared on the inner surface of zirconium oxide and/or titanium oxide tubular supports by a pore plugging hydrothermal synthesis. Five types of supports with different pore sizes ranging from 0.14 – 1.4 μm, were studied. The synthesized membranes were characterized by scanning electron microscope (SEM), electron diffraction spectrometer (EDS), x-ray diffraction (XRD), and gas permeation with pure and mixed gas feeds.

All membranes showed high concentrations of Si within the active layer of the support, suggesting successful pore-plugging of the membranes. The greater the pore size of the active layer of the support, the greater was the concentration of Si observed. In addition, large coffin-shape crystals, which are characteristics of silicalite-1, were also observed on top of each membrane. The analysis of XRD micrographs revealed that the crystals were mostly oriented with either the a- or b-axes perpendicular to the membrane surface, which is desirable from the point of view of minimizing the resistance to gas transport through the zeolite membrane. Except for the membranes synthesized using the supports with 0.14 μm pores, all membranes were very selective with CO_2/N_2 permselectivities up to 30 at low pressure differentials. At the same time, the membranes were very permeable with a CO_2 permeance in the order of 10^{-6} mol m^{-2} Pa^{-1} s^{-1}. Assuming the thickness of the selective

layer to be equivalent to the thickness of the active layer of the support, all membranes fell above the revised Robeson upper-bound line for CO_2/N_2 separation.

Keywords: Silicalite-1 membranes; Pore plugging synthesis; CO_2/N_2 separation, Titania/zirconia supports

5.1 Introduction

Zeolite membranes have become a subject of intensive research, which is evident from a number of excellent review articles in recent years [1-5]. Several types of zeolite membranes have been successfully prepared at the laboratory scale, with the most prominent examples of MFI [6], LTA [7], FAU [8], and SAPO-34 [9]. Most of the works reported on zeolite membranes, however, have focused on MFI-type zeolites, i.e. silicalite-1 and its Al-containing analogue, ZSM-5. With the pore size of ~ 5.5Å, MFI zeolite membranes are of particular interest for several industrial separations [10], including separation of CO_2/N_2, which is particularly important for capturing of CO_2 from flue gases.

The attractiveness of the MFI zeolite membranes for the CO_2/N_2 separation arises from the fact that CO_2 has much greater affinity towards silicalite-1 and ZSM-5 than N_2. As a result, despite a relatively similar kinetic diameters of CO_2 (3.3 Å) and N_2 (3.6 Å), which are both considerably smaller than 5.5 Å, the former may effectively prevent the latter from entering the pores of MFI crystals leading to high CO_2/N_2 selectivities. However, in the presence of large intercrystalline openings (defects), the selective properties of MFI membranes quickly disappear. To minimize the contributions of the non-selective transport in MFI membranes, the crystals must form a continuous layer, in which the individual crystals should be as uniformly oriented as possible, and preferably with the crystallographic a- or b-axes perpendicular to the membrane surface [11,12].

Consequently, virtually all studies on MFI zeolite membranes have focused on the synthesis of continuous and well-intergrown thin films on top of a porous support; the latter is to provide the mechanical resistance for the membrane. The thickness of the film on top of the

support varies from a fraction of a micrometer [13-15] to tens of micrometers [16-19]. In principle, smaller crystals that are more uniformly oriented allow minimizing the thickness of the film without compromising its selective properties [14,20]. At the same time, thinner films are desired to maximize the productivity of membrane. Pore size of the support is an important parameter in the synthesis of continuous MFI. Too large pores in the support may result in a collapse of the zeolite film under the pressure, but too small pores may lead to excessive resistance to gas transport. The thermal properties of the support are also important. Since the MFI membranes are synthesized in a hydrothermal process followed by calcination at high temperatures, the difference in the thermal expansion coefficients between the MFI crystals and the support material during the heating and the cooling, results in a temperature mismatch. This may lead to the development of defects in zeolite films [17,21].

An alternative approach, in which the active phase is embedded into the host ceramic porous network using so called pore plugging synthesis, was recently proposed by Dalmon's group [22, 23]. This architecture of MFI membranes avoids individual membrane defects to exceed the size of the support. In addition, it also provides a better mechanical resistance, as well as higher resistance to thermal shocks. Another consequence of this architecture is that the mass transfer within these membranes at high temperature is still governed by zeolite pores instead of intercrystalline openings that may appear in film-like configurations.

The pore-plugging syntheses reported in Ref. [22,23] were carried out using γ-alumina supports. However, under harsh hydrothermal environment such as the one that exists during

the synthesis of MFI membranes, Al^{3+} from the support may be integrated into the zeolite network. This is evidenced by lower than expected Si/Al ratios in the final MFI membranes. At the same time, this uncontrollable incorporation of Al^{3+} into the zeolite network is believed to promote defect formation in the MFI membranes [24]. Recently, we have synthesized silicalite-1 MFI membranes by the pore plugging method using porous alumina supports with an active layer consisting of only titanium oxide or titanium oxide/zirconium oxide [25, 26]. The MFI crystals on top of the supports as well as those embodied within the active layer of the supports were pure silicalite-1 and thus the active layers effectively prevented Al^{3+} ions from being incorporated into the zeolite network. Using the flat sheet supports we have reported on the effect of pore size of the support on the morphology of the resulting MFI membranes, in particular on the orientation of the silicalite-1 crystals within the pores of the active layer [25]. We have also investigated the effects of the total feed pressure and feed composition of CO_2/N_2 mixtures on transport properties of a tubular membrane synthesized using one specific pore size of the support [26]. Regardless of the operating conditions, the membrane showed very high CO_2/N_2 permselectivity; however, the corresponding CO_2 permeance was only around 6×10^{-8} mol m^{-2} Pa^{-1} s^{-1}.

In this work, we present a detailed investigation of the effect of pore size of tubular supports on the morphology and permeation/separation properties of silicalite-1 membranes synthesized by the pore plugging method. Similarly to the previously investigated flat sheet membranes, the supports had active layer consisting of titanium oxide or titanium oxide/zirconium oxide, and pore sizes ranging from 0.14 to 1.4 μm. The supports had perfectly vertical orientation during the hydrothermal synthesis. The morphology of the

membranes was characterized by X-ray diffraction (XRD), scanning electron microscope (SEM), and electron diffraction spectrometer (EDS) techniques. The transport and separation properties were investigated using pure gas and equimolar CO_2/N_2 mixtures at different feed pressures.

5.2 Experimental Procedures

5.2.1 Membrane supports

The membrane supports, commercial (INSIDE Ceram) ceramic asymmetric porous tubes, were purchased from TAMI Industries (Nyons, France). The tubes came pre-cut to 7 cm and had an outside diameter and a wall thickness of 10 mm and 2 mm, respectively. The active layer of the support was located at the inner side of the tube, and five different pore sizes (0.14, 0.2, 0.45, 0.8 and 1.4 μm) of the active layer were used. The larger pore size supports (0.8 and 1.4 μm) consisted of two layers, the active layer made of pure titanium oxide and the porous support layer made of pure aluminum oxide. The smaller pore size supports (0.14, 0.2 and 0.45 μm), consisted of three layers, the active layer made of a mixture of titanium oxide and zirconium oxide, the intermediate layer made of pure titanium oxide, and the porous mechanical support layer made of pure aluminum.

5.2.2 Membrane preparation

The membrane synthesis scheme used in this work is shown in Fig. 5-1. It was adapted from the procedure developed for the membrane synthesis on flat discs having the same pore size and the same composition of the active layer as the tubes used in this work [25].

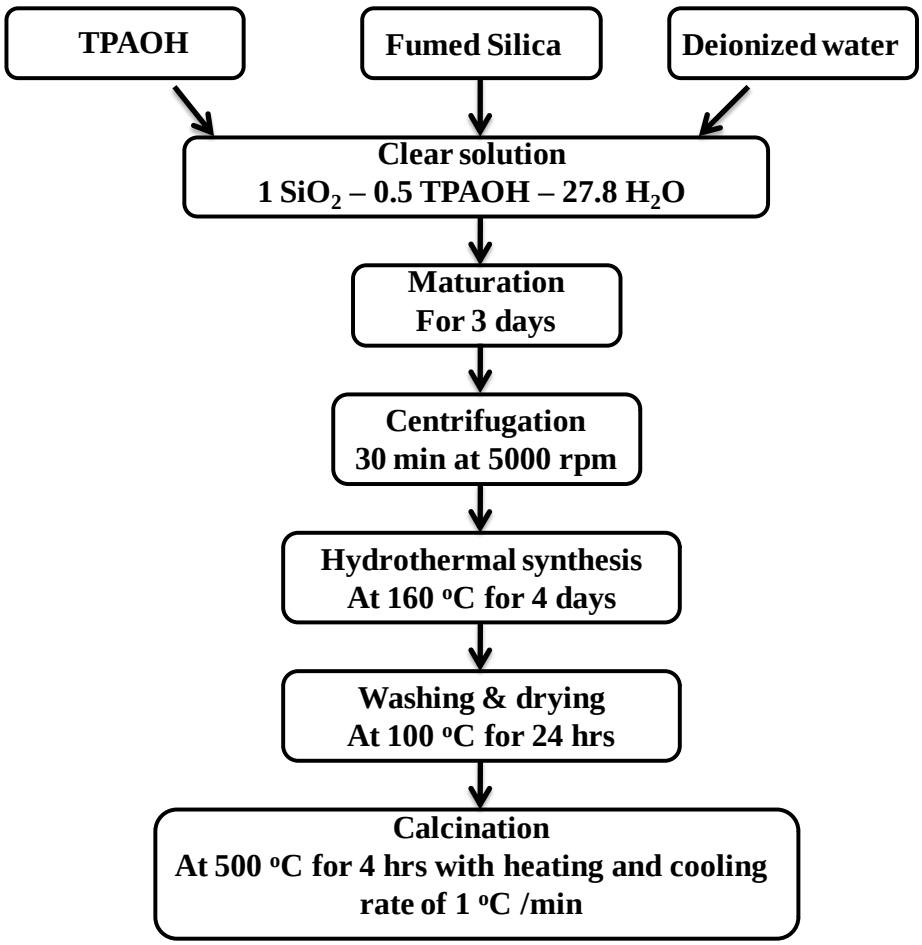

Figure 5-1 Preparation scheme used for silicalite-1 zeolite membranes.

Fumed silica (Sigma-Aldrich, Oakville, ON, Canada) was used as the silicone source. A 5.5 g were dissolved in 46 mL of 1 M tetrapropylammonium hydroxide (TPAOH) (Fluka's Purum, Sigma-Aldrich, Oakville, ON, Canada) solution. The TPAOH/Si mole ratio was chosen to be 0.5. The final concentration of the solution was adjusted by adding deionized water to obtain a 50 mL solution with the following overall molar composition: 1 SiO_2 – 0.5 TPAOH – 27.8 H_2O [22]. The solution was then left under stirring for 3 days at room temperature for maturation. The maturation was followed by subjecting the solution to a

centrifugal device for 30 min at 5000 rpm to remove any large particles that might exist in the solution, which would limit the precursor penetration inside the pores of the support.

The hydrothermal synthesis process was carried out inside a Teflon lined stainless steel autoclave. The autoclave was fitted with a Teflon insert that was specially designed to keep the supports in a vertical position during the hydrothermal synthesis. Keeping the supports in a vertical position is believed to prevent the formed crystals in the solution and the dust from being attached to the support surface [27]. The attached crystals or dust enhanced the crystallization on the surface which in turn limited the precursor penetration inside the pores of the support. It has been also shown in literature that keeping the supports in vertical position improved the zeolite membrane quality prepared by both in situ [28] and secondary growth [29] synthesis methods. The external surface of the supports was covered by a Teflon tape to ensure the growth of the zeolite only at the inside surface of the tubular supports. The zeolite precursor solution was poured into an autoclave containing the supports until the supports were completely immersed in the solution. After 30 min, the level of the solution inside the autoclave was checked and when necessary, more solution was added to compensate for the fraction that had penetrated inside the pores of the support to make sure that the tubular supports were completely immersed in the solution.

The autoclave was then closed and placed in an oven (Vulcan 3-550, Degussa-Ney Dental Inc., Yucaipa, CA, USA), that was preheated to 160^{o}C, for 4 days. After the synthesis, the membranes were removed from the autoclave, and washed with deionized water. The washed membranes were then dried at 100^{o}C for 24 h.

The calcination of the dried membranes was carried out inside a programmable oven (Vulcan 3-550, Degussa-Ney Dental Inc., Yucaipa, CA, USA) at 500^{o}C for 4 hr with a heating and cooling rate of 1.0^{o}C/min. The low heating and cooling rates were chosen to prevent any possible defect formation in the silicalite-1 layer due to the difference in thermal expansion between the silicalite-1 and the supports [17]. The calcination step was performed to remove the templates from the zeolite pores as well as to enhance the bonding between the zeolite layer and the support. After calcination, the samples were kept in a desiccator in dry atmosphere.

The zeolite powder collected from the autoclave Teflon lining wall was washed, calcined, and then kept in a desiccator in a dry atmosphere for further characterization.

5.2.3 Membrane characterization

Morphology and microstructure

The morphology of the silicalite-1 films was studied using scanning electron microscope (SEM) using a JEOL JSM-7500F Field Emission Scanning Microscope (from JEOL, Japan). The microscope is operating with primary electron beams of 2 keV. SEM top view imaging was used in the measurements of the surface coverage, crystals shape, crystals size and crystals size distribution, while the SEM side view images were used in the measurements of films thickness. The samples of the ceramic supports and the synthesized membranes were also analysed for their elemental composition in situ with an electron diffraction spectrometer (EDS) Tracor-Northen Series Z-II spectrometer (Zeiss, Oberkochem, Germany) coupled to the SEM (with roughly 1 μm spatial resolution). The EDS was

operating with primary electron beam of 20 keV accelerating voltages and 8 mm lens distance. The samples analysed by SEM and EDS were mounted on a specimen holder and covered with a conductive carbon tape.

X-Ray diffractometry (XRD) technique was used to examine the crystallinity and the orientation of the silicalite-1 crystals in membranes. This was performed using a Philips PW 3710 diffractometer equipped with Ni-filtered CuKα radiation (λ = 1.54059 Å) operating with a generator voltage of 45 kV and current of 40 mA. The angular range and the step width for the measurements were from 2θ of 0^o – 70^o and 0.03, respectively. The count time for the recording was 10 s per step. The samples were mounted on a specially designed holder. The XRD analyses were also performed using a sample with randomly oriented crystals. This sample was prepared by suspending the powder collected from the autoclave Teflon lining wall in a glycerol gel [30].

Gas permeation experiments

Gas permeation experiments were carried out in a constant pressure (CP) system, which allowed testing two membrane modules simultaneously. The diagram of the CP system showing one of the membrane modules is shown schematically in Fig. 5-2. The insert in Fig. 5-2 shows the details of the membrane module. The tubular membrane was connected to a 1/4 inch (0.635 cm) stainless steel flexible tube using epoxy resin. The membrane with one flexible tube at each end was then installed coaxially inside a 3/4 inch (1.905 cm) stainless steel tube. The tightness of the membrane module was verified with Gas Leak detector (MATHESON, model 8017) using helium before the actual gas permeation tests. The

experiments were carried out in a parallel flow configuration with the feed flowing inside the tubular membrane, the gas permeating through the membrane in the radial direction and the permeate flowing in the shell side of the module. The sweep line was not used. The feed flow rate and the feed composition were controlled by mass flow controllers MFC1 and MFC2 (MKS Instruments Inc., model M100B). All experiments were performed using the same total feed flow rate of 100 cm^3(STP)/min. The retentate and permeate flow rates were measured by a rotameter (RM) (Gilmont Instruments Co., PMR-010752) and a bubble flow meter (BFM) (Hewlett-Packard, model 0101-0113), respectively. The stage cut and the feed pressure were controlled by controlling the flow rate of the retentate using a needle valve (NV) (8-turn inter-changeable valve, Gilmont Instruments Co.). In other words, the feed pressure was coupled with the stage cut. The feed, retentate and permeate pressures were measured by a high accuracy pressure transducers (PT) (Cole-Parmer, Model 68075). A gas chromatograph (GC) (GOW-MAC Instruments Co., 40 series, Model 40-250) equipped with an 80x100 mesh Porapak Q column and a thermal conductivity detector (TCD) with helium as a carrier gas was used on-line to analyze the composition of the permeate and the retentate streams. In addition, the composition of the feed was verified using the GC prior and during the actual gas permeation experiments.

All membranes synthesized in this work were tested with single N_2 and CO_2 gases as well as with their equimolar mixture. The single and mixed gas permeation experiments were carried out at the total feed pressure up to 4.0 atm (absolute). In addition, one of the membranes synthesized using the support with 0.45 μm pore size was tested with single He, H_2, CH_4 and C_3H_8 gases at the feed pressure of 2 atm (absolute). The tests with He, N_2, H_2,

are CH_4 (low adsorbing gases) were carried out for 6 hours, while those with CO_2 and C_3H_8 (high adsorbing gases) for 24 hours to make sure that the system reached steady-state. The tests with mixed CO_2/N_2 feed were carried out for longer periods (48 hours) to give the system a chance to reach steady-state. After completion of the permeation tests with a given feed gas, the membranes were regenerated with pure He at the feed pressure of 2 atm (absolute) for 12 h before switching to another feed gas. All gas permeation tests as well as membrane regenerations were carried out at ambient temperature (~23ºC).

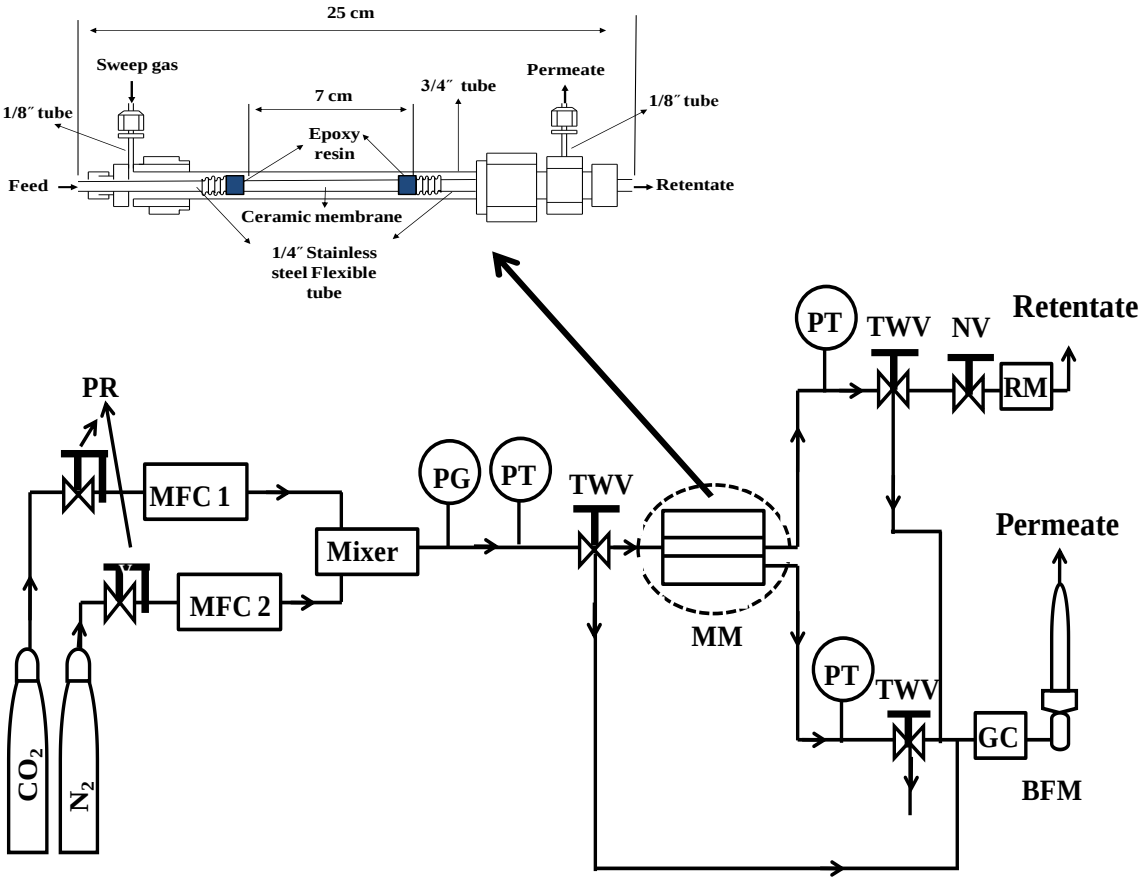

Figure 5-2 Gas permeation/separation setup (BFM: bubble flow meter, GC: gas chromatograph, MFC: mass flow controller, MM: membrane module, NV: needle valve PG: pressure gauge, PR: pressure regulator, PT: pressure transducer, RM: rotameter, TWV: three way valve).

Analysis of gas permeation experiments

The gas permeation tests allowed characterizing the synthesized membranes on the basis of the gas permeance and the permeance ratio. For gas *A*, the gas permeance (P_A), which is a measure of membrane productivity, is determined based on the steady state permeation rate of component A (V_A), the component A partial pressure difference across the membrane (Δp_A), and the membrane area (A_M):

$$P_A = \frac{V_A}{A_M \Delta p_A} \tag{5.1}$$

The selectivity of the membrane for separation of gases *A* and *B* is then evaluated based on respective gas permeances:

$$\alpha^*_{A/B} = \frac{P_A}{P_B} \tag{5.2}$$

In the case of single gas permeation tests the partial pressure difference is equal to the total pressure difference through the membrane, which is a measurable parameter, and hence the gas permeance and the corresponding permeance ratio are readily calculated from Eqs. (5.1) and (5.2), respectively. The permeance ratio based on single gas permeation tests is referred to as the ideal selectivity. In the case of gas permeation tests with a gas mixture and nonzero stage cut ($\theta > 0$), the recovery of the individual gas permeances and the permeance ratio requires an elaborative numerical procedure. The permeance ratio based on a mixed gas permeation test is referred to as the permselectivity. To recover the gas permeances and the

permselectivity from mixed gas permeation tests we have adapted the procedure presented in reference [31], which is described next.

Fig. 5-3 presents a schematic diagram of binary gas mixture permeation in a parallel flow membrane module, highlighting the transport in one differential element. The feed flow rate and the composition are L_f and x_f, respectively, where x, is the mole fraction of the more permeable component (i.e., CO_2) at the high pressure side of the membrane, for which the total pressure, p_h, is constant. The corresponding retentate flow rate and the retentate composition are L_o and x_o, respectively, while the corresponding permeate flow rate and the permeate composition are V_p and y_p, respectively. The total pressure at the low pressure side, p_l, is also constant. Since both the feed and permeate are in plug flow, the flow rate and the composition at the high pressure side (L and x) and at the low pressure side (V and y) vary along the module. The membranes used in this work were cylindrical. However, it will be shown later in Section (5.3.2) that the thickness of the selective layer of the membranes was at most 5 - 6 μm, which is very small compared to the inner diameter of the membranes (c.a. 6 mm). Consequently, it is justified to treat all the membranes synthesized in this work as flat sheet membranes and use rectangular geometry for the treatment of the membrane.

It can be shown that the changes in gas composition on both sides of a flat sheet membrane in parallel flow configuration are coupled by the following equation [31]:

$$\frac{dy}{dx} = \frac{\left(y - x_f\right)\left\{\left(1-y\right)\alpha^*_{A/B}\left(x - ry\right) - y\left[\left(1-x\right) - r\left(1-y\right)\right]\right\}}{\left(x - x_f\right)\left\{\left(1-x\right)\alpha^*_{A/B}\left(x - ry\right) - x\left[\left(1-x\right) - r\left(1-y\right)\right]\right\}} \tag{5.3}$$

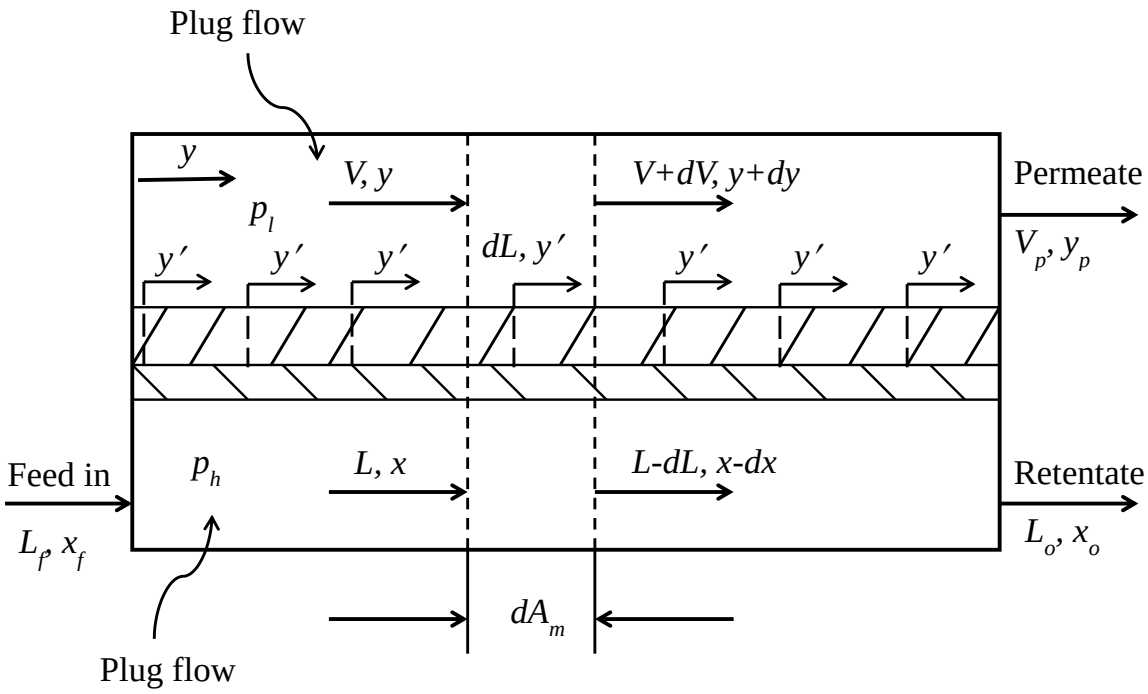

Figure 5-3 Permeation of a gas mixture in a parallel flow configuration membrane module (Adapted from reference [31]).

where $r = p_l/p_h$. The composition profile at the low pressure side of the membrane is obtained by numerical integration of Eq. (5.3) from the inlet (x_f) to the outlet (x_o) of the module using a step dx. Both x_f and x_o are measured during the experiment, while dx is chosen according to the desired precision for the numerical integration. For a differential element i, in which the composition of the gas at the high pressure side leaving the element is x_i, the corresponding composition of the gas at the low pressure side leaving the element i is calculated by:

$$y_i = y_{i-1} + \left.\frac{dy}{dx}\right|_{x_{i-1}} dx \tag{5.4}$$

where the subscript i -1 refers to the previous element, i.e., $x_i = x_{i-1} - dx$. Eq. (5.3) is applicable for the evaluation of dy/dx in any element of the module except for the first one, in which $x_{i-1} = x_f$, and the denominator is zero. Using L'Hospital's rule the numerator and denominator of Eq. (5.3) are di-fferentiated with respect to x, which leads to the following expression:

$$\left.\frac{dy}{dx}\right|_{x_f} = \frac{\left(y_f - x_f\right)\left[\alpha^*_{A/B} - y_f\left(\alpha^*_{A/B} - 1\right)\right]}{\left\{\alpha^*_{A/B}\left(1-x_f\right)\left(x_f - ry_f\right) - x_f\left[\left(1-x_f\right) - r\left(1-y_f\right)\right] - \left(y_f - x_f\right)\left[\left(\alpha^*_{A/B} - 1\right)\left(2ry_f - x_f - r\right) - 1\right]\right\}} \tag{5.5}$$

Application of Eq. (5.5) requires the knowledge of y_f, i.e., the composition of permeate corresponding to the composition of feed, x_f. Rearranging Eq. (5.1) and expressing the partial pressure difference in terms of mole fractions, the rate equations for the transport of A and B at the module entrance are given by:

$$dV_A = dVy_f = P_A\left[p_h x_f - p_l y_f\right]dA_M \tag{5.6}$$

$$dV_B = dV\left(1-y_f\right) = P_B\left[p_h\left(1-x_f\right) - p_l\left(1-y_f\right)\right]dA_M \tag{5.7}$$

were V_A and V_B are the steady state permeation rate of component A and B, respectively. Dividing Eq. (5.6) by Eq. (5.7) and after rearrangements leads to:

$$\frac{y_f}{1-y_f} = \frac{\alpha^*_{A/B}\left(x_f - ry_f\right)}{\left(1-x_f\right) - r\left(1-y_f\right)} \tag{5.8}$$

Eq. (5.8) is a quadratic equation in terms of y_f, and has two roots, but only one makes physical sense. Performing the numerical integration procedure for Eq. (5.3) from x_f to x_o, as explained earlier, should yield y_p at the outlet of the module, which is measured during the experiment.

The numerical integration procedure described above is equivalent to one equation, in which there are two unknowns, P_A and P_B. Therefore, determination of the unknown permeances requires another independent equation. It can be shown that a differential membrane area (dA_M) over which the composition at the high pressure side changes by dx is given by [31]:

$$\frac{dA_M}{dx} = \frac{L_0}{P_B p_h} \frac{\left[\left(y - x_f\right)/x - y\right]}{\left\{(1-x)\alpha^*_{A/B}(x - ry) - x\left[(1-x) - r(1-y)\right]\right\}} \tag{5.9}$$

The numerical integration of Eq. (5.9) from x_f to x_o using the previously determined relationship between y and x (Eq. 5.5) allows obtaining the total membrane area (A_M), which is known. Therefore, performing simultaneously the numerical integrations to determine $y = f(x)$ and A_M provides two independent equations from which P_A and P_B can be calculated.

5.3. Results and Discussion

5.3.1 SEM and EDS analyses

The external morphology, crystalline structure (shape and size), distinct layers, thickness and chemical composition of the synthesized membranes were investigated using SEM and EDS.

Fig. 5-4 shows the SEM micrographs of the top surface of synthesized membranes. It is evident that regardless of the pore size of the support, coffin shape crystals appear to be randomly distributed on the top surface of each membrane. This shape is a characteristic for the silicalite-1 crystals [32]. The size of the crystals ranges between 0.7 and 3 μm. Except for the membranes prepared using 0.8 and 1.4 μm pore size supports (hereafter the membranes will be called by the pore size of their supports' active layer, i.e. the membrane prepared using the 0.8 μm pore size support will be called the 0.8 μm membrane), the crystals appear to be completely covering the surface of the supports. It should be emphasized that although the crystals are primarily formed inside the pores of the support during the pore plugging synthesis, they can also be formed on top of the support, in particular when the pores are already plugged [25]. To further investigate the morphology of the synthesized membranes, Fig. 5-5 presents the SEM micrographs of their cross-sections.

It is evident from Fig. 5-5 that a continuous layer of silicalite-1 crystals on top of the membrane is evident in the cross-sections of the 0.14, 0.2 and 0.45 μm supports. The respective average thicknesses of this layer are 1.2, 1.4 and 2.0 μm. In the case of the cross-sections of the 0.8 and 1.4 μm membranes there is no continuous zeolite layer. This was expected because of their incomplete coverage evident in Fig. 5-4. In general, the effect of pore size on the formation of continuous layer and its uniformity observed in this study is consistent with the literature findings [33,34].

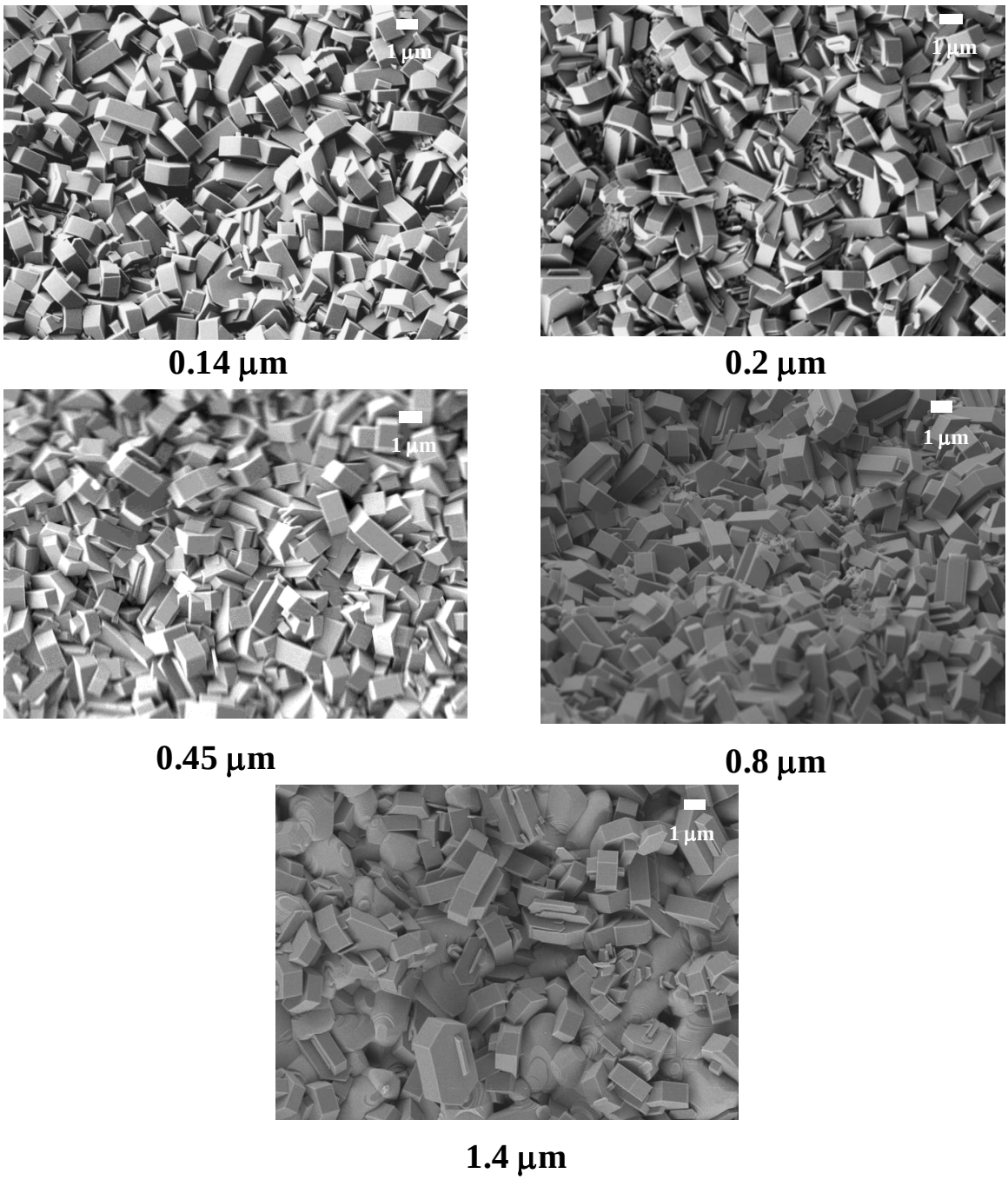

Figure 5-4 Surface SEM micrographs of synthesized membranes on supports with different pore sizes of the active layer as indicated below each micrograph.

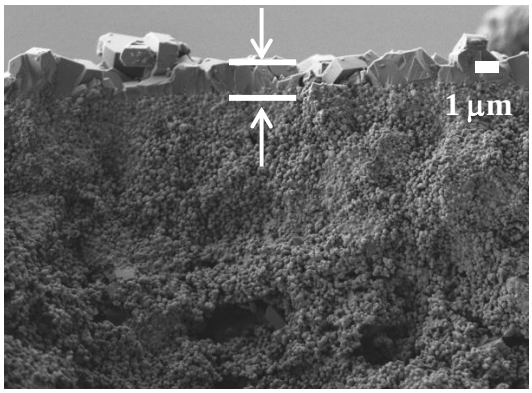

0.14 μm

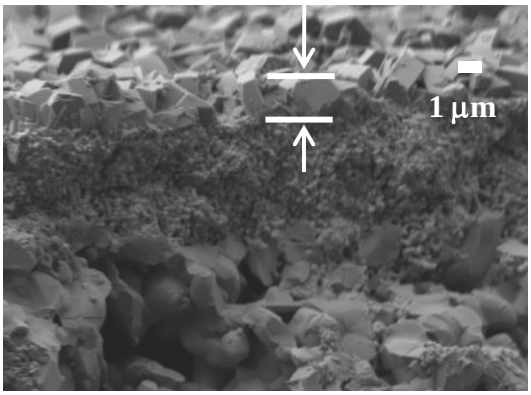

0.2 μm

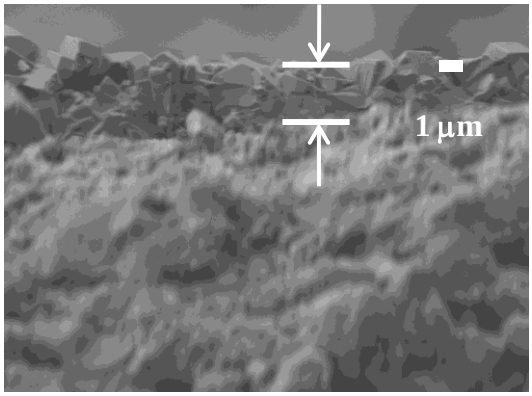

0.45 μm

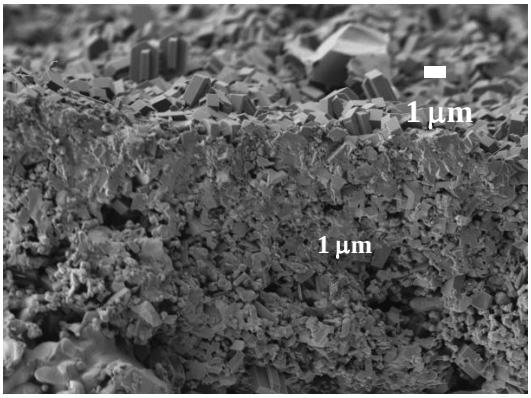

0.8 μm

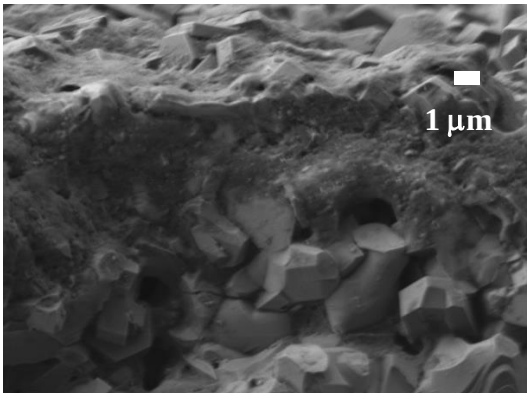

1.4 μm

Figure 5-5 Cross-section SEM micrographs of synthesized membranes for supports with different pore sizes as indicated below each micrograph.

In addition to a continuous or non-continuous silicalite-1 layer on top of the support, individual silicalite-1 crystals can also be observed 5 – 10 μm away from the top surface, in particular, in the case of the membranes prepared with supports that have larger pore-sizes. It is important to note that there appear to be no silicalite-1 crystals inside the pores of the active layer (according to the manufacturer, regardless of the pore size of the support, the thickness of the active layer is approximately 5 μm). On the other hand, any silicalite-1 crystals inside the pores of the active layer would be much smaller than those seen on top of the membranes in Fig. 5-4 that could prevent observing them at current resolution of SEM.

The actual proof for the formation of silicalite-1 crystals inside the pores of the active layer of the supports is provided by the EDS analyses. Fig. 5-6 shows the concentration of silicon as a function of the distance from the top surface of the membrane, as determined by the EDS analyses.

As expected, the concentration of Si decreases with the distance from the top surface of the membrane. The concentrations measured at 1 μm from the top surface ranges from 75% for the 0.8 μm membrane to 93% for the 0.45 μm membrane. In general, the concentration of Si in the smaller pore size membranes (0.14 μm, 0.20 μm, 0.45 μm) is clearly greater than that in the large pore size membranes (0.8 μm, 1.4 μm). This is consistent with the observed continuous zeolite layer on top of the smaller pore size membranes (Figs. 5-4 and 5-5). As the distance from the surface increases, there is a crossover in the Si concentrations between the smaller and the larger pore-size membranes. At the position of 5 μm from the top surface, the concentration of Si in the large pore size membranes is greater than that in the

smaller pore size membranes. More specifically, the Si concentration ranges from 30% for the 0.14 μm membrane to 60% for the 1.4 μm membrane. These high concentrations of Si 5 μm from the membrane surface would not be possible without formation of the silicalite-1 crystals in the active layer of the supports. This is further reinforced by the fact that according to the manufacturer, regardless of the pore size, the active layers had a relatively small porosity of approximately 23%.

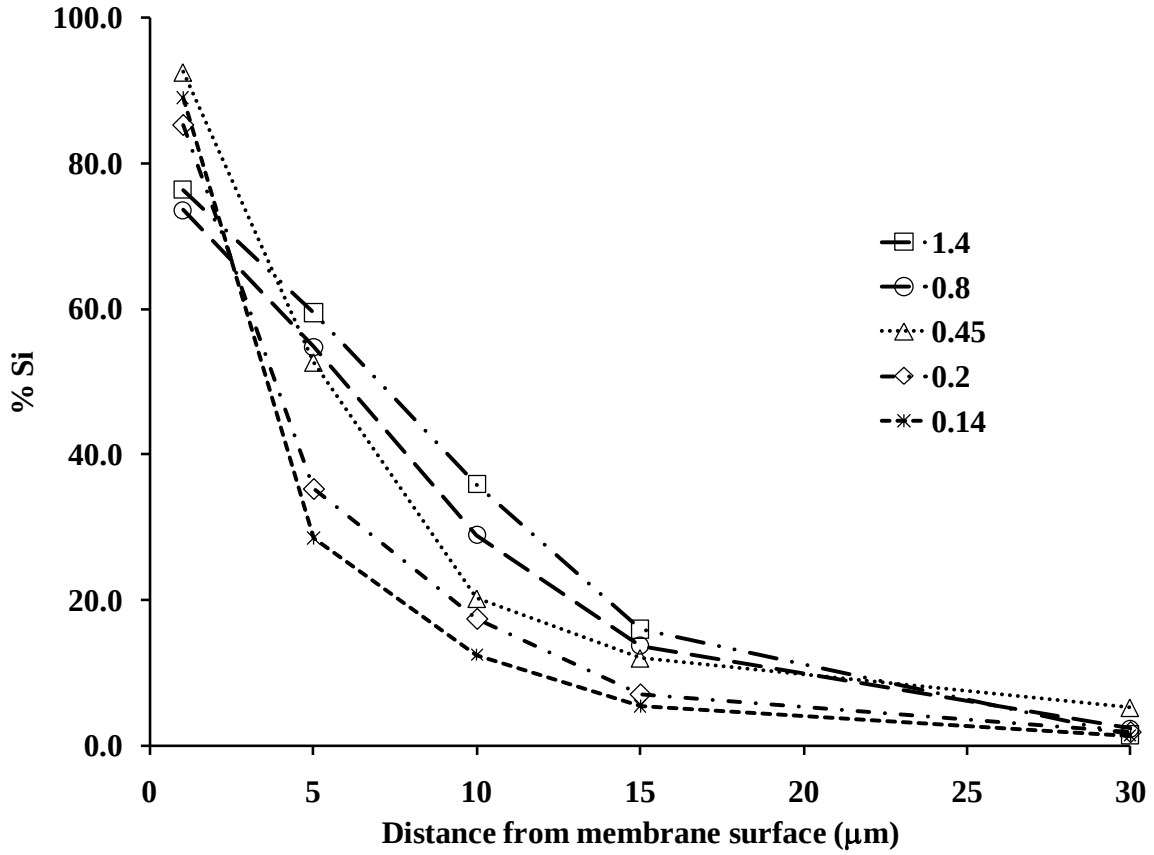

Figure 5-6 Distribution of silicone, as determined by the EDS analyses, from the membrane surface for supports with different pore size of the active layer; the dashed lines are a guide to the eye.

Based on that, greater concentrations of Si 5 μm from the top surface in the larger pore-size membranes (0.8 μm, 1.4 μm) may indicate more complete pore plugging of the active layer of these membranes. However, it should be kept in mind that for the smaller pore size membranes, and because of the continuous 1 – 2 μm zeolite layer on top of the support, the position 5 μm falls within the low-porosity active layer. On the other hand, 5 μm from the top surface of the larger pore size membrane (without a continuous zeolite layer) represents an interface between the low porosity active layer and a porous support, which could accommodate higher concentrations of silicalite-1 crystals. It should be pointed out that the concentrations of Si 10 μm from the top surface and further down are still quite high, in particular for the larger pore size membranes. However, considering that the supports beyond the active layer are very porous, the silicalite-1 crystals beyond the active layer are not expected to provide any selective properties for the synthesized membranes.

5.3.2 XRD analyses

To further investigate the morphology and the structure of the synthesized zeolite crystals, the membranes along with a powder collected from the autoclave lining were analyzed using XRD technique. The XRD patterns of all synthesized membranes, shown in Fig. 5-7, have peaks at $2\theta \approx 9^o$ and $2\theta \approx 24^o$, which correspond to silicalite-1 [35]. In addition, the XRD patterns confirm different compositions of the supports with large (0.8 and 1.4 μm) and small (0.14, 0.2 μm, 0.45 μm) pore sizes. The latter have three extra peaks at $2\theta \approx 31^o$, 33^o, 51^o and 61^o, which are the characteristics of zirconia [36]. On the other hand, the characteristics of titania peaks at $2\theta \approx 27^o$, 36^o, 55^o, 57^o, 64^o [37], and two small peaks at $2\theta \approx 42^o$ and 69^o, which are believed to originate from the alumina layer under the titania and

zirconia layers, appear in all patterns. Larger 2 pore size supports did not contain zirconia in the active layer.

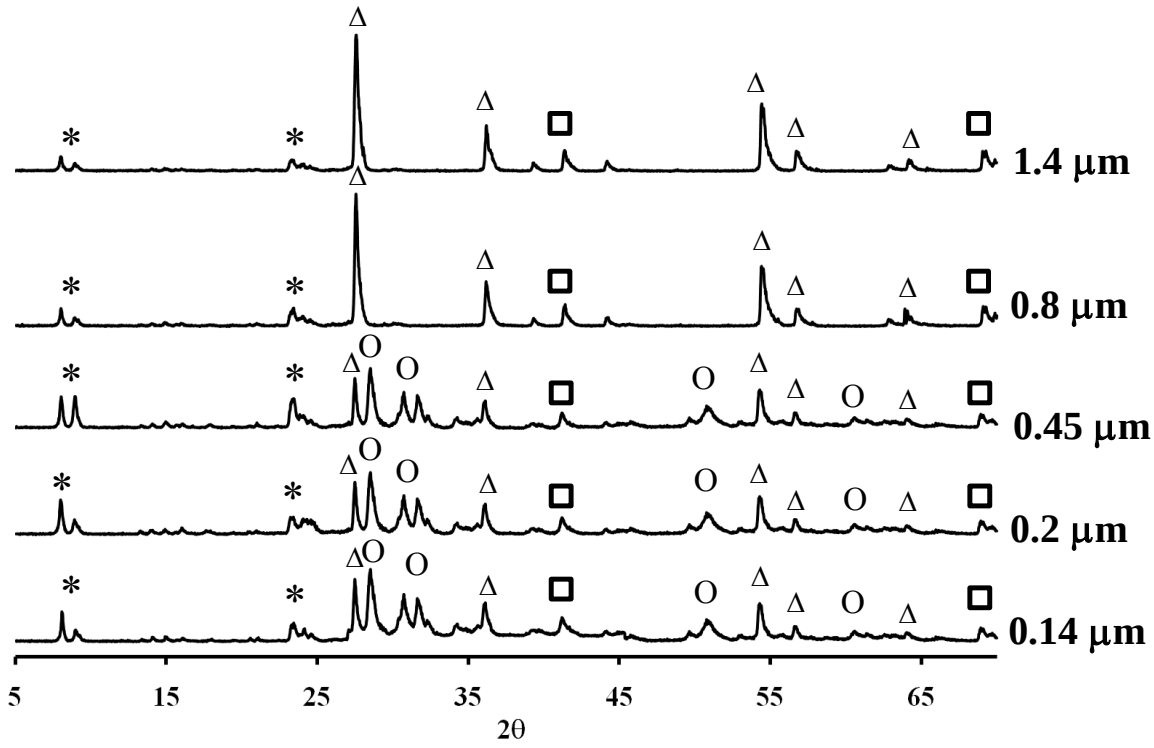

Figure 5-7 XRD patterns obtained for five supports with different pore sizes after growing the zeolite by the pore plugging method, where: ∗, Δ, O, and □ are are corresponding to the peaks of silicalie-1, titania, zirconia and the alumina, respectively.

Fig. 5-8 presents the patterns from Fig. 5-7 zoomed in a 2θ region between 5° and 27°, which is dominated by the silicalite-1 peaks. It is evident that the relative intensities of the silicalite-1 peaks differ depending on the pore size of the support. As a reference, Fig. 5-9 presents the XRD pattern of powder collected from the autoclave lining wall that was suspended in a glycerol gel. Such a prepared sample is assumed to have randomly oriented crystals [30]. Since the patterns in Fig. 5-8 are different from the reference pattern in Fig. 5-

9, it can be immediately concluded that the silicalite-1 crystals in the membranes are not randomly oriented. This may appear to contradict the apparently random distribution of the silicalite-1 crystals seen on the SEM micrographs shown in Fig. 5-4. On the other hand, it should be remembered that silicalite-1 crystals were primarily formed inside the pores of the active layer, which could not be directly observed by the SEM. At the same time, it is well known that XRD penetration depth could be up to hundreds of microns, and consequently the crystal in the pores of the active layer contributed to the patterns shown in Fig. 5-8.

A single silicalite-1 crystal, (top left in Fig. 5-9) consists of sinusoidal channels along the (100) axis (crystallographic a-axis) that are interconnected with the straight channels along the (010) axis (crystallographic b-axis). There are no direct channels on the (001) axis (crystallographic c-axis) [38,39]. From the practical point of view, it would be preferable to have silicalite-1 crystals with either the a- or b-axes perpendicular to the support surface of the membrane since straight channels will be easier for gas molecules to go through. In particular, the latter orientation would minimize the resistance to gas transport through the crystals. In the case of a secondary growth synthesis method, it is possible to control the orientation of zeolite layer by controlling the orientation of seeds on the support surface [40]. On the other hand, pore plugging method used in this work does not offer this advantage. Nevertheless, as already stated based on comparison of Fig. 5-8 with Fig. 5-9, the silicalite-1 crystals inside the pores of the active layer are not randomly oriented. A question arises, what is their orientation?

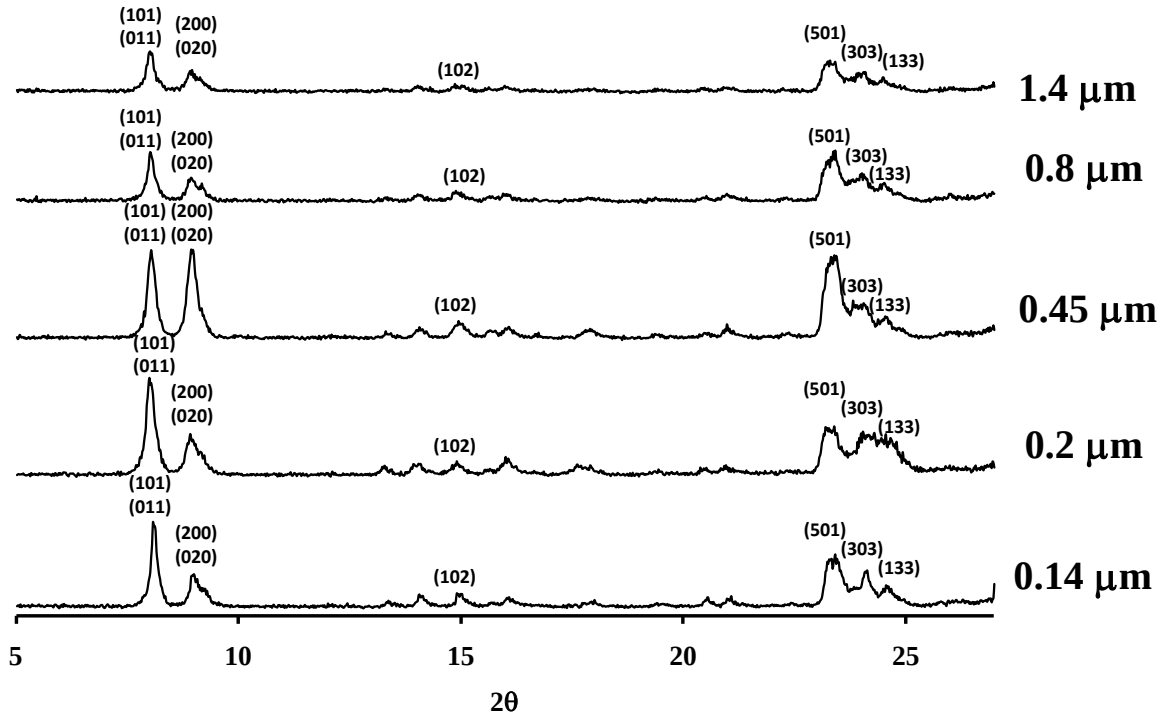

Figure 5-8 XRD patterns of the five supports in the 2θ region between 5º and 27º after growing the zeolite by the pore plugging method.

The crystallographic preferred orientation (CPO) of the silicalite-1 crystals in the synthesized membranes can be determined by comparing the relative intensities of peaks (*I*) that are representative for the specific crystallographic axes with the corresponding intensities of these peaks in a randomly oriented powder [41]:

$$\mathrm{CPO}\frac{(X)}{(Y)} = \frac{\left(\frac{I_S^{(X)}}{I_S^{(Y)}} - \frac{I_P^{(X)}}{I_P^{(Y)}}\right)}{\frac{I_S^{(X)}}{I_S^{(Y)}}} \tag{5.10}$$

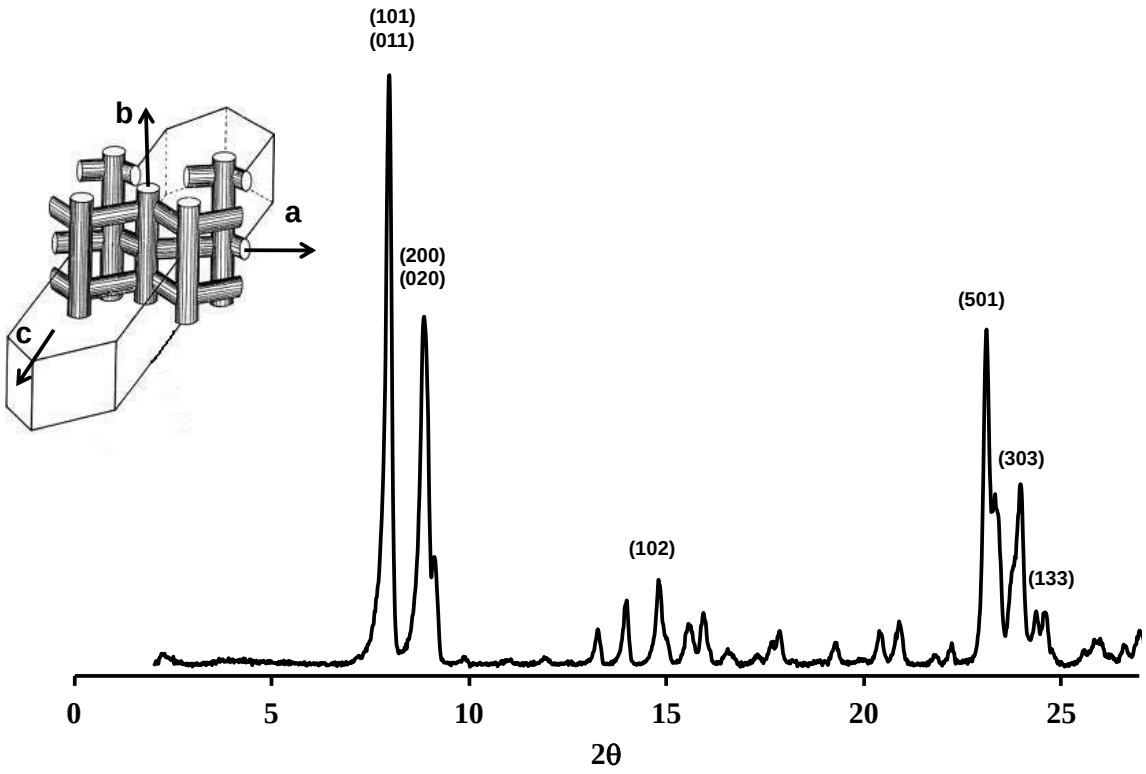

Figure 5-9 XRD pattern obtained for a random sample prepared from the zeolite powder collected from the autoclave lining wall. The top left insert shows a silicalite-1 crystal with the crystallographic faces and axes [5].

The superscripts (*X*) and (*Y*) refer to the representative peaks for two different crystallographic axes, while the subscripts *P* and *S* refer to the randomly oriented powder and the silicalite-1 membrane, respectively. It follows from Eq. (5.10) that if the synthesized membrane possessed randomly oriented crystals, the corresponding CPO would approach zero. On the other hand, if the synthesized membrane had crystals with a specific orientation, the CPO would approach unity (if the intensity of the X peak in the powder were zero), or a large negative number (if the intensity of the X peak in the sample were zero).

Theoretically, the CPO could be calculated using any two representative peaks, or a combination of peaks. However, from a practical point of view it is not suitable to use low intensity peaks. The peaks (200) and (020), which arise from the crystals having the preferred orientations along the a- and b-axes, respectively, cannot be separated. However, their combined intensity, (200)+(020), can be compared with the intensity of the (133) peak, which is indicative of the crystals with the c-axis at 35^{o} from the normal to the membrane surface [42]. The calculated CPO [(200)+(020)]/(133) values for all membranes are summarized in Table 5-1. It can be noticed that they range from 0.71 for the 1.4 μm membrane to 0.92 for the 0.45 μm membrane. This indicates that the latter membrane has the largest fraction of the crystals that are preferably oriented with either a- or b-axes perpendicular to the membrane surface. However, even in the 1.4 μm membrane and hence in all the other membranes the silicalite-1 crystals are preferably oriented with either the a- or b-axes perpendicular to the membrane surface.

To distinguish between the crystals with the a-axis perpendicular to the membrane surface from those with the b-axis perpendicular to membrane support surface, the CPO (501)/(133) values were determined. The intensity of the (501) peak is indicative of the crystals with the crystallographic b-axis that is parallel to the surface of the membrane, and thus with either a-axis or c-axis perpendicular to the membrane surface. Since it was already concluded that the crystals for all the membranes are preferably oriented with either the a- or b-axes perpendicular to the surface, the smaller the CPO (501)/(133) value, the more crystals with the b-axis perpendicular to the membrane surface compared to those with the a-axis perpendicular to the membrane surface. Therefore, for gases to pass through the membrane

easier, a smaller CPO (501)/(133) is preferred. These CPO values are summarized in Table 5-1. It can be noticed that except for the 0.45 μm membrane, the CPO (501)/(133) values are relatively constant ranging from 0.22 to 0.24. For the 0.45 μm membrane this value jumps to 0.58. Although, the 0.45 μm membrane has the highest fraction of the crystals that are preferably oriented with either the a- or b-axes perpendicular to the surface, which is desirable because of minimizing the resistance to gas transport, it also has a much higher contribution of the crystal with sinusoidal channels perpendicular to the surface compared to the other membranes. Since it would be most desirable to have the largest fraction of the crystal with the straight channels perpendicular to the surface, it cannot be concluded that the 0.45 μm membrane shows the most favorable morphology despite the largest CPO [(200)+(020)]/(133) value among the membranes synthesized in this work.

It is beyond the scope of this paper to understand the combined effect of the pore size and the chemistry on the orientation of the crystals in the pores of the active layer. However, it is important to emphasize that despite the absence of seeds that could control the orientation of the crystals formed in the pore plugging synthesis, the CPO values listed in Table 5-1 are comparable to those reported for the silicalite-1 membranes synthesized by the secondary growth method [11,42,43].

5.3.3 Gas permeation

Figure 5-10 presents the effect of the kinetic diameter of the penetrant on gas permeance for the membrane with 0.45 μm pore size support. The permeances reported in Fig. 5-10 were determined from the respective single gas permeation tests at the total pressure difference

across the membrane of 1 atm and ambient temperature. It is evident that the observed permeances are not correlated with the kinetic diameter of the penetrant, which was expected considering that the kinetic diameter of all tested gases was considerably smaller than the pore size of silicalite-1 crystals (5.5 Å). The highest permeance of 1.9 x 10^{-6} mol m^{-2} Pa^{-1} s^{-1} was observed for CO_2 while the lowest of 3.8 x 10^{-7} mol m^{-2} Pa^{-1} s^{-1} for CH_4. This large difference between permeances of CO_2 and CH_4 is attributed not only to the difference in their kinetic diameters (3.3 Å for CO_2 versus 3.8 Å for CH_4), but also to the difference in their adsorption capacities on silicalite-1.

Table 5-1 CPO and SEM main results.

Support pore size (μm)	CPO [(200)+(020)]/(133)	CPO (501)/(133)	Zeolite layer thickness (μm)
0.14	0.76	0.23	1.2
0.20	0.81	0.22	1.4
0.45	0.92	0.58	2.0
0.80	0.77	0.23	0.8
1.40	0.71	0.24	-

The comparison of single gas permeances provides information about the ideal selectivity of the membrane for a given pair of gases. In this work we were particularly interested in separation of CO_2/N_2 mixtures, which is of fundamental importance for capturing of CO_2 from flue gases. Based on Fig. 5-10, the ideal CO_2/N_2 selectivity of the membrane with 0.45 μm pore size support is 1.7.

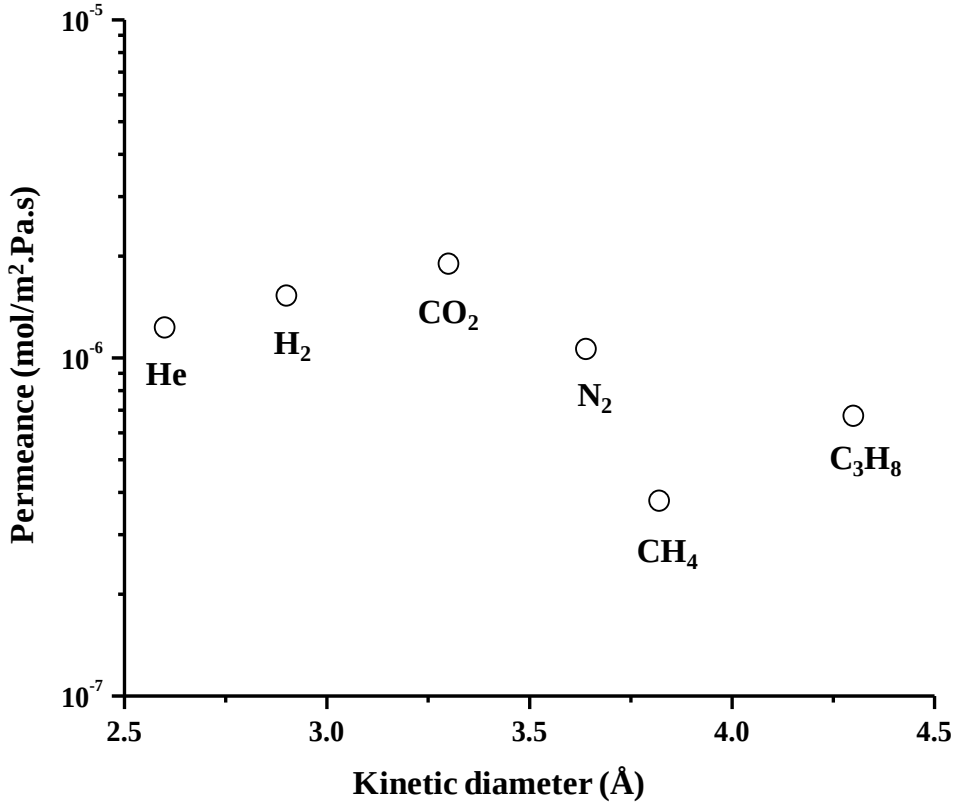

Figure 5-10 Gas permeance as a function of the kinetic diameter of the penetrant. Single gas permeation tests at 1 atm pressure difference and ambient temperature (293 K) on silicalite-1 membrane synthesized using 0.45 μm support.

The effect of the pressure gradient on single gas permeances of CO_2 and N_2 for all membranes is summarized in Fig. 5-11. It can be noticed that except for the 0.14 μm membrane, the N_2 permeance (as shown as open symbols in Fig. 5-11), appears to be independent of the pore size of the support and the feed pressure. The N_2 permeance of the 0.14 μm membrane is one order of magnitude greater than that of membranes synthesized using larger pore-size supports and one order of magnitude lower than that of supports before the zeolite synthesis [25]. Moreover, the N_2 permeance of this membrane is

comparable to its CO_2 permeance. This suggests the existence of the incomplete plugging of the 0.14 μm membrane pores. The latter is consistent with the results presented in Fig. 5-9, which show that among all membranes, the 0.14 μm membrane had the lowest percent of Si inside the pores of its active layer. At the same time, this suggests that the silicalite-1 layer observed on top of the 0.14 μm membrane (Figs. 5-4 and 5-5) is not selective despite its appearance of being continuous. This confirms the fact that the silicalite-1 layer on top of the membrane does not contribute much to the separation of these 2 gases.

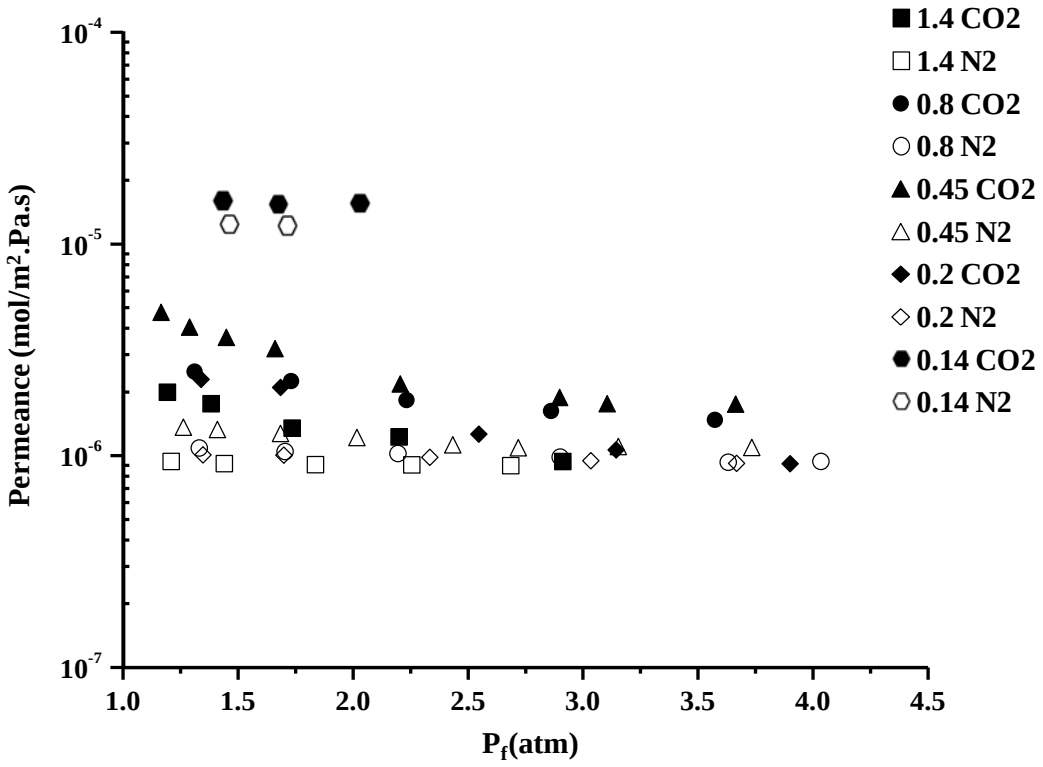

Figure 5-11 Single gas CO_2 and N_2 permeances through silicalite-1 membranes synthesized on supports with different pore sizes of the active layer at different total feed pressures. All experiments performed at ambient temperature (293 K) with permeate side open to atmosphere.

For the membranes synthesized using supports with pore sizes of 0.2 – 1.4 μm, the CO_2 permeance (the closed symbols in Fig. 5-11) decreases with increasing the feed pressure from about 4.8 x 10^{-6} to 1.0 x 10^{-6} mol m^{-2} Pa^{-1} s^{-1}. This effect is particularly clear at very low feed pressures. A decrease in the CO_2 permeance with feed pressure is due to the shape of the CO_2 adsorption isotherm with silicalite-1 (type I isotherm - concave down) [26]. In other words, in the range of feed pressures considered in this work, an increase in the surface occupancy by CO_2 is not directly proportional to the CO_2 pressure. It is important to highlight that the single gas permeances through the supports without the pore plugging with silicalite-1, were around 1.5 x 10^{-4} mol m^{-2} Pa^{-1} s^{-1}, regardless of the feed pressure and the pore size of the support.

The CO_2 permeances observed in this work are comparable to the values reported in the literature by Algieri et al. [44] for silicalite-1 membranes prepared using alumina support, but they are more than one order of magnitude greater than the CO_2 permeances reported by Zhu et al. [45], Bakker et al. [16] and Burggraaf et al [46]. These CO_2 permeances are also more than one order of magnitude greater than those we have reported previously for the silicalite-1 membrane that was synthesized using similar protocol, however without ensuring a perfect vertical position for the tubular support in the autoclave [26]. It appears that vertically positioned supports during hydrothermal synthesis promote preferential orientation of the MFI crystals with either the a- or b-axes perpendicular to the membrane surface. In turn, in these orientations, the resistance to gas transport through the MFI crystals is minimized. Considering the effect of pore-size of the support, it appears that the 0.45 μm

membrane is more permeable than the 1.4 μm membrane, but there is no clear trend between the CO_2 permeance and the pore size of the support.

Unlike the CO_2, the N_2 permeances are nearly constant for all membranes regardless of the feed pressure. It is important to emphasize that in the range of feed pressures considered in this work, the N_2 adsorption isotherm on silicalite-1 is linear [26]. Consequently, the changes in the N_2 surface occupancy are directly proportional to the pressure. In turn, the ideal CO_2/N_2 selectivity decreases with feed pressure from about 3 to unity (no selectivity).

The actual separation potential of the synthesized membranes was assessed based on gas permeation experiments with equimolar mixtures of CO_2 and N_2 at different feed pressures. All experiments were performed using the same feed flow rate of 100 cm^3(STP)/min, and consequently, the stage cut was controlled by the total feed pressure. In the case of the 0.14 μm membranes, virtually all feed permeated across the membranes at the total feed pressure of 1.35 atm while the resulting retentate had the composition similar to that of the feed. This confirmed no selectivity of the 0.14 μm membrane. It is important to note that altogether three membranes were synthesized using 0.14 μm support, and none of them showed any CO_2/N_2 selectivity. Therefore, the 0.14 μm membrane is not considered in the subsequent discussion.

In general, the membranes synthesized using larger pore-size supports were also very permeable. Except for the 0.2 μm membrane, the stage cut of unity was observed at the total feed pressure of 3 atm. In the case of the 0.2 μm membrane at 3 atm, the stage cut was 0.90.

At stage cuts greater than 0.9, the retentate stream contained more than 85% of N_2, which indicates that the membranes were selective.

The CO_2 and N_2 permeances from mixed gas permeation experiments were determined using the procedure discussed in the experimental section. This procedure relies on the assumption that the permeances of the individual components are independent of the feed and the permeate compositions. In the case of high stage cut permeation experiments the compositions of the feed and permeate varied considerably along the membrane because of a plug flow at both sides of the membrane.

Fig. 5-12 summarizes the effect of the total feed pressure on the CO_2 and N_2 permeances for all synthesized membranes using the supports with pore sizes ranging from 0.2 μm to 1.4 μm, for equimolar feed composition. The N_2 permeances (shown as empty symbols in Fig. 5-12), which range from 1.0×10^{-7} to 4.7×10^{-7} mol m^{-2} Pa^{-1} s^{-1}, are one order of magnitude lower than those from single gas permeation experiments shown in Fig 5-11. The reduction in the N_2 permeance of zeolite membrane in the presence of CO_2 is a well-known phenomenon. It results from a preferential adsorption of CO_2 on silicalite-1. The pore size of silicalite-1 (5.5 Å) is much larger than the kinetic diameter of CO_2 (3.3 Å), the preferentially adsorbed CO_2 molecules effectively block the N_2 molecules from entering the pores of the membrane. On the other hand, the CO_2 permeance in the presence of N_2, which ranges from 1.6×10^{-6} to 9.0×10^{-6} mol m^{-2} Pa^{-1} s^{-1}, appears to be greater than that from the single gas permeation tests. It should be emphasized that permeances in Fig. 5-12 are plotted versus the total feed pressure. Considering that at a high stage cut, the retentate contained more than

85% N_2, the actual partial pressure of CO_2 at the high pressure side of the membrane was only a fraction of the indicated total feed pressure. As shown in Fig. 5-11, the CO_2 permeance increases with a decrease in the CO_2 pressure. Consequently, the apparent increase in the CO_2 permeance in the presence of N_2 is not as great as it may appear when comparing Fig. 5-12 with Fig. 5-11. Nevertheless, the presence of N_2 enhances the CO_2 permeance in the silicalite-1 membranes synthesized in this study, which is desirable from the point of view of CO_2/N_2 separation. The reasons for this phenomenon are beyond the scope of the current paper, but it should be emphasized that similar behavior was also reported by Li and Fan for SAPO-34 membrane [47].

Similarly to the single gas permeation tests, CO_2 permeance decreases with the total feed pressure, and the membrane synthesized using 1.4 μm support appears to be least permeable at a given total feed pressure among the membranes prepared in this study. On the other hand, the 0.45 μm and 0.8 μm appear to be more permeable. Although the N_2 permeances from mixed gas permeation tests vary considerably, they are generally independent of the total feed pressure. As a result, CO_2/N_2 permselectivity decreases with the total feed pressure. Fig. 5-13 summarizes the effect of the total feed pressure on CO_2/N_2 permselectivity for all the membranes. At lowest total feed pressure of 1.3 atm absolute, the CO_2/N_2 permselectivity varies from 23 for the 0.8 μm pore size support to 30 for the 0.2 μm pore size support. As the total feed pressure increases, the CO_2/N_2 permselectivity drops to approximately 10, but the total feed pressure at which that occurs depends on the pore size of the membrane.

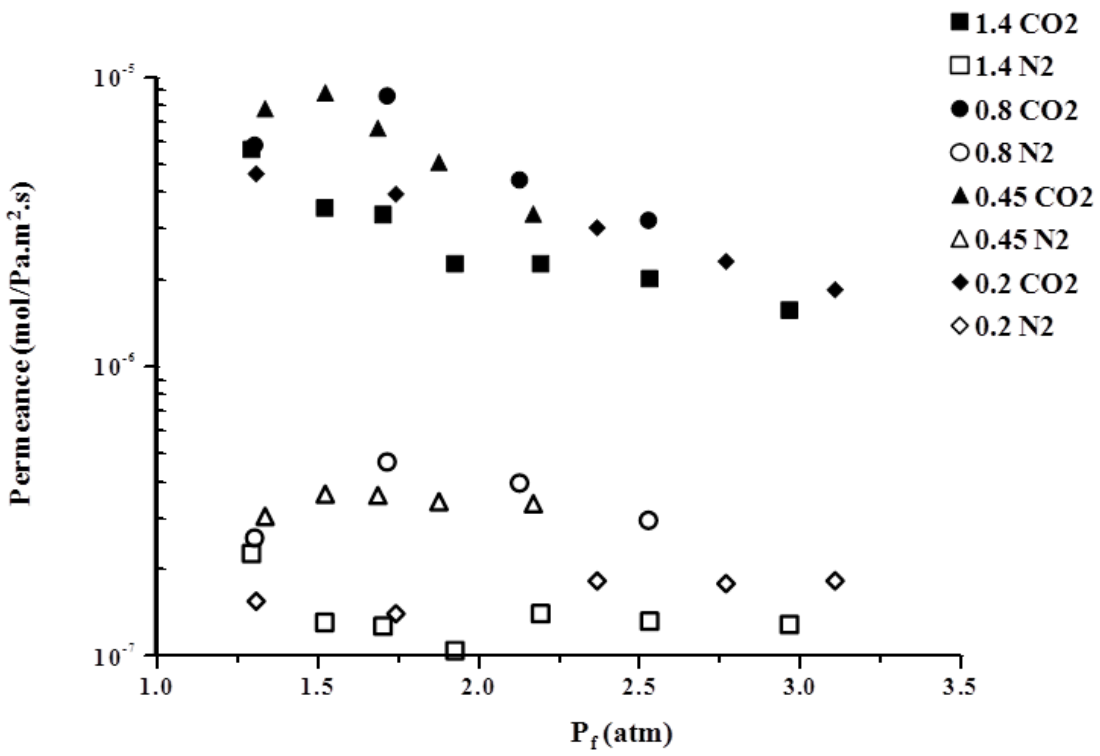

Figure 5-12 CO_2 and N_2 permeances of silicalite-1 membranes, synthesized on supports with different pore sizes of the active layer, as a function of the total feed pressure. All tests performed with equimolar feed (CO_2 + N_2) at ambient temperature (293 K) with permeate side open to atmosphere.

A decrease in the CO_2/N_2 permselectivity of the zeolite membranes with increasing total feed pressure could be expected because of two reasons. First of all, as pressure increases, the contribution of non-selective transport through defects (Knudsen diffusion and/or Poiseuille flow) increases. Also, as pressure increases, the relative difference between adsorption capacities for CO_2 and N_2 in MFI zeolites decreases [48]. There is however, one exception from this general trend between the CO_2/N_2 permselectivity and the total feed pressure. It can be noticed in Fig. 5-13 that for the membrane synthesized using the 1.4 μm support, the CO_2/N_2 permselectivity at the total feed pressure of 1.3 atm is less than that at

1.5 and 1.7 atm. Similar behaviour was also reported by Sebastian et al. (2007) for Na-ZMS-5 and B-ZMS-5 membranes [48].

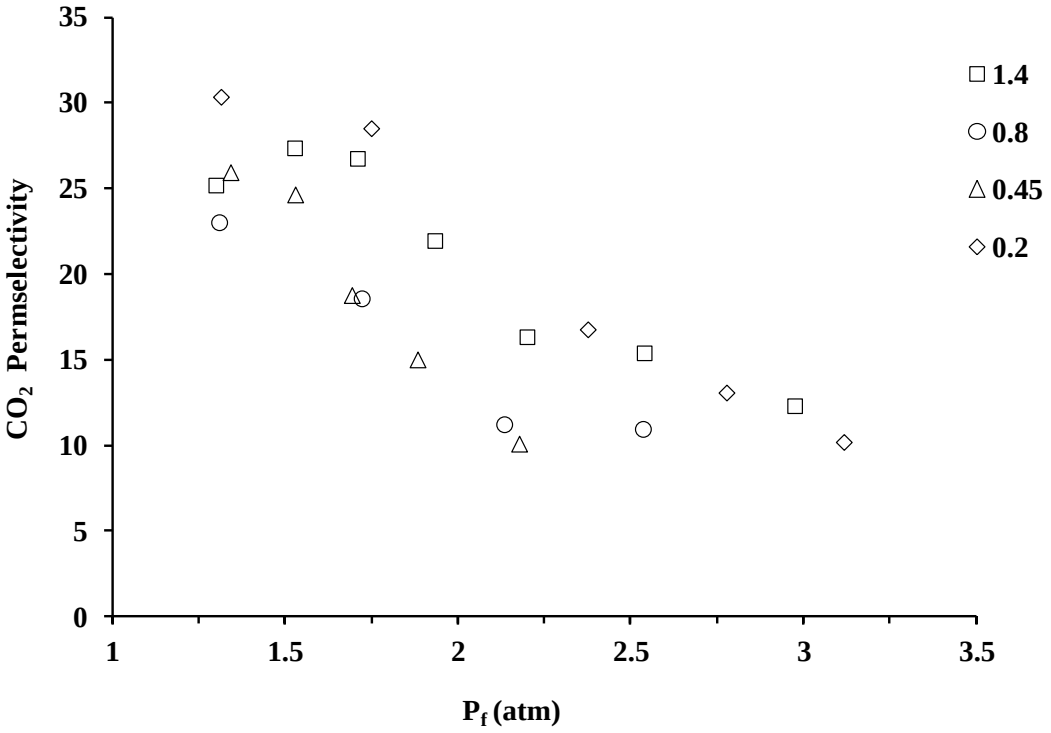

Figure 5-13 CO_2/N_2 permselectivity of silicalite-1 membranes, synthesized on supports with different pore sizes of the active layer, as a function of the total feed pressure. All tests performed with equimolar feed ($CO_2 + N_2$) at ambient temperature (293 K) with permeate side open to atmosphere.

To assess the potential of the silicalite-1 membranes synthesized in this work, their CO_2/N_2 permselectivity is plotted versus their permeability in Fig. 5-14 and compared with the revised Robeson upper bound for CO_2/N_2 separation [49]. In addition, the literature data for silicalite-1 membranes [45,46,48,50-53] and ZSM-5 membranes [54-62] are also shown in Fig. 5-14. To convert the permeance to the permeability, it was assumed that the thickness

of the selective layer in the synthesized membranes corresponds to the thickness of the active layer of the support (5 μm). It is important to note that for a given permeance, the calculated permeability is directly related to the membrane thickness; the greater the membrane thickness used in the calculation, the greater the permeability. As shown by the EDS analysis summarized in Fig. 5-6, except for the smallest pore size membranes (0.14 and 0.2 μm), silica is the major component even at 5 μm from the membrane surface, which suggests complete pore plugging of the active layer of the supports. Moreover, the assumed membrane thickness for the permeability calculations does not include the 1 - 2 μm layer of silicalite-1 crystals on top of the membranes, the inclusion of which would increase the calculated CO_2 permeability by 15 – 20%. It is also important to emphasize that according to the manufacturer, the porosity of the active layer of the supports was only 23%. This means that the actual area of the membranes is only 23% of the macroscopic area. However, in the calculations of the permeance and permeability, the macroscopic area ($A = \pi DL$) was used. Despite this the membranes synthesized in this project are 1 – 2 orders of magnitude more permeable than silicalite-1 and ZSM-5 membranes reported in the literature. At the same time, the CO_2/N_2 permselectivity of the synthesized membranes is greater or comparable to the most selective silicalite-1 and ZSM-5 membranes. Consequently, the combination of the CO_2 permeability and CO_2/N_2 permselectivity places the membranes synthesized in this work above the revised upper bound line for CO_2/N_2 system, which is evident in Fig. 5-14. The favorable location above the revised upper bound line of the membranes synthesized in this work arises primarily from their very high permeability. It is important to point out that sensitivity studies show that high CO_2 permeance is much more important than high selectivity in lowering the cost of CO_2 capture [63].

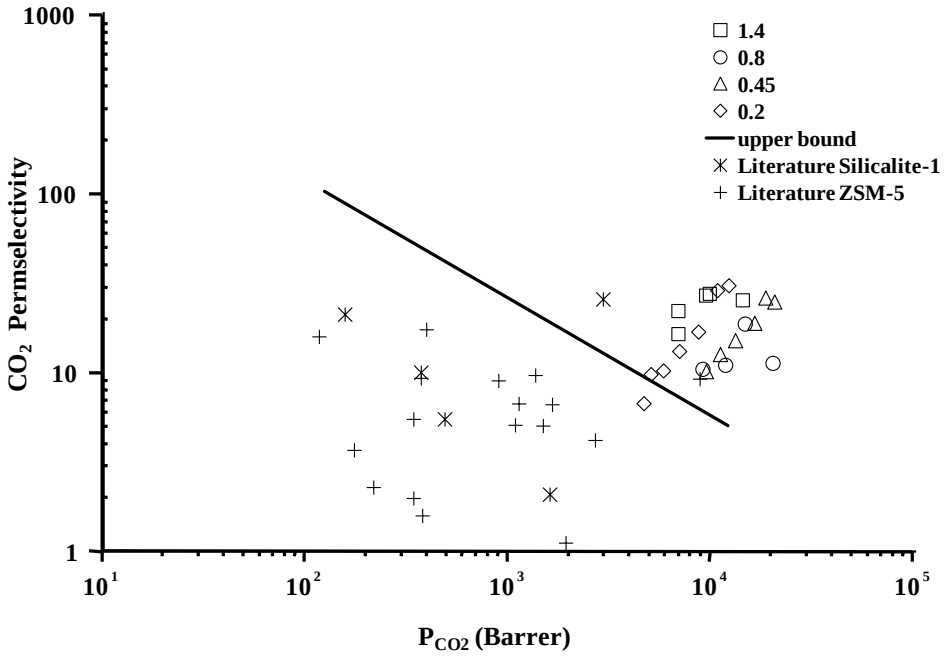

Figure 5-14 CO_2/N_2 performance of silicalite-1 membranes synthesized in this project in comparison with the revised upper-bound correlation for CO_2/N_2 separation [49], as well as, other silicalite-1 and ZSM-5 membranes reported in the literature. The thickness silicalite-1 layer in synthesized membrane was assumed to be equal of the active layer of the support.

5.4 Conclusions

In this work, the effect of pore size of tubular supports on the morphology and gas separation performance of silicalite-1 composite membranes was investigated. The membranes were prepared by a pore plugging hydrothermal synthesis on the supports whose active layer was alumina-free containing only titanium oxide and/or zirconium oxide. The synthesized membranes were characterized by SEM, EDS, XRD, and gas permeation with pure and mixed gas feeds.

Although large coffin-shape crystals were present on top of each membrane, the crystals responsible for the selective properties of the membranes were embedded in the pores of the active layer of the support. These crystals could not be observed directly on SEM micrographs of membranes' cross-section, but their presence was confirmed by the EDS analyses. Moreover, considering the pore size of the active layer of different supports, which varied from 0.14 to 1.4 μm, the crystals formed in the active layer must have been more than an order of magnitude smaller than those observed on the membrane surface. The latter, despite appearing to form a continuous zeolite layer on top of the smaller pore size membranes (0.14 μm, 0.2 μm, 0.45 μm), did not contribute to the selective properties of the membranes. This is evident on the example of the 0.14 μm membrane, which despite having the most continuous zeolite layer, was the only one without any CO_2/N_2 selectivity. At the same time, this membrane had the lowest concentration of Si inside the active layer among the membranes synthesized in this work, which suggests that its lack of selectivity was probably due to the incomplete pore plugging. The concentration of Si in the active layer increased with increasing pore size of the active layer.

The analysis of the XRD micrographs of the membranes revealed that silicalite-1 crystals were mostly oriented with either the a- or b-axes perpendicular to the membrane surface, which is desirable for minimizing the resistance to gas transport through the zeolite crystals. This was confirmed by very high CO_2 permeances, in the order of 10^{-6} mol m^{-2} Pa^{-1} s^{-1}, for all synthesized membranes. At the same time, the corresponding CO_2/N_2 permselectivities were also very high approaching the value of 30 at low total feed pressures. Although both the CO_2 permeance and the CO_2/N_2 permselectivity decreased with increasing total feed

pressure of equimolar CO_2/N_2 mixtures, generally all membranes synthesized in this work that were tested at the total feed pressure up to 3 atm absolute, fall above the revised upper bound line for CO_2/N_2 separation. This indicates their excellent potential for capturing CO_2 from flue gases.

Acknowledgements

The authors acknowledge the financial support received from Natural Science and Engineering Research Council (NSERC) of Canada, the Ontario Graduate Scholarship (OGS) program and from the University of Ottawa. The authors would also like to thank Dr. C. Detellier and Dr. S. Letaief from the Center for Catalysis Research and Innovation (CCRI), Department of Chemistry at University of Ottawa for their generous help in the morphology analyses.

5.5 References

1- J. Caro, M. Noack, Zeolite membranes – recent development and progress, *Microporous Mesoporous Mater*. 115 (2008) 215 – 233.

2- E.E. McLeary, J.C. Jansen, F. Kapteijn, Zeolite based films, membranes and membrane reactors: progress and prospects, Microporous Mesoporous Mater. 90 (2006) 198 – 220.

3- A. Julbe, Zeolite Membranes- A Short Overview, Stud. Surf. Sci. Catal. 157 (2005) 135 – 160.

4- M.P. Pina, R. Mallada, M. Arruebo, M. Urbiztondo, N. Navascués, O. de la Iglesia, J. Santamaria, Zeolite films and membranes. Emerging applications, Microporous Mesoporous Mater. 144 (2011) 19 – 27.

5- J. Caro, M. Noack, P. Kolsch, Zeolite membranes: from the laboratory scale to technical applications, Adsorption 11 (2005) 215 – 227.

6- J. Dong, Y.S. Lin, M.Z.-C. Hu, R.A. Peascoe, E.A. Payzant, Template removal associated microstructural development of ceramic supported MFI zeolite membranes, Microporous Mesoporous Mater. 34 (2000) 241 – 253.

7- K. Okamoto, H. Kita, K. Horii, K. Tanaka, Zeolite NaA membrane: preparation, single-gas permeation, and pervaporation and vapor permeation of water/organic liquid mixtures, *Ind. Eng. Chem. Res.* 40 (2001) 163 – 175.

8- C. Covarrubias, R. Garcia, R. Arriagada, J. Yanez, H. Ramanan, Z. Lai, M. Tsapatsis, Removal of trivalent chromium contaminant from aqueous media using FAU-type zeolite membranes, J. Membr. Sci. 312 (2008) 163 – 173.

9- M. Hong, S. Li, J.L. Falconer, R.D. Noble, Hydrogen purification using a SAPO-34 membrane, J. Membr. Sci. 307 (2008) 277 – 283.

10- H.H. Funke, M.G. Kovalchick, J.L. Falconer, R.D. Noble, Separation of hydrocarbon isomer vapors with silicalite zeolite membranes, Ind. Eng. Chem. Res. 35 (1996) 1575 – 1582.

11- J. Hedlund, Control of the preferred orientation in MFI films synthesized by seeding, J. Porous Mater. 7 (2000) 455 – 464.

12- J. Choi, S. Ghosh, Z. Lai, M. Tsapatsis, Uniformly a-oriented MFI zeolite films by secondary growth, Angew. Chem. 118 (2006) 1172 – 1176.

13- J. Motuzas, R. Mikutaviciute, E. Gerardin, A. Julbe, Controlled growth of thin and uniform TS-1 membranes by MW-assisted heating, Microporous Mesoporous Mater. 128 (2010) 136 – 143.

14- P.-S. Lee, X. Zhang, J.A. Stoeger, A Malek, W. Fan, S. Kumar, W.C. Yoo, S. Al Hashimi, R.L. Penn, A. Stein, M. Tsapatsis, Sub-40 nm zeolite suspensions via disassembly of three-dimensionally ordered mesoporous-imprinted Silicalite-1, J. Am. Chem. Soc. 133 (2011) 493 – 502.

15- V. Kumar, X. Zhang, B. Elyassi, D.D. Brewer, M. Gettel, S. Kumar, J.A. Lee, S. Maheshwari, A. Mittal, C.-Y. Sung, M. Cococcioni, L.F. Francis, A.V. McCormick, K.A. Mkhoyan, M. Tsapatsis, Dispersible exfoliated zeolite nanosheets and their application as a selective membrane, Science 334 (2011) 72 – 75.

16- W.J.W. Bakker, L.J.P. van den Broeke, F. Kapteijn, J.A. Moulijn, Temperature dependence of one-component permeation through a silicalite-1 membrane, AIChE J. 43 (1997) 2203 – 2214.

17- M. Pan, Y.S. Lin, Template-free secondary growth synthesis of MFI type zeolite membranes, Microporous Mesoporous Mater. 43 (2001) 319 – 327.

18- D. Shen, W. Xiao, J. Yang, N. Chu, J. Lu, D. Yin, J. Wang, Synthesis of silicalite-1 membrane with two silicon source by secondary growth method and its pervaporation performance, Sep. Purifi. Tech. 76 (2011) 308 – 315.

19- E. Dincer, A. Culfaz, H. Kalipcilar, Effect of seeding on the properties of MFI type zeolite membranes, Desalination 200 (2006) 66 – 67.

20- X. Xu, Y, Bao C. Song, W. Yang, J. Liu, L. Lin, Microwave-assisted hydrothermal synthesis of hydroxy-sodalite zeolite membrane, Microporous Mesoporous Mater. 75 (2004) 173 – 181.

21- J. Dong, Y.S. Lin, M.Z.-C. Hu, R.A. Peascoe, E.A. Payzant, Template removal associated microstructural development of ceramic supported MFI zeolite membranes, Microporous Mesoporous Mater. 34 (2000) 241 – 253.

22- S. Miachon, E. Landrivon, M. Aouine, Y. Sun, I. Kumakiri, Y. Li, O. Pachtova Prokopova, N. Guilhaume, A. Giroir-Fendler, H. Mozzanega, J.A. Dalmon, Nanocomposite MFI-alumina membranes via pore-plugging synthesis: preparation and morphological characterization, J. Membr. Sci. 281 (2006) 228 – 238.

23- S. Miachon, P. Ciavarella, L. van Dyka, I. Kumakiri, K. Fiaty, Y. Schuurman, J. A. Dalmona, Nanocomposite MFI-alumina membranes via pore-plugging synthesis: specific transport and separation properties, J. Membr. Sci. 298 (2007) 71 – 79.

24- A. M. McAleer, L. V. C. Rees, A. K. Nowak, Ion exchange and aluminum distributions in ZSM-5 zeolites, Zeolites *11 (1991) 329* – 336.

25- M. Tawalbeh, F.H. Tezel, B. Kruczek, S. Letaief, C. Detellier, Synthesis and characterization of silicalite-1 membrane prepared on a novel support by the pore plugging method, J. Porous Materials 20 (2013) 1047 – 1421.

26- M. Tawalbeh, B. Kruczek, F.H. Tezel, S. Letaief, C. Detellier, Separation of CO_2 and N_2 Gases Using A Novel Zeolite Membrane, Sep. Sci. Tech. 47 (2012) 1606 – 1616.

27- X. Xu, Y. Bao, Ch. Song, W. Yang, J. Liu, L. Lin, Microwave-assisted hydrothermal synthesis of hydroxyl-sodalite zeolite membrane, Microporous Mesoporous Mater. 75 (2004) 173 – 181.

28- W.F. Lai, US Pat. 5,763,347, assigned to Exxon Research and Engineering Company, 1998.

29- J.P. Verduijn, A.J. Bons, M.H. Anthonis, L.R. Czarnetzki, W.J. Mortier, US Pat. 6,090,289, assigned to Exxon Research and Engineering Company, 2000.

30- B.J. Buck, A.L. Brock, W.H. Johnson, A.L. Ulery, Corrosion of Depleted Uranium in an Arid Environment: Soil-Geomorphology, SEM/EDS, XRD, and Electron Microprobe Analyses, Soil and Sediment Contamination 13 (2004) 545 – 561.

31- C.J. Geankopolis, Transport processes and separation process principles, Fourth ed., Prentice Hall Press, NJ, USA, 2003.

32- I. Diaz, E. Kokkoli, O. Terasaki, M. Tsapatsis, Surface structure of zeolite (MFI) crystals, Chem. Mater. 16 (2004) 5226 – 5232.

33- G.E. Romanos, Th.A. Steriotis, E.S. Kikkinides, N.K. Kanellopoulos, V. Kasselouri, J.D.F. Ramsay, P. Langlois, S. Kallus, Innovative methods for preparation and testing of Al_2O_3 supported silicalite-1 membranes, J. Euro. Ceram. Soc. 21 (2001) 119 – 126.

34- E. Landrivon, S. Miachon, I. Kumakiri, M. Matsukata, J.-A. Dalmon, MFI-alumina composite membrane. Influence of the support porous structure on the separative performance, Fuel Chem. Div. Preprints 48 (2003) 394 – 395.

35- M.R. Othman, S.C. Tan, S. Bhatia, Separability of carbon dioxide from methane using MFI zeolite–silica film deposited on gamma-alumina support, Microporous Mesoporous Mater. 121 (2009) 138 – 144.

36- S.P. Naik, A.S.T. Chiang, R.W. Thompson, F.C. Huang, Formation of silicalite-1 hollow spheres by the self-assembly of nanocrystals, Chem. Mater. 15 (2003) 787 – 792.

37- Y. Ma, J. Guan, S. Wu, J. Liu, Q. Kan, W. Zhang, Synthesis and characterization of belt-like silicalite-1 nanocrystals with mesoporous structure, Mater. Letters 64 (2010) 2523 – 2525.

38- J. Motuzas, A. Julbe, R.D. Noble, A. van der Lee, Z.J. Beresnevicius, Rapid synthesis of oriented silicalite-1 membranes by microwave-assisted hydrothermal treatment, Microporous Mesoporous Mater. 92 (2006) 259 – 269.

39- M.C. Lovallo, M. Tsapatsis, Preferentially oriented submicron silicalite membranes, AIChE J. 42 (1996) 3020 – 3029.

40- G. Li, E. Kikuchi, M. Matsukata, The control of phase and orientation in zeolite membranes by the secondary growth method, *Microporous and Mesoporous Mater.* 62 (2003) 211 – 220.

41- J.P. Verduijn, A.J. Bons, M.H. Anthonis, L.H. Czarnetzki, Int. Patent Appl. PCT WO 96/01683.

42- J. Hedlund, S. Mintova, J. Sterte, Controlling the preferred orientation in silicalite-1 films synthesized by seeding, Microporous Mesoporous Mater. 28 (1999) 185 – 194.

43- M.A. Ulla, R. Mallada, J. Coronas, L. Gutierrez, E. Miro, J. Santamaria, Synthesis and characterization of ZSM-5 coatings onto cordierite honeycomb supports, Appl. Catal. A: General 253 (2003) 257–269.

44- C. Algieri, P. Bernardo, G. Golemme, G. Barbieri, E. Drioli, Permeation properties of a thin silicalite-1 (MFI) membrane, J. Membr. Sci. 222 (2003) 181 – 190.

45- W. Zhu, P. Hrabanek, L. Gora, F. Kapteijn, J.A. Moulijn, Role of adsorption in the permeation of CH_4 and CO_2 through a silicalite-1 membrane, Ind. Eng. Chem. Res. 45 (2006) 767 – 776.

46- A.J. Burggraaf, Z.A.E.P. Vroon, K. Keizer, H. Verweij, Permeation of single gases in thin zeolite MFI membranes, J. Membr. Sci. 144 (1998) 77 – 86.

47- S. Li, C.Q. Fan, High-Flux SAPO-34 membrane for CO_2/N_2 separation, *Ind. Eng. Chem. Res.* 49 (2010) 4399 – 4404.

48- V. Sebastian, I. Kumakiri, R. Bredesen, M. Menendez, Zeolite membrane for CO_2 removal: Operating at high pressure, J. Membr. Sci. 292 (2007) 92 – 97.

49- L.M. Robeson, The upper bound revisited, J. Membr. Sci. 320 (2008) 390 – 400.

50- Y. Ando, Y. Hirano, S. Mase, H. Taguchi, Preparation and characterization of monolithic and planar element of zeolite membranes, Proc. ICIM (1998) Nagoya, Japan, 124 – 127.

51- S. Mase, Y. Ando, Y. Hirano, H. Taguchi, Planer type module with zeolite (MFI) membranes, Proc. ICIM (1998) Nagoya, Japan, 652 – 655.

52- L.J.P. van den Broeke, W.J.W. Bakker, F. Kapteijn, J.A. Moulijn, Transport and separation properties of a silicalite-1 membrane – I. Operating conditions, Chem. Eng. Sci. 54 (1999) 245 – 258.

53- M.C. Lovallo, A. Gouzinis, M. Tsapatsis, Synthesis and characterization of oriented MFI membranes prepared by secondary growth, AIChE J. 44 (1998) 1903 – 1913.

54- T. Masuda, K. Hashimoto, F. Kapteijn, J.A. Moulijn, Selective permeation of CO_2 from mixture gas of CO_2 and N_2 through ZSM-5 zeolite membrane, Proc. ICIM'98, Nagoya, Japan, p. 128 (1998).

55- B.I. Kwak, S.H. Hyun and G.T. Kim, CO_2 separation characteristics of ZSM-5 composite membranes synthesized by the hydrothermal treatment, J. Mater. Sci. Letters 20 (2001) 1893 – 1896.

56- J. Hedlund, M. Noack, P. Kölsch, D. Creaser, J. Caro, J. Sterte, ZSM-5 membranes synthesized without organic templates using a seeding technique, J. Membr. Sci. 159 (1999) 263 – 273.

57- J.K. Kusakabe, S. Yoneshige, A. Murata, S. Morooka, Morphology and gas permeance of ZSM-5-type zeolite membrane formed on a porous α-alumina support tube, J. Membr. Sci. 116 (1996) 39 – 46.

58- Y. Yan, M.E. Davis, G.R. Gavalas, Preparation of zeolite ZSM-5 membranes by In-Situ crystallization on porous alpha-Al_2O_3, Ind. Eng. Chem. Res. 34 (1995**)** 1652 – 1661.

59- H-S. Oh, M-H. Kim, H-K. Rhee, Synthesis of ZSM-5 zeolite membrane on the inner surface of a ceramic tube, Stud. Surf. Sci. Catal. 105 (1997) 2217 – 2224.

60- M.P. Bernal, J. Coronas, M. Menendez, J. Santamaria, Separation of CO_2/N_2 mixtures using MFI-type zeolite membranes, AIChE J. 50 (2004) 127–135.

61- S.H. Hyun, J.K. Song, B.I. Kwak, J.H. Kim, S. A. Hong, Synthesis of ZSM-5 zeolite composite membranes for CO_2 separation, J. Mater. Sci. 34 (1999) 3095 – 3105.

62- D.W. Shin, S.H. Hyun, C.H. Cho, M.H. Han, Synthesis and CO_2/N_2 gas permeation characteristics of ZSM-5 zeolite membranes, Microporous Mesoporous Mater. 85 (2005) 313 – 323.

63- T. Merkel, H. Lin, X. Wei, J. He, B. Firat, K. Amo, R. Daniels, R. Baker, A membrane process to capture CO_2 from coal-fired power plant flue gas, NETL review meeting, March 24-26, 2009.

CHAPTER SIX

This Chapter is based on

Modeling the transport of CO_2, N_2 and their binary mixtures through a thin silicalite-1 membrane using Maxwell−Stefan equations

M. Tawalbeh, M. Al-Ismaily, D. Carter, B. Kruczek, F. H. Tezel

Department of Chemical and Biological Engineering, University of Ottawa, 161 Louis Pasteur Street, Ottawa, ON, Canada K1N 6N5

To be submitted to the Microporous and Mesoporous Materials

A model based on Maxwell−Stefan equations and Extended Langmuir isotherm is developed and presented in this paper. The developed model describes the transport of binary mixtures of CO_2 and N_2 through thin silicalite-1 membranes. In this paper, a modification was made to the permeation setup used in previous papers to allow the performance of the permeation experiments at very high feed flow rates (more than one order of magnitude higher) to minimize stage cut. This allowed to avoid converting the separation results to zero stage cut as it was done in the previous chapters. The effect of lowering the stage cut on the

permeation performance on four membranes with different support pore sizes is shown in Fig. A4-1 (Appendix A.4). It can be clearly seen from this figure that the effect on both CO_2 permeance and CO_2/N_2 permselectivity is less than 10% for the four membranes used in the study. It is important to emphasize that the low stage cut experiments were performed at the same total feed pressure and feed composition of the high stage cut experiments for each individual membrane. In this paper M. Al-Ismaily and David Carter were co-authors in addition to the supervisors. M. Al-Ismaily helped in coding the solution of the equations that was used to extract the exchange diffusivity from the mixture permeation experiments. M. Al-Ismaily also assisted with building the optimization program that allowed the exchange diffusivities extraction. D. Carter assisted with the performance of the permeation experiments at low stage cut values.

Chapter 6 - Modeling the transport of CO_2, N_2 and their binary mixtures through thin silicalite-1 membrane using Maxwell−Stefan equations

Abstract

A model based on Maxwell−Stefan equations and Extended Langmuir isotherm was developed for the transport of binary mixtures of CO_2 and N_2 through thin silicalite-1 membranes. The CO_2 and N_2 exchange diffusivities, $Đ_{12}$ and $Đ_{21}$, were determined at different total feed pressures up to 4 atm and five different feed compositions (CO_2 % mole) of 15%, 30%, 50%, 70% and 85%. All gas separation tests were carried out at stage cut not exceeding 5%. The CO_2 and N_2 diffusivities required by the model were determined experimentally from the respective single gas permeation tests at different feed pressures similar to mixed gas permeation tests.

The exchange coefficients calculated using the developed model and the experimental data were practically independent of the total feed pressure but were dependent on the concentration of the feed stream. As the concentration of CO_2 in the feed increased from 15% to 85%, $Đ_{12}$ decreased from 2.8 10^{-10} to 1.1 x 10^{-10} m^2 s^{-1}, while $Đ_{21}$ decreased from around 2.8 x 10^{-10} to 1.3 x 10^{-10} m^2 s^{-1}. In comparison, the N_2 permeance decreased by about one order of magnitude from 2.7 x 10^{-7} to 2.4 x $10^{-8\ 6}$ mol m^{-2} Pa^{-1} s^{-1} when the CO_2 concentration in the feed increased from 15% to 85%. Consequently, the exchange diffusivities showed considerably smaller dependence on the operating conditions compared

to the permselectivity and permeance values, and as such they are more appropriate to characterize the intrinsic transport properties of silicalite-1 membranes.

Keywords: Silicalite-1 membranes; Pore plugging synthesis; Diffusivity, Maxwell-Stefan, Modeling, CO_2/N_2 separation

6.1 Introduction

Zeolites have several properties that make them attractive as membrane materials. They demonstrate excellent chemical stability and are stable at high pressures and temperatures [1,2]. These properties allow zeolite membranes to operate in conditions that would be too harsh for most polymeric membranes. Zeolites also offer small pore sizes, uniform pore size distribution, and a regular three dimensional pore structure with highly ordered pores [3]. The highly ordered pores in zeolite membranes create a potential for high separation selectivity for species with small differences in the adsorption and transport properties. Supported MFI membranes have revealed the most reproducible permeation data among the studied zeolite membranes up to date [4,5]. The MFI type zeolites, i.e. silicalite-1 and its Al-containing analogue, ZSM-5, have channels defined by 10-membered oxygen rings with diameter of ~0.55 nm [6], which allow them to separate gases by the molecular sieving mechanism and/or surface diffusion. Due to the high selectivities achieved, more interest had been given for the use of zeolite membranes in gas separation [5,7–10]. These high selectivities are relying on the difference of the adsorption characteristics of the individual species in the mixture along with the diffusion characteristics of the adsorbed species [11].

Several factors can affect the membrane permeation properties such as the hydrodynamic boundary layer, the support layer resistance and the intercrystalline defects. The hydrodynamic boundary layer commonly leads to what is called concentration polarization. Avila et al. [12] showed that the fluxes of CO_2 and CH_4 through SAPO-34 membrane at high pressures were highly influenced by the concentration polarization effect. On the other hand, since the zeolite membranes usually consist of a thin zeolite film on top of a macroporous support, the support can introduce a significant resistance to the mass transport

through the membrane [13,14]. To simplify this mechanism, the intracrystalline diffusion is assumed to be the rate-limiting step. This means that the concentrations at the crystal surfaces are considered to be in equilibrium with the surrounding gas phase. Furthermore, a parallel flow might be generated by the passage of gases through the defects. These defects are usually formed during the heating and the cooling steps, originating from the difference in the thermal expansion coefficients between zeolite crystals and the support material [15–17].

The understanding of the multicomponent mass transport within the zeolite film is essential for accurate permeation modeling and successful design of any zeolite membrane based process. It is also crucial for the prediction of the dynamic behaviour, optimization of the operating conditions, and scaling up the process. However, it is more preferable if the mixtures permeation characteristics can be predicted based on the single component adsorption and diffusion properties [18]. Unlike the polymeric membrane, the permeation through zeolite membranes is governed by both the adsorption/surface diffusion and the activated micropore diffusion mechanisms. It has been shown [19–22] that the zeolite membranes characteristics, i.e. permselectivity and permeances, are highly dependent on operating conditions such as feed pressure, feed composition, operating temperature and sweep gas flow. Gas permeance can be decreased or increased by an order of magnitude by altering some of the above operating conditions. On the other hand, it is widely accepted that the Maxwell-Stefan approach is the most successful and physically sound approach to describe multicomponent mixtures diffusion through zeolite membranes [18,23,24]. Hence,

many recent studies have used M-S equations to interpret the results of the permeation experiments [17,25-27].

The main objective of this study was to develop a detailed model based on Maxwell-Stefan equations to describe the transport of CO_2/N_2 binary mixture through silicaite-1 membrane prepared on a tubular support. The model is to rely on the single component adsorption and diffusivity data for the silicalite-1 membrane, as well as the Extended Langmuir model to represent the behaviour of the gas mixture. The model is to yield the CO_2 and N_2 exchange diffusivities $Đ_{12}$ and $Đ_{21}$ that may provide a better characterization of the zeolite membrane compared to the respective gas permeances at varying operating conditions.

6.2 Experimental

6.2.1 Membrane Synthesis

The preparation of silicalite-1/ceramic composite membranes has been described in detail elsewhere [19,22,28]. The membrane used in this study was previously tested with different single gases, including CO_2 and N_2, as well as with different CO_2/N_2 binary mixtures in high stage cut separation experiments [28]. The membrane was prepared on a macroporous ceramic tube, with 0.45 μm pore size in the active layer purchased from TAMI Industries, Nyons, in France. The precursor was a clear solution of tetrapropylammonium hydroxide (TPAOH, 1M solution from Fluka's Purum, Sigma-Aldrich, Oakville, ON, Canada) and Fumed silica (Sigma-Aldrich, Oakville, ON, Canada). The pore plugging synthesis method was used to prepare the membrane [17,19,28,29]. The exact morphology of this membrane as determined by SEM, EDX and XRD was described elsewhere [28]. The selective

properties of this membrane were provided by small silicalite-1 crystals embedded inside a 5-μm thick active layer made of ZrO_2 and TiO_2. [28].

6.2.2 Permeation Tests

Gas permeation experiments were carried out with the prepared tubular membrane in a constant pressure (CP) system shown schematically in Fig. 6-1 and was described in detail elsewhere [19,28]. The inserts in Fig. 6-1 show the details of the membrane module as well as the schematic of the gas permeation through the composite silicalite-1 membrane. The membrane was tested with single N_2 and CO_2 gases as well as with their mixtures. The single and mixed gas permeation experiments were carried out at the total feed pressure up to 4.0 atm. The single N_2 experiments (low adsorbing gas) were carried out for 6 hours, while those with CO_2 (high adsorbing gas) were performed for 24 hours. The tests with mixed CO_2/N_2 feed were carried out for longer periods (48 hours) to ensure that the steady-state condition is reached. After the completion of the permeation tests with a given feed gas, the membranes were regenerated with pure helium purge at a feed pressure of 2 atm for 12 hr before switching to another feed gas. All gas permeation tests as well as membrane regenerations were carried out at ambient temperature (~23^{o}C).

The main difference in this study, compared to the previously reported separation tests on this membrane [28] was the use of the CO_2 and N_2 mass flow controllers with the maximum flow rate of 1000 cm^3(STP)/min each, i.e., one order of magnitude greater than the previously used mass flow controllers. This allowed carrying out the gas separation tests with much higher feed flow rates, thus decreasing the stage cut. Accordingly, all equimolar

binary experiments were performed using the same total feed flow rate of 1612 cm^3(STP)/min, while the total feed flow rate for non equimolar binary mixture was between 970 and 1310 cm^3(STP)/min depending on the feed composition. Nevertheless, in all experiments the stage cut was less than 5%.

The membrane performance at different conditions was evaluated on the basis of the gas permeance and the permeance ratio. For example, the permeance of component *A* (P_A) is determined based on the steady state permeation rate (V_A), the partial pressure difference across the membrane (Δp_A), and the membrane area (A_M):

$$P_A = \frac{V_A}{A_M \Delta p_A} \tag{6.1}$$

The selectivity of the membrane for separation of gases *A* and *B* is then evaluated based on respective gas permeances:

$$\alpha^*_{A/B} = \frac{P_A}{P_B} \tag{6.2}$$

In the case of single gas permeation tests the partial pressure difference is equal to the total pressure difference through the membrane. The permeance ratio based on single gas permeation tests is referred to as the ideal selectivity. Since the stage cut in all experiments was less than 0.05, the composition of the retentate was similar to the composition of the feed, and as a first approximation Δp_A in gas separation tests was determined based on the composition of the feed and permeate. More accurate determination of the individual permeances at relatively high stage cut experiments (stage cut approaching to 0.95) required an elaborative numerical procedure that is described in detail elsewhere [28]. The permeance ratio based on a mixed gas permeation test is referred to as the permselectivity.

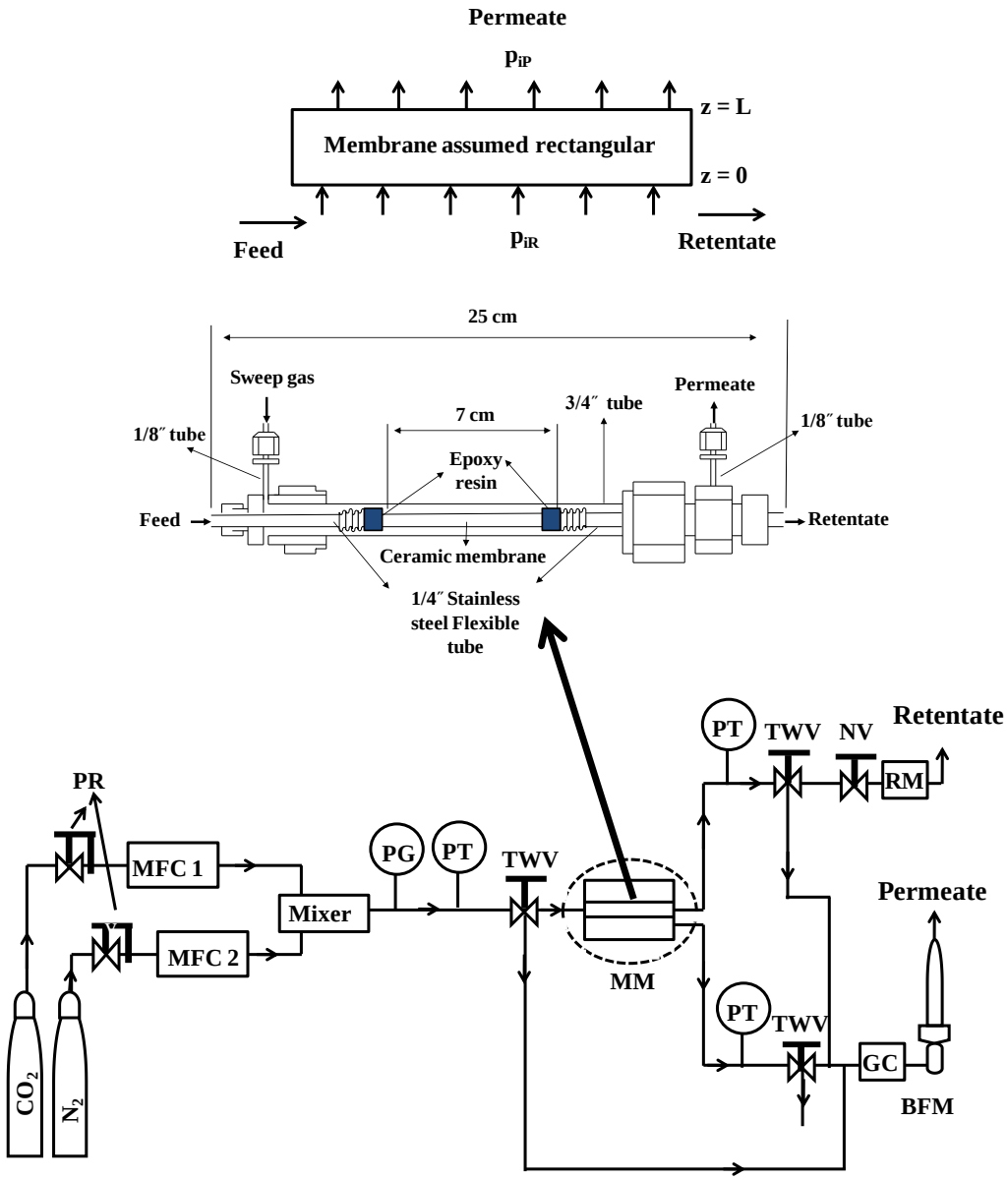

Figure 6-1 Gas permeation/separation setup with a schematic for the custom made tubular membrane module as well as a schematic diagram for the gas permeation through the composite membrane (BFM: bubble flow meter, GC: gas chromatograph, L: membrane thickness, MFC: mass flow controller, MM: membrane module, NV: needle valve PG: pressure gauge, P_{iP}: the pressure in the permeate side, P_{iR}: the pressure in the retentate side, PR: pressure regulator, PT: pressure transducer, RM: rotameter, TWV: Three way valve, z: the direction of the gas permeation)

6.3 Theory

6.3.1 Single Component Diffusion in Zeolites

It can be seen from Fig. 6-1 insert that the gas permeation is happening in the z direction while the high pressure feed stream is flowing parallel to the membrane length. It should be emphasized that the tubular membrane will be treated in this context as a flat sheet membrane since the zeolite layer L is very thin (few microns) compared to the inner diameter of the support (~6 mm) [19,28].

For a homogenous membrane under isothermal conditions the flux of gas *i* through the membrane is given by [30,31]:

$$J_i = -\varepsilon B_i c_i \frac{d\mu_i}{dz} \tag{6.3}$$

where B_i is the mobility of component *i* (mol.m^2/J.s), which is equivalent to the friction coefficient reciprocal (1/*f*), c_i is the concentration of component *i* (mol/m^3) and μ_i is the chemical potential for component *i* (J/mol). The effective surface area for permeation should be corrected with the porosity of the support (ε). This is due to the fact that the membrane surface area is partially blocked by the solid surface area (1-ε) of the support and most of the diffusion is taking place inside the zeolite, filling the pores in the active layer of the support. Furthermore, since the tubular membrane will be treated as a flat sheet membrane in rectangular coordinates, J_i is assumed to be constant. The chemical potential is given by:

$$\mu_i = \mu_i^0 + RT \ln p_i \tag{6.4}$$

where μ_i^0 is the chemical potential of component *i* at the standard state (J/ mol), *R* is the gas constant (8.314 J/mol.K) , *T* is the absolute temperature (K) and p_i is the partial pressure of

component i. Substituting q_i instead of c_i, where q_i is the gas concentration within the micropores (mol/kg), this would result in:

$$J_i = -\varepsilon B_i RT\rho_s \frac{d\ln p_i}{d\ln q_i}\frac{dq_i}{dz} \tag{6.5}$$

The density of the solid adsorbent (ρ_s) was introduced here when substituting c_i with q_i because of the different units of q_i (mol/kg) and c_i (mol/m^3). With $B_iRT = D_{0i}$ and $dlnp_i/dlnq_i = \Gamma_i$ [31,32], Eq. (6.5) can be rewritten as:

$$J_i = -\varepsilon D_{0i}\Gamma_i\rho_s \frac{dq_i}{dz} \tag{6.6}$$

where D_{0i} is the intrinsic or corrected diffusivity (m^2/s), which is equivalent to Maxwell-Stefan diffusivity (Đ$_i$) for single component. Γ_i is the thermodynamic correction factor. In addition, recognizing that:

$$\frac{d\ln p_i}{d\ln q_i} = \frac{q_i}{p_i}\frac{dp_i}{dq_i} \tag{6.7}$$

The expression for flux can also be written as:

$$J_i = -\varepsilon D_{0i}\rho_s \frac{q_i}{p_i}\frac{dp_i}{dq_i}\frac{dq_i}{dz} \tag{6.8}$$

Eq. (6.8) can be simplified to:

$$J_i = -\varepsilon D_{0i}\rho_s \frac{q_i}{p_i}\frac{dp_i}{dz} \tag{6.9}$$

If the equilibrium isotherm is described by Langmuir isotherm, Eq. (6.9) becomes:

$$J_i = -\varepsilon D_{0i}\rho_s \times \frac{\left(\frac{q_i^{sat} K_i p_i}{1+K_i p_i}\right)}{p_i}\frac{dp_i}{dz} \tag{6.10}$$

where q_i^{sat} and K_i are the saturation adsorption capacity (mol kg^{-1}) for component i and the Langmuir adsorption coefficient (atm^{-1}) for component i, respectively. Upon the rearrangement of Eq. 6.10, the following expression is obtained:

$$J_i dz = -\varepsilon D_{0i}\rho_s q_i^{sat} K_i \frac{dp_i}{1+K_i p_i} \tag{6.11}$$

Treating the membrane as a plane wall due to the fact that the thickness of the zeolite layer is very small compared to the radius of the membrane support as mentioned earlier, J_i is assumed to be independent of z. Then, integrating z from 0 to L (membrane thickness) and p_i from p_{iR} (feed pressure) to p_{ip} (permeate pressure) gives:

$$J_i = \frac{\varepsilon D_{0i}\rho_s q_i^{sat}}{\tau L}\ln\left(\frac{1+K_i p_{iR}}{1+K_i p_{iP}}\right) \tag{6.12}$$

Tortuosity (τ) is introduced in Eq. 6.12 as a correction to the membrane thickness since the diffusion path is not straight from z = 0 to z = L.

The values of the saturation adsorption capacity (q_i^{sat}) of the microporous material and the Langmuir adsorption coefficient (K_i) can be calculated from the pure adsorption isotherm [19]. The porosity (ε) of the support, according to the manufacturer, is 0.23, the particle density of silicalite-1 (ρ_s) is approximately 1800 kg/m^3 [13,18,24] and the tortuosity (τ) of silicalite-1 is considered as 1.2 [33]. Consequently, based on experimentally determined steady state flux across the silicalate-1 membrane in single gas permeation experiment, the diffusivity of component *i* , D_{0i}, can be evaluated from Eq. (6.12).

6.3.2 Binary Mixture Diffusion in Zeolites

The binary mixture diffusion has been described by the generalized Maxwell-Stefan (M-S) equations. The basis for of the Maxwell-Stefan theory is that the driving force for the movement that is acting on species is balanced by the friction experienced by that species. The generalized Maxwell-Stefan equation is given by Eq. (6.13) [32]:

$$-\nabla\mu_i = RT\frac{u_i}{\text{Đ}_i} + RT\sum_{\substack{j=1\\ j\neq i}}^{n}\theta_j\frac{u_i - u_j}{\text{Đ}_{ij}} \tag{6.13}$$

where $\nabla\mu_i$ (J/mol) represents the fundamental driving force (under isothermal conditions) for the mass transport acting on a certain species *i*. As a result, species *i* is tending to move along the surface with a velocity u_i (m/s). θ_i is the occupancy or fractional loading of component *i* (dimensionless). The flow resistance in the first term on the right hand side of Eq. (6.13) attributes to the friction between species *i* and the surface, while the flow resistance in the second term on the right hand side of the same equation attributes to the friction exerted by adsorbate *j*, on the surface motion of species *i*. Each component, (*i* and *j*) is moving with a certain velocity, u_j and u_i , (m/s) with respect to the surface. Đ_{ij} is the Maxwell-Stefan (M-S) surface diffusion coefficient (m^2/s) or the exchange diffusivity between molecules *i* and *j*, and Đ_i is the MS surface diffusion coefficient between molecule *i* and the wall (m^2/s). Đ_i is also called the corrected diffusivity in the literature [34]. It is assumed that the single component M-S diffusivities are independent of concentration which is reasonable for many systems [35,36], even though, it has been shown that they are dependent on concentration even at low loadings [35-38]. Eq. 6.13 can be rearranged, after multiplying each term with θ_i, as follows:

$$-\frac{\theta_i}{RT}\nabla\mu_i = \frac{\theta_i u_i}{Đ_i} + \sum_{\substack{j=1 \\ j\neq i}}^{n} \theta_i\theta_j \frac{u_i - u_j}{Đ_{ij}} \tag{6.14}$$

where θ_i and θ_j are the occupancy or fractional loading of components i and j (dimensionless), respectively and defined as follows:

$$\theta_i = \frac{q_i}{q_i^{sat}} \tag{6.15}$$

$$\theta_j = \frac{q_j}{q_j^{sat}} \tag{6.16}$$

Substituting Eq. (6.15) and Eq. (6.16) into the right hand side of Eq. (6.14), results in:

$$-\frac{\theta_i}{RT}\nabla\mu_i = \frac{q_i u_i}{q_i^{sat} Đ_i} + \sum_{\substack{j=1 \\ j\neq i}}^{n} q_i q_j \frac{u_i - u_j}{q_i^{sat} q_j^{sat} Đ_{ij}} \tag{6.17}$$

where q_j and q_j^{sat} are the molar loading and the saturation molar loading of component j (mol/kg), respectively. By defining the flux as the product of the zeolite density (ρ_s), adsorbed concentration and velocity, hence, the fractional occupancies are converted into fluxes using Eq. (6.18) [11]:

$$J_i = \rho_s q_i^{sat}\theta_i u_i = \rho_s q_i u \tag{6.18}$$

Rearrangement of Eq. 6.18 results in:

$$u_i = \frac{J_i}{\rho_s q_i^{sat}\theta_i} = \frac{J_i}{\rho_s q_i} \tag{6.19}$$

Substituting Eq. (6.19) into Eq. (6.17) gives:

$$-\frac{\theta_i}{RT}\nabla\mu_i = \frac{1}{\rho_s}\left(\frac{J_i}{q_i^{sat} Đ_i} + \sum_{\substack{j=1 \\ j\neq i}}^{n} \frac{q_j J_i - q_i J_j}{q_i^{sat} q_j^{sat} Đ_{ij}}\right) \tag{6.20}$$

The chemical potential gradient and the surface coverage gradient can be related via a matrix of thermodynamic factors given by [32]:

$$\frac{\theta_i}{RT}\nabla\mu_i = \sum_{j=1}^{n}\Gamma_{ij}\nabla\theta_j \tag{6.21}$$

where Γ_{ij} is a thermodynamic correction factor defined by:

$$\Gamma_{ij} = \theta_i \frac{\partial \ln p_i}{\partial \theta_j} = \frac{\theta_i}{p_i}\frac{\partial p_i}{\partial \theta_j} \tag{6.22}$$

The partial derivatives in Eq. (6.22) are defined by the adsorption equilibrium relation between p_i and θ_i. Assuming that the individual component loadings follow the single site Extended Langmuir isotherm that is given by [34]:

$$\theta_i = \frac{q_i}{q_i^{sat}} = \frac{K_i p_i}{1+\sum_{k=1}^{n} K_k p_k} \tag{6.23}$$

Then the Γ,s values for binary mixture are [24]:

$$\Gamma_{11} = \frac{1-\theta_2}{1-\theta_1-\theta_2} \tag{6.24}$$

$$\Gamma_{12} = \frac{\theta_1}{1-\theta_1-\theta_2} \tag{6.25}$$

$$\Gamma_{21} = \frac{\theta_2}{1-\theta_1-\theta_2} \tag{6.26}$$

$$\Gamma_{22} = \frac{1-\theta_1}{1-\theta_1-\theta_2} \tag{6.27}$$

Combining Eq. (6.20) and Eq. (6.21) and solving for the two fluxes yield:

$$J_1 = -\rho_s q_1^{sat} \mathcal{D}_1 \left[\frac{\left(\Gamma_{11} + \frac{\theta_1 \mathcal{D}_2}{\mathcal{D}_{21}} \Gamma_{11} + \frac{\theta_1 \mathcal{D}_2}{\mathcal{D}_{12}} \Gamma_{21} \right) \nabla \theta_1 + \left(\Gamma_{12} + \frac{\theta_1 \mathcal{D}_2}{\mathcal{D}_{21}} \Gamma_{12} + \frac{\theta_1 \mathcal{D}_2}{\mathcal{D}_{12}} \Gamma_{22} \right) \nabla \theta_2}{1 + \theta_2 \frac{\mathcal{D}_1}{\mathcal{D}_{12}} + \theta_1 \frac{\mathcal{D}_2}{\mathcal{D}_{21}}} \right]$$

(6.28)

$$J_2 = -\rho_s q_2^{sat} \mathcal{D}_2 \times \left[\frac{\left(\Gamma_{21} + \theta_2 \frac{\mathcal{D}_1}{\mathcal{D}_{21}} \Gamma_{11} + \theta_2 \frac{\mathcal{D}_1}{\mathcal{D}_{12}} \Gamma_{21} \right) \nabla \theta_1 + \left(\Gamma_{22} + \theta_2 \frac{\mathcal{D}_1}{\mathcal{D}_{21}} \Gamma_{12} + \theta_2 \frac{\mathcal{D}_1}{\mathcal{D}_{12}} \Gamma_{22} \right) \nabla \theta_2}{1 + \theta_2 \frac{\mathcal{D}_1}{\mathcal{D}_{12}} + \theta_1 \frac{\mathcal{D}_2}{\mathcal{D}_{21}}} \right]$$

(6.29)

Knowing the individual fluxes from the binary mixture experiments (J_1 and J_2), the pure component adsorption isotherm parameters (K_1, K_2, q_1^{sat} and q_2^{sat}) and the pure component diffusivity data ($\mathcal{D}_1$ and $\mathcal{D}_2$) allows the calculation of the M-S exchange diffusivities between molecules, i.e. $\mathcal{D}_{12}$ and $\mathcal{D}_{21}$ (m^2/s), from these 2 equations (6.28 and 6.29). To do that, the membrane thickness (6 μm) is divided into N differential elements of equal thickness (δz) along the direction of the gas permeation (z). The 1st differential element is the element in contact with high pressure side (feed stream) while the Nth differential element is the element in contact with the low pressure side (permeate stream). Starting with initial guesses for M-S exchange diffusivity values ($\mathcal{D}_{12}$, $\mathcal{D}_{21}$), and by using the individual fluxes from the binary mixture experiments (J_1 and J_2), the pure components' adsorption data (K_1, K_2, q_1^{sat} and q_2^{sat}) and the pure component diffusivity data ($\mathcal{D}_1$ and $\mathcal{D}_2$), Eq. 6.28 and Eq. 6.29 can be solved simultaneously for $\delta\theta_1$ and $\delta\theta_2$ for each differential element in sequence starting from the 1st differential element. This allows the determination of the surface coverage values for each differential element (θ_1 and θ_2) throughout the membrane as well as the surface coverage values (θ_1 and θ_2) at the low pressure side of the membrane.

These values are compared with the respective values that were determined experimentally at the low pressure side of the membrane. If they don't match, the above calculation is repeated using updated M-S exchange diffusivities, $\mathbb{D}_{12}$ and $\mathbb{D}_{21}$. This procedure continues until the surface coverage values (θ_1 and θ_2), at the low pressure side of the membrane evaluated using the guessed M-S exchange diffusivities match the respective values that were determined experimentally. The complete derivation of Eq. 6.28 and Eq. 6.29 as well as the detailed solution algorithm are presented in appendix in A2.

It is important to emphasize that the adsorption isotherm data as well as the adsorption parameters for the two gases under study were obtained from a previous work done by the current authors [19]. These adsorption data were obtained with a silicalite-1 sample prepared using the same synthesis procedure utilized to synthesize the membrane used in this study. Moreover, the adsorption isotherm temperature was the same as the permeation experiment temperature. The saturation adsorption capacities (q_i^{sat}) for CO_2 and N_2 were 2.993 and 1.697 (mol/kg), respectively, while the Langmuir adsorption coefficients (K_i) for CO_2 and N_2 were 1.194 and 0.153 (atm^{-1}), respectively.

Exchange diffusivities could be also estimated by assuming that $\mathbb{D}_{12}$ equals $\mathbb{D}_{21}$ using either Eq. 6.28 or Eq. 6.29. Each of these equations can be solved independently for the value of the exchange diffusivity. The estimated exchange diffusivity from Eq. 28 and Eq. 29 will be denoted in this context by D^* and D^{**}, respectively. The estimations above were performed using average values of the fractional occupancies, θ_1 and θ_2, in both sides of the membrane. Single site Extended Langmuir Isotherm (Eq. 6.23) was used to calculate these average

values based of the composition profile in each side of the membrane and by assuming a constant total pressure in both sides.

Exchange diffusivities could be as well estimated from M-S pure components diffusivities, $Đ_1$ and $Đ_2$, and fractional occupancies, θ_1 and θ_2, using the interpolation correlation proposed by Krishna [39] based on the Vignes formula [40]:

$$Đ_{12} = Đ_1^{\theta_1/(\theta_1+\theta_2)} Đ_2^{\theta_2/(\theta_1+\theta_2)} \tag{6.30}$$

Eq. 6.30 suggests that $Đ_{12}$ and $Đ_{21}$ are equal and it provides a good estimation of the exchange diffusivities when the adsorption saturation capacities for the two components in the mixture, q_1^{sat} and q_2^{sat}, are equal. However, when they are different, the symmetry assumption of the exchange diffusivities failed [41-43] and a more general analysis considering that the exchange diffusivities are not equal is required. It has been also shown that Eq. 6.30 overestimated the exchange diffusivities, suggesting that the interactions between the components are stronger than what is expected by the above interpolation formula [41]. The saturation adsorption capacities for CO_2 and N_2 gases on silicalite-1 were not equal as previously shown. Thus, it is more appropriate to consider the exchange diffusivities as non-equal when modeling CO_2 /N_2 mixtures permeation through silicalite-1 membranes. Nevertheless, both scenarios will be considered in this work and Eq. 6.28 and 6.29 will be solved twice. In first scenario the exchange diffusivities will be assumed equal while in the other, they will be assumed non equal. Furthermore, the exchange diffusivities

will be also estimated using Eq. 6.30 and compared to the exchange diffusivities resulted from both scenarios.

6.4. Results

6.4.1 Single Component Permeation

The single component fluxes of CO_2 and N_2 as a function of feed pressure at 23^{o}C are shown in Fig. 6-2. Both fluxes are increasing continuously with increasing feed pressure, however, the CO_2 flux is greater than the N_2 flux within the pressure range studied in this work. This behaviour can be described by the shape of their adsorption isotherms [19,44,45]. The kinetic diameter of CO_2 and N_2 (3.3 Å and 3.6 Å, respectively,) are smaller than the pore size of the silicalite-1 (~5.5 Å). This suggested that the surface diffusion is the transport mechanism of these two gases through silicalite-1 membrane [44,46]. In surface diffusion, the gas molecules are adsorbed and desorbed at the high pressure side and low pressure side of the membrane, respectively. The difference of the adsorption capacities creates the driving force for the molecule to diffuse from the high pressure side to the low pressure side of the membrane. Since this driving force is larger for CO_2, between these pressures, its flux is larger than that for N_2. Similar behaviour was reported by Sebastian et al. [47] for ZSM-5 membranes. Moreover, the CO_2 and N_2 fluxes observed in this work are comparable to the values reported by Sebastian et al. [47].

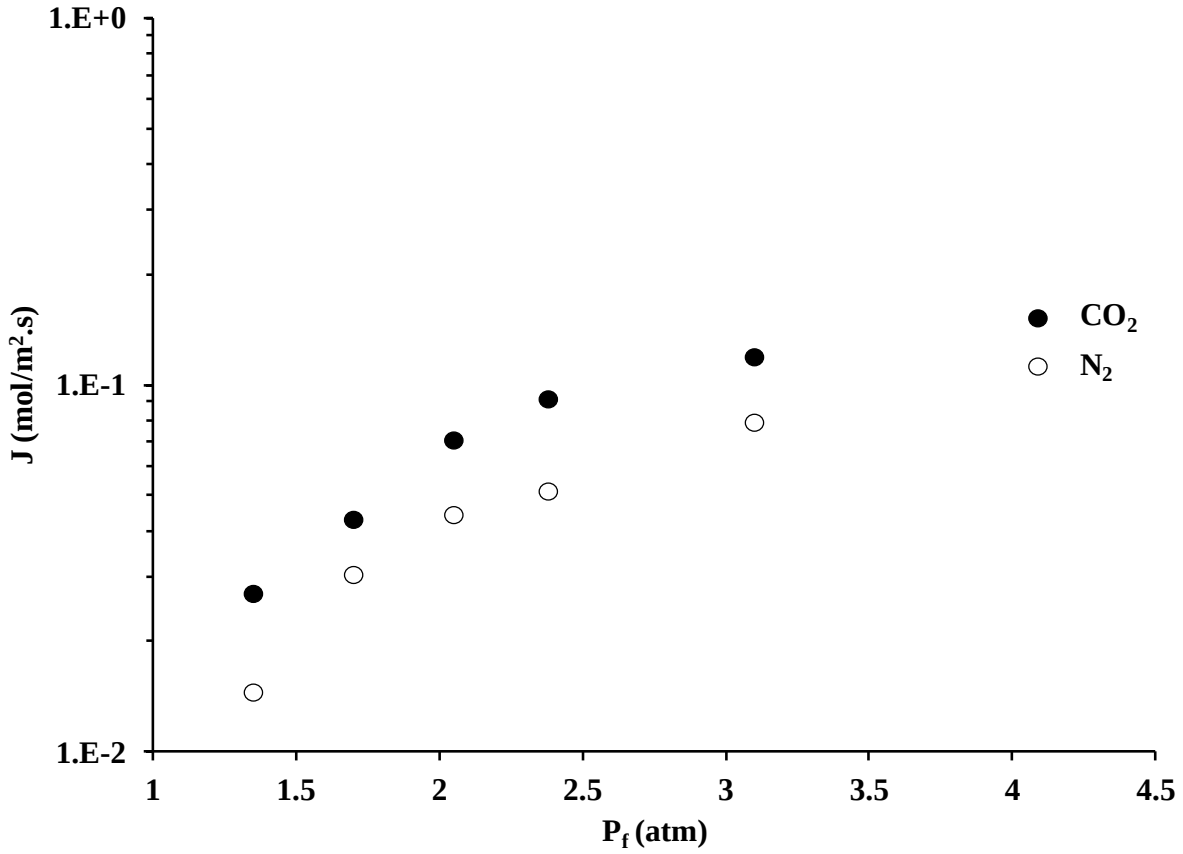

Figure 6-2 Single component CO_2 and N_2 permeation fluxes through silicalite-1 membrane as a function of feed pressure. All experiments were performed at ambient temperature (23ºC) with permeate side open to atmospheric pressure.

Fig. 6-3 shows the single component CO_2 and N_2 permeances as a function of feed pressure at 23ºC. Both permeances were decreasing continuously with increasing feed pressure. It can be also seen that the CO_2 permeances decrease slightly faster than the N_2 permeances with increasing feed pressure. This is also clear from the decrease of the CO_2/N_2 ideal selectivity, in the same figure, with increasing feed pressure. This behaviour is predictable from the shape of the CO_2 and N_2 adsorption isotherm. The CO_2 adsorption capacity increases with pressure, while the slope of the adsorption isotherm gradually decreases. On

the other hand, the N_2 adsorption isotherm is almost linear with a constant slope in the pressure range studied. The CO_2 and N_2 fluxes and permeances observed in this work are approximately one order of magnitude higher than that reported by Zhu et al. [44] and Bakker et al. [46]. However, the CO_2/N_2 ideal selectivities are comparable to the values reported by Bakker et al. [46] for silicalite-1 membrane supported on stainless steel, and Algieri, et al. [48] for silicalite-1 membrane supported on alumina.

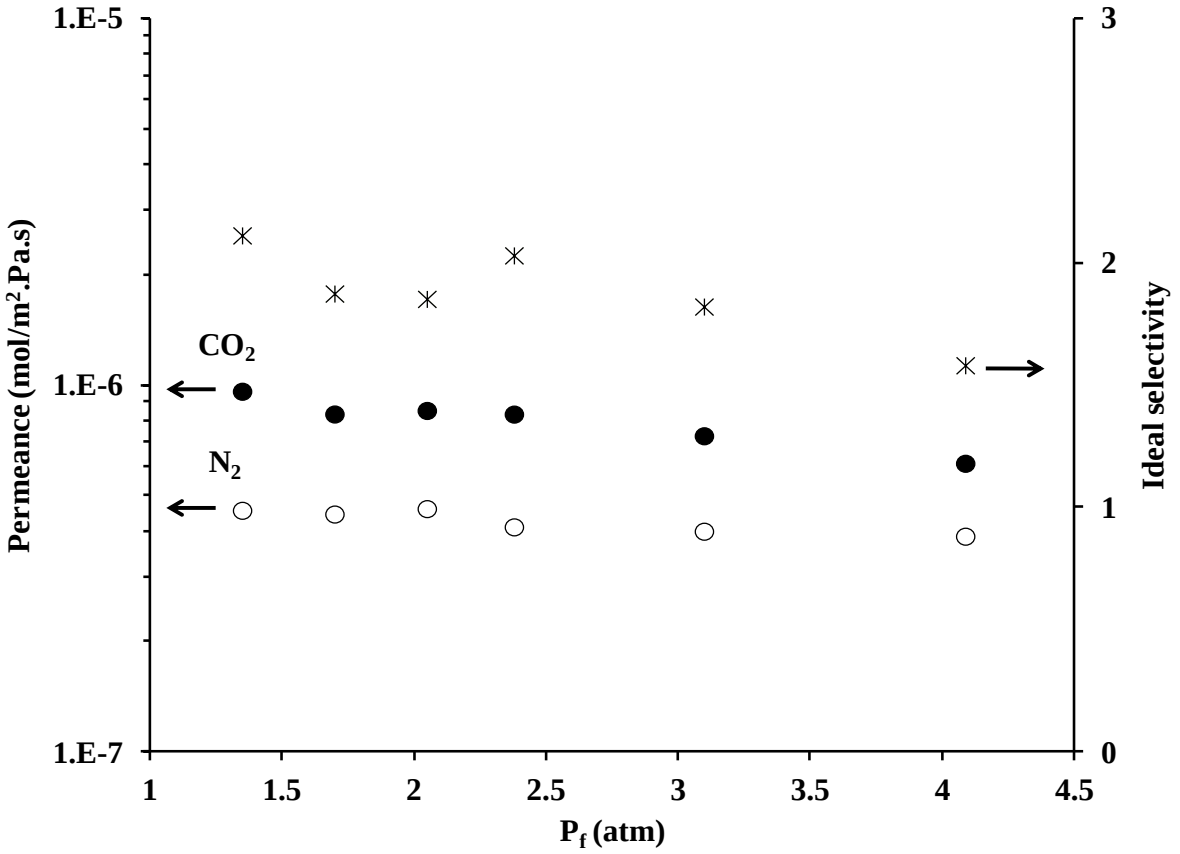

Figure 6-3 Single component CO_2 (●) and N_2 (○) permeances through silicalite-1 membrane as well as ideal selectivities (∗) as a function of feed pressure. All experiments were performed at ambient temperature (23°C) with permeate side open to atmospheric pressure.

6.4.2 Single Component Diffusivities

The dependence of the corrected diffusivity (m^2/s) or single component Maxwell-Stefan diffusivity ($Đ_i$) on the feed pressure at 23°C is revealed in Fig. 6-4. It is evident from Fig. 6-4 that both CO_2 and N_2 M-S diffusivities slightly decrease with increasing feed pressure. The N_2 diffusivities decrease from 3.5×10^{-9} to 3.0×10^{-9} (m^2/s), while the CO_2 diffusivities decrease from 1.3×10^{-9} to 1.1×10^{-9} (m^2/s) by increasing the feed pressure from 1.35 to 4.10 atm. The decrease of CO_2 and N_2 single component M-S diffusivities resulting from the increase of the total feed pressure is around 17% and 15%, respectively (from values in Fig. 6-4). On the other hand, the corresponding decrease of CO_2 and N_2 single component permeances resulting from the same increase of the total feed pressure is around 58% and 64%, respectively (from values in Fig. 6-3). Thus, the increase of the feed pressure has a less significant effect on the single component diffusivities compared to the single component permeances.

The CO_2 and N_2 single component M-S diffusivity values are comparable to those reported in literature by Bakker et al. [46] for silicalite-1 membranes prepared with stainless steel support and by Selassie et al. [49] for silicalite-1 membranes using molecular simulation. Selassie et al. [49] results showed similar slight decrease of the M-S diffusivities with increasing fractional loading. However, the diffusivity values reported in the present study are higher than the diffusivity values reported by Gardner et al. [50] for H-ZSM-5 for CO_2 and N_2 of around 1.5×10^{-10} and 8.2×10^{-10} (m^2/s), respectively. These lower diffusivity values reported by Gardner et al. can be explained by the lower adsorption capacity of CO_2 and N_2 on H-ZSM-5 [50] compared to silicalite-1 [19]. In contrast, the diffusivities reported in the present study are significantly lower than the CO_2 diffusivity of 1.76×10^{-7} (m^2/s)

reported by Zhu et al. [44] for silicalite-1 membrane prepared over stainless steel support, and the N_2 diffusivity of 5.6 x 10^{-8} (m^2/s) reported by Jareman et al. [14] for ZSM-5 membrane prepared over alumina support. These higher diffusivity values reported by Zhu et al. [44] resulted from simplifying Eq. 6.10 by assuming a linear adsorption isotherm instead of a Langmuir adsorption isotherm at low pressures. On the other hand, Jareman et al. [14] higher diffusivity values resulted from accounting for the defects flow and substrate effects.

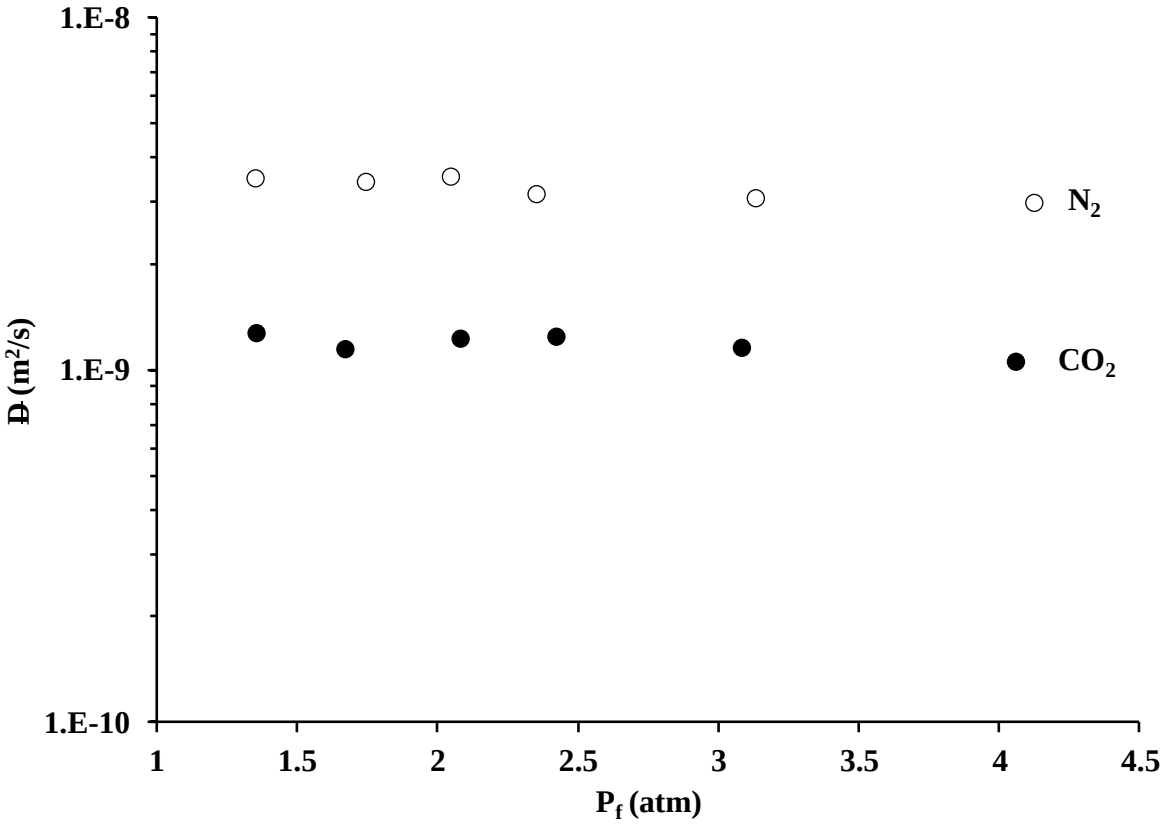

Figure 6-4 Single component CO_2 and N_2 M-S diffusivities in silicalite-1 membrane as a function of total feed pressure at 23°C.

6.4.3 Binary Mixture Permeation

The effect of the total feed pressure on the CO_2 and N_2 fluxes for equimolar binary mixtures in the feed stream at 23^oC are demonstrated in Fig. 6-5. Both fluxes increase continuously with increasing total feed pressure. Furthermore, the CO_2 flux is greater than the N_2 flux in the pressure range studied. The CO_2 flux is increasing at a rate higher than that observed for the N_2 flux as a function of the total feed pressure. It can be seen from Fig. 6-5 that the N_2 flux is levelling off and tends to reach a plateau with increasing total feed pressure. The fluxes from the equimolar binary mixture experiments are lower than the fluxes from single components experiments for N_2 and they are about the same for CO_2 (see Fig. 6-2 and Fig. 6-5). It is important to emphasize that when comparing Fig. 6-2 and Fig. 6-5, it has to be taken into account that P_f in Fig. 6-5 is the total feed pressure and the partial pressure of CO_2 and N_2 would be half of P_f for the equimolar binary mixture. This decrease of N_2 flux is a result of the competitive adsorption that is taking place between CO_2 and N_2.

It is also evident from comparing Fig. 6-2 and Fig. 6-5 that the decrease of N_2 permeation flux is significantly higher than the decrease of the CO_2 permeation flux for the equimolar binary results compared to the single components permeation results. This is due to the overwhelming control of the CO_2 - N_2 .binary behaviour by the CO_2 molecules. It is also clear from Fig. 6-5 that as the feed pressure increases the difference between CO_2 and the N_2 permeation fluxes increases for the equimolar binary experiments. This is also due to the competitive adsorption between CO_2 and N_2 molecules in silicalite-1 pores. Since CO_2 is more strongly adsorbed than N_2 by silicalite-1, CO_2 occupied most of the adsorption sites and blocked the N_2 permeation paths resulting in more decrease of the N_2 permeation rate compared to the single component results as the feed pressure increases.

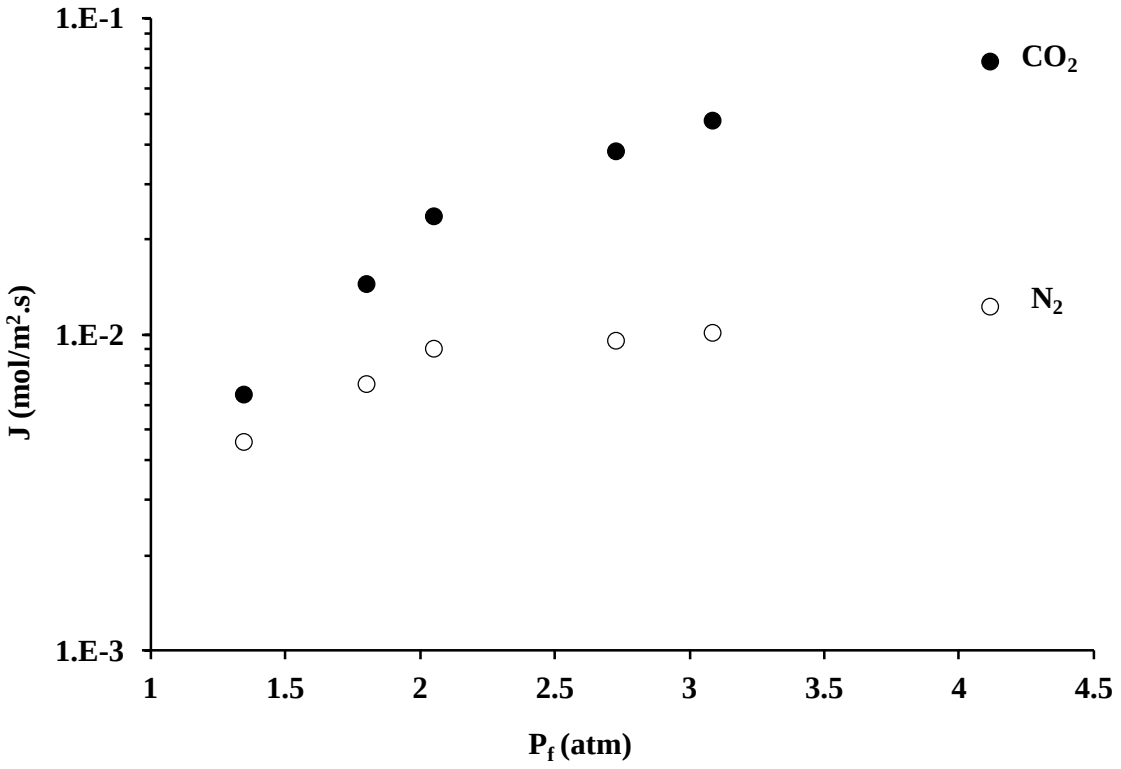

Figure 6-5 CO_2 and N_2 permeation fluxes through silicalite-1 membrane, from equimolar binary mixture experiments in the feed, as a function of total feed pressure. All experiments were performed at ambient temperature (23°C) with permeate side open to atmospheric pressure.

The CO_2 and the N_2 average fluxes from the single component experiments were 0.0840 and 0.0554 (mol/m^2.s), respectively, while the CO_2 and the N_2 average fluxes from the equimolar binary experiments were 0.0341 and 0.0088 (mol/m^2.s), respectively. The CO_2 and the N_2 flux values and behaviour observed in this work for the equimolar binary mixtures are comparable to the values and behaviour reported by Sebastian et al. [47] for ZSM-5 membranes.

Fig. 6-6 shows the CO_2 and the N_2 permeances as well as the CO_2/N_2 permselectivities as a function of the total feed pressure at 23^oC for equimolar binary mixture experiments in the feed stream. Both permeances are decreasing continuously with increasing total feed pressure in the pressure range studied. As the total feed pressure increases from 1.34 to 4.11 atm, the CO_2 permeances decrease from 2.3 x 10^{-6} to 9.6 x 10^{-7} mol/ m^2.s.Pa and the N_2 permeances decrease from 1.7 x 10^{-7} to 6.8 x 10^{-8} mol/ m^2.s.Pa. However, the CO_2 permeances are decreasing in a slightly higher rate than the N_2 permeances with the total feed pressure. This decrease can be also seen from the slight increase of the CO_2/N_2 permselectivities with increasing total feed pressure up to 2 atm, then the slight decrease of the permselectivities by increasing total feed pressure to higher values. This decrease in permselectivities at higher feed pressure values is expected and it is due to the increased contribution of the non-selective transport through defects as the pressure increases (Knudsen diffusion and/or Poiseuille flow). This could be also due to the decrease of the adsorption capacity difference between the CO_2 and the N_2 in silicalite-1 as the pressure increases [19,44,45,47]. Similar decrease of CO_2/N_2 permselectivities with increasing total feed pressure was also reported in reference [51].

It is evident from comparing Fig. 6-3 and Fig. 6-6 that the CO_2 permeances from single component experiments and from equimolar binary experiments are approximately the same, considering the fact that the total feed pressure, P_f, in Fig. 6-6 is twice the partial pressure of CO_2 and N_2, for the equimolar binary feed mixture. Conversely, the N_2 permeances from the single component experiments are almost seven times higher than the permeances from the equimolar binary experiments. This decrease of the N_2 permeances as

mentioned earlier is due to the competitive adsorption and the blocking effect due to the CO_2 presence in the silicalite-1 pores.

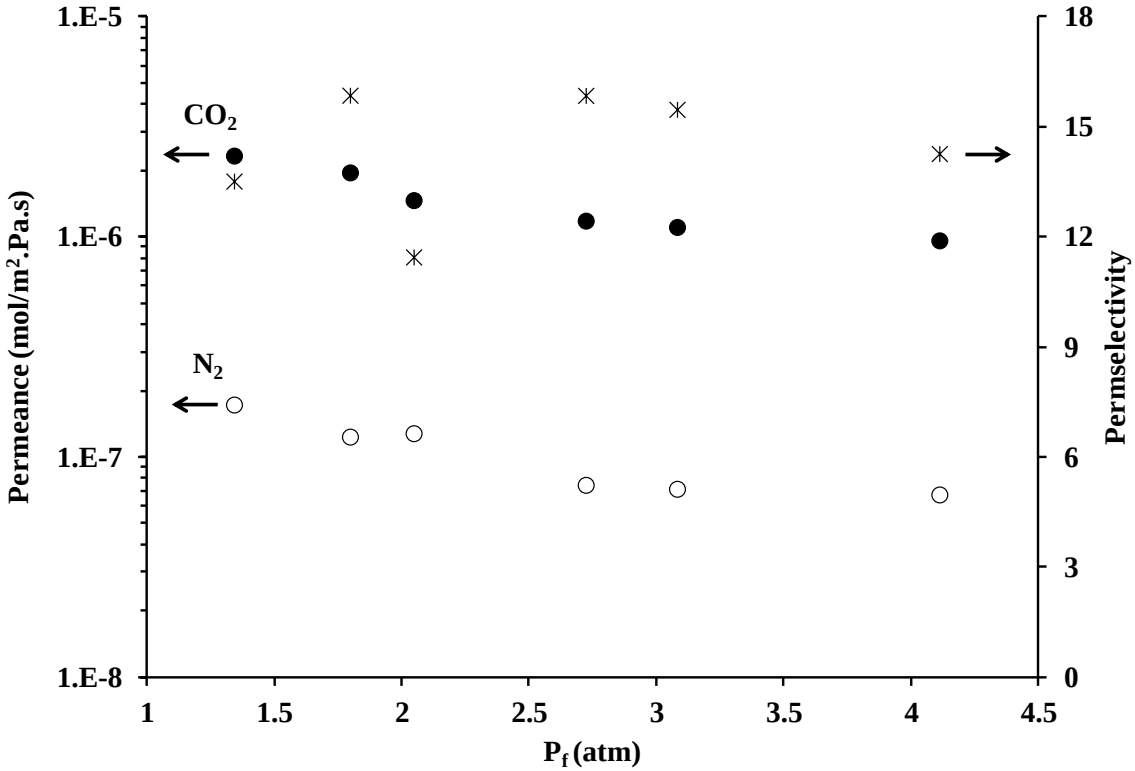

Figure 6-6 CO_2 (●) and N_2 (○) permeances through silicalite-1 membrane as well as permselectivities (∗), from equimolar binary mixture experiments in the feed, as a function of total feed pressure. All experiments were performed at ambient temperature (23ºC) with permeate side open to atmospheric pressure.

The effect of the feed composition on the fluxes of CO_2 and N_2 gases for their binary mixtures at 2 atm total feed pressure and 23ºC are presented in Fig. 6-7. As can be seen from this figure, when the CO_2 composition increases, the CO_2 flux increases gradually and the N_2 flux decreases sharply. Comparing these results with the single component results

(shown in Fig. 6-2), it is obvious that the flux of CO_2 is barely affected by the presence of N_2; however, the N_2 flux is notably reduced by the presence of CO_2. This behaviour is expected for mixtures consisted of a fast diffusing component (N_2) that is weakly adsorbed and a slow diffusing component (CO_2) that is strongly adsorbed, when both of them can fit easily inside the membrane pores [13,18,52]. This behaviour is attributed to the micropore diffusion mechanism, where the presence of the molecules of one component in the mixture hindered the permeation of the molecules of the other component.

Fig. 6-8 demonstrates the effect of CO_2 composition in the feed on the CO_2 and N_2 permeances, as well as the CO_2/N_2 permselectivities at 2 atm total feed pressure and 23^{o}C. It is clear from this figure that the N_2 permeances decrease continuously with the increase of the CO_2 composition in the feed, while the CO_2 permeances decrease when the CO_2 composition in the feed increases at low concentrations, and then level off and reach a plateau with the increase of the CO_2 composition in the feed at higher values. These binary CO_2 permeances are comparable to the CO_2 permeance values observed from the single component permeation experiments (see Fig. 6-3). On the other hand, the N_2 permeances drop from around 4.6×10^{-7} mol/ m^2.s.Pa for the single component at 2 atm (from Fig. 6-3) to around 3.7×10^{-8} mol/ m^2.s.Pa for the 85% CO_2 composition in the feed (from Fig. 6-8). The drop in the N_2 permeances is more than one order of magnitude. This drop of the N_2 permeances in the presence of CO_2 is a result of a preferential adsorption of CO_2 on silicalite-1 [19,44,45]. Furthermore, since the pore size of silicalite-1, which is around 5.5 Å, is less than the summation of the kinetic diameters of CO_2 (3.3 Å) and N_2 (3.6 Å), the adsorbed CO_2 molecules block the pores and reduce the N_2 molecules' access to the pores as

discussed earlier [13,18,52]. This leads to CO_2/N_2 permselectivities as high as 26.5 evident in Fig. 6-8.

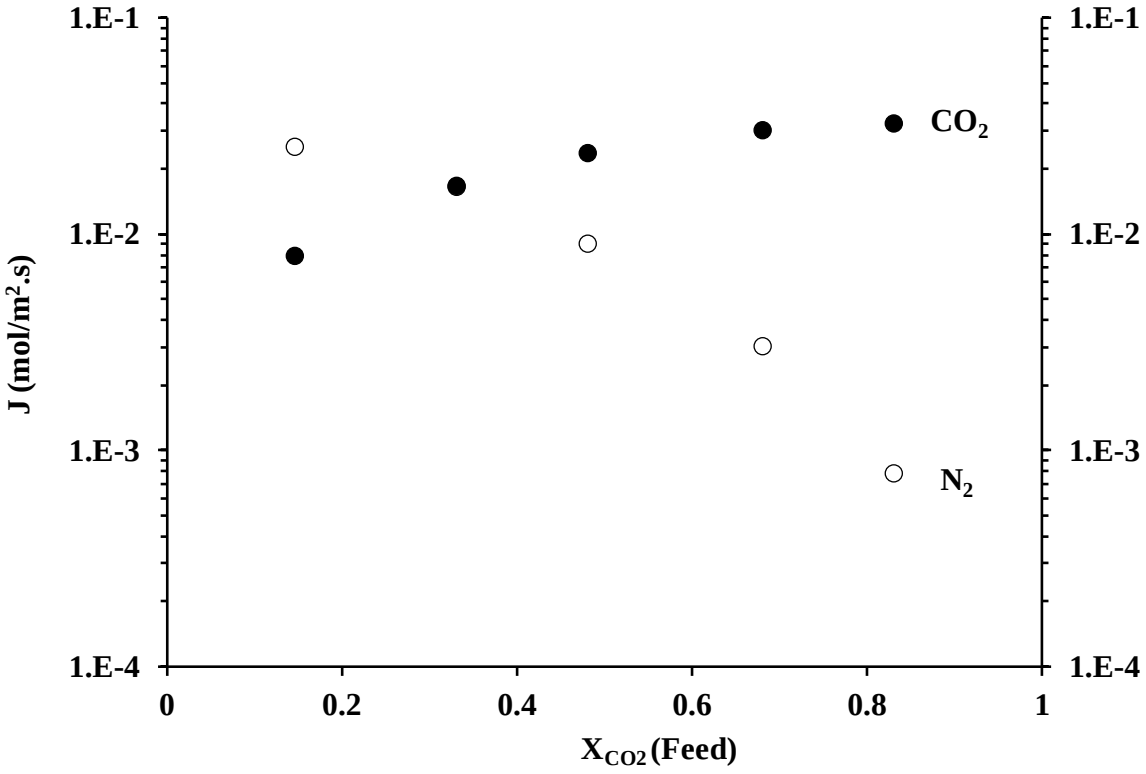

Figure 6-7 CO_2 and N_2 permeation fluxes through silicalite-1 membrane as a function of CO_2 mole fraction in the feed with 2 atm total feed pressure. All experiments were performed at ambient temperature (23°C) with permeate side open to atmospheric pressure.

It is evident from the previous permeation results that it is tricky to characterize the membrane using the CO_2/N_2 permselectivity and/or the CO_2 and N_2 permeances. These characteristics vary over a wide range and found to be highly dependent on the operating

conditions such as total feed pressure and feed composition. Hence, a better characterization of this membrane is required, where the aimed characteristics are independent or less dependent on the experimental conditions, than the permselectivity and the permeances. Maxwell- Stefan exchange diffusivities could provide a better characterization for the membrane and could be less dependent on the experimental conditions.

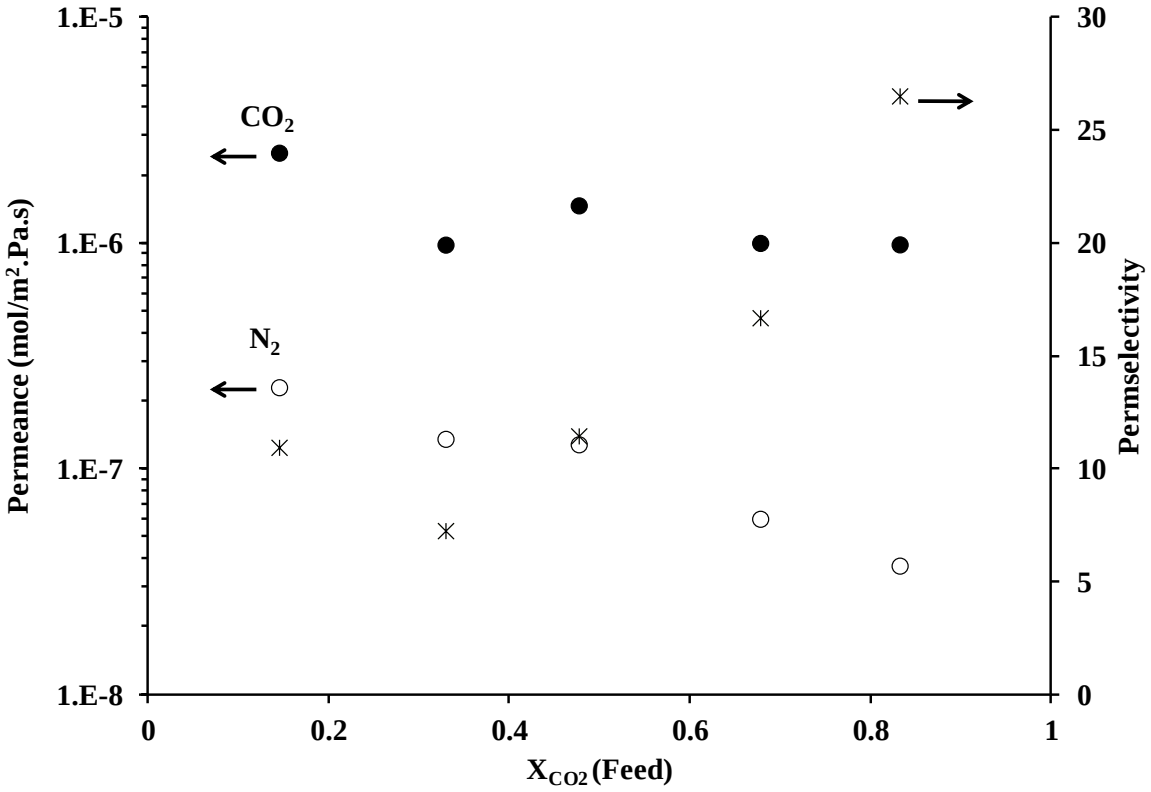

Figure 6-8 CO_2 (●) and N_2 (○) permeances through silicalite-1 membrane as well as permselectivities (✳) as a function of CO_2 mole fraction in the feed with 2 atm total feed pressure. All experiments were performed at ambient temperature (23°C) with permeate side open to atmosphere.

6.4.4 Binary Mixture Exchange Diffusivities

The effects of the total feed pressure and the feed composition on the M-S exchange diffusivities are illustrated in Fig 6-9 and Fig. 6-10. These figures show the calculated exchange diffusivities from the solution of Eq. (6.29) and Eq. (6.30) assuming that $Đ_{12}$ and $Đ_{21}$ are non-equal in one case ($Đ_{12}$ and $Đ_{21}$) and equal in another case ($Đ_{12}^{*}$ and $Đ_{12}^{**}$). The exchange diffusivity calculated using Vignes correlation (Eq. 6.30) is also shown in these figures.

As seen in Fig. 6-9, the M-S exchange diffusivities calculated assuming that $Đ_{12}$ and $Đ_{21}$ are non-equal ($Đ_{12}$ and $Đ_{21}$) appear to be somehow independent of the total feed pressure. The average $Đ_{12}$ and $Đ_{21}$ values are around 1.32×10^{-10} and 1.38×10^{-10} (m^2/s), respectively. It is expected that the increase in the total feed pressure would result in a decrease of the exchange diffusivities. This is due to the fact that an increase in the total feed pressure would result in an increase in total loading. The increase of the total loading leads usually to a decrease in the M-S exchange diffusivities [49,53]. This effect is anticipated given that the increase in the total loading results in more interactions between the molecules. These interactions lead to more resistance to the molecules' motion which in turn lowers the diffusivity values. It is evident from the relatively low values of $Đ_{12}$ and $Đ_{21}$ that there is a strong interaction between CO_2 and N_2 molecules. The opposite would imply a weak interaction between CO_2 and N_2 molecules [49]. When there is no interaction between the diffusing components, $Đ_{12}$ and $Đ_{21}$ would approach infinity and the binary diffusivities would approach the single components diffusivities.

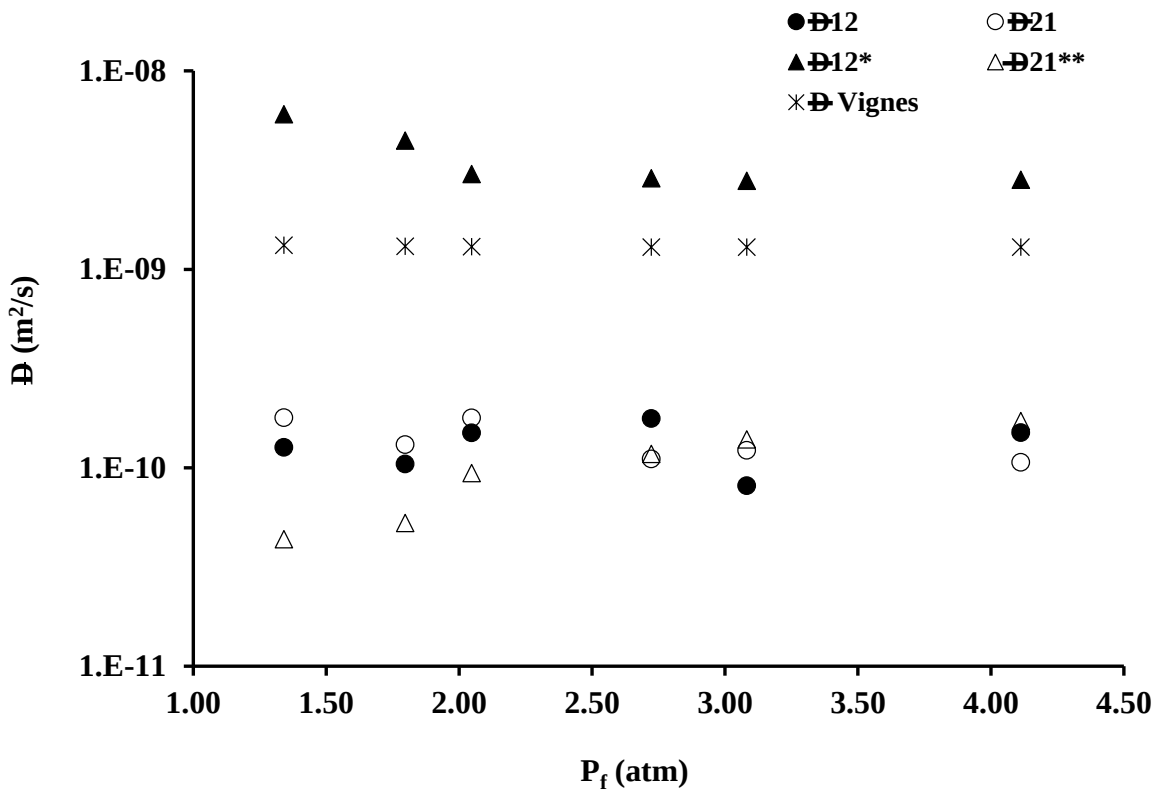

Figure 6-9 CO_2 and N_2 M-S exchange diffusivities estimated assuming non-equal diffusivities (D_{12}, D_{21}), assuming equal diffusivities (D_{12}^{*}, D_{12}^{**}), and by Vignes correlation (D Vignes) in silicalite-1 membrane as a function of total feed pressure for equimolar binary mixtures at 23°C.

The exchange diffusivity values calculated from Eq. 6.28 assuming $Đ_{12}$ and $Đ_{21}$ are equal ($Đ_{12}^{*}$) were decreasing with the increase of the total feed pressure. They were more than one order of magnitude higher than the calculated exchange diffusivity values obtained from Eq. 6.29 assuming $Đ_{12}$ and $Đ_{21}$ are equal ($Đ_{12}^{**}$). At low feed pressure up to 2 atm, the ($Đ_{12}^{**}$) values appear to be lower than the values of the exchange diffusivities calculated assuming $Đ_{12}$ and $Đ_{21}$ are non-equal. The ($Đ_{12}^{**}$) values were increasing with the feed pressure approaching the $Đ_{12}$ and $Đ_{21}$ values at feed pressures larger than 2.7 atm. Fig. 6-9 also shows

that the exchange diffusivities calculated using Vignes correlation are virtually constant and around 1.3 x 10^{-10} (m^2/s). They are less than the ($Đ_{12}^{*}$) values but much higher than the ($Đ_{12}^{**}$) values and the values of the exchange diffusivities calculated assuming $Đ_{12}$ and $Đ_{21}$ are non-equal.

It is evident from Fig 6-10 that the M-S exchange diffusivity values, calculated assuming that $Đ_{12}$ and $Đ_{21}$ are non-equal ($Đ_{12}$ and $Đ_{21}$), decrease with the increase of the CO_2 composition in the feed. As the CO_2 composition increased from 15% to 85%, $Đ_{12}$ and $Đ_{21}$ decreased from 2.8 x 10^{-10} to 1.1 x 10^{-10} (m^2/s) and from 2.8 x 10^{-10} to 1.3 x 10^{-10} (m^2/s), respectively. In comparison to the exchange diffusivities values calculated assuming they are equal ($Đ_{12}^{*}$ and $Đ_{12}^{**}$), the ($Đ_{12}^{**}$) were slightly lower than the values of the exchange diffusivities calculated assuming $Đ_{12}$ and $Đ_{21}$ are non-equal at CO_2 composition in the feed up to 50%. At higher CO_2 composition the ($Đ_{12}^{**}$) and $Đ_{12}$ and $Đ_{21}$ values were approximately the same. The ($Đ_{12}^{*}$) were decreasing with the increase of the CO_2 composition in the feed. They were around one order of magnitude higher than the exchange diffusivity values calculated from Eq. 6.29 assuming $Đ_{12}$ and $Đ_{21}$ are equal ($Đ_{12}^{**}$) and the exchange diffusivity values calculated assuming $Đ_{12}$ and $Đ_{21}$ are non-equal. The exchange diffusivities calculated using Vignes correlation were decreasing with increasing CO_2 composition in the feed. As seen previously in Fig. 6.9, the exchange diffusivities calculated using Vignes correlation in Fig. 6.10 were less than the ($Đ_{12}^{*}$) values but much higher than the ($Đ_{12}^{**}$) values and the values of the exchange diffusivities calculated assuming $Đ_{12}$ and $Đ_{21}$ are non-equal.

The dependency of the exchange diffusivities on the composition of the feed mixture is anticipated. This is due to the fact that the high adsorbed and slow diffusing component (CO_2) normally controls the flow inside the micropores, and as the slow diffusing component composition increases in the mixture, the exchange diffusivities decrease.

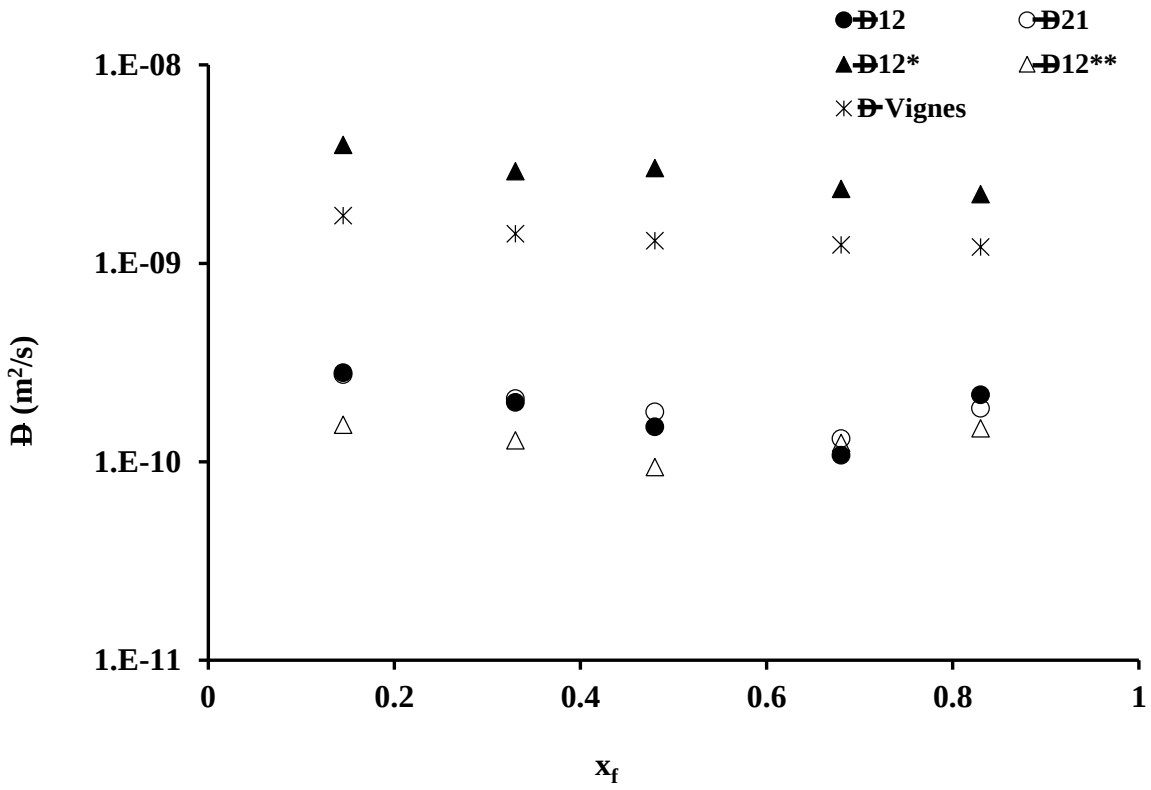

Figure 6-10 CO_2 and N_2 M-S exchange diffusivities estimated assuming non-equal diffusivities (D_{12}, D_{21}), assuming equal diffusivities (D_{12}^{*}, D_{12}^{**}), and by Vignes correlation (D Vignes) in silicalite-1 membrane as a function of CO_2 mole fraction in the feed with 2 atm total feed pressure at 23°C.

It should be emphasized that $Đ_{12}$ and $Đ_{21}$ values calculated using Eq. 6.28 and Eq. 6.29 assuming that the exchange diffusivities are non-equal are not identical but they were very

close to each other. This gives the impression that assuming them identical may not generate a significant error when estimating the mixture separation performance. However, when the calculations were repeated assuming them equal, exchange diffusivity values estimated by Eq. 6.28 were more than an order of magnitude higher than the exchange diffusivity values estimated by Eq. 6.29. This substantial difference could be due to the fact that the assumption of the equality of the exchange diffusivity is only valid when the adsorption saturation capacities for the two components in the mixture, q_1^{sat} and q_2^{sat}, are equal. This is not a valid assumption for CO_2 and N_2 mixtures with silicalite-1 zeolite. This also explains the significantly high exchange diffusivity values estimated using Vignes correlation. Vignes correlation overestimate the exchange diffusivities, [41] when adsorption saturation capacities for the two components in the mixture, q_1^{sat} and q_2^{sat}, are not equal.

Despite the significant difference between the exchange diffusivity values calculated using different correlations or assumptions, the results showed that the exchange diffusivities present a better characterization for the permeation through the silicalite-1 membrane with less dependency on the experimental conditions, i.e, total feed pressure and feed composition, compared to the permselectivity and permeance data. Hence, the use of the exchange diffusivities instead of permeances seems to provide a more accurate tool for designing zeolite membrane separation units.

6.5 Conclusions

The single component and binary mixtures of CO_2 and N_2 permeation using a silicalite-1 membrane was investigated in this study with respect to the total feed pressure and feed

composition. A total feed pressure of up to 4 atm and five different feed compositions (CO_2 mole% of 15%, 30%, 50%, 70% and 85%) were investigated. The gas permeation experiments revealed a very high permeable membrane with CO_2 permeances in the order of 10^{-6} mol/ m^2.s.Pa with a relatively high permselectivity of 26.5. Nevertheless, the membrane characteristics, i.e. CO_2/N_2 permselectivity as well as the CO_2 and N_2 permeances, were found to be varied over a wide range and highly dependent on the experimental operating conditions, such as the total feed pressure and the feed composition. For instance, the N_2 permeance decreased by around one order of magnitude from 2.7 x 10^{-7} to 2.4 x 10^{-8} mol/ m^2.s.Pa by increasing the CO_2 composition in the feed from 15% to 85%. A better characterization of the membrane using the Maxwell-Stefan exchange diffusivities is provided in this work, where the M-S exchange diffusivities could be less dependent on the experimental conditions.

Detailed models were successfully developed based on Maxwell-Stefan equations to describe the single component and the CO_2 - N_2 binary mixtures' diffusion through the silicalite-1 membrane. These models required the use of only pure component adsorption and diffusivity data and employed the Extended Langmuir adsorption isotherm. The developed models allowed the estimation of the single component corrected or M-S diffusivities for CO_2 and N_2 as well as the M-S exchange diffusivities, $Đ_{12}$ and $Đ_{21}$, for their binary mixtures.

The single component M-S diffusivities were found to be decreasing from 1.3 x 10^{-9} to 1.1 x 10^{-9} (m^2/s) for CO_2 and from 3.5 x 10^{-9} to 3.0 x 10^{-9} (m^2/s) for N_2, by increasing the feed

pressure from 1.35 to 4.10 atm. This decrease is found to be 15% at the most. Moreover, the M-S exchange diffusivities evaluated using the developed models and based on the experimental data, with assuming the exchange diffusivities are non-equal, were observed to be independent of the total feed pressure. However, they showed to be decreasing by increasing the concentration of CO_2 in the feed. As the latter increased from 15% to 85%, $Đ_{12}$ and $Đ_{21}$ decreased from 2.8 10^{-10} m^2/s to 1.1 x 10^{-10} and from 2.8 x 10^{-10} m^2/s to 1.3 x 10^{-10} (m^2/s), respectively. This confirmed that the exchange diffusivities provide significantly smaller dependence on the operating conditions compared to the permselectivity and permeance data. Thus, they offer a better characterization of the intrinsic transport properties of silicalite-1 membranes.

The exchange diffusivities values estimated using M-S equations model assuming equal exchange diffusivities and using Vignes correlation were significantly high compared to the estimated values using M-S equations assuming the exchange diffusivities are non-equal. That is due to the strong interaction between CO_2 and N_2 molecules and to the difference of their adsorption saturation capacities on silicalite-1.

Acknowledgments

The authors acknowledge the financial support received from Natural Science and Engineering Research Council (NSERC) of Canada, the Ontario Graduate Scholarship (OGS) program and from the University of Ottawa.

Nomenclatures:

A_m: membrane permeation area (m^2).

Å: Angstrom.

B_i: the mobility of component *i* ($mol.m^2/J.s$)

c: the molar concentration (mol/ m^3)

D: the transport diffusivities (m^2/s)

D_0: corrected transport diffusivities (m^2/s)

$\mathbb{D}_i$: Maxwell-Stefan diffusivity (m^2/s)

$\mathbb{D}_{ij}$: Maxwell-Stefan exchange diffusivity between components i and j (m^2/s)

f: friction coefficient ($J.s /mol.m^2$)

K: Langmuir adsorption coefficient (Pa^{-1})

L: zeolite membrane thickness (m)

J: molar flux across the membrane ($mol/m^2 .s$)

p: partial pressure in the bulk fluid (Pa)

P_i: membrane permeance of component *i* ($mol//m^2.Pa.s$).

q: molar loading of component i (mol/kg)

R: gas constant (8.314 J/mol·K)

T: absolute temperature (K)

u: the flow velocity with respect to the zeolite (m/s)

V: the steady state permeation rate (moles/s)

z: spatial coordinate (m)

Greek letters:

$\alpha^*_{A/B}$: the selectivity of the membrane for separation of gases *A* and *B* (dimensionless)

∇: gradient operator (m^{-1})

ε: porosity of the support (dimensionless)

Γ: elements of matrix of thermodynamic correction factor [Γ] (dimensionless)

θ: occupancy, fractional loading, or surface coverage of component i (dimensionless)

μ: chemical potential (J mol^{-1})

ρ: density (kg m^{-3})

τ: tortuousity (dimensionless)

Subscripts:

0: standard state

1, 2: components 1 and 2

i, j, k: components i, j and k

A: component A

P: membrane permeate side

R: membrane retentate side

s: solid zeolite

Superscript:

sat: saturation value

6.6 References

1- Y.S Lin, I. Kumakiri, N.B. Nair, H. Alsyouri, Microporous inorganic membranes, Sep. Purif. Methods 31 (2002): 229 – 379.

2- F. Jareman, C. Andersson, J. Hedlund, The influence of the calcination rate on silicalite-1 membranes, Microporous Mesoporous Mater. 79 (2005) 1 – 5.

3- Y. Hasegawa, T. Ikeda, T. Nagase, Y. Kiyozumi, T. Hanaoka, F. Mizukami, Preparation and characterization of silicalite-1 membranes prepared by secondary growth of seeds with different crystal sizes, J. Membrane Science, 280 (2006) 397 – 405.

4- S. Fan, J. Liu, F. Zhang, S. Zhou, S. Fun, Fabrication of zeolite MFI membranes supported by α-Al_2O_3 hollow ceramic fibers for CO_2 separation, J. Materials Research 28 (2013) 1870 – 1876.

5- A. Navajas, R. Mallada, C. Tellez, J. Coronas, M. Menendez, J. Santamaria, Study on the reproducibility of mordenite tubular membranes used in the dehydration of ethanol, J. Membrane Science 299 (2007) 166 – 173.

6- H.H. Funke, M.G. Kovalchick, J.L. Falconer, R.D. Noble, Separation of hydrocarbon isomer vapors with silicalite zeolite membranes, Ind. Eng. Chem. Res. 35 (1996) 1575.

7- J. Caro, M. Noack, Zeolite membranes – recent development and progress, Microporous Mesoporous Mater. (2008) 215 – 233.

8- J. Motuzas, R. Mikutaviciute, E. Gerardin, A. Julbe, Controlled growth of thin and uniform TS-1 membranes by MW-assisted heating. Microporous Mesoporous Mater. 128 (2010) 136 – 143.

9- M.P. Pina, R. Mallada, M. Arruebo, M. Urbiztondo, N. Navascués, O. de la Iglesia, J. Santamaria, Zeolite films and membranes. Emerging applications, Microporous Mesoporous Mater. 144 (2011) 19 – 27.

10- L. Rouleau, G. Pringruber, F. Guillou, C. Barrere-Tricca, A. Omegne, V. Valtchev, M. Pera-Titus, S. Miachon, J.A. Dalmon, Nanocomposite MFI-alumina and FAU-alumina membranes: synthesis, characterization and application to paraffin separation and CO_2 capture, Oil Gas Science Technology Rev. 64 (2009) 745 – 758.

11- R. Krishna, Diffusion of binary mixtures across zeolite membranes: entropy effects on permeation selectivity, Int. Comm. Heat Mass Transfer 28 (2001) 337 – 346.

12- A.M. Avila, H.H. Funke, Y. Zhang, J.L. Falconer, R.D. Noble, Concentration polarization in SAPO-34 membranes at high pressures, J. Membrane Science 335 (2009) 32 – 36.

13- J.M. van de Graaf, E. van der Bijl, A. Stol, F. Kapteijn, J.A. Moulijn, Effect of operating conditions and membrane quality on the separation performance of composite silicalite-1 membranes, Ind. Eng. Chem. Res. 37 (1998) 4071 – 4083.

14- F. Jareman, J. Hedlund, D. Creaser, J. Sterte, Modeling of single gas permeation in real MFI membranes, J. Membrane Science 236 (2004) 81 – 89.

15- M. Pan, Y.S. Lin, Template-free secondary growth synthesis of MFI type zeolite membranes, Microporous Mesoporous Mater. 43 (2001) 319 – 327.

16- J. Dong, Y.S. Lin, M.Z.-C. Hu, R.A. Peascoe, E.A. Payzant, Template removal associated microstructural development of ceramic supported MFI zeolite membranes, Microporous Mesoporous Mater. 34 (2000) 241 – 253.

17- S. Miachon, P. Ciavarella, L. van Dyka, I. Kumakiri, K. Fiaty, Y. Schuurman, J. A. Dalmona, Nanocomposite MFI-alumina membranes via pore-plugging synthesis: specific transport and separation properties, J. Membrane Science 298 (2007) 71 – 79.

18- J.M. van de Graaf, F. Kapteijn, J.A. Moulijn, Modeling permeation of binary mixtures through zeolite membranes, AIChE J. 45 (1999) 497 – 511.

19- M. Tawalbeh, B. Kruczek, F.H. Tezel, S. Letaief, C. Detellier, Separation of CO_2 and N_2 gases using a novel zeolite membrane, Separation Science Technology 47 (2012) 1606 – 1616.

20- M. P. Bernal, J. Coronas, M. Menendez, and J. Santamarıa, Separation of CO_2/N_2 mixtures using MFI-type zeolite membranes, AIChE J. 50 (2004) 127 – 135.

21- D.W. Shin, S.H. Hyun, C.H. Cho, M.H. Han, Synthesis and CO_2/N_2 gas permeation characteristics of ZSM-5 zeolite membranes, Microporous Mesoporous Mater. 85 (2005) 313 – 323.

22- M. Tawalbeh, F.H. Tezel, B. Kruczek, S. Letaief, C. Detellier, Synthesis and characterization of silicalite-1 membrane prepared on a novel support by the pore plugging method, J. Porous Materials 20 (2013) 1047 – 1421.

23- R. Krishna, R. Baur, Analytical solution of the Maxwell-Stefan equations for multicomponent permeation across a zeolite membrane, Chemical Engineering J. 97 (2004) 37 – 45.

24- J.G. Martinek, T.Q. Gardner, R.D. Noble, J.L. Falconer, Modeling transient permeation of binary mixture through zeolite membranes, Ind. Eng. Chem. Res. 45 (2006) 6032 – 6043.

25- M. Kanezashi, Y.S. Lin, Gas permeation and diffusion characteristics of MFI-type zeolite membranes at high temperatures, J. Physical Chemestry C 113 (2009) 3767 – 3774.

26- R. Krishna, J.M. van Baten, Hydrogen bonding effects in adsorption of water−alcohol mixtures in zeolites and the consequences for the characteristics of the Maxwell−Stefan diffusivities, Langmuir 26 (2010) 10854 – 10867.

27- M. Pera-Titus,C. Fite, V. Sebastian, E. Lorente, J. Llorens, F. Cunill, Modeling pervaporation of ethanol/water mixtures within ‘real' zeolite NaA membranes, Ind. Eng. Chem. Res. 47 (2008) 3213 – 3224.

28- M. Tawalbeh, F. H. Tezel, M. Al-Ismaily, B. Kruczek, Effect of support pore size on morphology and performance of tubular silicalite-1 membranes” submitted to J. Membrane Science (2013).

29- S. Miachon, E. Landrivon, M. Aouine, Y. Sun, I. Kumakiri, Y. Li, O. Pachtova Prokopova, N. Guilhaume, A. Giroir-Fendler, H. Mozzanega, J.A. Dalmon, Nanocomposite MFI-alumina membranes via pore-plugging synthesis: preparation and morphological characterization, J. Membrane Science 281 (2006) 228 – 238.

30- J. Karger & D.M. Ruthven, Diffusion in zeolites and other microporous solids, Wiley, New York, 1992.

31- R Taylor & R. Krishna, Multicomponent Mass Transfer, Wiley, New York, 1993.

32- R. Krishna, A unified approach to the modelling of intraparticle diffusion in adsorption processes, Gas Separation Purification 7 (1993b) 91 – 104.

33- P. Ciavarella, H. Moueddeb , S. Miachon , K.Fiaty, Experimental study and numerical simulation of hydrogen/isobutene permeation and separation using MFI-zeolite membrane reactor, Catalysis Today 56 (2000) 253 – 264.

34- D.M. Ruthven, Principles of adsorption and adsorption processes, Wiley, New York, 1984.

35- A.I. Skoulidas, D.S. Sholl, Transport diffusivities of CH_4, CF_4, He, Ne, Ar, Xe, and SF_6 in silicalite from atomistic simulations, J. Phys. Chem. B 106 (2002) 5058 – 5067.

36- A.I. Skoulidas, D.S. Sholl, Molecular dynamics simulations of self-diffusivities, corrected diffusivities, and transport diffusivities of light gases in four silica zeolites to assess influences of pore shape and connectivity, J. Phys. Chem. B 107 (2003) 10132 – 10141.

37- R. Krishna, D. Paschek, R. Baur, Modeling the occupancy dependence of diffusivities in zeolites, Microporous Mesoporous Mater. 76 (2004) 233 – 246.

38- R. Krishna, J.M. van Baten, Diffusion of alkane mixtures in zeolites: Validating the Maxwell-Stefan formulation using MD simulations, J. Phys. Chem. B 107 (2005) 6386 – 6396.

39- R. Krishna, Multicomponent surface diffusion of adsorbed species: a description based on the generalized Maxwell-Stefan equations, Chemical engineering Science 45 (1990) 1779 – 1791.

40- A. Vignes (1966) Diffusion in binary solutions, Ind. Eng. Chem. Fundam 5 (1966) 189 – 199.

41- R. Krishna, J.M. van Baten, F. Garcia-Perez, S. Calero, Incorporating the loading

dependence of the Maxwell-Stefan diffusivity in the modeling of CH_4 and CO_2 permeation across zeolite membranes, Ind. Eng. Chem. Res. 46 (2007) 2974 – 2986.

42- A.I. Skoulidas, D.S. Sholl, R. Krishna, effects in diffusion of CH_4/CF_4 mixtures in MFI zeolite. A study linking MD simulations with the Maxwell-Stefan formulation. Langmuir 19 (2003) 7977 – 7988.

43- T.Q. Gardner, J.B. Lee, R.D. Noble, J.L. Falconer, Adsorption and diffusion properties of butanes in ZSM-5 zeolite membranes, Ind. Eng. Chem. Res. 41 (2002) 4094 – 4105.

44- W. Zhu, P. Hrabanek, L. Gora, F. Kapteijn, J.A. Moulijn, Role of adsorption in the permeation of CH_4 and CO_2 through a silicalite-1 membrane, Ind. Eng. Chem. Res. 45 (2006) 767 – 776.

45- P. Li, F.H. Tezel, Pure and binary adsorption equilibria of carbon dioxide and nitrogen on silicalite, J. Chem. Eng. Data 53 (2008) 2479 – 2487.

46- W.J.W. Bakker, L.J.P. van den Broeke, F. Kapteijn, J.A. Moulijn, Temperature dependence of one-component permeation through a silicalite-1 membrane, AIChE J. 43 (1997) 2203 – 2214.

47- V. Sebastian, I. Kumakiri, R. Bredesen, M. Menendez, Zeolite membrane for CO_2 removal: Operating at high pressure, J. Membrane Science 292 (2007) 92 – 97.

48- C. Algieri, P. Bernardo, G. Golemme, G. Barbieri, E. Drioli, Permeation properties of a thin silicalite-1 (MFI) membrane, J. Membrane Science 222 (2003) 181 – 190.

49- D. Selassie, D. Davis, J. Dahlin, E. Feise, G. Haman, D.S. Sholl, D. Kohen, Atomistic simulations of CO_2 and N_2 diffusion in silica zeolites: The impact of pore size and shape, J. Phys. Chem C. 42 (2008) 16521 – 16531.

50- T.Q. Gardner, A.I. Flores, R.D. Noble, J.L. Falconer, Transient measurement of adsorption and diffusion in H-ZSM-5 membranes, AIChE J. 48 (2002) 1155 – 1167.

51- H. Guo, G. Zhu, H. Li, X. Zou, X. Yin, W. Yang, S. Qiu, R. Xu, Hierarchical growth of large-scale ordered zeolite silicalate-1 membranes with high permeability and selectivity for recycling CO_2, Angew. Chem Int. Ed. 45 (2006) 7053 – 7056.

52- W.J.W. Bakker, F. Kapteijn, J. Poppe, J.A. Moulijn, Permeation characteristics of a metal supported silicalite-1 zeolite membrane, J. Membrane Science 117 (1996) 57 – 78.

53- R. Krishna, D. Paschek, Molecular simulations of adsorption and siting of light alkanes in silicalite-1, D. Phys. Chem. Chem. Phys. 3 (2001) 453 – 562.

CHAPTER SEVEN

CONCLUSIONS, CONTRIBUTIONS TO ORIGINAL KNOWLEDGE, AND RECOMMENDATIONS FOR FUTURE WORK

Chapter 7 Conclusions, Contributions to Original Knowledge, and Recommendations for Future Work

7.1 Conclusions

Silicalite-1/ceramic composite membranes were successfully prepared on a novel zirconium oxide /titanium oxide support by the pore plugging synthesis zeolite. Five supports, with different active layer pore sizes in the range of 0.14 – 1.4 μm were investigated to study the effect of the support's pore size on the morphology and permeation performance of the prepared membranes. The morphology studies were performed for the membranes prepared on both flat and tubular shape supports, while the permeation studies were investigated for the tubular membranes only.

The morphology of the prepared membranes was performed mainly by X-ray diffraction (XRD), scanning electron microscope (SEM) and electron diffraction spectrometer (EDS) analysis. The results confirmed the presence of a typical silicalite-1 zeolite structure with a high internal crystalline order grown inside the pores of the active layer of the supports, with a dense film covering most of the supports active layers. Silicalite-1 crystals in the prepared membranes were preferably oriented with either a- or b-axes perpendicular to the support surface. The pure silicalate-1 layers that was formed on top of some of the supports were not expected to provide any selectivity since the size of the silicalite-1 crystals in these layers is comparable to their thickness and any selective properties of the prepared membranes should arise from the embedded silicalite-1 films formed inside the pores of the active layer of the supports.

The permeation performance of the prepared membranes was investigated by single gas and binary gas mixtures permeation tests. Single gas permeation results for six different gases (He, H_2, N_2, CO_2, CH_4, C_3H_6) illustrated that the observed permeances were not directly related to the kinetic diameter of permeants, and that the transport of the tested gases through the prepared membranes occurred by adsorption followed by surface diffusion mechanism. Mixed gas permeation experiments showed that the prepared membranes were highly permeable with CO_2 permeances in the order of 10^{-6} mol m^{-2} Pa^{-1} s^{-1} while maintaining a relatively high CO_2/N_2 permselectivities of 30 at low total feed pressures. This high CO_2/N_2 permselectivities were due to both competitive adsorption between CO_2 and N_2 molecules and to the blocking effect to N_2 molecules transport caused by adsorbed CO_2 molecules. These results also showed that both CO_2 permeances and CO_2/N_2 permselectivities decreased with increasing the total feed pressure of equimolar CO_2/N_2 mixtures and both CO_2 and N_2 permeances were found to be varied over a wide range and highly dependent on the experimental operating conditions, such as the total feed pressure and the feed composition.

The silicalite-1 membranes prepared in this work were compared with the MFI (silicalite-1 and ZSM-5) membranes reported in literature based on the Robeson upper bound correlation. Generally all the membranes prepared in this work were falling above the revised Robeson upper bound line for CO_2/N_2 separation and above most of the MFI membranes reported in the literature.

Detailed models were successfully developed based on Maxwell-Stefan equations to describe the single component and the CO_2 - N_2 binary mixtures diffusion through silicalite-1 membranes. The developed models allowed the estimation of the single component corrected or M-S diffusivities for CO_2 and N_2 as well as the M-S exchange diffusivities, $Đ_{12}$ and $Đ_{21}$, for their binary mixture of the CO_2 and N_2 using only the pure component adsorption and diffusivity data by employing the Extended Langmuir isotherm. The diffusivities were calculated using the developed models and appeared to be less dependent on the operating conditions compared to the selectivities and permeances data. Due to this less dependency on the operating conditions, these diffusivities offer a better characterization of the intrinsic transport properties of silicalite-1 membranes. Hence, these diffusivities instead of permeances would provide a more accurate tool for designing zeolite membrane separation units.

7.2 Contributions to Original Knowledge

The following is a list of the major contributions to original knowledge, resulted from this thesis.

1. This thesis described the synthesis of composite silicalite-1 zeolite membranes on a novel zirconium oxide and/or titanium oxide active layers supports by the pore plugging zeolite synthesis method. The combination of this composite membrane with these novel supports being prepared by pore plugging method is described for the first time.

2. This thesis confirmed the successful formation of the silicalite-1 crystals and these crystals are not randomly oriented. This is shown for the first time in literature for the silicalite-1 zeolite prepared by pore plugging method on this novel supports.

3. Most of the prepared membranes in this work were very highly permeable while maintaining a relatively high permselectivities. This result was not previously presented in literature for this type of zeolite membrane.

4. In this thesis, detailed models were successfully developed for the first time in literature based on Maxwell-Stefan equations to describe the single gas and binary gas mixtures transport through the newly prepared silicalite-1 membrane on the novel zirconium oxide and/or titanium oxide active layers supports.

5. The models presented in this thesis were developed using the assumption of $Đ_{12}$ and $Đ_{21}$ are not equal for the first time in literature.

6. It was shown in this thesis that the calculated diffusivities using the developed models were less dependent on the operating conditions compared to the selectivity and permeance data.

7.3 Recommendations for Future Work

In this section, a few recommendations for future research are presented.

1. Comparing the results of the low stage cut experiments from Chapter 3 and the high stage cut experiments from Chapter 6 regarding the effect of feed composition on CO_2 and N_2 permeances showed that as the CO_2 composition in the feed increases, for the high stage cut experiments, the CO_2 and N_2 increase. They decrease as the CO_2 composition in the feed increases for the low stage cut experiments. This leads to the

importance of studying the effect of the stage cut on the permeances while keeping the total feed pressure and the feed composition constant.

2. The effect of some important synthesis parameters such as synthesis time, synthesis temperature, aging time and Si/TPAOH ratio should be investigated to determine the best synthesis conditions.
3. This thesis reported the effect of total feed pressure and feed composition on the permeation performance of the prepared membranes at constant temperature. Hence, the effect of temperature on the permeation performance should be further investigated.
4. For more accurate estimation of the exchange diffusivities, experimental binary adsorption data can be employed in the developed model instead of using Extended Langmuir isotherm.

.

Thesis Nomenclatures

A_m: membrane permeation area (m^2).

Å: Angstrom.

B_i: the mobility of component *i* (mol m^2 J^{-1} s^{-1})

c: the molar concentration (mol m^{-3})

D: the transport diffusivities (m^2 s^{-1})

D_0: corrected transport diffusivities (m^2 s^{-1})

~~D_i~~: Maxwell-Stefan diffusivity (m^2 s^{-1})

~~D_{ij}~~: Maxwell-Stefan exchange diffusivity between components i and j (m^2 s^{-1})

f: friction coefficient (J s mol^{-1} m^{-2})

I: peak intensity (counts/step),

J: molar flux across the membrane (mol m^{-2} s^{-1})

K: Langmuir adsorption coefficient (Pa^{-1})

L: zeolite membrane thickness (m)

p: partial pressure in the bulk fluid (Pa)

P: membrane permeance of component *i* (mol m^{-2} Pa^{-1} s^{-1}).

P: the randomly oriented powder

q: molar loading (mol kg^{-1})

Q: permeation rate through the membrane (mol s^{-1})

R: gas constant (8.314 J mol^{-1} K^{-1})

S: the zeolite layer sample

T: absolute temperature (K)

u: the flow velocity with respect to the zeolite (m s^{-1})

V: the steady state permeation rate (mol s^{-1})

x: composition in the retentate stream.

X: XRD peak considered for comparison with subscripts

y: composition in the permeate stream.

Y: XRD peak considered for comparison

z: spatial coordinate (m)

Greek Letters

α : membrane apparent selectivity **(dimensionless)**

α^* : membrane permselectivity **(dimensionless)**

α_{CO_2/N_2}^{Ads} : pure gas adsorption selectivity of CO_2 and N_2 at any given pressure

∇: gradient operator (m^{-1})

ε: porosity of the support (dimensionless)

Γ: elements of matrix of thermodynamic correction factor [Γ] (dimensionless)

θ: occupancy, fractional loading, or surface coverage of component i (dimensionless)

μ: chemical potential (J mol^{-1})

ρ: density (kg m^{-3})

τ: tortuousity (dimensionless)

Subscripts:

0: standard state

1, 2: components 1 and 2

i, j, k: components i, j and k

A: component A

B: component B

F: membrane feed side

P: membrane permeate side

R: membrane retentate side

s: solid zeolite

Superscript:

sat: saturation value

Abbreviations

BET: Brunauer–Emmett–Teller

BFM: bubble flow meter

BJH: Barrett-Joyner-Halenda data interpretation method

CP: cross polarization

CPO: crystallographic preferred orientation

DSC: differential scanning calorimeter

DTA: differential thermal analysis

DTGA: differential thermal gravimetric analysis

EDS: electron diffraction spectrometer

FAU: Faujasite type zeolites

GC: gas chromatograph

GIS: Gismondine type zeolites

IUPAC: International Union of Pure and Applied Chemistry

IZA: International Zeolite Association

LTA: Linde Type A zeolite

MAS: magic angle spinning

MFC: mass flow controller

MFI: Mordenite Framework Inverted

MM: membrane module

MOR: Mordenite zeolite type

NaA: sodium form of the Linde Type A **zeolite**

NaX: Sodium **type** X **zeolite**

NaY: Sodium **type** Y **zeolite**

NMR: nuclear magnetic resonance

NV: needle valve

PC: permeation cell

PG: pressure gauge

ppm: Parts per million

PR: pressure regulator

PT: pressure transducer

RM: rotameter

RPM: Rotations per minute

SAPO-34: silicoaluminophosphate – 34 zeolites

SEM: scanning electron microscope

SOD: Sodalite type zeolite

STP: standard temperature and pressure

TAOH: tetrapropylammonium hydroxide

TCD: thermal conductivity detector

TGA: thermal gravimetric analysis

TPA: tetrapropylammonium

TWV: three way valve

XRD: X-Ray diffraction

ZSM-5: Zeolite Socony Mobil five

Appendices

Appendix 1 – Summary of permeation data presented in Chapters 3, 4, 5 and 6

Table 1A1.1 Summary of Chapter 3 permeation data

Feed pessure (atm)	Permeate pressure (atm)	feed flow (ml STP/min)	Feed composition (CO2% mole)	Permeate composition (CO2% mole)	Permeate flow (ml (STP)/s)	CO2 permeance (mol/m2.Pa.s)	N2 permeance (mol/m2.Pa.s)	Permselectivity (CO2/N2)	stage cut %
2.4904	1.000	100	0.5	0.856	0.034	2.78706E-08	1.61E-09	17.32046068	2.03
3.1709	1.000	100	0.5	0.904	0.095	4.89228E-08	2.19E-09	22.38613129	5.67
3.8513	1.000	100	0.5	0.921	0.137	4.99575E-08	2.09E-09	23.89267345	8.23
5.2123	1.000	100	0.5	0.921	0.239	5.50924E-08	2.27E-09	24.3190499	14.31
6.5732	1.000	100	0.5	0.915	0.325	5.43275E-08	2.90E-09	18.71995829	19.51
7.6619	1.000	100	0.5	0.876	0.414	5.49485E-08	4.52E-09	12.15130958	24.86
5.2123	1.000	100	0.15	0.498	0.056	4.18861E-08	2.60E-09	16.12410168	3.34
5.2123	1.000	100	0.3	0.819	0.115	5.45981E-08	2.14E-09	25.54323843	6.88
5.2123	1.000	100	0.7	0.968	0.396	5.76223E-08	2.65E-09	21.76083065	23.77
5.2123	1.000	100	0.85	0.987	0.554	6.18223E-08	2.91E-09	21.21228159	33.27

Table A1.2 Summary of supports single gas permeation data presented in Chapter 4.

Gas		N2					He		
Pore Size	Feed Pressure (atm)	Delta P (atm)	Flow (ml STP/s)	Permeance (mole/m2.Pa.s)		Feed Pressure (atm)	Delta P (atm)	Flow (ml STP/s)	Permeance (mole/m2.Pa.s)
0.14 µm	1.1901	0.00426	1.0813	1.10E-04		1.2045	0.00178	0.8346	2.03E-04
	1.3103	0.00765	1.6405	9.26E-05		1.3340	0.00402	1.7468	1.88E-04
	1.4637	0.01191	2.4661	8.94E-05		1.4819	0.00929	2.6760	1.24E-04
	1.7848	0.01800	4.1507	9.96E-05		1.6952	0.01284	4.0400	1.36E-04
	1.8982	0.01599	4.7876	1.29E-04		1.8825	0.01195	5.4377	1.97E-04
0.2 µm	1.1576	0.00282	0.8028	1.23E-04		1.210	0.00185	1.015	2.37E-04
	1.3143	0.00632	1.6444	1.12E-04		1.337	0.00633	1.727	1.18E-04
	1.4573	0.00932	2.4365	1.13E-04		1.516	0.00856	2.550	1.29E-04
	1.7125	0.01529	4.2031	1.19E-04		1.726	0.01522	4.263	1.21E-04
	1.8582	0.01545	4.5898	1.28E-04		1.874	0.01661	5.168	1.34E-04
0.45 µm	1.1795	0.00579	1.3288	9.98E-05		1.0995	0.00352	0.8547	1.06E-04
	1.2298	0.00735	1.6884	9.99E-05		1.2719	0.00850	2.0681	1.06E-04
	1.3526	0.01092	2.6607	1.06E-04		1.3734	0.01151	2.7484	1.04E-04
	1.4332	0.01261	3.2427	1.12E-04		1.4164	0.01184	3.0359	1.11E-04
	1.6419	0.01576	4.1199	1.14E-04		1.6628	0.01345	3.7797	1.22E-04
	1.8763	0.01711	5.0123	1.27E-04		1.8609	0.01810	4.8917	1.17E-04
0.8 µm	1.2084	0.00178	0.9201	2.23E-04		1.1721	0.00212	0.8900	1.81E-04
	1.3431	0.00398	1.6415	1.78E-04		1.3583	0.00408	1.6745	1.77E-04
	1.5081	0.00669	2.5460	1.64E-04		1.5164	0.00613	2.6717	1.88E-04
	1.6711	0.00868	3.5449	1.76E-04		1.7366	0.00972	4.0518	1.80E-04
	1.8547	0.01396	4.8888	1.51E-04		1.8825	0.01331	5.4377	1.76E-04
1.4 µm	1.1892	0.00184	0.8691	2.03E-04		1.1793	0.00193	0.9484	2.13E-04
	1.3499	0.00536	1.8281	1.47E-04		1.3145	0.00567	1.6414	1.25E-04
	1.5012	0.00792	2.6346	1.44E-04		1.5724	0.00708	3.1373	1.91E-04
	1.6789	0.00913	3.5723	1.69E-04		1.7138	0.00962	4.1037	1.84E-04
	1.9395	0.01289	4.9469	1.66E-04		2.0386	0.01525	6.5958	1.87E-04

Table A1.4 summary of Chapter 5 single gas permeation data.

0.8	Pf (atm)	Qf (CC/min) STP	QR (CC/min) STP	QP (CC/min) STP	Xf	XR	Yp
	1.31	100.00	79.98	20.02	0.50	0.48	0.58
	1.72	100.00	34.71	65.29	0.50	0.41	0.55
	2.13	100.00	13.64	83.36	0.50	0.35	0.53
	2.53	100.00	2.56	97.44	0.50	0.24	0.51
0.45	Pf (atm)	Qf (CC/min) STP	QR (CC/min) STP	QP (CC/min) STP	Xf	XR	Yp
	1.34	100.00	74.53	25.48	0.50	0.46	0.61
	1.53	100.00	49.88	50.12	0.50	0.41	0.59
	1.69	100.00	36.02	63.98	0.50	0.38	0.57
	1.88	100.00	19.72	80.28	0.50	0.32	0.54
	2.18	100.00	8.55	91.45	0.50	0.29	0.52
	2.29	100.00	1.32	98.68	0.50	0.19	0.50
0.2	Pf (atm)	Qf (CC/min) STP	QR (CC/min) STP	QP (CC/min) STP	Xf	XR	Yp
	1.31	100.00	85.41	14.59	0.50	0.48	0.60
	1.75	100.00	64.87	35.13	0.50	0.41	0.66
	2.38	100.00	36.55	63.45	0.50	0.30	0.61
	2.78	100.00	27.97	72.04	0.50	0.27	0.59
	3.12	100.00	11.91	88.09	0.50	0.21	0.54
1.4	Pf (atm)	Qf (CC/min) STP	QR (CC/min) STP	QP (CC/min) STP	Xf	XR	Yp
	1.30	100.00	81.09	18.91	0.50	0.48	0.59
	1.53	100.00	76.89	23.11	0.50	0.46	0.65
	1.71	100.00	66.59	33.41	0.50	0.42	0.67
	1.93	100.00	58.66	41.34	0.50	0.38	0.68
	2.20	100.00	43.17	56.83	0.50	0.32	0.63
	2.54	100.00	3.50	96.50	0.50	0.24	0.51
	2.97	100.00	1.93	98.07	0.50	0.12	0.51

Table A1.4 summary of Chapter 5 single gas permeation data.

		N2				CO2	
Feed pessure (atm)	Permeate pressure (atm)	Permeate flow (ml STP/min)	N2 permeance (mole/m2.Pa.s)	Feed pessure (atm)	Permeate pressure (atm)	Permeate flow (ml STP/min)	CO2 permeance (mole/m2.Pa.s)
1.3478	1.0325	0.3316	4.55E-07	1.3513	1.0740	0.6161	9.62E-07
1.7410	1.0658	0.6939	4.45E-07	1.6677	1.1584	0.9809	8.34E-07
2.0436	1.0930	1.0105	4.60E-07	2.0782	1.2585	1.6142	8.52E-07
2.3487	1.1128	1.1717	4.10E-07	2.4194	1.3338	2.0896	8.33E-07
3.1298	1.1733	1.8047	3.99E-07	3.0802	1.4602	2.7213	7.27E-07
4.1216	1.2492	2.5680	3.87E-07	4.0563	1.5972	3.4755	6.12E-07

Table A1.5 Summary of Chapter 5 binary mixture permeation data.

Feed pessure (atm)	Permeate pressure (atm)	feed flow (ml STP/min)	Feed composition (CO2% mole)	Permeate composition (CO2% mole)	Permeate flow (ml (STP)/s)	CO2 permeance (mol/m2.Pa.s)	N2 permeance (mol/m2.Pa.s)	Permselectivity (CO2/N2)	stage cut %
1.341	1.043	1612	0.477	0.585	0.251	2.27E-06	1.68E-07	13.49	0.94
1.797	1.151	1612	0.477	0.675	0.488	1.85E-06	1.22E-07	15.21	1.82
2.723	1.177	1612	0.477	0.808	1.071	1.15E-06	7.35E-08	15.59	3.99
3.082	1.218	1612	0.477	0.824	1.313	1.08E-06	7.05E-08	15.26	4.89
4.112	1.321	1612	0.477	0.856	1.943	9.43E-07	6.02E-08	15.67	7.23
2.047	1.128	1612	0.477	0.712	0.757	1.41E-06	1.26E-07	11.22	2.82
2.056	1.114	971	0.145	0.238	0.757	2.81E-06	2.75E-07	10.24	4.68
2.034	1.088	1309	0.329	0.503	0.757	1.42E-06	1.98E-07	7.20	3.47
2.062	1.141	1220	0.678	0.909	0.757	8.53E-07	5.28E-08	16.16	3.72
2.054	1.196	993	0.833	0.976	0.757	6.02E-07	2.40E-08	25.08	4.57

Appendix 2 - Diffusion through zeolite membranes modeling: single and two components

A2.1 Single Component

The molar flux of component i can be defined by the following equation [1]:

$$J_i = u_i \times c_i \tag{A2.1}$$

Where J_i, u_i and c_i are the molar flux of component i (mol m^{-2} s^{-1}), the flow velocity of component i (m s^{-1}), and the molar concentration of component i (mol m^{-3}), respectively. However, since the discussion here is about the gas concentration within the micropores, so q_i (mol kg^{-1}) will be used instead of c_i (mol m^{-3}). Hence, Eq. A2.1 will be written as follows:

$$J_i = u_i \times \rho_s q_i \tag{A2.2}$$

The density of the solid adsorbent (ρ_s) (kg m^{-3}) was introduced here when substituting c_i with q_i because of the different units of q_i and c_i. If the diffusive flux is considered as a flow driven by the gradient of chemical potential (μ) and opposed by the frictional forces then [2]:

$$f \times u_i = -\frac{d\mu_i}{dz} \tag{A2.3}$$

where f is a friction coefficient (J s mol^{-1} m^{-2}), μ_i is the molar chemical potential of component i (J mol^{-1}) and z is the spatial coordinate (m). By relating the chemical potential to the concentration, and assuming ideal gas behavior, i.e. activity equal vapor pressure, then Eq. A2.3 can be written as follows:

$$f \times u_i = \frac{d}{dz}\left(\mu_i^0 + RT \ln p_i\right) \tag{A2.4}$$

where μ_i^0 is the molar chemical potential at the standard state (J mol^{-1}), R is the gas constant (8.314 J mol^{-1} K^{-1}), T is the absolute temperature (K) and p_i is the partial pressure of component i. Rearrangement of Eq. A2.4 resulted in:

$$u_i = -\frac{RT}{f} \times \frac{d \ln p_i}{dz} \tag{A2.5}$$

Substituting Eq. A2.5 in Eq. A2.2 result in:

$$J_i = -\frac{RT}{f} \times \frac{d \ln p_i}{dz} \times \rho_s \times q_i \tag{A2.6}$$

Taking into consideration that:

$$d \ln q_i = \frac{dq_i}{q_i} \tag{A2.7}$$

Substitution of Eq. A2.7 into Eq. A2.6 gives:

$$J_i = -\rho_s \times \frac{RT}{f} \times \frac{d \ln p_i}{d \ln q_i} \times \frac{dq_i}{dz} \tag{A2.8}$$

After the rearranging of Eq. A2.8 the following equation obtained:

$$J_i = -\rho_s \times \left(\frac{RT}{f} \times \frac{d \ln p_i}{d \ln q_i} \right) \times \frac{dq_i}{dz} \tag{A2.9}$$

Eq. A2.9 can be further simplified to:

$$J_i = -\rho_s \times D_i \times \frac{dq_i}{dz} = -\rho_s \times Đ_i \times \frac{d \ln p_i}{d \ln q_i} \times \frac{dq_i}{dz} \tag{A2.10}$$

Where D_i and $Đ_i$ are the transport and the corrected transport diffusivities (m^2 s^{-1}) [3], respectively. The corrected diffusivity is equal to the Maxwell-Stefan diffusivity in single component systems. Both the transport and the corrected transport diffusivities are defined in the following equations:

$$D_i = \frac{RT}{f} \times \frac{d \ln p_i}{d \ln q_i} \tag{A2.11}$$

$$Đ_i = \frac{RT}{f} \tag{A2.12}$$

Where ($d\ ln\ P_i/d\ ln\ q_i$) is an expression represents the gradient of the equilibrium isotherm in logarithmic coordinates. Nevertheless, the Fick's diffusivity (D_i) is equal to the Maxwell-Stefan diffusivity ($Đ_i$) times the thermodynamic correction factor (Γ). The main difference between these two models is that M-S approach separates diffusional effects from thermodynamic non idealities effects while Fick approach accounts for the non-idealities in the diffusion coefficients. Hence, Eq. A2.11 can be re written as follows

$$D_i = Đ_i \times \Gamma \tag{A2.13}$$

Rewriting the thermodynamic correction factor as follows:

$$\frac{d \ln p_i}{d \ln q_i} = \frac{q_i}{p_i} \frac{dp_i}{dq_i} \tag{A2.14}$$

And substituting Eq. A2.14 in Eq. A2.10, results in:

$$J_i = -\rho_s \times Đ_i \times \frac{q_i}{p_i} \frac{dp_i}{dq_i} \times \frac{dq_i}{dz} \tag{A2.15}$$

Eq. A2.15 can be further simplified as follows:

$$J_i = -\rho_s \times Đ_i \times \frac{q_i}{p_i} \frac{dp_i}{dz} \tag{A2.16}$$

If the equilibrium isotherm is described by Langmuir adsorption isotherm, then Eq. A2.16 becomes:

$$J_i = -\rho_s \times Đ_i \times \frac{\left(\frac{q_i^{sat} K_i p_i}{1 + K_i p_i}\right)}{p_i} \times \frac{dp_i}{dz} \tag{A2.17}$$

where q_i^{sat} and Ki are the saturation molar loading of component i (mol kg^{-1}) and the Langmuir adsorption coefficient (Pa^{-1}), respectively. Upon the arrangement of Eq. A2.17, this gives:

$$J_i dz = -\rho_s Đ_i q_i^{sat} K_i \frac{dp_i}{1 + K_i p_i} \tag{A2.18}$$

Treating the membrane as a plane wall due to the fact that the thickness of the zeolite layer is very small compared to the radius of the membrane support as mentioned earlier, J_i is assumed to be independent of z. Hence, integrating z from 0 to L (membrane thickness) and p_i from p_{iR} (feed pressure) to p_{ip} (permeate pressure) gives:

$$J_i = \frac{\rho_s q_i^{sat} Đ_i}{\tau L} \times \ln\left(\frac{1 + K_i p_{iR}}{1 + K_i p_{iP}}\right) \tag{A2.19}$$

Tortuosity (τ) is introduced in Eq. A2.19 as a correction to the membrane thickness since the diffusion path is not straight from z = 0 to z = L. Eq. A2.19 should be also corrected with respect to the porosity (ε) of the support, because most of the diffusion is taking place inside the zeolite filling the support active layer pores. Thus, the final equation describing the flux of a single component through zeolite membrane will be as follows:

$$J_i = \frac{\rho_s . \varepsilon . q_i^{sat} Đ_i}{\tau L} \times \ln\left(\frac{1 + K_i p_{iR}}{1 + K_i p_{iP}}\right) \tag{A2.20}$$

The q_i^{sat} and Ki values can be calculated from the pure adsorption isotherm. The value of the porosity of the support is provided by the manufacturer as 0.23. The density and the tortuosity of solid silicalite-1 are around 1.8 g/cm3 [4] and around 1.2 [5], respectively.

In order to calculate the Maxwell-Stefan diffusivity, Eq. A2.20 should be rearranged to as follows:

$$Đ_i = \frac{J_i \tau L}{\rho_s . \varepsilon . q_i^{sat} \times \ln\left(\frac{1 + K_i p_{iR}}{1 + K_i p_{iP}}\right)} \tag{A2.21}$$

A2.2 Binary mixtures:

The most successful approach to describe mixture diffusion through zeolite membranes is the generalized Maxwell-Stefan approach which is given by the following equation [6]:

$$-\nabla \mu_i = RT \frac{u_i}{Đ_i} + RT \sum_{\substack{j=1 \\ j \neq i}}^{n} \theta_j \frac{u_i - u_j}{Đ_{ij}} \tag{A2.22}$$

where $\nabla \mu_i$ (J mol^{-1}) represents the fundamental driving force (under isothermal conditions) for the mass transport acting on a certain species *i*. As a result, species *i* is tending to move along the surface with a velocity u_i (m s^{-1}). θ_i is the occupancy or fractional loading of component *i* (dimensionless). The flow resistance in first term on the right hand side of Eq. A2.22 attributes to the friction between species *i* and the surface, while the flow resistance in the second term on the right hand side of the same equation attributes to the friction exerted

by adsorbate *j*, on the surface motion of species *i*. Each component, (*i* and *j*) is moving with a certain velocity, u_j and u_i, (m s^{-1}) with respect to the surface. $Đ_{ij}$ is the Maxwell-Stefan (M-S) surface diffusion coefficient (m^2 s^{-1}) or the exchange diffusivity between molecules *i* and *j*, and $Đ_i$ is the MS surface diffusion coefficient between molecule *i* and the wall (m^2 s^{-1}). $Đ_i$ is also called the corrected diffusivity in the literature [3]. Eq. A2.22 can be rearranged, after multiplying each term with θ_i, as follows:

$$-\frac{\theta_i}{RT}\nabla\mu_i = \frac{\theta_i u_i}{Đ_i} + \sum_{\substack{j=1 \\ j\neq i}}^{n} \theta_i\theta_j \frac{u_i - u_j}{Đ_{ij}} \tag{A2.23}$$

where θ_i and θ_j are the occupancy or fractional loading of component i and j (dimensionless), respectively, and defined as follows:

$$\theta_i = \frac{q_i}{q_i^{sat}} \tag{A2.24}$$

$$\theta_j = \frac{q_j}{q_j^{sat}} \tag{A2.25}$$

Substituting Eq. (A2.24) and Eq. (A2.25) into the right hand side of Eq. (A2.23), results in:

$$-\frac{\theta_i}{RT}\nabla\mu_i = \frac{q_i u_i}{q_i^{sat} Đ_i} + \sum_{\substack{j=1 \\ j\neq i}}^{n} q_i q_j \frac{u_i - u_j}{q_i^{sat} q_j^{sat} Đ_{ij}} \tag{A2.26}$$

where q_j and q_j^{sat} are the molar loading and the saturation molar loading of component *j* (mol kg^{-1}), respectively. By defining the flux as the product of the zeolite density (ρ_s), adsorbed concentration and velocity, hence, the fractional occupancies are converted into fluxes using Eq. A2.27 [7]:

$$J_i = \rho_s q_i^{sat} \theta_i u_i = \rho_s q_i u_i \tag{A2.27}$$

Eq. A2.27 can be rearranged as follows:

$$u_i = \frac{J_i}{\rho_s q_i^{sat} \theta_i} = \frac{J_i}{\rho_s q_i} \tag{A2.28}$$

Substituting Eq. A2.28 in Eq. A2.26 results in:

$$-\frac{\theta_i}{RT}\nabla\mu_i = \frac{1}{\rho_s}\left(\frac{J_i}{q_i^{sat}Đ_i} + \sum_{\substack{j=1 \\ j\neq i}}^{n} \frac{q_j J_i - q_i J_j}{q_i^{sat} q_j^{sat} Đ_{ij}}\right) \tag{A2.29}$$

The chemical potential gradient and the surface coverage gradient can be related via a matrix of thermodynamic factors given in [6] as follows:

$$\frac{\theta_i}{RT}\nabla\mu_i = \sum_{j=1}^{n} \Gamma_{ij} \nabla\theta_j \tag{A2.30}$$

Where Γ_{ij} is a thermodynamic correction factor that is defined by Krishna [6] as follows:

$$\Gamma_{ij} = \theta_i \frac{\partial \ln p_i}{\partial \theta_j} = \frac{\theta_i}{p_i}\frac{\partial p_i}{\partial \theta_j} \tag{A2.31}$$

The partial derivatives in Eq. A2.31 are defined by the adsorption equilibrium relation between p_i and θ_i. Hence, the values for Γ,s can be determined from the mixture adsorption isotherms. Moreover, Γ,s can be also expressed in absolute loadings as follows [7]:

$$\Gamma_{ij} = \left(\frac{q_j^{sat}}{q_i^{sat}}\right)\frac{q_i}{p_i}\frac{\partial p_i}{\partial q_j} \tag{A2.32}$$

Combining Eq. A2.29 and Eq. A2.30, results in:

$$\sum_{j=1}^{n}\Gamma_{ij}\nabla\theta_j = -\frac{1}{\rho_s}\left(\frac{J_i}{q_i^{sat}Đ_i}+\sum_{\substack{j=1\\ j\neq i}}^{n}\frac{q_jJ_i - q_iJ_j}{q_i^{sat}q_j^{sat}Đ_{ij}}\right) \tag{A2.33}$$

Eq. A2.33 can be written for two components as follows:

$$\Gamma_{11}\nabla\theta_1+\Gamma_{12}\nabla\theta_2 = -\frac{1}{\rho_s}\left(\frac{J_1}{q_1^{sat}Đ_1}+\frac{q_2J_1 - q_1J_2}{q_1^{sat}q_2^{sat}Đ_{12}}\right) \tag{A2.34}$$

$$\Gamma_{21}\nabla\theta_1+\Gamma_{22}\nabla\theta_2 = -\frac{1}{\rho_s}\left(\frac{J_2}{q_2^{sat}Đ_2}+\frac{q_1J_2 - q_2J_1}{q_2^{sat}q_1^{sat}Đ_{21}}\right) \tag{A2.35}$$

To solve Eq. A2.34 and Eq. A2.35 simultaneously for J_1 and J_2, these equations should be written in a matrix form as follows

$$\begin{bmatrix}\Gamma_{11} & \Gamma_{12}\\ \Gamma_{21} & \Gamma_{22}\end{bmatrix}\begin{pmatrix}\nabla\theta_1\\ \nabla\theta_2\end{pmatrix} = -\frac{1}{\rho_s}\begin{bmatrix}\frac{q_2}{q_1^{sat}q_2^{sat}Đ_{12}}+\frac{1}{q_1^{sat}Đ_1} & -\frac{q_1}{q_1^{sat}q_2^{sat}Đ_{12}}\\ -\frac{q_2}{q_1^{sat}q_2^{sat}Đ_{21}} & \frac{q_1}{q_1^{sat}q_2^{sat}Đ_{21}}+\frac{1}{q_2^{sat}Đ_2}\end{bmatrix}\begin{pmatrix}J_1\\ J_2\end{pmatrix} \tag{A2.36}$$

Eq. A2.36 can be also expressed in vector notation as follows:

$$-\rho_s[\Gamma](\nabla\theta) = [B'](J) \tag{A2.37}$$

Where the elements of [*B'*] matrix are given by the following equations [8]:

$$B'_{11} = \frac{q_2}{q_1^{sat}q_2^{sat}Đ_{12}}+\frac{1}{q_1^{sat}Đ_1} \tag{A2.38}$$

$$B'_{12} = -\frac{q_1}{q_1^{sat}q_2^{sat}Đ_{21}} \tag{A2.38}$$

$$B'_{21} = -\frac{q_2}{q_1^{sat}q_2^{sat}Đ_{12}} \tag{A2.39}$$

$$B'_{22} = \frac{q_1}{q_1^{sat} q_2^{sat} Đ_{21}} + \frac{1}{q_2^{sat} Đ_1} \tag{A2.40}$$

Matrix [B'] is given as follows:

$$\left[B'\right] = \begin{bmatrix} \frac{q_2}{q_1^{sat} q_2^{sat} Đ_{12}} + \frac{1}{q_1^{sat} Đ_1} & -\frac{q_1}{q_1^{sat} q_2^{sat} Đ_{12}} \\ -\frac{q_2}{q_1^{sat} q_2^{sat} Đ_{21}} & \frac{q_1}{q_1^{sat} q_2^{sat} Đ_{21}} + \frac{1}{q_2^{sat} Đ_2} \end{bmatrix} \tag{A2.41}$$

Right hand side of Eq. A2.41 can be presented as a multiplication of two matrices as given below:

$$\left[B'\right] = \begin{bmatrix} \frac{\theta_2}{Đ_{12}} + \frac{1}{Đ_1} & -\frac{\theta_1}{Đ_{12}} \\ -\frac{\theta_2}{Đ_{21}} & \frac{\theta_1}{Đ_{21}} + \frac{1}{Đ_2} \end{bmatrix} \begin{bmatrix} \frac{1}{q_1^{sat}} & 0 \\ 0 & \frac{1}{q_2^{sat}} \end{bmatrix} \tag{A2.42}$$

However, Eq. A2.41 can be written in a simple way as follows:

$$\left[B'\right] = \left[B\right]\left[q^{sat}\right]^{-1} \tag{A2.43}$$

Where matrix *[B]* and matrix $[q^{sat}]^{-1}$ are given by the following equations:

$$\left[B\right] = \begin{bmatrix} \frac{\theta_2}{Đ_{12}} + \frac{1}{Đ_1} & -\frac{\theta_1}{Đ_{12}} \\ -\frac{\theta_2}{Đ_{21}} & \frac{\theta_1}{Đ_{21}} + \frac{1}{Đ_2} \end{bmatrix} \tag{A2.44}$$

$$\left[q^{sat}\right]^{-1} = \begin{bmatrix} \frac{1}{q_1^{sat}} & 0 \\ 0 & \frac{1}{q_2^{sat}} \end{bmatrix} \tag{A2.45}$$

where the matrix $[q^{sat}]^{-1}$ is the inverse of the $[q^{sat}]$ matrix. However the inverse of matrix, for matrix [a] as example, is given as follows:

$$\left[a\right]\left[a\right]^{-1} = I_1 \tag{A2.46}$$

Where the I_1 matrix is the identity matrix or the unit matrix. The identity matrix for size n matrix (n x n square matrix) is the matrix with ones on the main diagonal and zeros elsewhere. For square matrix the identity matrix is given below:

$$I_1 = \begin{bmatrix} 1 & 0 \\ 0 & 1 \end{bmatrix} \tag{A2.47}$$

So for a square matrix [a] defined as follows:

$$[a] = \begin{bmatrix} a_{11} & a_{12} \\ a_{21} & a_{22} \end{bmatrix} \tag{A2.48}$$

The inverse of [a] given as follows:

$$[a]^{-1} = \frac{1}{Det[a]} \begin{bmatrix} a_{22} & -a_{12} \\ -a_{21} & a_{11} \end{bmatrix} \tag{A2.49}$$

Where *Det [a]* is the determinant of matrix *[a]* and is given below:

$$Det[a] = a_{11} \times a_{22} - a_{12} \times a_{21} \tag{A2.50}$$

It is important to high light the following relation between matrix inverses, if matrix *[a]* is given as follows:

$$[a] = [b][c]^{-1} \tag{A2.51}$$

Then inverse of matrix [a] is given as follows:

$$[a]^{-1} = [b]^{-1}[c] \tag{A2.52}$$

Based on that the inverse of matrix [B'] is given as follows:

$$\left[B'\right]^{-1} = \left[B\right]^{-1}\left[q^{sat}\right] \tag{A2.53}$$

Using Eq. A2.53 and solving Eq. A2.37 for the fluxes, results in:

$$\left(J\right) = -\rho_s\left[B'\right]^{-1}\left[\Gamma\right]\left(\nabla\theta\right) \tag{A2.54}$$

Eq. A2.54 can be also rewritten as follows:

$$\left(J\right) = -\rho_s\left[q^{sat}\right]\left[B\right]^{-1}\left[\Gamma\right]\left(\nabla\theta\right) \tag{A2.55}$$

The inverse of matrix *[B]* can be calculated as follows:

$$\left[B\right]^{-1} = \frac{\begin{bmatrix} \frac{\theta_1}{Đ_{21}} + \frac{1}{Đ_2} & \frac{\theta_1}{Đ_{12}} \\ \frac{\theta_2}{Đ_{21}} & \frac{\theta_2}{Đ_{12}} + \frac{1}{Đ_1} \end{bmatrix}}{\frac{\theta_1}{Đ_1 Đ_{21}} + \frac{\theta_2}{Đ_2 Đ_{12}} + \frac{1}{Đ_1 Đ_2}} \tag{A2.56}$$

Eq. A2.56 can be rewritten as follows:

$$\left[B\right]^{-1} = \frac{\begin{bmatrix} Đ_1 & 0 \\ 0 & Đ_2 \end{bmatrix}\begin{bmatrix} 1+\frac{\theta_1 Đ_2}{Đ_{21}} & \frac{\theta_1 Đ_2}{Đ_{12}} \\ \frac{\theta_2 Đ_1}{Đ_{21}} & 1+\frac{\theta_2 Đ_1}{Đ_{12}} \end{bmatrix}}{\frac{\theta_1 Đ_2}{Đ_{21}} + \frac{\theta_2 Đ_1}{Đ_{12}} + 1} \tag{A2.57}$$

Hence, Eq. A2.55 for two component system can be written as follows:

$$\begin{pmatrix} J_1 \\ J_2 \end{pmatrix} = -\rho_s \frac{\begin{bmatrix} q_1^{sat} & 0 \\ 0 & q_2^{sat} \end{bmatrix}\begin{bmatrix} \mathcal{D}_1 & 0 \\ 0 & \mathcal{D}_2 \end{bmatrix}\begin{bmatrix} 1+\frac{\theta_1\mathcal{D}_2}{\mathcal{D}_{21}} & \frac{\theta_1\mathcal{D}_2}{\mathcal{D}_{12}} \\ \frac{\theta_2\mathcal{D}_1}{\mathcal{D}_{21}} & 1+\frac{\theta_2\mathcal{D}_1}{\mathcal{D}_{12}} \end{bmatrix}\begin{bmatrix} \Gamma_{11} & \Gamma_{12} \\ \Gamma_{21} & \Gamma_{22} \end{bmatrix}\begin{pmatrix} \nabla\theta_1 \\ \nabla\theta_2 \end{pmatrix}}{\frac{\theta_1\mathcal{D}_2}{\mathcal{D}_{21}} + \frac{\theta_2\mathcal{D}_1}{\mathcal{D}_{12}} + 1} \tag{A2.58}$$

Before any further mathematical derivation, it is important to show briefly how the multiplication of matrices performed. If [a] is a square given by Eq. A2.48, then the multiplication of matrix [a] with a scalar C is given as follows:

$$C \times \begin{bmatrix} a_{11} & a_{12} \\ a_{21} & a_{22} \end{bmatrix} = \begin{bmatrix} C \times a_{11} & C \times a_{12} \\ C \times a_{21} & C \times a_{22} \end{bmatrix} \tag{A2.59}$$

However when a matrix multiplied by another matrix, the columns in the first matrix should equal the rows of the second matrix. If matrix [a] has two columns matrix [b] should have two rows. Eq. A2.60 shows an example of dot multiplication of matrices [a] and [b]:

$$[a].[b] = \begin{bmatrix} a_{11} & a_{12} \\ a_{21} & a_{22} \end{bmatrix}.\begin{bmatrix} b_{11} & b_{12} \\ b_{21} & b_{22} \end{bmatrix} = \begin{bmatrix} a_{11}\times b_{11} + a_{12}\times b_{21} & a_{11}\times b_{12} + a_{12}\times b_{22} \\ a_{21}\times b_{11} + a_{22}\times b_{21} & a_{21}\times b_{12} + a_{22}\times b_{22} \end{bmatrix} \tag{A2.60}$$

Based on that and after performing all matrix multiplications in Eq. A2.58, the two fluxes will be given by the following equations:

$$J_1 = -\rho_s q_1^{sat} \mathcal{D}_1 \times \left[\frac{\left(\Gamma_{11} + \theta_1 \frac{\mathcal{D}_2}{\mathcal{D}_{21}}\Gamma_{11} + \theta_1 \frac{\mathcal{D}_2}{\mathcal{D}_{12}}\Gamma_{21}\right)\nabla\theta_1 + \left(\Gamma_{12} + \theta_1 \frac{\mathcal{D}_2}{\mathcal{D}_{21}}\Gamma_{12} + \theta_1 \frac{\mathcal{D}_2}{\mathcal{D}_{12}}\Gamma_{22}\right)\nabla\theta_2}{1 + \theta_2 \frac{\mathcal{D}_1}{\mathcal{D}_{12}} + \theta_1 \frac{\mathcal{D}_2}{\mathcal{D}_{21}}} \right] \tag{A2.61}$$

$$J_2 = -\rho_s Đ_2 q_2^{sat} \times \left[\frac{\left[\Gamma_{22} + \theta_2 \frac{Đ_1}{Đ_{12}} \Gamma_{22} + \theta_2 \frac{Đ_1}{Đ_{21}} \Gamma_{12} \right] \nabla \theta_2 + \left[\Gamma_{21} + \theta_2 \frac{Đ_1}{Đ_{12}} \Gamma_{21} + \frac{\theta_2 Đ_1}{Đ_{21}} \Gamma_{11} \right] \nabla \theta_1}{1 + \theta_2 \frac{Đ_1}{Đ_{12}} + \theta_1 \frac{Đ_2}{Đ_{21}}} \right] \quad \text{(A2.62)}$$

Furthermore, the thermodynamic factors (Γ,s) defined by Eq. A2.32 is given for two component system as follows:

$$\Gamma_{11} = \left(\frac{q_1^{sat}}{q_1^{sat}} \right) \frac{q_1}{p_1} \frac{\partial p_1}{\partial q_1} \quad \text{(A2.63)}$$

$$\Gamma_{12} = \left(\frac{q_2^{sat}}{q_1^{sat}} \right) \frac{q_1}{p_1} \frac{\partial p_1}{\partial q_2} \quad \text{(A2.64)}$$

$$\Gamma_{21} = \left(\frac{q_1^{sat}}{q_2^{sat}} \right) \frac{q_2}{p_2} \frac{\partial p_2}{\partial q_1} \quad \text{(A2.65)}$$

$$\Gamma_{22} = \left(\frac{q_2^{sat}}{q_2^{sat}} \right) \frac{q_2}{p_2} \frac{\partial p_2}{\partial q_2} \quad \text{(A2.66)}$$

Single Site Extended Langmuir adsorption isotherm given as follows [3]:

$$q_i = \frac{q_i^{sat} K_i p_i}{1 + \sum_{k=1}^{n} K_k p_k} \quad \text{(A2.67)}$$

If Single Site extended Langmuir adsorption isotherm is applicable, then the Γ,s are given as follows [9]:

$$\Gamma_{11} = \frac{1 - \theta_2}{1 - \theta_1 - \theta_2} \quad \text{(A2.68)}$$

$$\Gamma_{12} = \frac{\theta_1}{1 - \theta_1 - \theta_2} \quad \text{(A2.69)}$$

$$\Gamma_{21} = \frac{\theta_2}{1 - \theta_1 - \theta_2} \quad \text{(A2.70)}$$

$$\Gamma_{22} = \frac{1-\theta_1}{1-\theta_1-\theta_2} \tag{A2.71}$$

Substituting Γ_{11}, Γ_{12}, Γ_{21}, *and* Γ_{22} obtained from using extended Langmuir in Eq. A2.61 gives:

$$J_1 = -\rho_s q_1^{sat} Đ_1 \times \left[\frac{\left(\frac{1-\theta_2}{1-\theta_1-\theta_2} + \left(\theta_1 \frac{Đ_2}{Đ_{21}} \frac{1-\theta_2}{1-\theta_1-\theta_2} \right) + \left(\theta_1 \frac{Đ_2}{Đ_{12}} \frac{\theta_2}{1-\theta_1-\theta_2} \right) \right) \nabla\theta_1 + \left(\frac{\theta_1}{1-\theta_1-\theta_2} + \left(\theta_1 \frac{Đ_2}{Đ_{21}} \frac{\theta_1}{1-\theta_1-\theta_2} \right) + \left(\theta_1 \frac{Đ_2}{Đ_{12}} \frac{1-\theta_1}{1-\theta_1-\theta_2} \right) \right) \nabla\theta_2}{1+\theta_2 \frac{Đ_1}{Đ_{12}} + \theta_1 \frac{Đ_2}{Đ_{21}}} \right] \tag{A2.72}$$

While substituting Γ_{11}, Γ_{12}, Γ_{21}, *and* Γ_{22} obtained from using extended Langmuir in Eq. A2.62 gives:

$$J_2 = -\rho_s Đ_2 q_2^{sat} \times \left[\frac{\left[\frac{1-\theta_1}{1-\theta_1-\theta_2} + \left(\theta_2 \frac{Đ_1}{Đ_{12}} \frac{1-\theta_1}{1-\theta_1-\theta_2} \right) + \left(\theta_2 \frac{Đ_1}{Đ_{21}} \frac{\theta_1}{1-\theta_1-\theta_2} \right) \right] \nabla\theta_2 + \left[\frac{\theta_2}{1-\theta_1-\theta_2} + \left(\theta_2 \frac{Đ_1}{Đ_{12}} \frac{\theta_2}{1-\theta_1-\theta_2} \right) + \left(\frac{\theta_2 Đ_1}{Đ_{21}} \frac{1-\theta_2}{1-\theta_1-\theta_2} \right) \right] \nabla\theta_1}{1+\theta_2 \frac{Đ_1}{Đ_{12}} + \theta_1 \frac{Đ_2}{Đ_{21}}} \right] \tag{A2.73}$$

Since the diffusion is assumed only in z-direction (r), then:

$$\nabla\theta_i = \frac{d\theta_i}{dz} \tag{A2.74}$$

$$\nabla q_i = \frac{dq_i}{dz} \tag{A2.75}$$

Based on that Eq. A2.72 and Eq. A2.73 can be written as:

$$N_1 = -\rho q_1^{sat} Đ_1 \times \left[\begin{array}{l} \dfrac{\left(\dfrac{1-\theta_2}{1-\theta_1-\theta_2} + \left(\theta_1 \dfrac{Đ_2}{Đ_{21}} \dfrac{1-\theta_2}{1-\theta_1-\theta_2} \right) + \left(\theta_1 \dfrac{Đ_2}{Đ_{12}} \dfrac{\theta_2}{1-\theta_1-\theta_2} \right) \right) \dfrac{d\theta_1}{dz}}{1+\theta_2 \dfrac{Đ_1}{Đ_{12}} + \theta_1 \dfrac{Đ_2}{Đ_{21}}} \\ + \dfrac{\left(\dfrac{\theta_1}{1-\theta_1-\theta_2} + \left(\theta_1 \dfrac{Đ_2}{Đ_{21}} \dfrac{\theta_1}{1-\theta_1-\theta_2} \right) + \left(\theta_1 \dfrac{Đ_2}{Đ_{12}} \dfrac{1-\theta_1}{1-\theta_1-\theta_2} \right) \right) \dfrac{d\theta_2}{dz}}{1+\theta_2 \dfrac{Đ_1}{Đ_{12}} + \theta_1 \dfrac{Đ_2}{Đ_{21}}} \end{array} \right] \tag{A2.76}$$

$$N_2 = -\rho Đ_2 q_2^{sat} \times \left[\begin{array}{l} \dfrac{\left[\dfrac{1-\theta_1}{1-\theta_1-\theta_2} + \left(\theta_2 \dfrac{Đ_1}{Đ_{12}} \dfrac{1-\theta_1}{1-\theta_1-\theta_2} \right) + \left(\theta_2 \dfrac{Đ_1}{Đ_{21}} \dfrac{\theta_1}{1-\theta_1-\theta_2} \right) \right] \dfrac{d\theta_2}{dz}}{1+\theta_2 \dfrac{Đ_1}{Đ_{12}} + \theta_1 \dfrac{Đ_2}{Đ_{21}}} \\ + \dfrac{\left[\dfrac{\theta_2}{1-\theta_1-\theta_2} + \left(\theta_2 \dfrac{Đ_1}{Đ_{12}} \dfrac{\theta_2}{1-\theta_1-\theta_2} \right) + \left(\dfrac{\theta_2 Đ_1}{Đ_{21}} \dfrac{1-\theta_2}{1-\theta_1-\theta_2} \right) \right] \dfrac{d\theta_1}{dz}}{1+\theta_2 \dfrac{Đ_1}{Đ_{12}} + \theta_1 \dfrac{Đ_2}{Đ_{21}}} \end{array} \right] \tag{A2.77}$$

Rearranging Eq. A2.76 to have the derivatives of the surface coverage in one side of the equation gives:

$$-\frac{N_1\left(1+\theta_2\frac{Đ_1}{Đ_{12}}+\theta_1\frac{Đ_2}{Đ_{21}}\right)}{\rho q_1^{sat}Đ_1}=\left[\begin{array}{l}\left(\frac{1-\theta_2}{1-\theta_1-\theta_2}+\left(\theta_1\frac{Đ_2}{Đ_{21}}\frac{1-\theta_2}{1-\theta_1-\theta_2}\right)+\left(\theta_1\frac{Đ_2}{Đ_{12}}\frac{\theta_2}{1-\theta_1-\theta_2}\right)\right)\frac{d\theta_1}{dz}\\+\left(\frac{\theta_1}{1-\theta_1-\theta_2}+\left(\theta_1\frac{Đ_2}{Đ_{21}}\frac{\theta_1}{1-\theta_1-\theta_2}\right)+\left(\theta_1\frac{Đ_2}{Đ_{12}}\frac{1-\theta_1}{1-\theta_1-\theta_2}\right)\right)\frac{d\theta_2}{dz}\end{array}\right] \quad \text{(A2.78)}$$

Eq. A2.78 can be also rearranged to have the derivative of the component 1 surface coverage as a function of the derivative of component 2 surface coverage as follows:

$$\frac{d\theta_1}{dz}=\frac{-\frac{N_1\left(1+\theta_2\frac{Đ_1}{Đ_{12}}+\theta_1\frac{Đ_2}{Đ_{21}}\right)}{\rho q_1^{sat}Đ_1}-\left(\frac{\theta_1}{1-\theta_1-\theta_2}+\left(\theta_1\frac{Đ_2}{Đ_{21}}\frac{\theta_1}{1-\theta_1-\theta_2}\right)+\left(\theta_1\frac{Đ_2}{Đ_{12}}\frac{1-\theta_1}{1-\theta_1-\theta_2}\right)\right)\frac{d\theta_2}{dz}}{\left(\frac{1-\theta_2}{1-\theta_1-\theta_2}+\left(\theta_1\frac{Đ_2}{Đ_{21}}\frac{1-\theta_2}{1-\theta_1-\theta_2}\right)+\left(\theta_1\frac{Đ_2}{Đ_{12}}\frac{\theta_2}{1-\theta_1-\theta_2}\right)\right)} \quad \text{(A2.79)}$$

Eq. A2.77 can be also rearranged to have Eq. A2.80:

$$\frac{-N_2\left(1+\theta_2\frac{Đ_1}{Đ_{12}}+\theta_1\frac{Đ_2}{Đ_{21}}\right)}{\rho q_2^{sat}Đ_2}=\left[\begin{array}{l}\left[\frac{1-\theta_1}{1-\theta_1-\theta_2}+\left(\theta_2\frac{Đ_1}{Đ_{12}}\frac{1-\theta_1}{1-\theta_1-\theta_2}\right)+\left(\theta_2\frac{Đ_1}{Đ_{21}}\frac{\theta_1}{1-\theta_1-\theta_2}\right)\right]\frac{d\theta_2}{dz}\\+\left[\frac{\theta_2}{1-\theta_1-\theta_2}+\left(\theta_2\frac{Đ_1}{Đ_{12}}\frac{\theta_2}{1-\theta_1-\theta_2}\right)+\left(\frac{\theta_2Đ_1}{Đ_{21}}\frac{1-\theta_2}{1-\theta_1-\theta_2}\right)\right]\frac{d\theta_1}{dz}\end{array}\right] \quad \text{(A2.80)}$$

Substituting Eq. A2.79 in Eq. A2.80 gives:

$$\frac{-N_2\left(1+\theta_2\frac{Đ_1}{Đ_{12}}+\theta_1\frac{Đ_2}{Đ_{21}}\right)}{\rho q_2^{sat}Đ_2}=\left[\begin{array}{l}\left[\frac{1-\theta_1}{1-\theta_1-\theta_2}+\left(\theta_2\frac{Đ_1}{Đ_{12}}\frac{1-\theta_1}{1-\theta_1-\theta_2}\right)+\left(\theta_2\frac{Đ_1}{Đ_{21}}\frac{\theta_1}{1-\theta_1-\theta_2}\right)\right]\frac{d\theta_2}{dz}\\+\left[\frac{\theta_2}{1-\theta_1-\theta_2}+\left(\theta_2\frac{Đ_1}{Đ_{12}}\frac{\theta_2}{1-\theta_1-\theta_2}\right)+\left(\frac{\theta_2Đ_1}{Đ_{21}}\frac{1-\theta_2}{1-\theta_1-\theta_2}\right)\right]\times\\\left(\frac{-N_1\left(1+\theta_2\frac{Đ_1}{Đ_{12}}+\theta_1\frac{Đ_2}{Đ_{21}}\right)}{\rho q_1^{sat}Đ_1}-\left(\frac{\theta_1}{1-\theta_1-\theta_2}+\left(\theta_1\frac{Đ_2}{Đ_{21}}\frac{\theta_1}{1-\theta_1-\theta_2}\right)+\left(\theta_1\frac{Đ_2}{Đ_{12}}\frac{1-\theta_1}{1-\theta_1-\theta_2}\right)\right)\frac{d\theta_2}{dz}\right)\\\left(\frac{1-\theta_2}{1-\theta_1-\theta_2}+\left(\theta_1\frac{Đ_2}{Đ_{21}}\frac{1-\theta_2}{1-\theta_1-\theta_2}\right)+\left(\theta_1\frac{Đ_2}{Đ_{12}}\frac{\theta_2}{1-\theta_1-\theta_2}\right)\right)\end{array}\right] \quad \text{(A2.81)}$$

Eq. A2.81 can be written as follows:

$$-A=\left[B\frac{d\theta_2}{dz}+C\times\left(\frac{-D-E\dfrac{d\theta_2}{dz}}{F}\right)\right] \tag{A2.82}$$

Where:

$$A=\frac{N_2\left(1+\theta_2\dfrac{Đ_1}{Đ_{12}}+\theta_1\dfrac{Đ_2}{Đ_{21}}\right)}{\rho q_2^{sat}Đ_2} \tag{A2.83}$$

$$B=\frac{1-\theta_1}{1-\theta_1-\theta_2}+\left(\theta_2\frac{Đ_1}{Đ_{12}}\frac{1-\theta_1}{1-\theta_1-\theta_2}\right)+\left(\theta_2\frac{Đ_1}{Đ_{21}}\frac{\theta_1}{1-\theta_1-\theta_2}\right) \tag{A2.84}$$

$$C=\frac{\theta_2}{1-\theta_1-\theta_2}+\left(\theta_2\frac{Đ_1}{Đ_{12}}\frac{\theta_2}{1-\theta_1-\theta_2}\right)+\left(\frac{\theta_2Đ_1}{Đ_{21}}\frac{1-\theta_2}{1-\theta_1-\theta_2}\right) \tag{A2.85}$$

$$D=\frac{N_1\left(1+\theta_2\dfrac{Đ_1}{Đ_{12}}+\theta_1\dfrac{Đ_2}{Đ_{21}}\right)}{\rho q_1^{sat}Đ_1} \tag{A2.86}$$

$$E=\frac{\theta_1}{1-\theta_1-\theta_2}+\left(\theta_1\frac{Đ_2}{Đ_{21}}\frac{\theta_1}{1-\theta_1-\theta_2}\right)+\left(\theta_1\frac{Đ_2}{Đ_{12}}\frac{1-\theta_1}{1-\theta_1-\theta_2}\right) \tag{A2.87}$$

$$F=\frac{1-\theta_2}{1-\theta_1-\theta_2}+\left(\theta_1\frac{Đ_2}{Đ_{21}}\frac{1-\theta_2}{1-\theta_1-\theta_2}\right)+\left(\theta_1\frac{Đ_2}{Đ_{12}}\frac{\theta_2}{1-\theta_1-\theta_2}\right) \tag{A2.88}$$

Eq. A2.82 can be rearranged and simplified as follows:

$$-A = \left[B\frac{d\theta_2}{dz} + C \times \left(\frac{-D - E\dfrac{d\theta_2}{dz}}{F} \right) \right] \tag{A2.89}$$

$$-A = \left[B\frac{d\theta_2}{dz} + \frac{-C \times D}{F} - \frac{C \times E\dfrac{d\theta_2}{dz}}{F} \right] \tag{A2.90}$$

$$-A + \frac{C \times D}{F} = \left(B - \frac{C \times E}{F} \right)\frac{d\theta_2}{dz} \tag{A2.91}$$

Finally the derivative of the surface coverage of component 2 is given as follows:

$$\frac{d\theta_2}{dz} = \frac{\dfrac{C \times D}{F} - A}{\left(B - \dfrac{C \times E}{F} \right)} \tag{A2.92}$$

Eq. A2.92 can be rewritten to provide the change of the component 2 surface coverage ($d\theta_2$) for any small change of the membrane thickness (dz)

$$d\theta_2 = \frac{\dfrac{C \times D}{F} - A}{\left(B - \dfrac{C \times E}{F} \right)} dz \tag{A2.92}$$

Eq. A2.79 can be also written as follows:

$$\frac{d\theta_1}{dz} = -\frac{D - (E)\dfrac{d\theta_2}{dz}}{(F)} \tag{A2.93}$$

Eq. A2.93 can be rearranged to provide the change of the component 1 surface coverage ($d\theta_1$) for any change of component 2 surface coverage ($d\theta_2$) as follows:

$$d\theta_1 = -\frac{Ddz - (E)d\theta_2}{(F)} \qquad \text{(A2.94)}$$

Based on that the proposed algorithm to evaluate the M-S exchange diffusivities ($Đ_{12}$ and $Đ_{21}$) from Eq. A2.92 and Eq. A2.94 is as follows:

Known: ρ, L, q_1^{sat}, q_2^{sat} , θ_{1h}, θ_{1l}, θ_{2h}, θ_{2l}, $Đ_1$, $Đ_2$,

Assume: $Đ_{12}$, $Đ_{21}$, N. (where N is the number of differential elements)

1- Start by dividing the membrane over all thickness (6 μm) to number of differential elements (N) equal in thickness (δz)

$$\delta z = \frac{L}{N} \qquad \text{(A2.94)}$$

2- Calculate $\delta\theta_{21}$ for the first differential element using the high pressure side values of the surface coverage ($\theta_{11} = \theta_{1h}$ and $\theta_{21} = \theta_{2h}$) and the assumed M-S exchange diffusivities ($Đ_{12}$ and $Đ_{21}$) using Eq. A2.95 (Eq. A2.92) as follows:

$$\delta\theta_{21} = \frac{\frac{C \times D}{F} - A}{\left(B - \frac{C \times E}{F}\right)} \delta z \qquad \text{(A2.95)}$$

3- Calculate $\delta\theta_{11}$ for the first differential element using the high pressure side values of the surface coverage ($\theta_{11} = \theta_{1h}$ and $\theta_{21} = \theta_{2h}$) and the assumed M-S exchange diffusivities ($Đ_{12}$ and $Đ_{21}$) as well as the $\delta\theta_{21}$ calculated by Eq. A2.95 using Eq. A2.96 (Eq. A2.94) as follows:

$$\delta\theta_{11} = -\frac{Ddz - (E)\delta\theta_{21}}{(F)} \qquad \text{(A2.96)}$$

4- Evaluate the surface coverage for both component 1 and component 2 for the second differential element (θ_{12} and θ_{22}) values using Eq. A2.97 and Eq. A2.97 as follows:

$$\theta_{12} = \theta_{11} + \delta\theta_{11} \tag{A2.97}$$

$$\theta_{22} = \theta_{21} + \delta\theta_{21} \tag{A2.98}$$

5- Calculate $\delta\theta_{22}$ for the second differential element using the values of the surface coverage calculated by Eq. A2.97 and Eq. A2.98 (θ_{12} and θ_{22}) using Eq. A2.95.

6- Calculate $\delta\theta_{12}$ for the second differential element using the values of the surface coverage calculated by Eq. A2.97 and Eq. A2.98 (θ_{12} and θ_{22}) and $\delta\theta_{22}$ calculated by Eq. A.95 using Eq. A2.96.

7- Evaluate the surface coverage for both component 1 and component 2 for the second differential element (θ_{12} and θ_{22}) values using Eq. A2.97 and Eq. A2.98.

8- Calculate $\delta\theta_{2i}$ for the ith differential element using the values of the surface coverage calculated by Eq. A2.97 and Eq. A2.98 for the ith differential element (θ_{1i} and θ_{2i}) using Eq. A2.99.

$$\delta\theta_{2i} = \frac{\frac{C \times D}{F} - A}{\left(B - \frac{C \times E}{F}\right)} \delta z \tag{A2.99}$$

9- Calculate $\delta\theta_{1i}$ for the ith differential element using the values of the surface coverage $_{1i}$ and θ_{2i} and $\delta\theta_{2i}$ calculated by Eq. A2.99 using Eq. A2.100.

$$\delta\theta_{1i} = -\frac{Ddz - (E)\delta\theta_{2i}}{(F)} \tag{A2.100}$$

10- Evaluate the surface coverage for both component 1 and component 2 for the i+1 differential element ($\theta_{1(i+1)}$ and $\theta_{2(i+1)}$) values using Eq. A2.101 and Eq. A2.102 as follows:

$$\theta_{1(i+1)} = \theta_{1i} + \delta\theta_{1i} \quad \text{(A2.101)}$$

$$\theta_{2(i+1)} = \theta_{2i} + \delta\theta_{2i} \quad \text{(A2.102)}$$

11- Continue using the same procedure until differential element number N. If the low pressure side component 1 and component 2 surface coverage values calculated using Eq. A2.101 and Eq. A2.102 match the known experimental values provided (θ_{1l} and θ_{2l}), then the assumed $Đ_{12}$ and $Đ_{21}$ values are the correct M-S exchange diffusion coefficients. If they don't match then update the $Đ_{12}$ and $Đ_{21}$ values and repeat the previous step until they match. The values of the $Đ_{12}$ and $Đ_{21}$ are updated following the optimization procedure explained in Appendix 3

Nomenclatures:

B: elements of matrix [B] defined in Eq. A2.44

B': elements of matrix [B'] defined in Eq. A2.41

c: the molar concentration (mol m^{-3})

D: the transport diffusivities (m^2 s^{-1})

D_0: corrected transport diffusivities (m^2 s^{-1})

$Đ$: Maxwell-Stefan diffusivity (m^2 s^{-1})

$Đ_{ij}$: Maxwell-Stefan exchange diffusivity between components i and j (m^2 s^{-1})

f: friction coefficient (J.s/mol.m^2)

K: Langmuir adsorption coefficient (Pa^{-1})

L: zeolite membrane thickness (m)

J: molar flux across the membrane (mol m^{-2} s^{-1})

p: partial pressure in the bulk fluid (Pa)

q: molar loading of component i (mol kg^{-1})

R: gas constant (8.314 J mol^{-1} K^{-1})

T: absolute temperature (K)

u: the flow velocity with respect to the zeolite (m s^{-1})

z: spatial coordinate (m)

Greek letters:

∇: gradient operator (m^{-1})

ε: porosity of the support (dimensionless)

Γ: elements of matrix of thermodynamic correction factor [Γ] (dimensionless)

θ: occupancy, surface coverage or fractional loading of component i (dimensionless)

μ: molar chemical potential (J mol^{-1})

ρ: density of zeolite (kg m^{-3})

τ: tortuousity (dimensionless)

Subscripts:

1, 2: components 1 and 2

i, j, k: components i, j and k

P: membrane permeate side

R: membrane retentate side

s: zeolite solid density

Superscript:

sat: saturation value

0: standard state

A2.3 References

1- R Taylor, R. Krishna, Multicomponent Mass Transfer, Wiley, New York, 1993.

2- J. Karger, D.M. Ruthven, Diffusion in Zeolites and other microporous solids, Wiley, New York, 1992.

3- D.M. Ruthven, Principles of adsorption and adsorption processes, Wiley, New York, 1984.

4- J.M. van de Graaf, E. van der Bijl, A. Stol, F. Kapteijn, J.A. Moulijn, Effect of operating conditions and membrane quality on the separation performance of composite silicalite-1 membranes, Ind. Eng. Chem. Res. 37 (1998) 4071 – 4083.

5- P. Ciavarella, H. Moueddeb, S. Miachon, K.Fiaty, Experimental study and numerical simulation of hydrogen/isobutene permeation and separation using MFI-zeolite membrane reactor, Catalysis Today 56 (2000) 253–264.

6- R. Krishna, A unified approach to the modelling of intraparticle diffusion in adsorption processes, Gas Separation Purification 7 (1993b) 91 – 104.

7- R. Krishna, Diffusion of binary mixtures across zeolite membranes: entropy effects on permeation selectivity, Int. Comm. Heat Mass Transfer 28 (2001) 337 – 346.

8- A.I. Skoulidas, D.S. Sholl, R. Krishna, Correlation effects in diffusion of CH_4/CF_4 mixtures in MFI zeolite. A study linking MD simulations with the Maxwell−Stefan formulation, Langmuir 19 (2003) 7977 – 7988.

9- J.G. Martinek, T.Q. Gardner, R.D. Noble, J.L. Falconer, Modeling transient permeation of binary mixture through zeolite membranes, Ind. Eng. Chem. Res. 45 (2006) 6032 – 6043.

Appendix 3 – Optimization Procedure

The tool used to extract the permeances (P_{CO2} and P_{N2}) as well as the exchange diffusivities ($\not{D}_{12}$ and $\not{D}_{21}$) from the gas mixtures permeation tests is a custom-built optimizer. The optimizer is developed in-house and it utilizes a combination of convex programming and a pre-determined understanding of the system.

The optimizer would attempt to determine the best combination of input variables, (CO_2 permeance and CO_2/N_2 permselectivity in the case of extracting the permeances or $\not{D}_{12}$ and $\not{D}_{21}$ in the case of extracting the exchange diffusivities) in a two-objective optimization problem, where it is tasked to minimize the difference between the estimated parameters values with the experimentally determined values. The permeate composition and the total membrane area were used for minimization parameters with extracting the permeances, while the surface coverage values at the low pressure side of the membrane for components 1 and 2 ($\Theta_{1l,}$ Θ_{1h}) were used in the case of extracting the exchange diffusivities. The optimization procedure was the same in both cases; however, the latter will be described as an example, since it was more complex than the former case.

The optimization was performed to optimize the exchange diffusivities by minimizing the difference between the estimated surface coverage (Θ_{cl}^{*}) and experimental measured surface coverage (Θ_{cl}) values at the permeate side surface for components 1 and 2 in a binary system (c = 1,2) as follows:

$$\begin{aligned} &\min_{\theta_{cl}^*}\left\{f_c\left(\theta_{cl}^*\right)\right\}, && c=1,2 \\ &\text{subject to } f_c\left(\theta_{cl}^*\right)=\left|\theta_{cl}^*-\theta_{cl}\right|\le 0, && \theta_{cl}^*\in\theta^* \end{aligned} \tag{A3.1}$$

$$\min_{\theta^*} g\left(\theta_{1l}^*,\theta_{2l}^*\right)=w_1\left(\left|\theta_{1l}^*-\theta_{1l}\right|\right)+w_2\left(\left|\theta_{2l}^*-\theta_{2l}\right|\right) \tag{A3.2}$$

The added complexity and potentially conflicting nature of this multi-objective problem, is likely to render simple trial and error methodologies as ineffective; especially if the model being optimized has a rigid and nontrivial structural design [1]. One of the methods employed to overcome such obstacles is scalarizing the multi-objective problem into a single-objective function, represented as the weighted sum of the two objectives (Eq. A3.2). This simplified approach is applicable and justified by the homogenous nature of the two objective functions [2]. The optimizer scans for a local minimum for the weighted sum of the two objectives by altering the value of the surface coverage of one component while fixing the value of the surface coverage of the other component. Then the procedure is repeated by altering the value of the surface coverage of the other component while fixing the value of the surface coverage of the first component. Depending on a specified tolerance, the optimization precision increases accordingly with each iteration performed until a global minimum is obtained.

The source code used to simulate the permeations details, for the Maxwell-Stefan exchange diffusivities, was developed separately. Moreover, using the binary mixture flux models described earlier, the simulator will estimate the concentration profile along with the film and the resulting permeate side surface coverage values, for both components, depending on the provided inputs. During an optimization session, the simulator will work in conjecture

with the optimizer in determining the exchange diffusivities. This is illustrated more clearly in Fig. A3-1 as shown below.

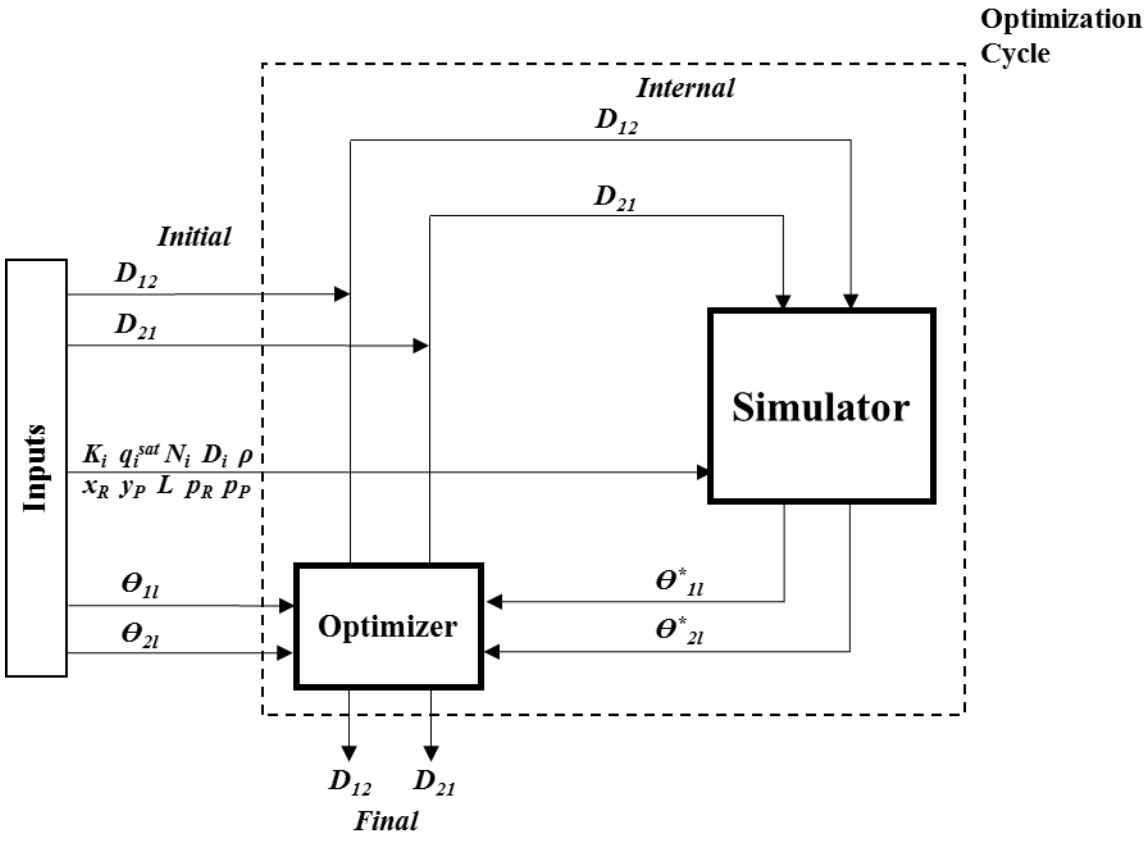

Figure A3-1 Flow chart presenting the optimization cycle and interaction between the optimizer and simulator source codes.

One of the challenges encountered during the development, was to properly assign the values of the weights (w_1, w_2) in Eq. A3.2. It was established that the weights were never constant, and always changed depending on the stage cut and feed compositions. In conditions where the permeate-side surface coverage of one component is orders of magnitude in difference with another component, a large bias would exist with one of the

component which frequently results in a non-converging situation or in solution that doesn't make sense. This is easily overcome by assigning one of the weights to unity, while the other is represented as the log mean average between the surface coverage ratios of the two components. This is shown in Eq. A3.3 and Eq. A3.4 given below:

$$w_1 = \frac{\theta_{1h}\theta_{2l} - \theta_{2h}\theta_{1l}}{\theta_{1l}\theta_{2l} \ln\left(\frac{\theta_{1h}\theta_{2l}}{\theta_{2h}\theta_{1l}}\right)} \tag{A3.3}$$

$$w_2 = 1.0 \tag{A3.4}$$

A3. References:

1- K. Deb, Multi-objective optimization using Evolutionary Algorithms, John Wiley & Sons (2001).

2- C.L. Hwang, A.S. Masud, Multiple objective decision making, methods and applications: a state-of-the-art survey, Springer-Verlag (1979).

Appendix 4 – Lowering stage cut effect on permeances and permselectivity

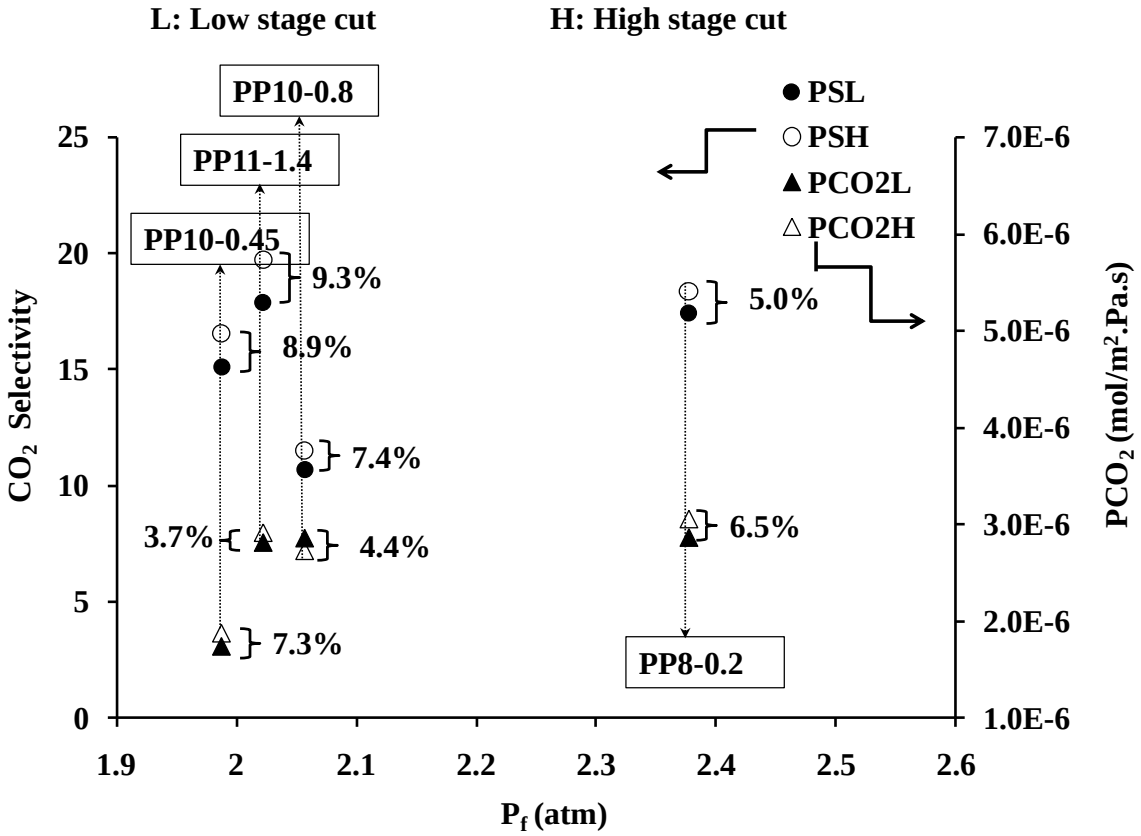

Figure A4-1 Comparison between high and low stage cut permeation experiments for four membranes synthesized on supports with different pore sizes of the active layer. All experiments performed at ambient temperature (293 K) and equimolar CO_2/N_2 feed composition with the permeate side open to atmosphere